



HAL
open science

Flexible Metal Organic Frameworks for new generation of Li-Air batteries

Yujie Zhang

► **To cite this version:**

Yujie Zhang. Flexible Metal Organic Frameworks for new generation of Li-Air batteries. Material chemistry. Université Paris-Saclay, 2022. English. NNT : 2022UPAST002 . tel-03667952

HAL Id: tel-03667952

<https://theses.hal.science/tel-03667952>

Submitted on 13 May 2022

HAL is a multi-disciplinary open access archive for the deposit and dissemination of scientific research documents, whether they are published or not. The documents may come from teaching and research institutions in France or abroad, or from public or private research centers.

L'archive ouverte pluridisciplinaire **HAL**, est destinée au dépôt et à la diffusion de documents scientifiques de niveau recherche, publiés ou non, émanant des établissements d'enseignement et de recherche français ou étrangers, des laboratoires publics ou privés.

Nouvelle génération de batteries Li-Air basées sur l'utilisation des MOFs flexibles (Metal-Organic Frameworks)

Flexible Metal-Organic Frameworks for new generation of Li-Air batteries

Thèse de doctorat de l'université Paris-Saclay

École doctorale n°573 Interfaces : matériaux, systèmes, usages (INTERFACES)

Spécialité de doctorat : Chimie

Graduate School : Sciences de l'ingénierie et des systèmes

Référent : Université de Versailles-Saint-Quentin-en-Yvelines

Thèse préparée dans l'unité de recherche **NIMBE** (Université Paris-Saclay, CEA, CNRS),
sous la direction de **Hicham KHODJA**, directeur de recherche, le co-encadrement de
Suzy SURBLE, cadre scientifique des EPIC

Thèse soutenue à Saint-Aubin, le 04 avril 2022, par

Yujie ZHANG

Composition du Jury

Thomas DEVIC

Directeur de recherche, CNRS -ST2E

Président

Rita BADDOUR-HADJEAN

Directrice de recherche, CNRS - ICMPE

Rapporteur & Examinatrice

Christophe VOLKRINGER

Professeur des universités, Centrale Lille – UCCS

Rapporteur & Examineur

Vanessa PIMENTA

Maître de conférences, ESPCI - IMAP

Examinatrice

Hicham KHODJA

Directeur de recherche, Université Paris Saclay,
CEA/IRAMIS/NIMBE/LEEL

Directeur de thèse

Titre : Nouvelle génération de batteries Li-Air basées sur l'utilisation de MOFs flexibles (Metal-Organic Frameworks)

Mots clés : batteries lithium-air, MOFs (Metal-Organic Frameworks), caractérisations structurale et électrochimique

Résumé : La technologie Li-O₂ offre des densités énergétiques très prometteuses (1700 Wh/kg vs 160 Wh/kg pour les batteries Li-ion actuelles). Cependant, leurs performances sont souvent limitées par le rendement des réactions ORR/OER, ainsi que par la formation de peroxydes de lithium Li₂O₂ bouchant progressivement les pores de la cathode. Ceci explique la perte rapide des performances après seulement quelques cycles. Les solides poreux de type MOF (Metal-Organic Framework) possèdent de grandes surfaces spécifiques et une forte porosité. Leur structure avec une charpente ouverte fournit non seulement un réseau hôte pour la diffusion des ions Li⁺ et de l'oxygène, mais aussi un espace suffisant pour le dépôt des produits de décharge. Certains MOFs présentent des propriétés de flexibilité structurale qui permettent de modifier réversiblement la taille et donc le volume des pores en fonction des molécules adsorbées et seraient aptes à stocker des produits de décharge.

L'objectif de ce travail est d'étudier les performances électrochimiques de matériaux flexibles MIL-53(Al), MIL-53(Fe). Les solides MIL-53(Al) ont été synthétisés par deux voies de synthèse conduisant à des morphologies et tailles de particules différentes.

Les analogues Al et Fe présentent des comportements de flexibilité différents : le solide MIL-53(Al) présente des pores contractés en présence de molécules hôtes tandis que les pores du solide MIL-53(Fe) sont ouverts.

Les trois solides synthétisés dans cette thèse présentent des capacités de décharge intéressantes au 1^{er} cycle (~1000 mAh/g pour MIL-53(Al) et ~2000 mAh/g pour MIL-53(Fe)). La voie de synthèse utilisée pour les solides MIL-53(Al) ne semble pas impacter les capacités de 1^{ère} décharge ou le comportement observé. En effet, dans certains cas (~33%), une étape d'activation semble nécessaire afin d'observer une capacité (ORR efficace). L'expansion de volume constatée pour le MIL-53(Fe) (ouverture des pores) semble être en faveur d'une meilleure répartition des produits de décharge mais favoriserait également leur dissolution lors de la charge de la batterie (OER efficace).

Des analyses ex-situ (XRD, SEM, XPS) ont permis d'identifier Li₂O₂ comme principal produit de décharge. Sa morphologie évolue en fonction des capacités de décharge observées (plaquettes, toroïds ou particules sphériques).

Title : Flexible Metal-Organic Frameworks for new generation of Li-Air batteries

Keywords : lithium-air batteries, MOFs (Metal-Organic Frameworks), structural and electrochemical characterizations

Abstract : Li-O₂ technology offers very promising energy densities (1700 Wh/kg vs 160 Wh/kg for current Li-ion batteries). However, their performance is often limited by the efficiency of the ORR/OER reactions, as well as by the formation of lithium peroxide Li₂O₂ that progressively clog the cathode's pores. This explains the rapid loss of performance after only a few cycles. Porous MOF (Metal-Organic Framework) solids have high specific surface areas and high porosity. Their open framework structure provides not only a host network for Li⁺ ion and oxygen diffusion, but also sufficient space for the deposition of discharge products. Some MOFs exhibit structural flexibility properties that allow the pore size and thus the volume of the pores to be reversibly modified by adsorbed molecules and would be suitable for storing discharge products.

The objective of this work is to study the electrochemical performance of flexible MIL-53(Al), MIL-53(Fe) materials. MIL-53(Al) solids were synthesized by two synthesis routes leading to different morphologies and particle sizes. The

Al and Fe analogues exhibit different flexibility behaviors: MIL-53(Al) solid pores contract in the presence of host molecules while the MIL-53(Fe) solid pores are open.

The synthesized three solids in this thesis show interesting discharge capacities in the 1st cycle (~1000 mAh/g for MIL-53(Al) and ~2000 mAh/g for MIL-53(Fe)). The synthesis route used for MIL-53(Al) solids does not seem to impact the 1st discharge capacities or the observed behavior. Indeed, in some cases (~33%), an activation step seems to be necessary in order to observe an effective ORR capacity. The volume expansion observed for MIL-53(Fe) (pore opening) seems to be in favor of a better distribution of the discharge products and would also favor their dissolution during the charging of the battery (effective OER).

Ex-situ analyses (XRD, SEM, XPS) have identified Li₂O₂ as the main discharge product. Its morphology evolves according to the observed discharge capacities (platelets, toroids or spherical particles).

Résumé

Dans un contexte de demande croissante en stockage mobile d'énergie, de nombreuses recherches sont menées pour trouver des dispositifs de forte efficacité. Les batteries Li-ion sont ainsi devenues les batteries de référence notamment pour les appareils électroniques grand public. Cependant, leurs performances en termes de capacité et d'énergies spécifiques semblent atteindre leurs limites et seront insuffisants pour les besoins à long terme de notre société. Il s'avère donc nécessaire de développer une nouvelle technologie de batteries offrant de nouvelles perspectives en matière de capacité de stockage et de sécurité, en particulier dans le domaine de l'automobile. La technologie Li-O₂ offre des densités énergétiques très prometteuses (1700 Wh/kg vs 160 Wh/kg pour les batteries Li-ion actuelles). Cependant, leurs performances sont souvent limitées par le rendement des réactions ORR/OER, ainsi que par la formation de peroxydes de lithium Li₂O₂ bouchant progressivement les pores de la cathode à air. Ceci explique la perte rapide des performances après seulement quelques cycles. Les solides poreux de type MOF (Metal-Organic Framework) possèdent de grandes surfaces spécifiques et une forte porosité. Leur structure avec une charpente ouverte fournit non seulement un réseau hôte pour la diffusion des ions Li⁺ et de l'oxygène, mais aussi un espace suffisant pour le dépôt des produits de décharge. Quelques MOFs rigides présentent de bonnes capacités de décharge en tant de cathode à air dans les batteries Li-O₂. Certains MOFs présentent par ailleurs des propriétés de flexibilité structurale qui permettent de modifier réversiblement la taille et donc le volume des pores en fonction des molécules adsorbées et seraient aptes à stocker des produits de décharge. Néanmoins, les études concernant les MOFs « pristines » pour les batteries Li-O₂ restent encore très limitées jusqu'à présent.

L'objectif de ce travail est d'étudier les performances électrochimiques de matériaux flexibles MIL-53(Al), MIL-53(Fe) et rigide MOF-5, tous trois constitués du même ligand (acide benzène-1,4-dicarboxylique). Différentes méthodes de synthèse ont été utilisées. Les solides MIL-53(Al) ont été synthétisés par voie hydrothermale et par micro-ondes. La synthèse hydrothermale du MIL-53(Al) conduit à des cristallites en plaquette de taille d'environ 2 μm, tandis que celle par micro-ondes mène à des nano-sphères de taille d'environ 500 nm. Les matériaux MIL-53(Fe) et MOF-5 ont été synthétisés par reflux. Leurs performances électrochimiques ont été explorées et rationalisées par rapport à leurs propriétés de flexibilité structurale, du mode d'ouverture des pores, et de leur morphologie. Les analogues Al et Fe présentent des comportements de flexibilité différents selon la nature du métal : le solide MIL-53(Al) présente des pores contractés en présence de molécules hôtes tandis que ceux de MIL-53(Fe) sont ouverts. La flexibilité du MOF est prometteuse pour l'amélioration de l'accueil de produits de décharge. Avec une formulation de cathode contenant une faible teneur en MOF, le solide flexible MIL-53(Al) présente une capacité de décharge initiale plus de deux fois supérieure à celle du MOF-5 (~3400 mAh/g pour MIL-53(Al) et ~1390 mAh/g pour MOF-5). Pour un teneur en MOF plus importante, les deux solides flexibles synthétisés dans cette thèse présentent des capacités de décharge intéressantes au 1er cycle : ~1000 mAh/g pour MIL-

53(Al) et ~2000 mAh/g pour MIL-53(Fe). La voie de synthèse utilisée pour les solides MIL-53(Al) ne semble pas impacter les capacités de 1^{ère} décharge ou le comportement observé. Nous avons observé un écart important de capacité de 1^{ère} décharge parmi les nombreuses électrodes testées. Dans environ 1/3 des cas, une étape d'activation au cours du 1^{er} cycle semble nécessaire afin d'observer une capacité de charge (ORR efficace). L'expansion de volume constatée pour le MIL-53(Fe) semble être en faveur d'une meilleure répartition des produits de décharge et favoriserait également leur dissolution lors de la charge de la batterie (OER efficace). Des analyses *ex-situ* (XRD, SEM, XPS) ont enfin permis d'identifier le peroxyde de lithium Li₂O₂ comme étant le principal produit de décharge. Sa morphologie évolue en fonction des capacités de décharge accumulées observées (plaquettes, toroïdes ou particules sphériques).

Acknowledgments

This thesis marks the end of an almost four-year journey at LEEL. It is not easy but it was memorable for me, particularly because of all the wonderful people that I have met and the precious moment that we passed together.

First, I would like to thank my thesis director, Hicham KHODJA, for allowing me join the LEEL to undertake this thesis work. Also, I thank him for the guidance and supports along with the thesis. Hicham's passion for science is always the source of inspiration for me.

In parallel, I would like to express my sincere gratitude to my supervisor, Suzy SURBLE, for her guidance, willingness to accompany me, and kind encouragement. I admire very much her rigorous attitude to science and profound knowledge. I appreciate also her patience for all my questions and for teaching me indispensable skills all along with my work. I would like also to thank her for enlightening me on crystallography and the complex refinement method. I would like also to thank her for the help needed at any time, whether at work or in my personal life. I would not finish this work without her support and encouragement.

I gratefully acknowledge the referees and examiners of my Ph.D. committee, Rita BADDOUR-HADJEAN, Christophe VOLKRINGER, Thomas DEVIC and Vanessa PIMENTA for their interests in my work and spending time reading my thesis. I appreciate also deeply Mme. BADDOUR-HADJEAN for her kind advice for revisions.

My appreciations also go to Magali Gauthier for her willingness to help and suggestions on the electrochemistry, for the practice of software exploration, and for contributing her time reading and correcting my thesis.

I also acknowledge gratefully for people that I used to work with for this work: the colleagues at ESPCI, Eddy FOY, Servane COSTA, Vincent MERTENS, Jocelyne LEROY. My sincere thanks go also to my office mates and colleagues for the joyful discussion and easy ambient in LEEL: Jim, Raphaël, Yann, Pascal, Ben, Irshad, Hoang, Sacris, Christian, and Hervé.

Many thanks to Yu, Bixiu, Weimin and Yang for making me at home and for the cheerful moment we created together.

Last but not least, I would like to thank my beloved family, thanks to whom I was able to follow my studies abroad. I deeply acknowledge my parents for supporting me behind unconditionally and always encouraging me whenever I need them.

行文至此，落笔为终。已经到了论文的最后一步。博士研究生涯也要告一段落了。始于2018年金秋，终于2022年初春。目之所及，皆是回忆。凡心所向，素履以往。

平生感知己，方寸岂悠悠。感谢娱，璧秀，伟民和阳对我的帮忙和照顾。感谢你们对我的关怀，让我在异国求学之余充满了回忆。花开花落总无情，唯有友情留心中。祝各位前程似锦，再相逢依旧如故。

最后，由衷地感谢我挚爱的家人们！这十年来的留学生活，特别感谢家父家母一直作为我坚强的后盾，对我无条件地支持和理解！

To my dear grandparents

致远方的爷爷，姥爷和姥姥

Glossary

Acronyms

Abbreviation	Definition
BDC	benzene-1,4-dicarboxylic acid
BE	binding energy
C_{sp}	Super P carbon black
DME	1,2-dimethoxyethane
EV	electric vehicle
H	hydrothermal
HKUST	Hong-Kong University of Science and Technology
LIB	lithium-ion battery
LiTFSI	lithium bis(trifluoromethanesulfonyl)imide
LOB	lithium-oxygen battery
MIL	Material of Institute Lavoisier
MOF	Metal Organic Framework
MW	microwave-assisted
NMP	N-Methyl-2-pyrrolidone
OCV	open circuit voltage
OER	oxygen evolution reaction
ORR	oxygen reduction reaction
PVDF	Polyvinylidene fluoride
Q₁	capacity at the first cycle
Q₂	capacity at the second cycle
R	reflux
SEI	solid electrolyte interphase
SEM	scanning electronic microscopy
TEGDME	Tetraethylene glycol dimethyl ether

Techniques

Abbreviation	Definition
BET	Brunauer-Emmett-Teller
GCPL	galvanostatic cycling with potential limitation
SEM	scanning electronic microscopy
TGA	thermogravimetric analysis
XPS	X-ray photoelectron spectroscopy
XRD	X-ray diffraction

Unit

Abbreviation	Definition
mA/g	current density with respect to the mass of MOF and C_{sp}
mAh/g	capacity with respect to the mass of MOF and C_{sp}
mg/cm²	mass loading of MOF and C_{sp} per surface
ppm	parts per million
V	voltage versus Li ⁺ /Li
wt. %	weight ratio

Table of content

Introduction.....	- 1 -
Chapter I. State of the art.....	- 9 -
I.1. Batteries overview.....	- 11 -
I.1.1. Definition and key parameters of a battery	- 11 -
I.1.2. From the voltaic pile to the development of current batteries	- 13 -
I.1.2.1. Birth of batteries.....	- 13 -
I.1.2.2. Current lithium-ion batteries.....	- 15 -
a. Cathode materials.....	- 15 -
b. Anode materials.....	- 18 -
c. Electrolyte	- 19 -
I.1.2.3. Post-lithium-ion battery technologies.....	- 19 -
a. Introduction	- 19 -
b. Technologies based on lithium metal	- 20 -
c. Technologies based on other metal cations.....	- 21 -
I.2. Li-air or Li-O₂ batteries	- 23 -
I.2.1. Principle of Li-O ₂ batteries.....	- 23 -
I.2.2. Architecture types.....	- 24 -
I.2.3. Li ₂ O ₂ formation mechanisms	- 26 -
I.2.3.1. Surface mechanism vs. solution-mediated mechanism	- 26 -
I.2.3.2. Li ₂ O ₂ morphology	- 28 -
I.2.3.3. Properties of the electrolytes in Li-air batteries	- 30 -
a. Solvent - 30 -	
b. Salt anions	- 32 -
I.2.4. Challenges of Li-O ₂ batteries.....	- 32 -
I.2.4.1. Safety issues of lithium metal.....	- 33 -
I.2.4.2. Active singlet oxygen intermediate formation	- 34 -
I.2.4.3. Air cathode challenges.....	- 35 -
I.2.5. Air cathode development	- 37 -
I.2.5.1. Carbon-based materials	- 37 -
I.2.5.2. Carbon-free materials	- 40 -
I.2.6. Reproducibility issue	- 42 -
I.3. Metal-Organic Frameworks.....	- 43 -
I.3.1. Definition.....	- 43 -
I.3.2. Isoreticular chemistry and functionalization.....	- 45 -
I.3.3. Well-known MOFs.....	- 47 -
I.3.3.1. Rigid solids	- 47 -
I.3.3.2. Flexible solids	- 50 -

I.3.4. Overview of MOF applications	- 54 -
I.3.4.1. Generalities.....	- 54 -
I.3.4.2. MOFs for energy applications	- 55 -
a. Fuel cell.....	- 55 -
b. Li-ion battery	- 57 -
c. Li-S battery	- 59 -
I.3.4.3. MOF for Li-O ₂ battery applications	- 61 -
a. Pristine MOFs.....	- 61 -
b. MOF derivatives and MOF composites.....	- 65 -
I.4. Conclusion.....	- 67 -
I.5. References.....	- 68 -
Chapter II. Experimental procedures	- 83 -
II.1 Synthesis routes.....	- 85 -
II.1.1. Conventional solvothermal synthesis.....	- 85 -
II.1.2. Microwave-assisted solvothermal method	- 86 -
II.1.3. Reflux synthesis.....	- 87 -
II.2 Electrochemical characterization.....	- 88 -
II.2.1. Preparation of electrodes and electrolyte	- 88 -
II.2.1.1. Preparation of air cathode	- 88 -
II.2.1.2. Preparation of electrolyte.....	- 90 -
II.2.2. Battery assembly	- 91 -
II.2.3. Galvanostatic cycling with potential limitation.....	- 92 -
II.3 Structural and physical characterizations.....	- 93 -
II.3.1. X-ray diffraction.....	- 93 -
II.3.1.1. X-ray basis: X-ray/material interactions	- 93 -
II.3.1.2. Apparatus and experimental setup.....	- 94 -
a. MIL-53 materials and pristine electrode analyses	- 94 -
b. <i>Ex situ</i> MIL-53 electrode analyses.....	- 94 -
II.3.2. Thermogravimetric analysis	- 95 -
II.3.3. Brunauer-Emmett-Teller measurement	- 95 -
II.3.4. Scanning electron microscopy.....	- 96 -
II.3.5. X-ray photoelectron spectroscopy.....	- 97 -
II.4 References.....	- 98 -

Chapter III. Synthesis and characterizations.....	- 101 -
III.1 The flexibility of MIL-53.....	- 103 -
III.2 Synthesis and characterizations	- 105 -
III.2.1. Synthesis.....	- 105 -
III.2.2. Structure characterizations.....	- 106 -
III.2.3. Other characterizations	- 109 -
III.3 Studies of the breathing transition	- 111 -
III.4 Conclusion	- 114 -
III.5 References.....	- 116 -
Chapter IV. MOF electrode cycling performances	- 119 -
IV.1 Flexible MOF	- 121 -
IV.1.1. MIL-53(Al).....	- 121 -
IV.1.1.1. MW-MIL-53(Al) electrochemical behavior and performances.....	- 121 -
IV.1.1.2. H-MIL-53(Al) electrochemical behavior and performances.....	- 124 -
IV.1.1.3. Effect of morphology.....	- 125 -
IV.1.2. MIL-53(Fe)	- 127 -
IV.1.2.1. Introduction.....	- 127 -
IV.1.2.2. Electrochemical behavior and performance of MIL-53(Fe).....	- 128 -
IV.1.3. Conclusion on the pore opening effect.....	- 131 -
IV.2 Rigid vs. flexible MOF	- 131 -
IV.2.1. Electrochemical behavior and performance of R-MOF-5	- 132 -
IV.2.2. Comparison with MIL-53(Al) and effect of flexibility	- 134 -
IV.3 Discussion	- 136 -
IV.3.1. Comparison with literature	- 137 -
IV.3.2. Reproducibility issues	- 139 -
IV.4 Conclusion.....	- 142 -
IV.5 References.....	- 144 -

Chapter V. <i>Ex situ</i> characterizations	- 147 -
V.1 Nature and morphology of discharge products.....	- 149 -
V.1.1. <i>Ex situ</i> X-ray diffraction.....	- 149 -
V.1.2. <i>Ex situ</i> scanning electronic microscopy.....	- 153 -
V.2 X-ray photoelectron spectroscopy investigations	- 159 -
V.3 Conclusion.....	- 161 -
V.4 References	- 163 -
General conclusion.....	- 165 -
References	- 169 -
Appendixes	- 171 -
Appendix 1- List of chemical products.....	- 173 -
Appendix 2- Synthesis and characterization of MOF-5.....	- 174 -
Appendix 3- Nitrogen adsorption isotherm of MIL-53(Al).....	- 179 -
Appendix 4- C_{sp} cathode electrochemical performance	- 180 -
Appendix 5- <i>Ex situ</i> characterization of C_{sp} carbon cathode	- 185 -

Introduction

The development of the societies has benefited deeply from the energy source. The energy mix system has been transformed dramatically since the Industrial Revolution in the mid-18th century. Since then, four successive industrial revolutions (Figure 1) have liberated people from the labor, increased the production of goods, and boosted the economy and technological innovations, as well as the standard of living [1].

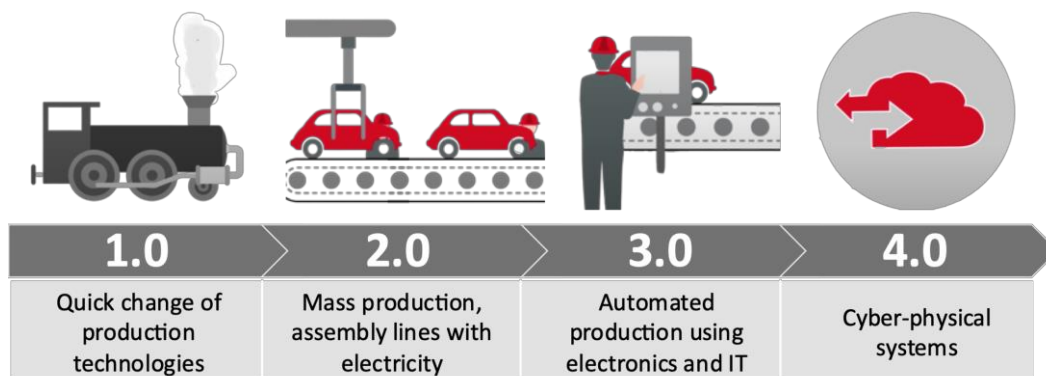
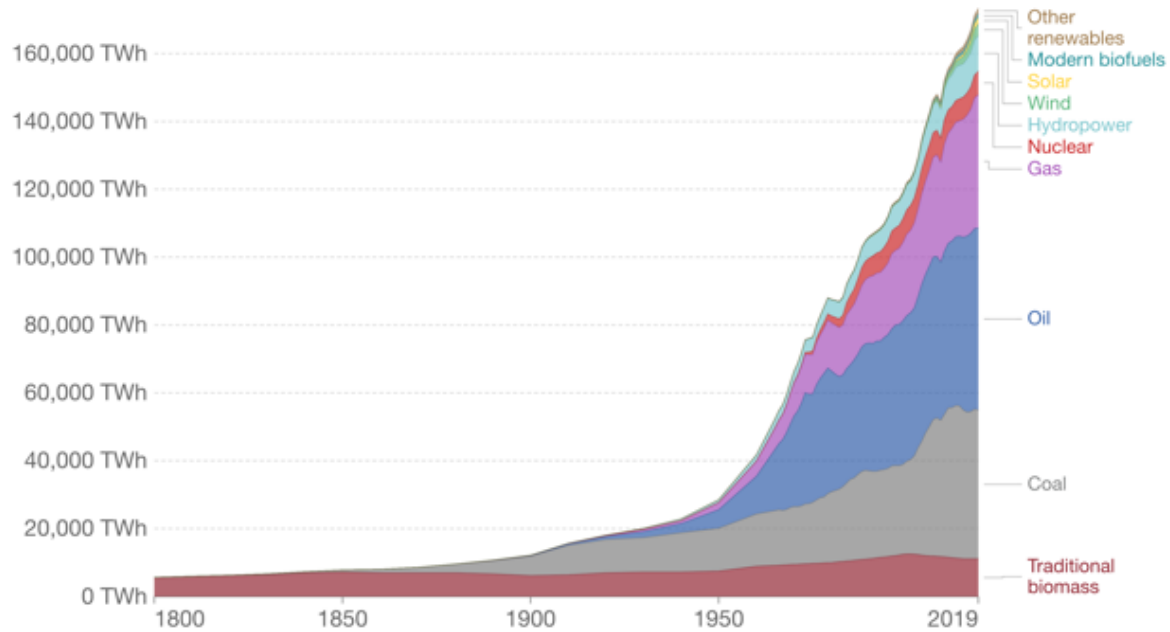


Figure 1 : Overview of the Industrial Revolutions and the future view. Compilation from Desoutter Industrial Tools [1].

Society development brought the rise of coal, followed by oil and gas. Demand for energy has continuously increased across the world with the economic and population growth year by year. The search for alternative renewable energies due to the limited storage of fossil fuels on our planet never stops. The modern renewables, excluding hydropower which came by the turn of the 20th century, solar, and wind, were only added in the 1980s. Nowadays, the global energy mix of many countries is still relying heavily on fossil fuels, which account for more than 80 % of the energy consumption (Figure 2) [2].

Global primary energy consumption by source

Primary energy is calculated based on the 'substitution method' which takes account of the inefficiencies in fossil fuel production by converting non-fossil energy into the energy inputs required if they had the same conversion losses as fossil fuels.



Source: Vaclav Smil (2017) & BP Statistical Review of World Energy

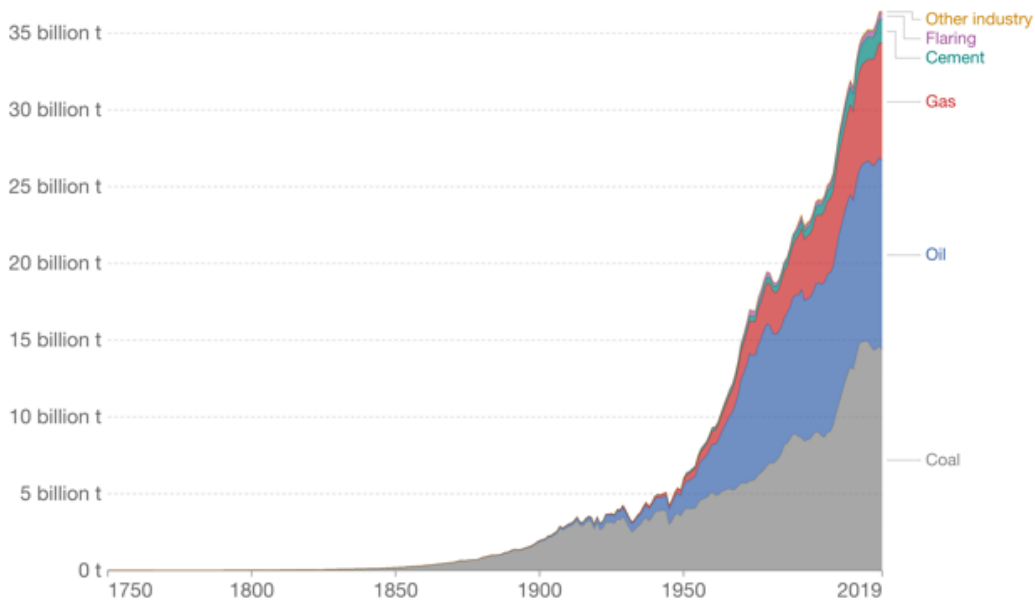
OurWorldInData.org/energy • CC BY

Figure 2 Global primary energy consumption by source. Copyright from OurWorldData.org.

As a result, the current energy mix state is implicated deeply for the global climate, since three-quarters of global greenhouse gases (CO₂, N₂O, NH₄, CFC) come from the consumption of fossil fuels [2]. Over the last few decades, global temperatures have risen sharply to approximately 0.7°C higher than in 1961-1990. When extended back to 1850, temperatures were a further 0.4°C colder than the baseline. Overall, this would amount to an average temperature rise of 1.1°C (Figure 3). The changing climate has a range of potential ecological, physical, and health impacts, including extreme weather events (such as floods, droughts, storms, and heatwaves); sea-level rise; altered crop growth; and disrupted water systems [3]. It's urgent to make efforts for reducing CO₂ emissions by shifting towards low-carbon sources of energy and renewable technologies.

CO₂ emissions by fuel type, World

Annual carbon dioxide (CO₂) emissions from different fuel types, measured in tonnes per year.

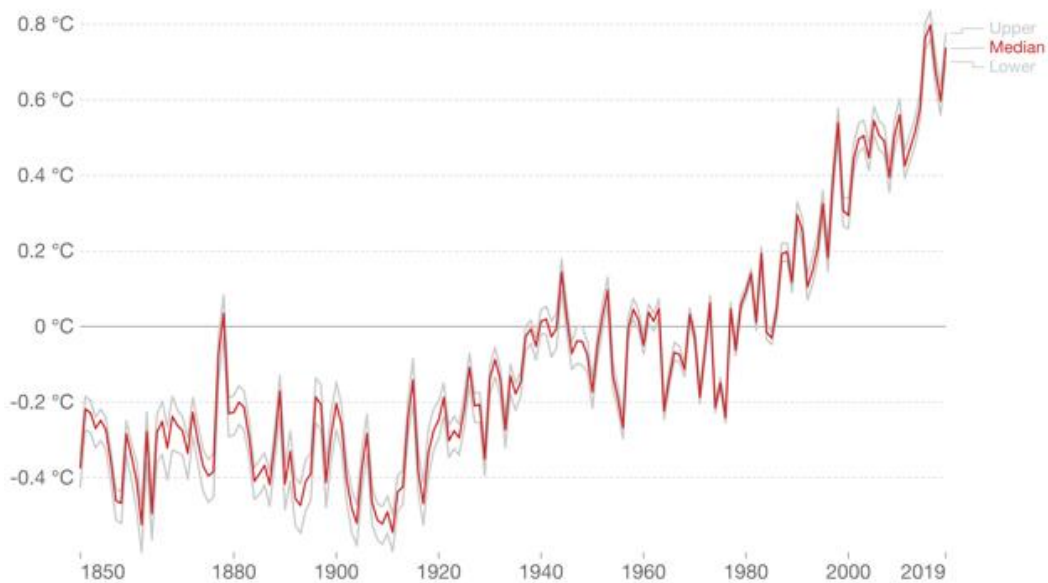


Source: Global Carbon Project

OurWorldInData.org/co2-and-other-greenhouse-gas-emissions/ • CC BY

Average temperature anomaly, Global

Global average land-sea temperature anomaly relative to the 1961-1990 average temperature.



Source: Hadley Centre (HadCRUT4)

OurWorldInData.org/co2-and-other-greenhouse-gas-emissions • CC BY

Note: The red line represents the median average temperature change, and grey lines represent the upper and lower 95% confidence intervals.

Figure 3 Correlation between (top) the CO₂ emission by fuel consumption and (bottom) the global warming anomaly. Copyright from OurWorldData.org.

Among the low-carbon source of energy, the hydroelectric power accounts for more than 60 % of the renewable sources (except traditional biomass) [2]. Even though this energy is ecological and renewable, it is intermittent and requires devices for conversion, storage, and transportation. Among the diverse developed energy storage systems, the electrical storage devices take advantage of portability and lowering the energy supply costs.

The battery has been considered as the current reference energy storage device, especially the lithium-ion batteries (LIBs), since the first commercialization by Sony in 1991 [4]. The current LIBs are dominating largely the market for portable devices and are broadening largely their markets in the field of electric vehicles (EV). The total LIB market capacity size is projected to reach more than a seven-fold increase to over 1.2 TWh by 2030 (from 160 GWh in 2018), especially for the automotive field (Figure 4 (a)). It is expected to grow at a compound annual growth rate (CAGR) of 12.3 % for the next decade [5]. LIBs for automotive applications have shown rapid development; as shown in Figure 4 (b), the global market share of electric vehicles within new vehicles sold has increased from 3.3 % in 2015 to 19.5 % in 2020 [6].

Moreover, driven by the surging requirement for continuous power supply from critical infrastructures in wake of the sudden pandemic COVID-19, demands have been significantly affected by the economic repercussion for EVs, battery-operated material-handling equipment in industries due to automation, and smart devices.

Besides, some governments implement also incentive policies for pushing the EV's development. For instance, Europe's global car market contracted 22 % in 2020. Yet, new EV registrations increased a sale share of 10 % to 1.4 million. Norway reached a record high sales share of 75 %, up about one-third from 2019. Sale shares of EV exceeded 32 % in Sweden and reached 25 % in the Netherlands. In the largest market, Germany registered 395 000 new EVs, and France registered 185 000. The United Kingdom more than doubled registrations to reach 176 000. While in some other countries, EV markets saw sale shares of 4.2 % (Canada), 2.9 % (Korea), and 0.6 % (Japan), respectively (Figure 4 (c)). Despite the encouragement for enlarging the users, but also better battery performance is required to value the EVs competition. High power and high energy batteries ensuring a long-distance driving (> 500 km) and fast charging (< 30 min for 80 % state of charge) for electric vehicles are also required [7].

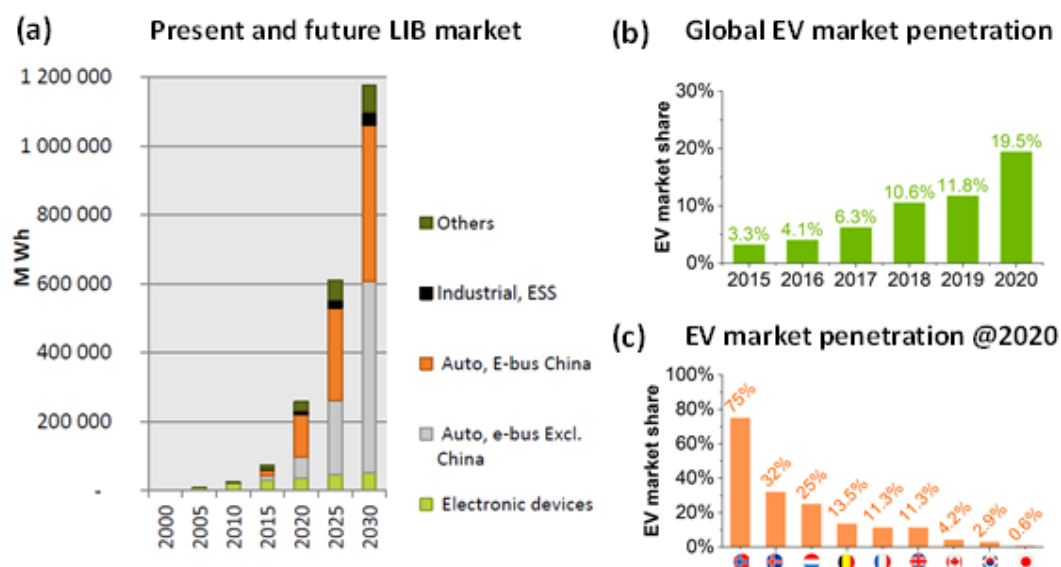


Figure 4 (a) The present and future (predicted values in 2019-2030) LIB market including electronic devices, EVs (auto, E-bus), industrial & stationary (ESS) energy, and others (medical devices, power tools, gardening tools, e-bikes...). Copyright AVICENNE ENERGY 2019. (b) Global EV market share in the new car sales from 2015-2020, and (c) the EV market penetration of different countries within its total domestic vehicles sold in 2020. Compilations from IEA Global EV Outlook 2021.

Considering the overall intense energy demand, we are urged to develop new electrode materials and technology with higher power and energy density to maintain the well-being of our society. Among the alternative light batteries, the lithium-air (Li-air) batteries have attracted much attention for the last two decades thanks to their high energy theoretical discharge capacity (1168 mAh/g_{Li}) and cost-competitive source from the air. The Li-air batteries could offer 5-10 times higher capacities than the current LIBs, in theory. Even though Li-air batteries have a high energy density (11140 Wh/kg) comparable to that of gasoline, they are still far from practical due to material challenges.

A Li-air battery consists of a porous air cathode, electrolyte impregnated separators, and a lithium anode. The discharge products generate from the reaction of lithium ions and the O₂. These products need to be stored inside the air cathode and thus releasing electrons during the charge. One of the major challenges for the Li-air battery is the proper porous material in the air cathode. Their performances are limited by the rapid capacity loss within a few discharge/charge cycles due to the decreased available porosity.

MOFs have been known for their highly porous structure. The MOFs and their derivatives have been already explored in lithium batteries as active materials (Li-ion, Li-S, Li-air). Among them, some materials show structural flexibility upon adsorbing guest molecules, which makes it promising to accommodate the discharge products in the Li-air batteries.

This thesis enrolls into the research of a flexible MOF material - MIL-53- as air cathode in the Li-air batteries, including the preparation and characterizations of the MIL-53 air cathode and characterizations of discharge products on the cycled air cathodes in the aprotic Li-air batteries. The air cathode based on MIL-53 is then also compared to other MOF compositions.

This work is thus divided into five chapters:

Chapter I starts with a general introduction to the basic concepts of different types of batteries and the applications of porous MOF materials as active material in batteries. The state-of-the-art and the current issues are summarized.

Chapter II focuses on synthesis methods used for our work (conventional solvothermal, microwave-assisted solvothermal, and reflux syntheses) and gives the details for the preparation of MIL-53 electrodes and for the battery assembly. We then describe the experimental characterization techniques, including structural and physical characterizations of the MOF materials (XRD, TGA, BET, and SEM), electrochemical characterization of the Li-Air battery (GCPL), identification of the discharge products (*ex situ* characterizations: XRD, SEM, and XPS).

Chapter III explores in detail the synthesis and structural / physical characterizations of two flexible MIL-53 analogues (Al, and Fe). At first, we synthesize the MIL-53(Al) with conventional hydrothermal and microwave-assisted hydrothermal methods, and the MIL-53(Fe) with reflux method. The obtained MIL-53 solids are characterized by a combination of techniques (XRD, TGA and BET, and SEM). The special flexibility of MIL-53 with the solvents used (PVDF@NMP, NMP) for the preparation of air cathode in Li-air batteries is also investigated by XRD. Discussions of breathing behaviors concerning MIL-53(Al) with two synthesis methods, as well as the two analogues will end this chapter.

Chapter IV addresses the studies for electrochemical performances of the MIL-53 air cathodes in the Li-air batteries. With a high MOF content electrode formulation, on one hand, we investigate the influence of MIL-53(Al) crystallite size over the battery performance; on the other hand, we discuss how the breathing behaviors with MIL-53(Al) and MIL-53(Fe) impact the discharge product accommodation upon cycling. In addition, we compare the electrochemical performance between the flexible MIL-53 and the reported robust material MOF-5 with a low MOF content electrode formulation. At last, the general electrochemical behavior of these MOF electrodes will be discussed.

Chapter V is dedicated to the characterizations of discharge products on the MIL-53 air cathodes after discharge-charge cycling. We reveal the lithium peroxide as the main discharge product by XRD identification and observe their morphologies over cycles with all MIL-53 air cathodes. We hence promote a possible growth mechanism of Li_2O_2 particles. Beyond the above Li_2O_2 identification, we explore deeper the surface chemical composition of the discharged cathodes with XPS.

The main results of this PhD work are summarized at the end, their impacts and implications on further battery research are discussed along with the remaining issues.

References

- [1] "Social Effects of the Industrial Revolution", <https://www.lcps.org/cms/>.
- [2] "Hannah Ritchie and Max Roser", 2020. <https://ourworldindata.org/energy-mix>."
- [3] "Fifth Assessment Report IPCC.", 2021 <https://www.ipcc.ch/assessment-report>.
- [4] J.-M. Tarascon, "Histoire et évolution des technologies d'accumulateurs," 2011.
- [5] "Lithium-Ion Battery Market Size Trends Global Forecast to 2030 | MarketsandMarkets™ <https://www.marketsandmarkets.com/Market-Reports/lithium-ion-battery-market-49714593.html>..
- [6] "Global EV Outlook 2021", IEA. <https://www.iea.org/reports/global-ev-outlook-2021>, <https://www.iea.org/reports/global-ev-outlook-2021,%20https://www.iea.org/reports/global-ev-outlook> .
- [7] Y. S. Meng, "Introduction: Beyond Li-Ion Battery Chemistry", *Chem. Rev.*, vol. 120, n° 14, pp. 6327–6327, 2020.

Chapter I. State of the art

Recently, Metal-Organic frameworks (MOFs) appeared as an emerging class of materials for electrochemical energy storage. This chapter will first give an overview of the different battery technologies, commercialized or still in development. Then in the second part, we will describe the motivation of this thesis: the lithium-air batteries, with their principle, limitations, and the current state of the art in terms of cathode materials. The MOF materials and their potential applications, such as gas storage, biomedicine *etc.*, and especially as electrode materials for battery applications will be presented in a third part.

I.1. Batteries overview

I.1.1. Definition and key parameters of a battery

A battery consists of a combination of electrochemical cells in a series or in parallel that converts chemical energy into electrical energy. The term “battery” is commonly used to define a single cell in the scientific community, which would be the case in this manuscript. A battery is composed of a negative electrode and a positive electrode (called commonly anode and cathode respectively) immersed in an electrolyte and isolated by a separator (Figure I-1). Batteries store and produce electrical energy through oxidation-reduction processes. The redox reactions occur both at the negative electrode and at the positive electrode – during the discharge: oxidation at the negative electrode and reduction at the positive electrode; the roles are reversed during the charge: reduction at the negative side and oxidation at the positive one. During discharge, ions produced from oxidation migrate from the negative electrode to the positive electrode through the electrolyte. Electrons travel through the external circuit to the positive electrode. While the battery is charging, an external current is applied to cause a reversal of the redox reactions and migration of the charged species from the positive electrode to the negative electrode. In the thesis, we will use the terms “anode” for the negative electrode and “cathode” for the positive electrode, regardless of the reactions occurring.

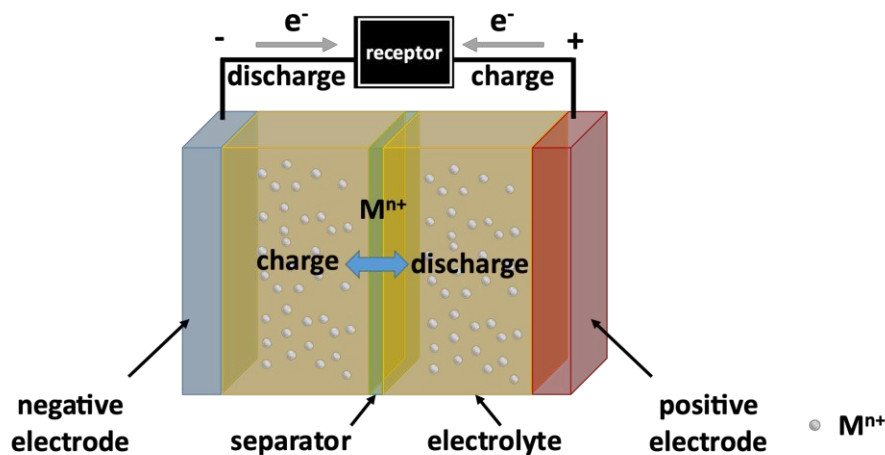


Figure I-1 : Schematic representation of an electrochemical cell.

The nature of the electrodes used imposes an electrochemical potential, which is equivalent to the potential difference of the redox reactions that take place at each electrode. This **potential E** is of the order of a few volts and varies depending on the state of charge. The **capacity Q** – expressed in ampere-hour (Ah) – corresponds to the maximum electric charges that an electrochemical cell can store during the discharge or supply during the charge. This quantity corresponds to the number of electrons that a battery or an active material can exchange (Equation I-1).

$$Q = \int_0^t I(t) dt \quad \text{Equation I-1}$$

In order to compare the active materials with each other, the scientific community has defined the **theoretical specific capacity C** of the electrode material itself. It corresponds to the amount of electricity stored in the material, which is usually expressed in mAh/g. It is defined by the number of ions inserted relative to the molar mass of active material present in the electrode according to the Faraday's law (Equation I-2):

$$C = \frac{x z F}{M} \quad \text{Equation I-2}$$

F - Faraday constant (96485 C/mol)

x - number of inserted ions

z - charge number of intercalated ion

M - molar mass of active material (in g/mol)

The **stored energy ϵ** corresponds to the product of the capacity Q by the potential E , and is expressed in watt-hours (Wh) or joule (J). The energy density can be reported by weight (gravimetric energy density – Wh/kg) or by volume (volumetric energy density –Wh/L). To increase the energy of a battery, it is therefore necessary to increase either its capacity Q or its potential E (Figure I-2).

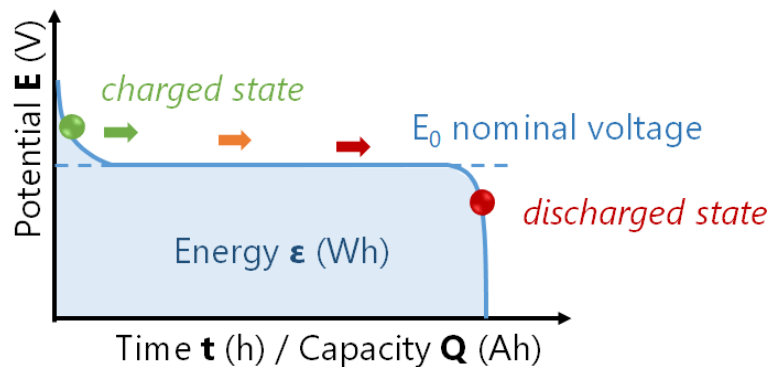


Figure I-2 : Typical discharge curve of a battery.

The **Coulombic efficiency CE** is the ratio (expressed in percentage) between the charge capacity and the discharge capacity over a full cycle.

The **open-circuit voltage E_{ocv}** corresponds to the difference of the potential across the electrodes of the battery when no current is flowing. The **overpotential η** is the potential difference (voltage) between the half-reaction thermodynamic reduction potential E_0 and the potential at which the redox reaction is observed experimentally.

I.1.2. From the voltaic pile to the development of current batteries

I.1.2.1. Birth of batteries

Figure I-3 presents an overview of the development of battery technologies since the discovery of the **voltaic pile** by the Italian scientist Alessandro Volta in 1800. The voltaic pile consists of a stack of copper and zinc plates separated by cloth soaked in a saline solution [1]. In 1802, William Cruickshank invented the **trough battery** – a variant of the voltaic pile – built from brine-soaked pieces of cloth sandwiched between zinc and copper discs, piled in a stack [2].

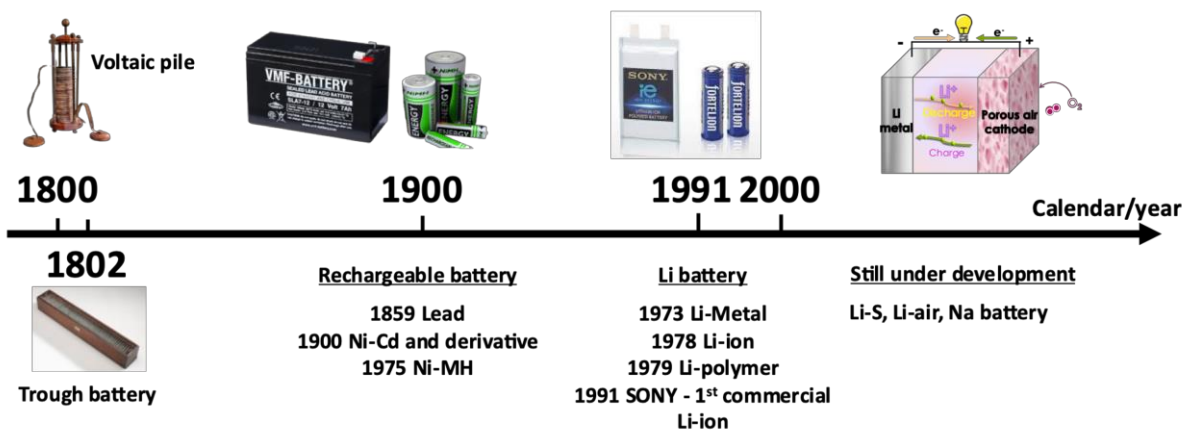


Figure I-3 : Timeline development of batteries.

In 1859, the French physicist Gaston Planté created the first rechargeable battery (**lead-acid battery**). It consists of a spiral roll of two sheets of pure lead separated by a linen cloth immersed in a glass container filled with a solution of sulfuric acid. It has the advantage of delivering high currents but suffers from low energy densities (25 - 55 Wh/kg) and a short lifespan (200 - 300 cycles). They are still used in traditional combustion vehicles [3].

In the 1900s, others technologies emerged such as **Nickel-Cadmium** (Ni-Cd) batteries or their derivatives **Nickel-Iron** (Ni-Fe), **Nickel-Zinc** (Ni-Zn) [1]. These rechargeable batteries have the same nickel oxide hydroxide cathode (NiOOH) and alkaline electrolyte (potassium hydroxide KOH), but the metallic anode varies with the type of batteries (Cd, Fe, or Zn). These systems are generally used in applications requiring a long lifespan such as emergency medical equipment, professional cameras, or two-way radios. Since 2006 the Ni-Cd batteries have been prohibited due to cadmium toxicity.

In 1988, the **Nickel-Metal Hydride (Ni-MH)** battery replaced the Ni-Cd battery [1]. The cathode is still the hydroxide oxide nickel whereas the anode is now made of a hydrogen-absorbing alloy and not a "consumption" anode. The Ni-MH battery was used to power the first generation of commercialized hybrid vehicles such as the Toyota Prius in 1997. However, its specific energy density is still relatively low (80 Wh/kg).

In order to increase the specific and volumetric energies, lithium is considered as a good anode candidate. Indeed, lithium is the lightest metal ($M = 6.94 \text{ g/mol}$) and the most reducing element (-3.04 V vs. standard hydrogen electrode (SHE)), which provides a high cell potential. It also possess a high capacity (3860 mAh/g). In the 1970s, Whittingham proposed the first **lithium-metal battery** based on intercalation materials such as MoS_2 and TiS_2 [4]. The specific energy of lithium-metal batteries is more than two times higher than other technologies. Unfortunately, due to the strong reaction of lithium metal with the electrolyte, this technology presents significant safety problems which limit its commercialization [1]. This is due to the formation of dendrites, leading to short-circuits and in some cases to explosions. This point will be developed in Section I.2.4.1. Two strategies are then considered to prevent the safety issue: the replacement of the electrolyte or of the lithium metal anode.

Yoshino discovered that petroleum coke could reversibly intercalate lithium ions at a low potential of $\sim 0.5 \text{ V}$ vs. Li^+/Li without structural destruction [5]. In parallel, Goodenough *et al.* proposed in 1979 to use a cathode material based on lamellar lithium cobalt LiCoO_2 [6]. Later in 1991, Sony commercialized the first lithium-ion battery based on two intercalation materials: a LiCoO_2 cathode and a LiC_6 anode with a liquid electrolyte [7]. The Nobel Prize in Chemistry 2019 [8] was awarded to Goodenough, Whittingham, and Yoshino for their great contributions to the development of the current **lithium-ion batteries** (LIBs). To this day, this technology is still prominent in our life as it equips various mobile applications. However, Li-ion batteries have a high cost and also can present safety issues due to the use of flammable electrolytes.

In 1980, Armand proposed replacing the liquid electrolyte with a polymer such as polyethylene oxide (PEO) coupled with a lithium salt, that prevents the formation of lithium dendrite [9]. The **lithium metal polymer battery** with a solid polymer electrolyte appears safer thanks to the use of a volatile solvent-free technology. However, the conductivity of the electrolyte at room temperature is low and requires an increase of the operating temperature ($\sim 70^\circ\text{C}$). Despite the above limitation, this technology has been developed for electric vehicles as in the Bluecar by Bolloré [10].

Figure I-4 compares the energy densities for the different battery technologies mentioned above. Although the energy density of LIBs has increased gradually since their discovery, they seem to reach their limits and will be insufficient for the long-term needs of our society. In the next section, we will present the current Li-ion batteries to better understand their limitations.

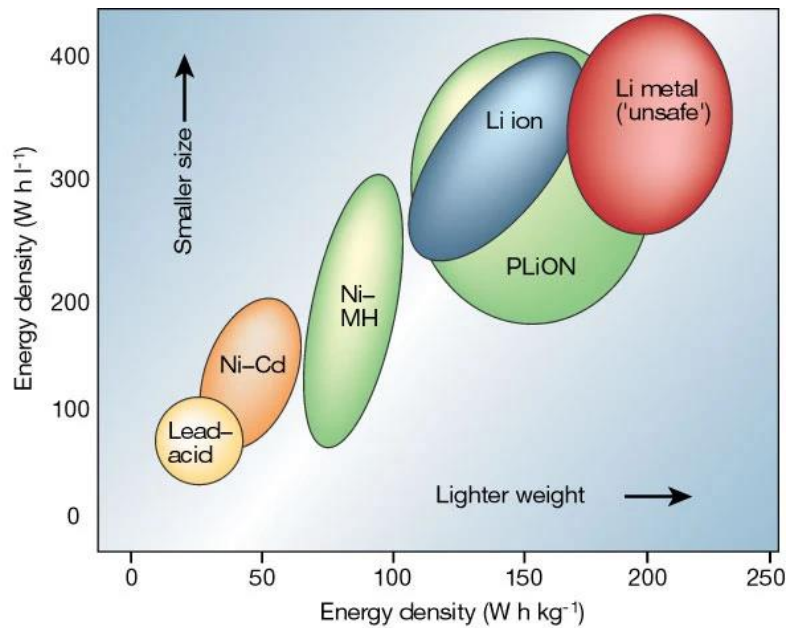
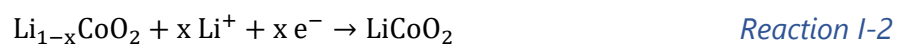


Figure I-4 : Ragone plot of the different battery technologies. Reprinted from [11].

I.1.2.2. Current lithium-ion batteries

Since the commercialization of the first rechargeable **Li-ion battery** (LIB) by Sony in 1991 [7], the demand and improvement in energy density for LIBs have increased rapidly, driven by the development of portable devices and electric vehicle market.

Currently, the LIB relies mainly on the Li^+ intercalation mechanism in cathode and anode materials. In the conventional LiCoO_2 / graphite LIB, the electrode reactions during discharge can be written as:



During the discharge, the oxidation of the anode leads to the deintercalation of Li^+ ions from the graphite laminar structure. In opposition, Li^+ ions intercalate in cathode by a reduction reaction of the LiCoO_2 with electrons coming from the anode through the external circuit. By applying an opposite current, these reactions are forced in the opposite direction and then allow to charge the battery.

To increase energy density and overcome the safety issues of lithium metal, the research focuses on finding higher voltage cathode materials and / or other Li-containing compounds that can replace lithium metal at the anode.

a. Cathode materials

As mentioned earlier, the nature of the electrodes used determines the working potential of the battery. The oxides family is extensively studied as it gives higher potentials compared to chalcogenides (TiS_2 , MoS_2 ,...) [12].

Layered oxides with the formula LiMO_2 ($M=\text{Co}, \text{Mn}, \text{Ni}$) are the most used /commercialized cathode materials for LIBs. LiCoO_2 (Figure I-5 (a)) was first suggested as intercalation compound by Goodenough *et al.* [6] and then commercialized by Sony [7]. This material is still used in commercial batteries. A capacity of only 140 mAh/g is obtained experimentally with LiCoO_2 , much lower than the theoretical one (274 mAh/g). It is in fact difficult to remove more than 0.5 Li^+ without damaging the structure [13]. To solve this issue, it is necessary to decrease or remove the Co content by a partial or total substitution, notably with Ni. Among the nickel-based layered oxide compounds, the NCA and the NMC families – with the formula $\text{Li}(\text{Ni}_{1-x-y}\text{Co}_x\text{Al}_y)\text{O}_2$ and $\text{Li}(\text{Ni}_x\text{Mn}_y\text{Co}_z)\text{O}_2$ respectively – are identified as potential high specific capacity materials with working potential larger than 4 V vs. Li^+/Li . Some NMC and NCA cathode materials are already commercialized; for example, the phase NMC-811 is commercialized by the Chinese company Contemporary Amperex and a NCA from Panasonic is already deployed in the Tesla Model 3 batteries [14].

The Li-rich compounds – with the formula $y\text{Li}_{2-x}\text{MnO}_3 \cdot (1-y)\text{Li}_{1-x}\text{MO}_2$ (with $M=\text{Ni}, \text{Co}, \text{Mn}$) or $\text{Li}_{1+y}\text{M}_{1-y}\text{O}_2$ – are obtained by substituting the metallic cations in the MO_2 layer by lithium (Figure I-5 (a)). These electrodes can provide specific capacities larger than 250 mAh/g in a wide potential range (2.0 - 4.8 V vs. Li^+/Li), even often higher than their theoretical capacities [15]. This phenomenon is explained by the redox activity of the anion network (or oxide ions) that adds to the usual cationic redox [16], [17].

Among Co-free materials, the spinel LiMn_2O_4 benefits from good structural stability, a 3D lithium diffusion pathway in vacant interstitial sites (Figure I-5 (b)), as well as high electrical and Li^+ ion conductivities, thereby allowing a high operating voltage of 4.1 V vs. Li^+/Li [18], [19]. However, its practical specific capacity is in the range of 100 -120 mAh/g for about 700 cycles [13]. Moreover it suffers from a dissolution of Mn from the lattice when H^+ traces exist in the electrolyte. One alternative to improve the structural stability of LiMn_2O_4 is the partial substitution of Mn^{4+} by Ni^{2+} or Fe^{2+} [20], [21]. Especially, the $\text{LiNi}_{0.5}\text{Mn}_{1.5}\text{O}_4$ could operate at about 4.7 V vs. Li^+/Li with a capacity of about 90 mAh/g, resulting in a high energy density. However, this substituted spinel solid suffers from capacity fading due to the lack of stable electrolyte operating at such high voltages [21].

Other structures have been investigated as potential high voltage cathode materials. Among the polyanion class of cathode materials, the olivine LiFePO_4 (Figure I-5 (c)) is considered as a promising cathode due to its low cost, abundance, and environmental friendliness [22]. It achieves a specific capacity of 170 mAh/g (close to its theoretical capacity) with a good cyclability. Besides its low energy density, the LiFePO_4 suffers from a low electronic conductivity. The low electronic conductivity can be further solved by carbon coating or making a composite with carbon.

An overview of aforementioned representative crystal structures of intercalation cathode materials for LIBs is shown in Figure I-5.

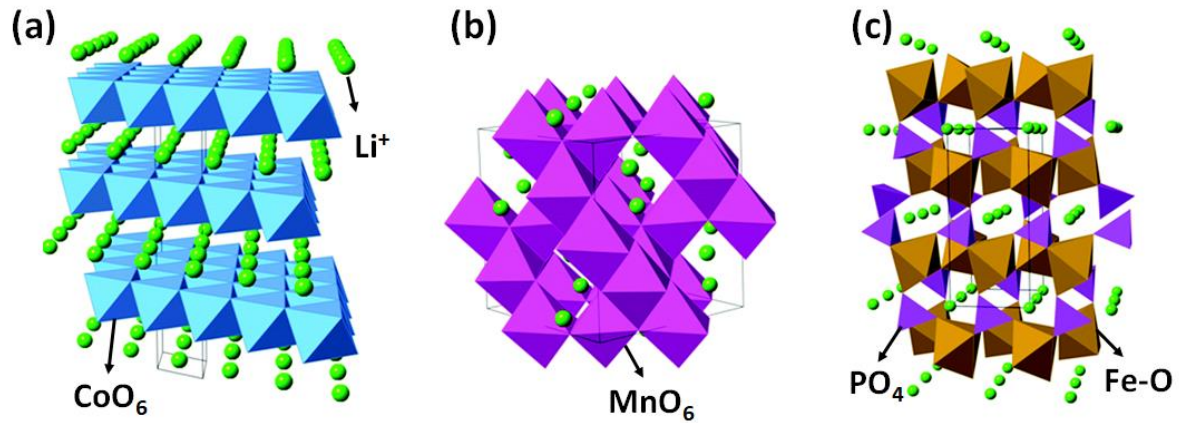


Figure I-5 : Representative crystal structures of cathode materials for LIBs: (a) layered LiCoO_2 ; (b) LiMn_2O_4 spinel; and (c) olivine LiFePO_4 . Li^+ ions are shown as light green spheres, CoO_6 octahedra in blue; MnO_6 octahedra in mauve; Fe-O polyhedra in brown, and PO_4 tetrahedra in purple. Black lines demarcate one unit cell in each structure. Reprinted from [23].

The layered V_2O_5 also attracts interest due to its initial capacity of about 300 mAh/g, which is higher than LiMn_2O_4 , LiFePO_4 , or even Li-rich cathodes [24]. However, the practical application of V_2O_5 is impeded by its slow Li^+ diffusion (10^{-12} - 10^{-13} cm^2/s), its poor electrical conductivity (10^{-2} - 10^{-3} S/cm) as well as its structural instability. One way to enhance the electrochemical behavior is to fabricate nanostructured V_2O_5 materials. For example, nano- V_2O_5 exhibited a good cycling stability with a specific capacity of 200 mAh/g retained after 50 cycles between 2.0 – 4.0 V vs. Li^+/Li [25]. More recent studies show that the cathode fabricated from 50 nm V_2O_5 thin film delivered a high discharge capacity of 271 mAh/g at 0.5 C, and 129 mAh/g at a very high current of 20 C. When the current is decreased from 20 C to 0.5 C, 91.1 % of the initial discharge capacity is still maintained [26].

An overview of the specific capacity and the operating voltage of the aforementioned cathodes is given in Table I-1.

Table I-1 : The characteristics of Li-Ion battery positive electrode materials [13], [27].

Material	Structure	Potential (V vs. Li^+/Li)	Specific capacity (mAh/g)	Cycle number
LiCoO_2	Layered	3.8	140	500-1000
$\text{LiNi}_{0.8}\text{Co}_{0.15}\text{Al}_{0.05}\text{O}_2$ (NCA)	Layered	3.7	180-200	500
$\text{LiNi}_{1/3}\text{Co}_{1/3}\text{Mn}_{1/3}\text{O}_2$ (NMC)	Layered	3.7	160-170	1000-3000
$\text{LiNi}_{0.5}\text{Mn}_{1.5}\text{O}_4$	Layered	4.7	130-140	300-1000
Li-rich NMC	Layered	4.8	150-200	500-700
LiMn_2O_4	Spinel	4.1	100-120	300-700
LiFePO_4	Olivine	3.3	150-170	1000-2000
V_2O_5	Layered	3.3, 3.1 and 2.1	100 – 140	500 – 1000

b. Anode materials

As already mentioned, the development of LIB benefits mainly from the intercalation chemistry. Many efforts have been devoted to develop new electrodes with Li intercalation compounds, allowing the insertion of Li atoms between layers of the host. Other types of materials that could react with Li are also investigated as potential anode materials, with generally structural changes during the electrochemical reactions. As shown in Figure I-6, these compounds are classified into three types according to their reaction mechanisms with lithium: (i) insertion/intercalation, (ii) alloying, and (iii) conversion.

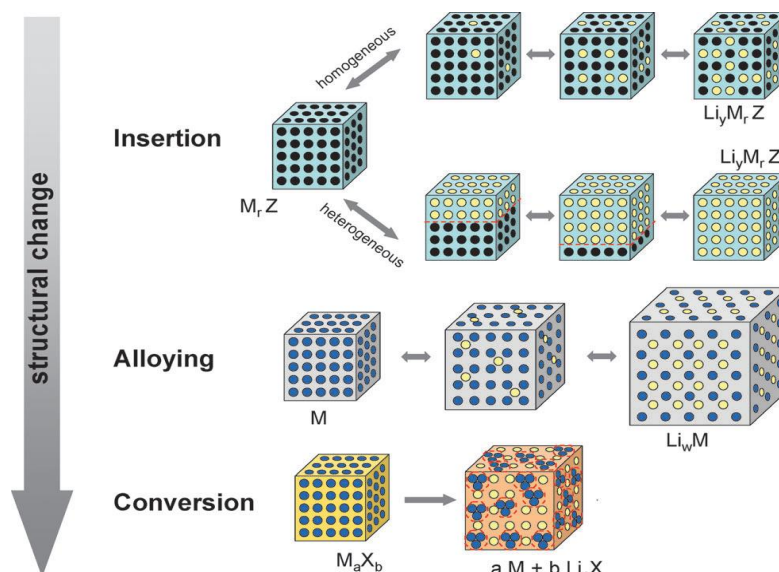


Figure I-6 : Schematic representation of the different reaction mechanisms occurring in negative electrode material for LIBs. Black circles: voids in the crystal structure, blue circles: metal, yellow circles: lithium. Reprinted from [28].

To avoid safety issues, graphite is identified as a good candidate to replace lithium metal at the anode. Although its theoretical capacity is much lower than lithium metal (372 mAh/g vs. 3860 mAh/g, respectively), lithium ions could intercalate in graphite at a low potential around 0.1 V vs. Li^+/Li [7]. It has been commercially used in LIBs for its high reversibility and low volumetric expansion. In the 1990s, the spinel $\text{Li}_4\text{Ti}_5\text{O}_{12}$ material was proposed for Li-ion batteries and has been successfully commercialized due to its superior thermal stability, high rate, and high cycle life [29]. Its theoretical specific capacity is low (175 mAh/g) but it presents a well-defined charge/discharge plateau and a high rate capability.

In addition to insertion compounds, some materials can alloy electrochemically with lithium at ambient temperature (Li-Al, Li-Si, Li-Sn, etc.) [30]. The silicon-based anodes are certainly the most well-known examples. They have a low working potential of ~ 0.2 V vs. Li^+/Li with a theoretical capacity of 3579 mAh/g. However, a huge volume expansion upon lithiation is observed leading to severe particle pulverization, loss of electrical contact, and formation of unstable interface layers[30], which limit the battery lifespan.

More recently, the conversion electrode has attracted attention due to the high capacity. The conversion reaction is defined as the reduction of binary transition metal M_aX_b (with M =transition metal, $X=O, S, F...$) to its metallic state (Li_yX). The main exception is the fluoride, which reacts at voltage close to 3.0 V vs. Li^+/Li . However, the main drawback of the conversion electrode is the large voltage hysteresis between the discharging and charging, resulting in a poor energy efficiency [31].

c. Electrolyte

The electrolyte is also a key component of the LIB since it serves as the medium for ion transport. Its critical features concern safety (thermal stability), cell rate capability (conductivity), and reactivity (electrochemical stability window) [32]. Electrolytes are generally composed of a lithium salt dissolved in a liquid organic solvent. The most common solvents for LIBs are based on carbonate species, ethylene carbonate (EC), propylene carbonate (PC), dimethyl (DMC), ethyl methyl (EMC), or diethyl (DEC) carbonates [33]–[36]. Lithium hexafluorophosphate ($LiPF_6$) and lithium bis(trifluoromethane)-sulfonimide ($LiTFSI$) are the most widely used salts in LIBs. A concentration from 0.5 to 1 mol/L produces a conductivity of around 1 mS/cm at room temperature [11]. The liquid electrolyte decomposes on the surface of the negative electrode when the potential is less than 1 V vs. Li^+/Li . This decomposition is responsible for the formation of a solid multicomponent layer on the surface of the negative electrode, called SEI (solid electrolyte interphase)[37]. Despite the fact that the SEI formation induces irreversible consumption of electrons and ions, the formation of the SEI is beneficial in the case of $Li-Li_xC_6$ for example, as it is stable and prevents further degradation. In order to improve the characteristics of electrolytes, such as thermal stability, conductivity, *etc.* additives can be used such as Lewis base stabilizer additives [38], flame retardant additives, *etc.* [39]. These may stabilize the SEI and then increase the performance of the battery.

I.1.2.3. Post-lithium-ion battery technologies

a. Introduction

Although significant progress are made for LIBs through decades of research to achieve good power and energy density, Li low availability, low abundance and high cost cannot meet the dramatically increasing demand for electrochemical energy storage for portable electronics devices and for the growing market of electric or hybrid vehicles. It is therefore necessary to develop a new technology of batteries offering new prospects for storage capacity, safety, cost and energy density competitive with fossil fuels such as gasoline. This section provides a brief overview of the most studied technologies.

b. Technologies based on lithium metal

To increase the energy density, the use of lithium metal as the anode is still ideal due to its low potential (-3.04 V vs. SHE) and its high gravimetric capacity (3860 mAh/g) [3]. However, the use of lithium metal leads to safety issues, which include uncontrolled growth of dendrites, relatively infinite volume expansion, and an unfavorable solid electrolyte interphase that is caused by the high reactivity of lithium metal. We will detail later the dendritic formation with the description of non-aqueous lithium-air batteries (Section 1.2.4.1).

In **all-solid-state LIB batteries**, the presence of a solid electrolyte should solve the problems of LIB with liquid electrolyte - where flammable solvents are generally used, making the battery safer. It should also allow to use lithium metal, providing a higher capacity than liquid-based LIBs. The solid electrolytes can be classified into organic such as polyethylene oxide [40], and inorganic compounds such as Garnets, NASICON, perovskites, or sulfides [41]. These batteries may provide an energy density up to a range of 300 - 400 Wh/kg. Despite improvements in safety issues and energy densities, all-solid-state batteries suffer from a high resistance at the electrodes / solid electrolyte interfaces, hindering fast charging and discharging and providing low cycle life (~100 cycles). This technology still requires some developments before eventually being commercialized.

During the last decade, **lithium-sulfur** (Li-S) and **lithium-air/lithium-oxygen** (Li-O₂) **batteries** have attracted attention due to their extremely high theoretical energy density [42]–[44]. In the case of Li-S batteries, sulfur offers a high theoretical specific capacity of 1675 mAh/g and a high theoretical energy density of 2500 Wh/kg. Moreover, sulfur is an abundant and low-cost element and - which may drastically decrease the cost of the battery. Li-S batteries are based on the electrochemical reaction of sulfur with lithium to form the final product lithium sulfide (Li₂S). The working mechanism is very complex and implies 16 electrons; the reduction of the sulfur is accompanied by the shuttle formation of lithium polysulfides (Li₂S_x). Figure I-7 shows a typical cycling profile of a Li-S battery with the formation of the intermediate products.

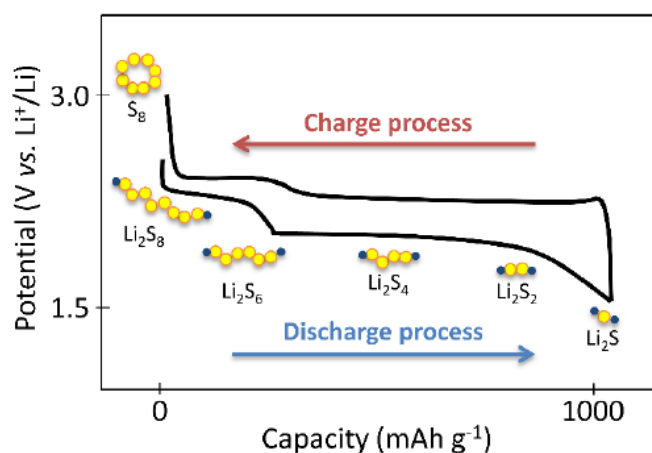


Figure I-7 : Classical discharge-charge profile of Li-S battery. Reprinted from [44].

Many challenges remain for the Li-S battery development [42]. Lithium polysulfide intermediates Li_2S_x are soluble and can easily diffuse into the aprotic liquid electrolyte, leading to a rapid capacity loss. Considerable efforts have been devoted to improve cycling performances by preventing this shuttle mechanism, such as the utilization of solid or polymer electrolytes as a physical barrier, the encapsulation of sulfur and sulfide in porous materials by physical adsorption, or the reinforcement of sulfur species by chemical adsorption with metal oxide additives [45]–[48].

c. Technologies based on other metal cations

Inspired by the development of intercalation LIBs, the community investigated other alkali-metal, such as **sodium-ion batteries** and **potassium-ion batteries**. The sodium-ion batteries are now close to commercialization. In 2015, the French research network on electrochemical energy storage (RS2E) developed the first sodium-ion battery in a 18650 industrial prototype [49]. This battery has an energy density of 90 Wh/kg and is able to deliver its energy at fast charging / discharging rates. Cathode materials with similar structures than Li-ion application have also been investigated as cathode materials for Na-ion batteries, such as layered transition metal oxides, P2/P'2 $\text{Na}_{2/3}\text{MnO}_2$, polyanionic compounds such as NaFePO_4 or NASICON-type $\text{Na}_3\text{V}_2(\text{PO}_4)_3$ [50]. The potassium has a reduction potential lower than the sodium and is very close to lithium (Table I-2). However, potassium-ion batteries suffer from a limited choice of electrode materials due to the large ionic radius (1.33 Å) and heavy atomic mass of potassium compared to lithium and sodium. A recent study shows that a Prussian Blue $\text{K}_{1.82}\text{Mn}[\text{Fe}(\text{CN})_6]_{0.96}\cdot 0.47\text{H}_2\text{O}$ cathode exhibits a discharge capacity of 160 mAh/g and 120 mAh/g at 300 mA/g and 2,500 mA/g, respectively, and sustains 130,000 cycles (more than 500 days) with negligible capacity loss. Pairing this cathode with a 3,4,9,10-perylenetetracarboxylic diimide anode yields a full potassium-ion cell that delivers an energy density as high as 92 Wh/kg and retains 82.5% of the initial capacity after 6500 cycles at 1500 mA/g [51].

Batteries based on **multivalent metal-ions**, **metal-sulfur**, and **metal-air** are also investigated. Table I-2 gives some characteristic parameters of some metals. Although the gravimetric and volumetric capacities obtained with Na, K, Mg, Al, Ca... are lower than with lithium, these abundant elements benefit from low-cost, decreasing potentially the total cost of the battery.

Table I-2 : Characteristic parameters of some metals. Data are collected from [52], [53].

Element	Potential (V vs. SHE)	Gravimetric capacity (mAh/g)	Volumetric capacity (mAh/cm ³)	Cost (\$/kg)
Li	-3.0	3861	2062	17.00
Na	-2.7	1166	1131	0.15
K	-2.9	685	591	0.74
Mg	-2.4	2205	3833	0.28
Al	-1.7	2980	8046	0.56
Zn	-0.8	820	5887	3.02

The **metal-air battery** technology attracts attention thanks to its great theoretical energy density, which is 3 - 30 times higher than commercial LIBs (Table I-3) [54]. Metal-oxygen batteries consist of a pure metal anode, a cathode that theoretically uses ambient air, and an electrolyte (aqueous or non-aqueous). The air cathode is exposed to the ambient air using specifically O₂ to store and convert energy. The working principle is based on the reversible electrochemical reaction between the metal ions and the O₂. Table I-3 compares the theoretical energy density of some metal-air systems. As these batteries are semi-open cells, it could lead to significant battery weight reduction. Among these technologies, the **Zn-air battery** is the most mature. The first primary Zn-air battery was dated back to 1878 with a porous platinized carbon air electrode [55]. Primary Zn-air batteries have been commercialized for medical and telecommunication applications. Commercialization of rechargeable Zn-air batteries has already begun for grid energy storage systems. The Zn-air batteries are usually filled with a high concentration of alkaline solutions [56]. During the discharge, the Zn(OH)₄²⁻ ions are generated in the solution until its saturation, after which the ZnO will precipitate as the final product. However, in comparison to their high energy densities, the power output capability is far from satisfactory due to the inefficiency of air catalysts available. The ZnO that are not deposited on the Zn anode may cause the battery capacity loss. The Zn(OH)₄²⁻ could also migrate to the air cathode and the final coated product ZnO influence the performance of the air cathode. In order to have a rechargeable system, research on zinc electrodes in Zn-air batteries has focused on developing a rigid conductive porous network and minimal inactive material that is self-sufficient in confining the dissolved zincate ions, promoting distribution of Zn/ZnO deposition.

Table I-3 : Characteristic parameters of some metal-air batteries [57].

Battery	Reaction	E_0 (V vs. M^{n+}/M)	Theoretical energy density (Wh/kg)
Li-air	$4 \text{ Li} + 2 \text{ O}_2 \rightarrow 2 \text{ Li}_2\text{O}$	2.91	11140
Al-air	$4 \text{ Al} + 3 \text{ O}_2 \rightarrow 2 \text{ Al}_2\text{O}_3$	2.73	8130
Ca-air	$2 \text{ Ca} + \text{ O}_2 \rightarrow 2 \text{ CaO}$	3.12	4180
Zn-air	$2 \text{ Zn} + \text{ O}_2 \rightarrow 2 \text{ ZnO}$	1.65	1350

I.2. Li-air or Li-O₂ batteries

Lithium-air batteries have attracted unprecedented attention due to their high theoretical energy density, which is comparable to gasoline. As already mentioned, the lithium-air battery provides a theoretical energy density of 11140 Wh/kg based on the mass of lithium (without considering the mass of gas) [56]. The capacity of lithium-air batteries is generated from electrochemical reactions between Li ions and the O₂ present in the air atmosphere, which is thus abundant and “free”. The first lithium-air battery was reported by Jiang and Abraham in 1996 [58]. It consists of a lithium metal anode and a thin conductive carbon composite cathode with an organic polymer electrolyte membrane. This non-optimized electrochemical cell showed a good energy density in the range of 250 - 350 Wh/kg (considering the weight of the electrodes and electrolytes). Although the safety issues related to the lithium metal anode remain challenging, most of the reported studies are still performed with a lithium metal anode and generally a porous carbon with a high surface area as cathode, separated by a membrane soaked with electrolyte.

I.2.1. Principle of Li-O₂ batteries

During the discharge process, the lithium metal anode releases lithium ions (Li⁺) into the electrolyte, while generating an electron flow through the external circuit to the cathode. In the meantime, O₂ is reduced at the cathode via the oxygen reduction reaction (ORR). The O₂ molecules incorporated into the porous electrode are first dissolved into the electrolyte and then react with Li⁺ at the surface of the cathode. The nature of the discharge products differs from the type of electrolyte used, as we will discuss in the subsection below. During the charge process, the reverse reaction of ORR occurs via the oxygen evolution reaction (OER) at the cathode and the deposition of lithium metal at the anode. While the Li-air batteries ideally involve O₂, there are other compounds than O₂ in air. The air consists of 78% N₂, but it has been proved that N₂ is electrochemically inert on the cathode whereas the metallic Li reacts with N₂. The generated Li₃N plays the role of SEI on the anode and is suitable for Li⁺ migration, but its low electronic conductivity (10⁻¹² S/cm) impedes easy electron transfer. Nevertheless,

the CO_2 and H_2O in air can cause irreversible parasitic reactions in Li-air batteries, leading to a loss of capacity and a reduced cyclability [59]. Many studies at the laboratory scale are thus based on the use of pure oxygen to avoid these undesired reactions and the systems are thus better referred to as **Li- O_2 batteries**. Even if both terms Li-air and Li- O_2 batteries are usually used in the literature without distinction, it is more accurate to use the term Li- O_2 batteries rather than Li-air batteries [54], as studies usually use pure O_2 at the cathode.

I.2.2. Architecture types

As shown in Figure I-8, Li- O_2 batteries can be classified into four systems designated by the nature of the electrolyte: (a) aprotic, (b) aqueous, (c) hybrid *i.e.* mixed aprotic / aqueous, or (d) solid-state [60]. In all architectures, the fundamental electrochemical reactions at the anode are the same, *i.e.* the dissolution / deposition of lithium metal. For the cathode, the discharge / charge reactions depend on the electrolyte used, leading to different discharge products such as LiOH , Li_2O_2 and / or Li_2O .

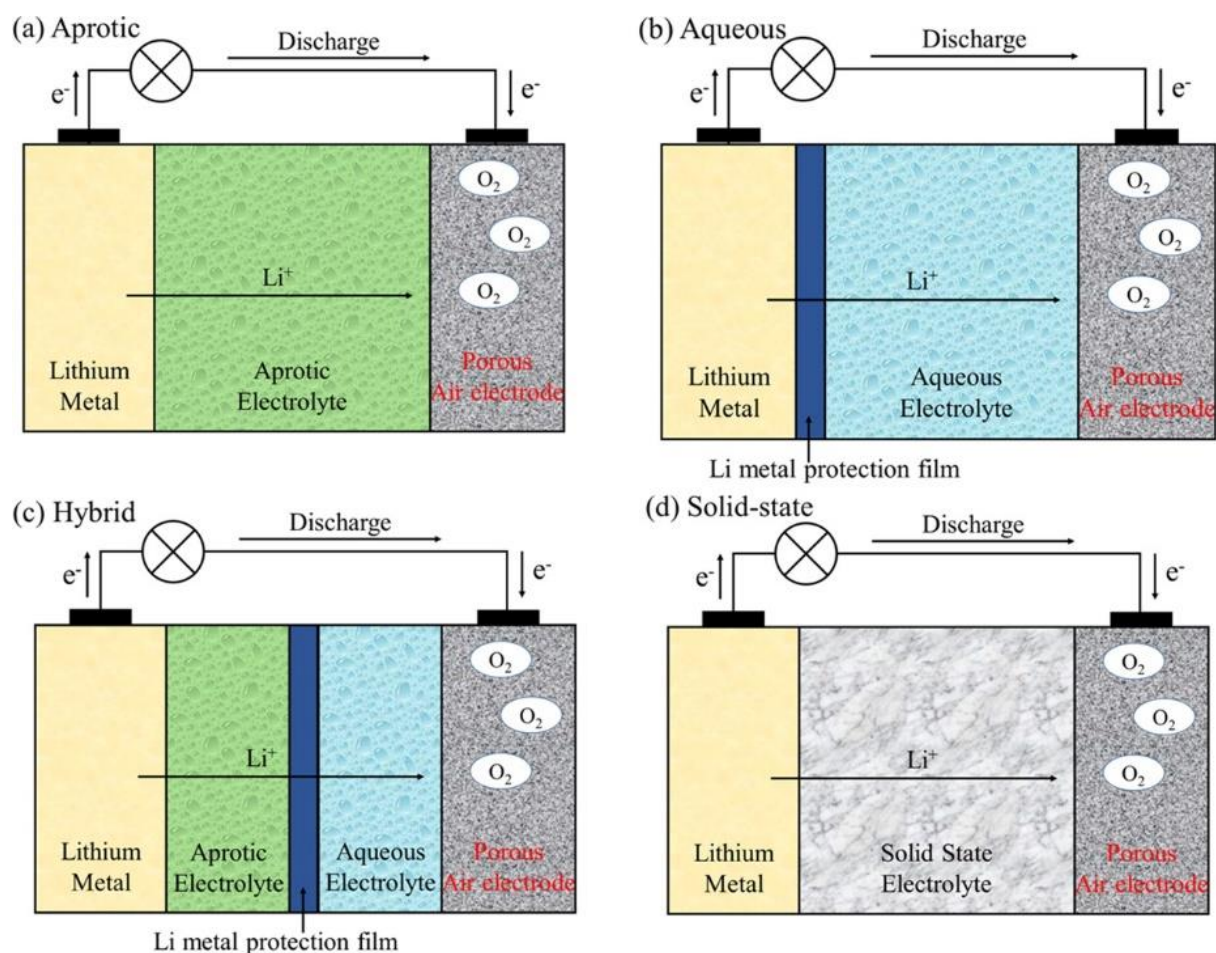
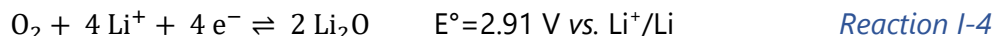
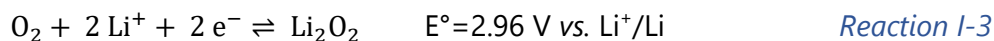


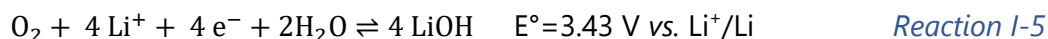
Figure I-8 : Schematic battery configurations for the four types of Li- O_2 batteries. Reprinted from [60].

Aprotic Li-O₂ batteries – The electrolyte is composed of a lithium salt dissolved in a non-aqueous organic solvent, similar to the ones used in Li-ion batteries [61]. As the solvent is often aprotic, this type of battery is also called an aprotic Li-O₂ battery. The desired electrochemical reaction in the Li-O₂ battery with an aprotic electrolyte leads to the formation of Li₂O₂ and also possibly Li₂O [61] following Reaction I-3 and Reaction I-4:



The resulting insulating discharge products Li₂O₂ / Li₂O are insoluble in the aprotic solvents and deposit on the surface or in the pores of the cathode. The mechanisms of formation / decomposition of Li₂O₂ / Li₂O via the ORR/OER reactions are in fact complex and can be influenced by many factors such as electrode potential, current density, air cathode materials, or the nature of electrolyte [62]. Often, a catalyst is required in order to reduce the activation energy of the sluggish oxygen evolution reaction (OER) and accelerate the reversibility of Li₂O₂ / Li₂O formation and decomposition reactions [54]. In the following Section I.2.3, we describe more in detail the main discharge product formation mechanisms.

Aqueous Li-O₂ batteries – The most common aqueous electrolyte used for the Li-O₂ batteries is generally an alkaline solution, although acidic electrolytes can be also used. In contrast to aprotic electrolytes, the water molecules participate in the electrochemical ORR (Reaction I-5).



The reduction potential of the couple O₂/LiOH being even higher than the couple O₂/Li₂O₂ (3.43 V vs. 2.96V vs. Li⁺/Li, respectively) [61], the oxidation will thus take place at a higher potential for the OER reaction with an aqueous electrolyte. As LiOH is formed in the electrolyte, the capacity is in fact limited by the solubility of LiOH (~5.3 M) [60]. LiOH•H₂O precipitates at the surface of the electrodes and leads to pore clogging once the solubility limit of LiOH is reached. Compared to flammable organic electrolytes, the use of aqueous electrolyte appears safer. However, lithium can react vigorously with water. To prevent this reaction, the lithium anode must be insulated with a ceramic membrane that ensures the exchange of Li⁺ ions (Figure I-8 (b)). Bograchev *et al.* have proposed to use a protective bilayer between the aqueous electrolyte and the lithium electrode [63]. They used a ceramic glass such as LISICON (lithium superionic conductor – Li_(1+x+y)Al_xTi_{2-x}Si_yP_{3-y}O₁₂) combined with a LiPON (Lithium phosphorous oxynitride Li_xPO_yN) coating to prevent reactions between the ceramic glass and the lithium metal. However, the decomposition of LiOH•H₂O during charge requires activation energy, resulting in a higher charge overpotential. This is accompanied with an important loss of specific energy compared to the aprotic electrolyte, making the aqueous system less competitive than the aprotic system [54].

Hybrid Li-O₂ batteries – The hybrid architecture combines both aqueous and aprotic electrolytes (Figure I-8 (c)). The anode side is filled with an aprotic electrolyte whereas the cathode is in contact with an aqueous electrode. This arrangement offers a stable behavior of the Li⁺ ions and Li metal anode in the aprotic organic solvent as well as the high solubility of the discharge products LiOH in the water-based electrolyte [61].

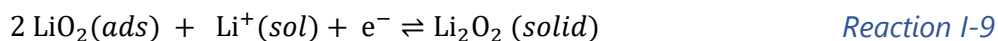
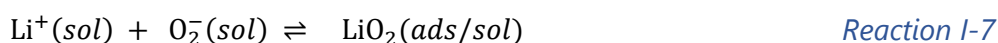
Solid-state Li-O₂ batteries – The electrolyte is here a solid phase. Based on the development of solid electrolytes for all-solid-state batteries, the electrolyte can be a polymer (PEO) or an inorganic compound (LISICON) [61]. However, these batteries face the same problems as the all-solid-state batteries: the low ionic conductivity of the solid electrolyte and the loss of contact at the interfaces between electrodes and the electrolyte.

Currently, the aprotic Li-O₂ architecture is dominating the research efforts due to its sustainable rechargeability compared with the other three architectures. Hereafter, we concentrate on the aprotic Li-O₂ architecture. A better understanding of the complex discharge-charge mechanisms could help improve the corresponding Li-O₂ battery performance.

I.2.3. Li₂O₂ formation mechanisms

I.2.3.1. Surface mechanism vs. solution-mediated mechanism

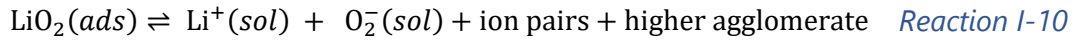
Jiang and Abraham have first proposed a stepwise reaction mechanism [58]: the O₂ molecules incorporated in the cathode are first dissolved in the electrolyte to form a superoxide O₂^{•-}, which combines with Li⁺ to form a surface adsorbed LiO₂(*ads*) and / or soluble LiO₂(*sol*) (Reaction I-6 and Reaction I-7). This intermediate product LiO₂ is thermodynamically unstable and is quickly transformed to Li₂O₂ (lithium peroxide) via disproportionation (Reaction I-8) or by receiving a second electron (Reaction I-9).



The competition between these two last reactions (Reactions I-6 and I-7) depends on various factors such as current density, overpotentials, or whether LiO₂ is soluble in the electrolyte solution [43]. A suitable electrolyte should present here the following properties:

- High oxygen solubility and diffusivity for the ORR/OER reaction processes.
- High electrochemical stability and resistance to oxygen reduction intermediate species, such as superoxide radicals O₂^{•-}.
- Good compatibility with the lithium anode, via the formation of a stable SEI film.
- High physicochemical stability, including low volatility to avoid the evaporation of the solvent, low viscosity to ensure fast kinetics, and high ionic conductivity.

Chen et al. have investigated the impact of aprotic solvents on the ORR mechanisms in Li-O₂ batteries [61]. As the solvation energy of Li⁺ is higher in high donor number (DN) solvents (typically DMSO), the ORR intermediate LiO₂ dissociates to solvated Li⁺ and O₂⁻ ions in solution (Reaction I-10). A solution-mediated mechanism to form directly large Li₂O₂ particles from the solution is then promoted.



However, in low DN solvents (typically ether), LiO₂ is adsorbed dominantly on the surface and transforms to Li₂O₂ directly on the electrode surface, thereby promoting a surface mechanism (Figure I-9). High acceptor number (AN) additives, particularly protic ones, are found to favor large discharge capacities with the formation of big toroidal Li₂O₂ particles [43]. For example, some trace amounts of H₂O could increase the solvation of the intermediate compound LiO₂ and promotes the solution-mediated mechanism. Water molecule acts as a proton donor and increase the lifetime of superoxide species thus allowing the formation of large Li₂O₂ particles [64]. However, it must be noted that water traces also trigger overpotentials during the charge of the battery [61], which is a serious issue for a practical system. The use of redox mediators which can also significantly reduce the overpotentials is an effective strategy to achieve a more stable reactive oxygen species [54].

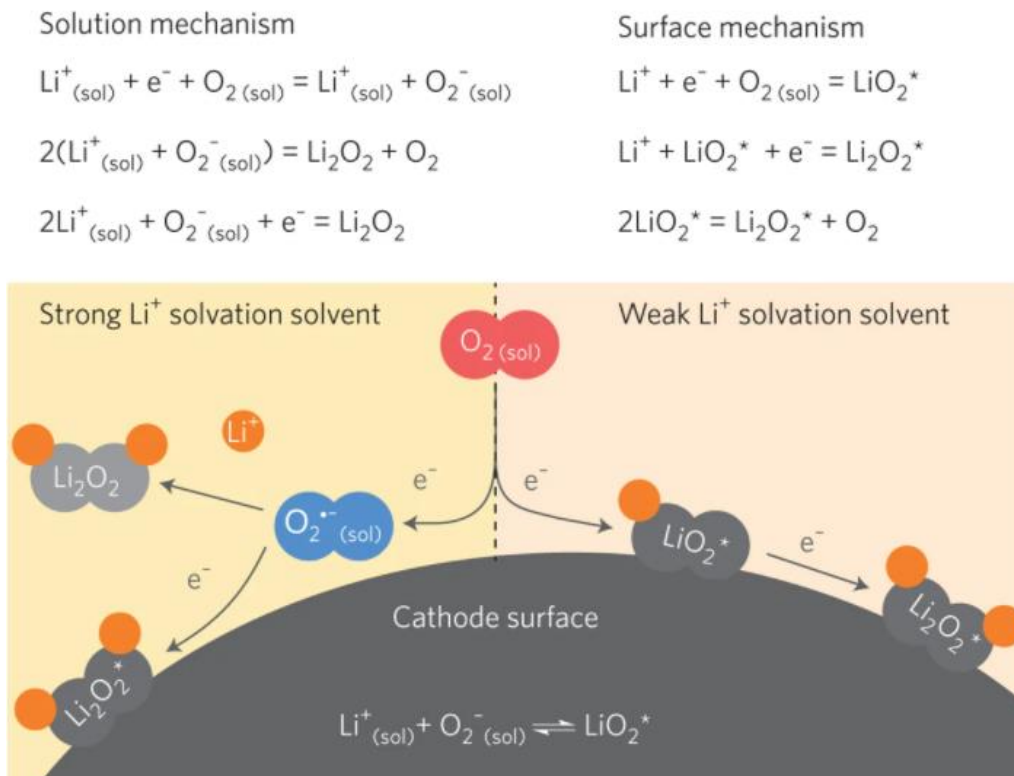


Figure I-9 : Solution-mediated and surface mechanisms for the formation of Li₂O₂ [64].

I.2.3.2. Li_2O_2 morphology

The two mechanisms (surface or solution) lead to different morphologies of the discharge products and thus a difference of capacity. In the surface model, thin-film Li_2O_2 is deposited on the electrode surface, yielding to a low charge overpotential but a small discharge capacity. In the solution model, toroidal Li_2O_2 grows on the electrode surface, yielding a large discharge capacity but a high charge overpotential (Figure I-10) [65] .

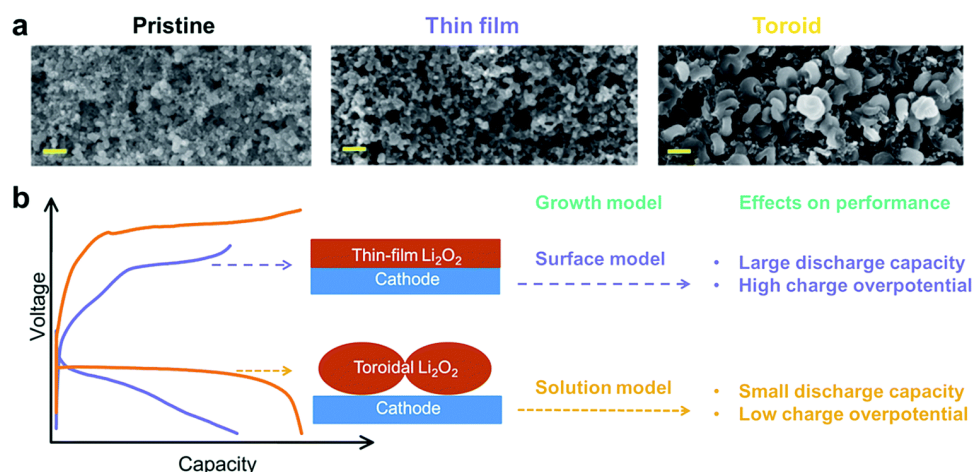


Figure I-10 : (a) SEM images of the cathode with thin-film and toroidal Li_2O_2 morphologies after full discharge. (b) Schematic of the effect of the typical Li_2O_2 morphologies on battery performance via different growth models. Reprinted from [65].

The current density plays an important role in the formation of discharge products and influences the discharge capacity. As shown in Figure I-11 (a), the discharge capacities and the sizes of Li_2O_2 of the Li_2O_2 toroids decrease with increasing current density [65]. Li_2O_2 toroids with a relatively good crystallinity can be produced at low current densities, while dominantly quasi-amorphous thin film are formed at high current densities (Figure I-11 (b)). Nazar *et al.* further propose a mechanism to explain the differences in Li_2O_2 morphology at different current densities [66]. At low current density, the electron transfer rate is slower than the LiO_2 solvation rate, leading to the disproportion to crystalline Li_2O_2 ; while at high current density, the electron transfer rate is fast, and the LiO_2 are generated dominantly at high concentration on the cathode surface, from where they can directly accept the electrons, leading to a film morphology.

Nevertheless, apart from the current density, the electrolyte formulation implies also different Li_2O_2 morphologies. Figure I-12 summarizes different Li_2O_2 morphologies generated with carbon-based electrodes in aprotic systems. Besides small thin toroids (100-200 nm in size) [68], Thompson *et al.* [69] have observed the growth of toroids as large as near 1 μm in diameter with increasing depth-of-discharge. Other Li_2O_2 morphologies, such as needles, crescents, or pseudo-spheres, are observed on carbon electrodes in ether Li- O_2 systems (Figure I-12) [69], [67], [70]–[73].

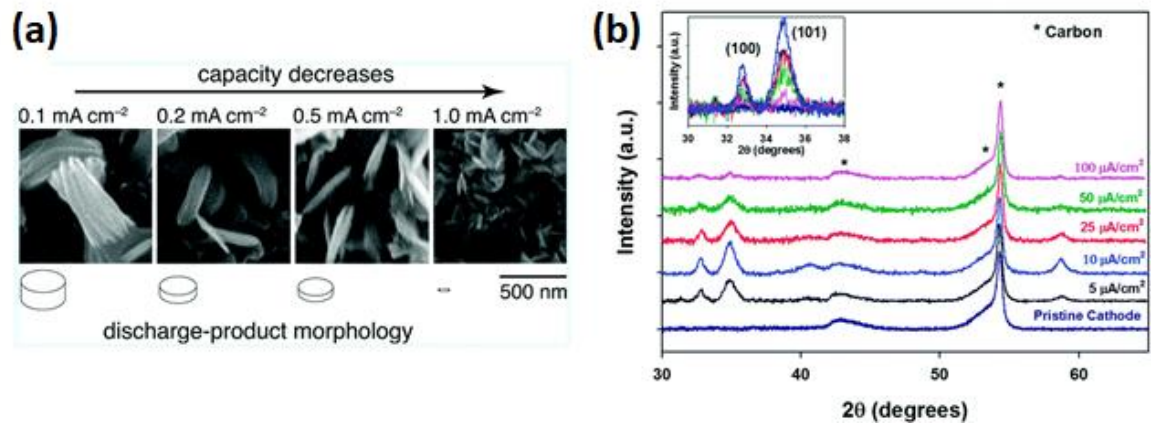


Figure I-11 : (a) Schematic of the discharge capacity and Li_2O_2 morphology with increasing current density. (b) XRD patterns after full discharge at the corresponding current rates. All the peaks, with the exception of carbon arising from the gas diffusion electrode, could be indexed to Li_2O_2 . The inset displays a close-up of the (1 0 0) and (1 0 1) reflections. (c) Proposed ORR mechanism as a function of the current density. Reprinted from [67].

Needle [67]	Platelet [70]	Toroid [69]
Electrolyte: 1M LiTFSI in DME Cathode: GDL	Electrolyte: 1 M LiTFSI in DME Cathode: Vulcan XC72 carbon	Electrolyte: 0.1 M LiClO_4 in DME Cathode: CNT
Film [71]	Crescent [72]	Pseudo-sphere [73]
Electrolyte: 1 M LiPF_6 in EC:DMC Cathode: CNF	Electrolyte: 0.5 M LiTFSI in DiGME Cathode: Carbon paper	Electrolyte: 1 M LiCF_3SO_3 in TEGDME Cathode: Activated carbon

Figure I-12 : Overview of several discharge product morphologies of Li-O_2 batteries reported in literature [67] [47-51].

1.2.3.3. Properties of the electrolytes in Li-air batteries

The mechanisms of formation / decomposition of Li_2O_2 via the ORR / OER reactions are complex. Many factors contribute to the discharge/charge mechanism involved in the Li- O_2 batteries. As mentioned above, low current densities favor the solution-mediated formation of Li_2O_2 due to the low electron transfer. And the surface mechanism for Li_2O_2 formation is involved at high current densities as the adsorbed LiO_2 species receive electrons directly from the surface.

a. Solvent

The nature of the solvent in Li- O_2 is critical and influences the reaction mechanisms, the reversibility of the systems, and it also influences the discharge capacity [57]. The viscosity, polarity and basicity are the main physical properties of solvent which impact the discharge mechanism of the Li- O_2 battery. At first, a low solvent viscosity facilitates O_2 gas transport, favoring both the ORR kinetics and discharge capacity [74]. Secondly, the solvent polarity of the solvent is also an important factor. On one hand, it should enable the facile dissolution of Li-containing salts; on the other hand, low polarity is more suitable to ensure the electrolyte wettability on the hydrophobic carbon-based air electrode. As already mentioned in section 1.2.3.1, another important parameter is the Lewis basicity of the solvents, measured by the Gutmann donor number (DN) [54]. It impacts the solubility and the dissociation of lithium superoxide LiO_2 and thus governs the two competitive mechanisms for the formation of Li_2O_2 . Table I-4 gives some physical parameters of usual solvents for Li- O_2 batteries.

The early studies on Li - O_2 batteries used the conventional Li-ion batteries electrolytes based on carbonate solvents. However, carbonates are not suitable for aprotic Li- O_2 batteries and were quickly abandoned due to their instability in the presence of reduced oxygen species. Carbonated-based solvents decompose irreversibly at the cathode to form side products such as Li_2CO_3 , C_3H_6 (OCO_2Li)₂ or $\text{CH}_3\text{CO}_2\text{Li}$ with little or no evidence of Li_2O_2 formation [61].

Overall, almost all the solvents are subject to decomposition under the oxidative environment in Li- O_2 batteries. The decomposition of solvent can occur following different reactions (i) nucleophilic attack, (ii) acid / base reaction, (iii) auto-oxidation, (iv) proton-mediated reactions, and (v) reduction at the lithium anode [57]. These parasitic reactions consume oxygen and lead to the formation of undesirable products, which can be deposited onto the surface of the electrodes, reducing in the end the efficiency of the battery. As shown in Figure I-13, carbonate-, sulfoxide-, and amide-based electrolytes are susceptible to nucleophilic attack by the superoxide. Through acid / base chemistry, dimethyl sulfoxide (DMSO) can be easily deprotonated by superoxide and peroxide, leading to the decomposition of the solvent and the generation of parasitic byproducts [76]. In contrast, special attention is given to ethers, including dimethoxyethane (DME) and tetraethylene glycol dimethyl ether (TEGDME), which are proven to be more stable during operation and Li_2O_2 formation [43].

Table I-4 : Key parameters of some solvents used in metal- O_2 batteries [75]. The acronyms are specified in Section Glossary.

Solvent	EC	DEC	DMSO	DMF	DME	TEGDME
Category	carbonate	carbonate	sulfoxide	amide	ether	ether
Molar mass (g/mol)	88.06	118.13	78.13	73.09	46.07	222.28
Viscosity (cP)	1.90	0.75	1.95	0.92	0.46	4.05
Dipolar moment (debye)	4.61	0.96	3.96	3.86	1.71	2.60
Acceptor number (AN)	-	-	19.3	16.0	10.2	11.7
Donor number (DN)	-	16.0	29.8	26.6	20.0	16.6
Li^+ conductivity (mS/cm)	-	-	2.11	-	1.16	0.30
O_2 solubility (mM/cm ³)	-	-	2.1	-	9.57	4.43

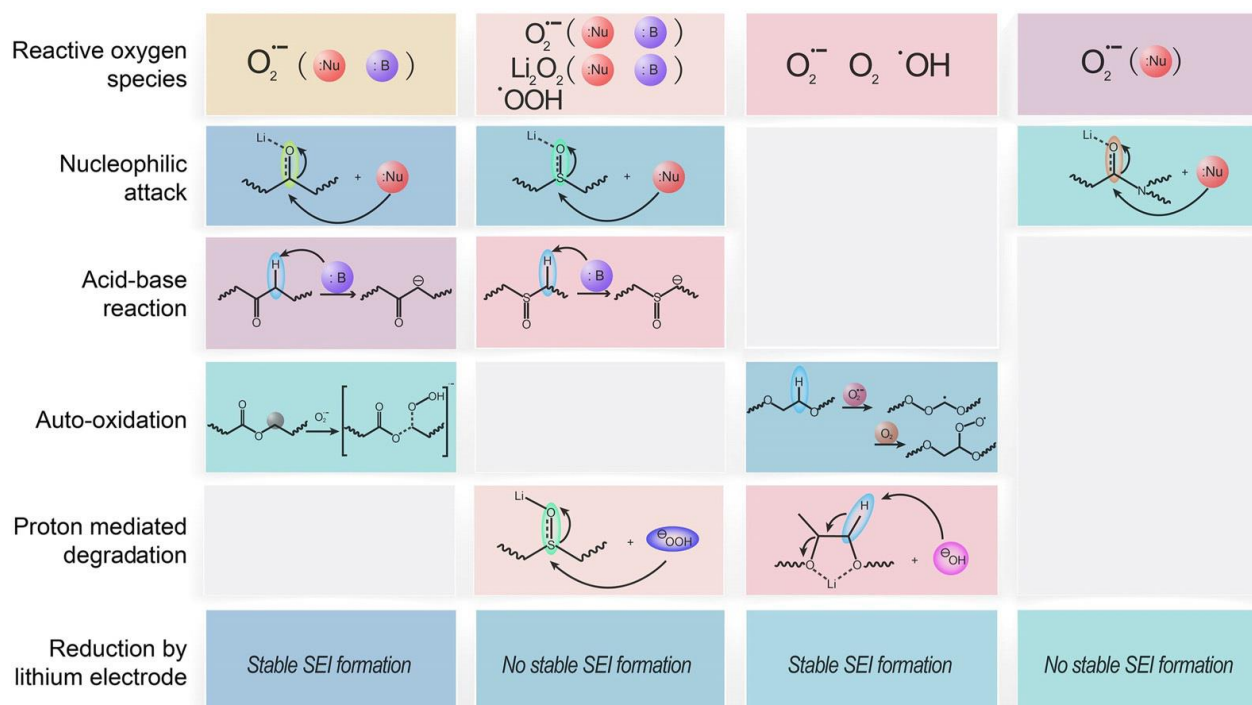


Figure I-13 : Decomposition pathways of the solvents and related reactive O_2 species. Reprinted from [61].

b. Salt anions

The solubility of lithium salts in aprotic solvents primarily depends on the solvation of the Li^+ cations by the solvent molecules, while interactions between the Li^+ and other high AN species (such as anions) are also observed to play an important role in LiO_2 solubility and the ORR mechanism. It is interesting to note that Li_2O_2 formation mechanism in aprotic solvents depends primarily on the solvation of Li^+ rather than the species (O_2^-) actually formed on reduction. In other words, O_2^- radicals can be stabilized indirectly by the anions of lithium salts that can strongly associate with Li^+ ions and decrease their acidity or reactivity [77].

The stability of lithium salts plays an important role in the cyclability and capacity of Li-O_2 cells especially in the presence of reduced oxygen species [78], but has not been systematically investigated in rechargeable Li-O_2 batteries. Ehrenberg *et al.* have investigated the stability of LiPF_6 and LiClO_4 [79]. The formation of LiF is observed by XPS once LiPF_6 is in contact with the lithium peroxide Li_2O_2 while the salt LiClO_4 is more stable. Amine *et al.* have investigated the stability of the most common salts such as LiPF_6 and LiTFSI ($\text{LiC}_2\text{NO}_4\text{F}_6\text{S}_2$) dissolved in various solvents [80]. They show that the stability of the electrolyte depends on the compatibility of lithium salt with solvent. Table I-5 compares the advantages and disadvantages of lithium salts used in Li-O_2 batteries [77].

Table I-5 : Comparison of common Li salts used in Li-O_2 batteries [77].

Li salt	Advantages	Inconveniences
LiClO_4	Conductivity Stability	Explosive
LiTFSI	Thermal stability Electrochemical stability	Conductivity
LiPF_6	Conductivity	Thermal instability HF formation in the presence of H_2O trace

I.2.4. Challenges of Li-O_2 batteries

As early mentioned in Section I.2.1, the exploration of Li-O_2 batteries is still at its early stage. There are some critical barriers for the practical application of Li-O_2 batteries. Figure I-14 gives an overview of some general challenges of Li-O_2 batteries [81]. They concern both the anode, such as the safety issue related to the dendrite formation and high reactivity of lithium metal through parasitic reactions, and the electrolyte with the reactivity with oxygen species, including singlet oxygen. In terms of performance, there are still many problems that need to be solved, including low capacity, poor rate-capability, low round-trip efficiency (large voltage gaps between discharging and charging) of the ORR/OER, and short cycle life. However, these later issues are more or less related to the cathode side, as will be described below.

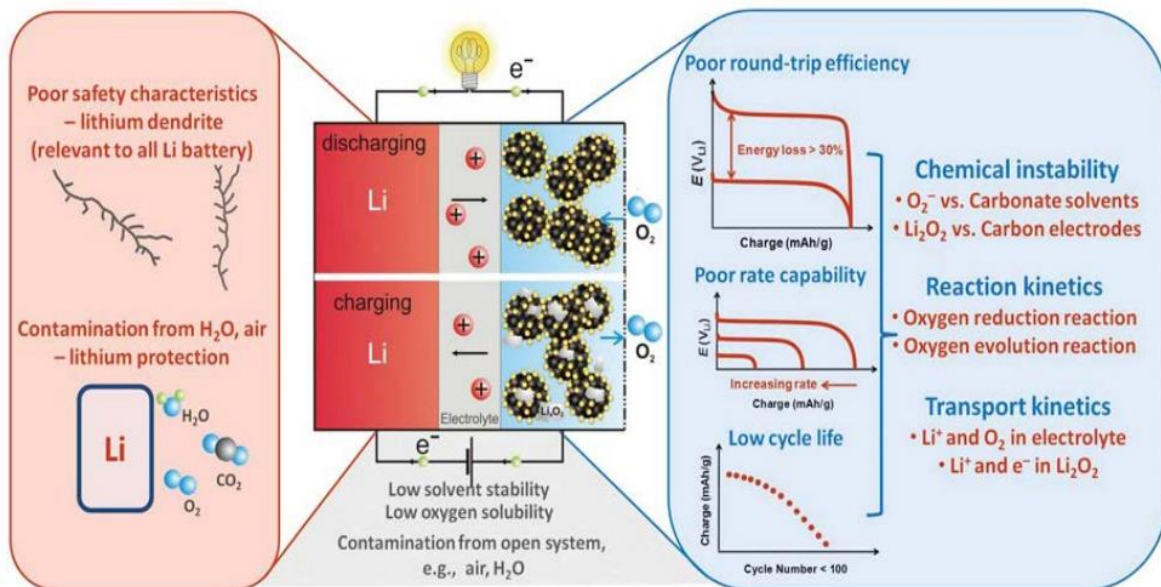


Figure I-14 : Major challenges of Li-O₂ batteries. Reprinted from [81].

I.2.4.1. Safety issues of lithium metal

As mentioned earlier, the problem of the lithium metal anode is not specific to Li-O₂ batteries but general for Li metal-based batteries. Lithium is very reactive and forms spontaneously a passivation layer in contact with organic electrolytes [82]. During the discharge process, Li⁺ - generated from the oxidation of the lithium anode - fissures the SEI before dissolving into the electrolyte (Figure I-15). During the charge process, the reverse reaction occurs: lithium metal is redeposited onto the surface of the electrode (lithium plating), leading to a non-homogeneous SEI layer. The uncontrolled growth of lithium dendrites leads to the formation of non-active lithium ("dead lithium") which causes irreversible capacity loss. Moreover, the dendrites formed upon cycling may break through the separator which can cause internal short-circuits and lead to explosion hazards [83].

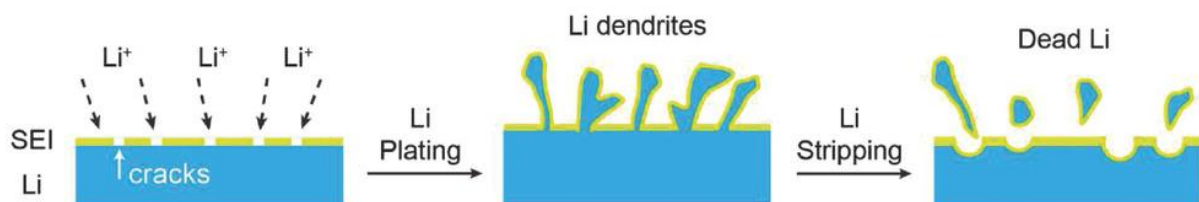


Figure I-15 : Dendrite formation observed on a lithium metal anode during the charge-discharge processes of a lithium-metal battery. Reprinted from [83].

In order to overcome the above challenges concerning formation, researchers have investigated different approaches [3]. The first consists of coating lithium metal with an ionic-conductive ceramic protection layer (LISICON), like for the aqueous Li-O₂ batteries. This layer also protects lithium from atmospheric contaminants such as H₂O or CO₂. Another possibility is to optimize the electrolyte formulation by changing the composition (solid electrolyte, mix of various solvents), by increasing the salt content, or by adding additives that stabilize the SEI (fluoroethylene carbonate (FEC), lithium nitrate, *etc.*). Another strategy is to create a stable artificial SEI by using a polymer electrolyte such as polyethylene oxide (PEO). These electrolytes should be able to block the dendrite formation through their solid polymer matrix while maintaining a good ionic conductivity. Still at the laboratory scale, the use of lithium metal anode leads to a massive excess of lithium. Consequently, its degradation can occur without limiting the capacity and does not strongly affect the study of others components such as the electrolyte or the air cathode.

1.2.4.2. Active singlet oxygen intermediate formation

The fundamental understanding of the complex mechanisms in non-aqueous Li-O₂ batteries is essential for the further development of these batteries. Recent studies have investigated the active singlet oxygen intermediate by *operando* electron paramagnetic resonance spectroscopy [84]–[86] and suggested its role in electrolyte and cathode decomposition in Li-O₂ batteries. Freunberger *et al.* have given concrete substance to this hypothesis [87]. They showed that producing singlet oxygen in typical ether-based electrolytes leads to the same decomposition products as observed in actual Li-O₂ batteries (Li carbonate, Li formate, and Li acetate). They achieved the measurement of singlet oxygen concentration produced in Li-O₂ batteries indirectly via an *operando* fluorescence probe of a chemical trap (dimethylantracene), which reacts rapidly with the singlet oxygen. They found that singlet oxygen is produced both during discharge and at the onset of charge. The singlet oxygen content increases substantially upon charging, as the potential rises or with added trace H₂O to the electrolyte. This behavior matches the rate of parasitic chemistry occurring in Li-O₂ batteries [88]. Parasitic reactions can be estimated by coupling the quantification of Li₂O₂ formation / decomposition to the O₂ consumption / evolution [89]. This is illustrated in Figure I-16, where the regions shaded yellow represent the difference between the amount of O₂ consumed or evolved and the amount of Li₂O₂ produced or consumed during discharge or charge, respectively. This difference could be due in large part to parasitic chemistry caused by singlet oxygen. The researchers suggested that the formation of active singlet oxygen in Li-O₂ batteries is the dominant source of the parasitic reactions observed [88]. They also showed that, by using a high concentration of singlet oxygen quenchers (1,4-diazabicyclo[2.2.2]octane), the parasitic reactions in Li-O₂ batteries can be effectively reduced.

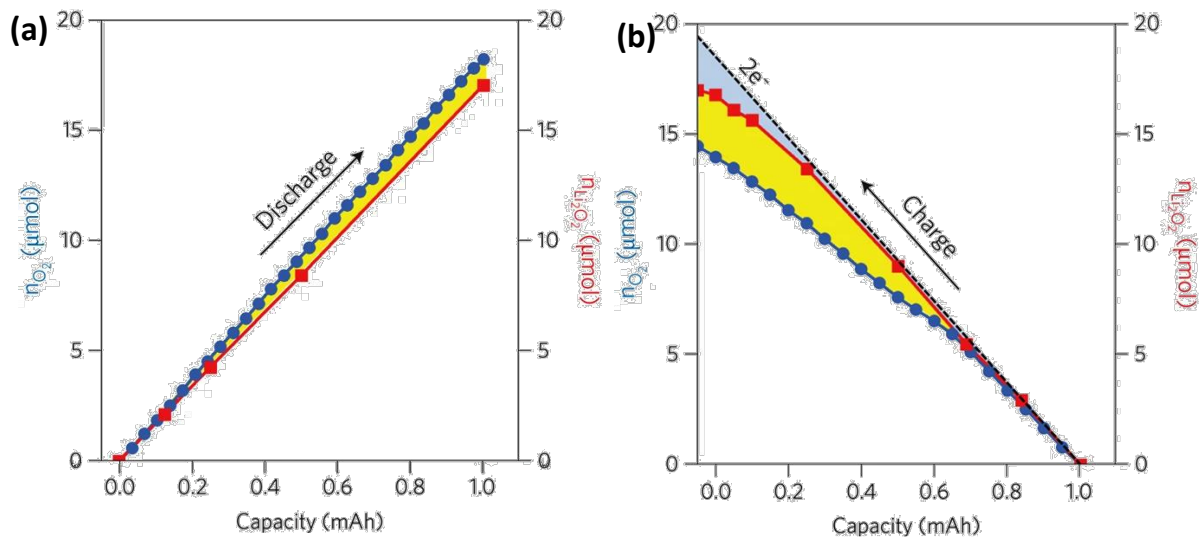


Figure I-16 : (a) Number of moles of O_2 consumed (n_{O_2} , blue) and of Li_2O_2 formed ($n_{Li_2O_2}$, red) during a 1 mAh Li- O_2 discharge. The ideal line for two electrons per O_2 consumed is indistinguishable from the blue points. (b) Number of moles of O_2 evolved (n_{O_2} , blue) and Li_2O_2 consumed ($n_{Li_2O_2}$, red) during recharge of the battery above. The ideal line for $2e^-$ consumption reflects the total charging current. The region in yellow for both discharge and charge reflects the parasitic contribution that could arise from singlet oxygen. The region in blue on charge is due to parasitic oxidation of species unrelated to Li_2O_2 and therefore presumably not related to singlet oxygen formation. Reprinted from [89].

I.2.4.3. Air cathode challenges

The drawback of Li- O_2 batteries is mainly the sluggish oxygen reduction reaction (ORR) and oxygen evolution reaction (OER) kinetics and the slow mass transport on the cathode [54]. Hence, many researchers devoted their works to finding new cathodes where the ORR / OER takes place and where the discharge products are hosted. The cathode must possess a high electronic conductivity to facilitate the electron transfer for the electrochemical reactions, and high porosity to 1) facilitate the O_2 gas and Li^+ diffusions and 2) store mainly the insoluble lithium peroxide Li_2O_2 [3]. The O_2 , electrons and Li^+ ions in the electrolyte solution meet at triple-phase boundaries where discharge product are generated [59]. The cathode material itself must be stable towards the active intermediate species (superoxide, singlet oxygen) and the final product Li_2O_2 . Many works focus on the optimization of the cathode materials, tuning the morphology, surface structure and pore distribution [90], [91]. The air cathode materials are generally composed of catalysts, conductive carbon and binders (polyvinylidene fluoride PVDF, polytetrafluoroethylene PTFE, etc.) loaded on a current collector (steel mesh, Ni foam, carbon paper, etc.). In general, the mass loading of active material on the cathode is about 1 mg/cm^2 [92], [93].

At first, an essential criterion of air cathode is the catalytic activity for ORR and/or OER, which plays an important role in reducing overpotentials in both ORR / OER reactions. The high overpotential (η) is mainly due to the sluggish decomposition of Li_2O_2 during the OER reaction [94]. Figure I-17 illustrates a typical discharge-charge profile of a Li- O_2 cell, where the overpotentials in both charge and discharge (η_{charge} and $\eta_{\text{discharge}}$) are depicted. These high overpotentials in turn could cause electrolyte decomposition, and consequently, the cell's life may be diminished with low energy efficiency. Ideally, the cathode material should help decrease the overpotential values. The use of intrinsic catalyst on the cathode or a redox mediator may improve the ORR and / or OER kinetics by reducing the overpotential.

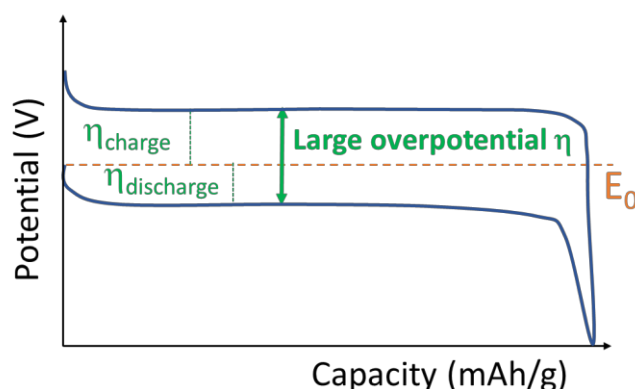


Figure I-17 : Discharge-charge profile of Li- O_2 battery.

The second critical point of the cathode is the porosity. As aforementioned, aside from the O_2 and Li^+ ions diffusion, the porosity of the cathode material ensures also the battery capacity via the storage of generated Li_2O_2 products. Open micropores and mesopores are favorable for improved discharge capacity. Studies have shown that the pore size impacts the discharge capacity [95], [96], and the mesoporous electrodes are more effective in the pore volume utilization than micropores electrodes [97]. Additionally, even for the electrodes with micropores, the open pores can promote O_2 diffusion [98].

The wettability of the electrode is an additional important parameter that influences the discharge capacity in the Li- O_2 battery. Li and Wang have demonstrated that the wettability of the electrode is highly related to the nature of the binder in the electrode. The lyophilicity favors the wettability of the electrode by the aprotic solvent while the lyophobicity favors a fast O_2 diffusion. The generally used PVDF binder is lyophilic while the PTFE is lyophobic [99]. Carbon electrodes with the same content of binder deliver a discharge capacity of 1666 mAh/g and 4161 mAh/g for 15 % PVDF (36.5°C) and 15 % PTFE respectively. As a consequence, the number of triple points for the ORR / OER might be impacted by the difference in the electrode wettability, thereby influencing the Li- O_2 battery performances.

I.2.5. Air cathode development

Air cathode materials in Li-O₂ batteries can be divided into two groups: carbon-based materials and carbon-free materials. We selected some typical reports on each kind of cathode material and introduce them in this section. However, the electrodes described in the literature hardly ensure full reversibility, and their cyclability is still poor.

I.2.5.1. Carbon-based materials

Owning excellent electrical conductivity, high surface area and possible catalytic activity, carbon materials have been widely used as air cathodes for Li-O₂ batteries with impressive capacities. Especially, tailoring pore size could enhance the battery performance [95], [100], [101].

Commercially available carbons, such as Super P, Vulcan XC-72, Ketjenblack, and carbon nanotubes (CNTs) are largely used as conductive additives or materials in cathode in Li-O₂ batteries. Table I-6 reports discharge capacities of various carbon materials [100]. Although activated carbon has a high surface area, this material exhibits the lowest discharge capacity. In contrast, carbon Super P shows a high specific capacity while it possesses a low surface area. The high capacity can be explained by the large pore diameter inside this carbon. Upon discharge, lithium oxide products accumulate inside the pore during the ORR reaction. However, they also deposit on the surface of the air cathode, blocking thus the access to the pores (Figure I-18). As Li₂O₂ particles are electrical insulators, their accumulation on the cathode interferes also on further electron transport [101].

Table I-6 : Discharge capacity for various carbon materials at 50 mA/g [100].

Carbon materials	Discharge capacity (mAh/g)	Surface area (m ² /g)	Pore diameter (nm)
Super P	1736	62	50
Vulcan XC-72	762	250	2
Activated carbon	414	2100	2
Carbon nanotubes	583	40	10
Mesocellular carbon foam	2500	824	30

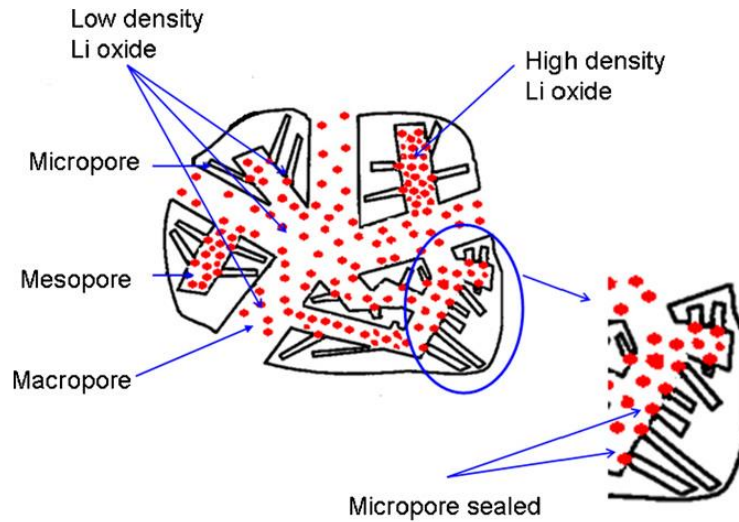


Figure I-18 : Accommodation of lithium oxides in various-sized pores of carbon materials. Reprinted from [101].

Liu *et al.* have demonstrated that the increase of carbon pore size from 20 nm to 80 nm, increases the discharge capacity from 3343 mAh/g to over 7000 mAh/g (Figure I-19) [95]. The slightly smaller discharge capacity at the pore size of 100 nm suggests that, for sufficiently large pore size (when the access to the surface inside pores and the blockage of Li_2O_2 are unlikely issues), the BET surface area could play a role where a larger surface area enables a higher capacity (859 cm^2/g vs. 823 cm^2/g). A physical model is proposed by the authors to illustrate the influence of the carbon pore size on cell capacity, in which a monolayer of Li_2O_2 with a thickness of 7.8 nm forms inside the carbon pores during the discharge process.

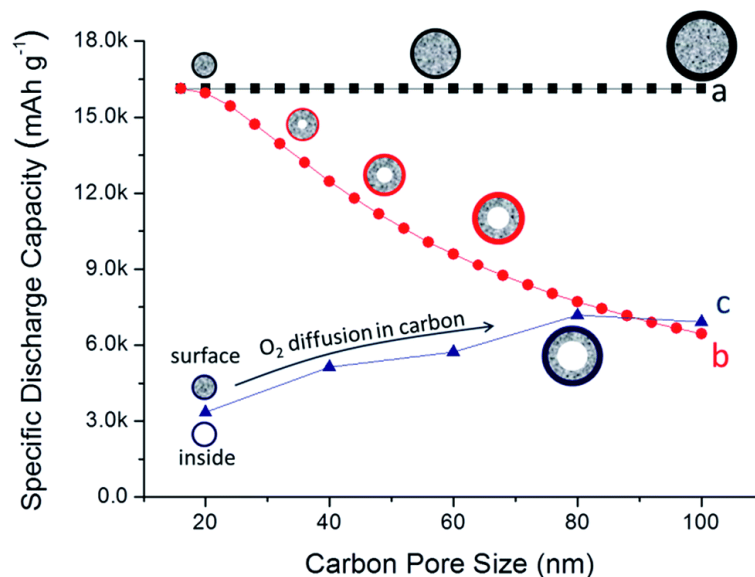


Figure I-19 : Physical models of Li_2O_2 stored in porous carbon: line a represents that all carbon pores are fully filled by Li_2O_2 ; line b assumes the formation of a monolayer of Li_2O_2 (with a thickness of 7.8 nm) inside carbon pores; line c is the experimental data. Reprinted from [95].

Despite the evidence of large capacities achieved with carbon electrodes, many studies have demonstrated that these carbon materials suffer from irreversible surface decomposition under the oxidative environment in the Li-O₂ batteries. Moreover, carbon materials are unstable in Li-O₂ batteries at high charging overpotentials [54], [65]. As aforementioned, the intermediate oxygen radical product O₂⁻ is reactive, it could also attack the carbon cathode to generate side products. An early study has proved the presence of a thin layer of Li₂CO₃ at both carbon / Li₂O₂ and Li₂O₂ / electrolyte interfaces since the onset of the charge process [54]. As shown in Figure I-20, the deposit may also contain some carbonate dispersed in the Li₂O₂ deposit due to an electrochemical reaction with the electrolyte during discharge (point A). During charging, the Li₂O₂ layer also becomes partially covered by carbonate (Li₂CO₃ and LiRCO₃) through the electrochemical reaction of Li₂O₂ with the electrolyte, and by accumulation at the surface of any dispersed carbonate formed in discharge that does not oxidize at low voltage (point B). As charging continues, the surface becomes fully covered by carbonate (point C). Because of the ever-smaller fraction of Li₂O₂ at the surface during charging, the overpotential for OER must continuously increase to maintain a constant galvanostatic charge rate until at high voltage. However, this rising potential is unfavorable for electrochemical stability of the electrolyte and for the round-trip efficiency.

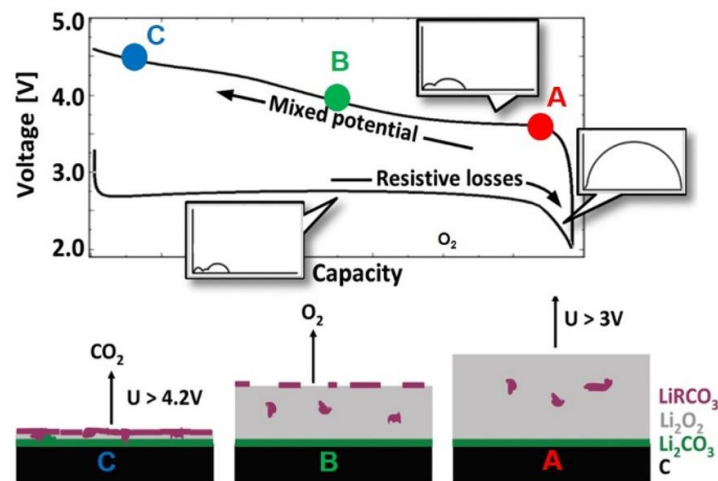


Figure I-20 : Electrochemical impedance behavior of Li₂O₂ formation and decomposition processes at various stages of charge, A–C. A substantial increase in polarization resistance occurs toward the end of the discharge, whereas at the beginning of the charging, this polarization resistance decreases compared to that at the end of the prior discharge. Reprinted from [54].

Generally speaking, the carbon porous materials exhibit good performance in the ORR reaction owing to its good electrical conductivity but high charge overpotentials in the OER, where electrolyte decomposition may occur [54], [57]. The use of catalysts is thus required to reduce the charge potential to avoid this issue so as to increase the cycle life of the cells.

I.2.5.2. Carbon-free materials

Alternatively, carbon-free materials have also been a research topic for the cathode in Li-O₂ batteries, such as noble metals, their oxides, and transition metal-based materials [102]. These metal-based materials usually show good catalytic activity for the ORR/OER reactions.

Noble metals are important catalysts for ORR and OER applications [102]. Up to now, many studies have reported the superiority of noble metals and their oxides including Au, Ru, Pt, Pd [102]–[104]. For instance, nanoporous Au cathodes achieve a capacity of 320 mAh/g (equivalent to 3000 mAh/g of carbon) and retain 95% of their capacity after 100 cycles. The kinetic of charge is 10-fold higher in the case of Au cathode than carbon cathode. In addition, the Au cathodes reduce the charge overpotential below 4.0 V vs. Li⁺/Li. Other noble metals including Pt, Pd, Ru, and their oxides are also promising for both ORR and OER electrocatalysts in Li–O₂ batteries [105], [106]. Although admirable achievements have been made by using noble metals to reduce the overpotentials of Li–O₂ batteries, their high costs make themselves unsuitable for practical applications.

To replace the expensive noble metals, many researchers have chosen the cheap transition metal-based materials as the cathode of Li–O₂ batteries, such as metal carbides / oxides. For instance, compared to the carbon electrode, Zhou and coworkers have reported significant OER catalytic activity of a Li–O₂ battery using Ruthenium/Indium Tin Oxide (Ru/ITO) as air cathode. The ITO electrode has very limited discharge capacity and cannot be recharged. Upon adding Ru nanoparticles into ITO electrode, the charge potential of Ru/ITO is significantly lower by 600 mV vs. Li⁺/Li compared with the corresponding Super P carbon electrode [107]. Besides, Liu's group prepared the vacancy-bearing CoO (CoO-A) and vacancy-free CoO (CoO-N). They found a synergetic effect of CoO and oxygen vacancies that can significantly reduce the overpotential by about 0.4 V vs. Li⁺/Li and achieves much better cycling stability (Figure I-21) [108]. The authors demonstrated that oxygen vacancies can facilitate the electronic conductivity and Li⁺ migration as well as serve as active sites for O₂ and Li₂O₂. The CoO-A shows an initial capacity of 3421 mAh/g. After 8 cycles, still 72 % of the capacity is retained. Upon cycling with a cut-off capacity of 1000 mAh/g, the coulombic efficiency of CoO-A maintains nearly 100 % during the first 25 cycles, while the coulombic efficiency of CoO-N is much lower than the CoO-A and unstable.

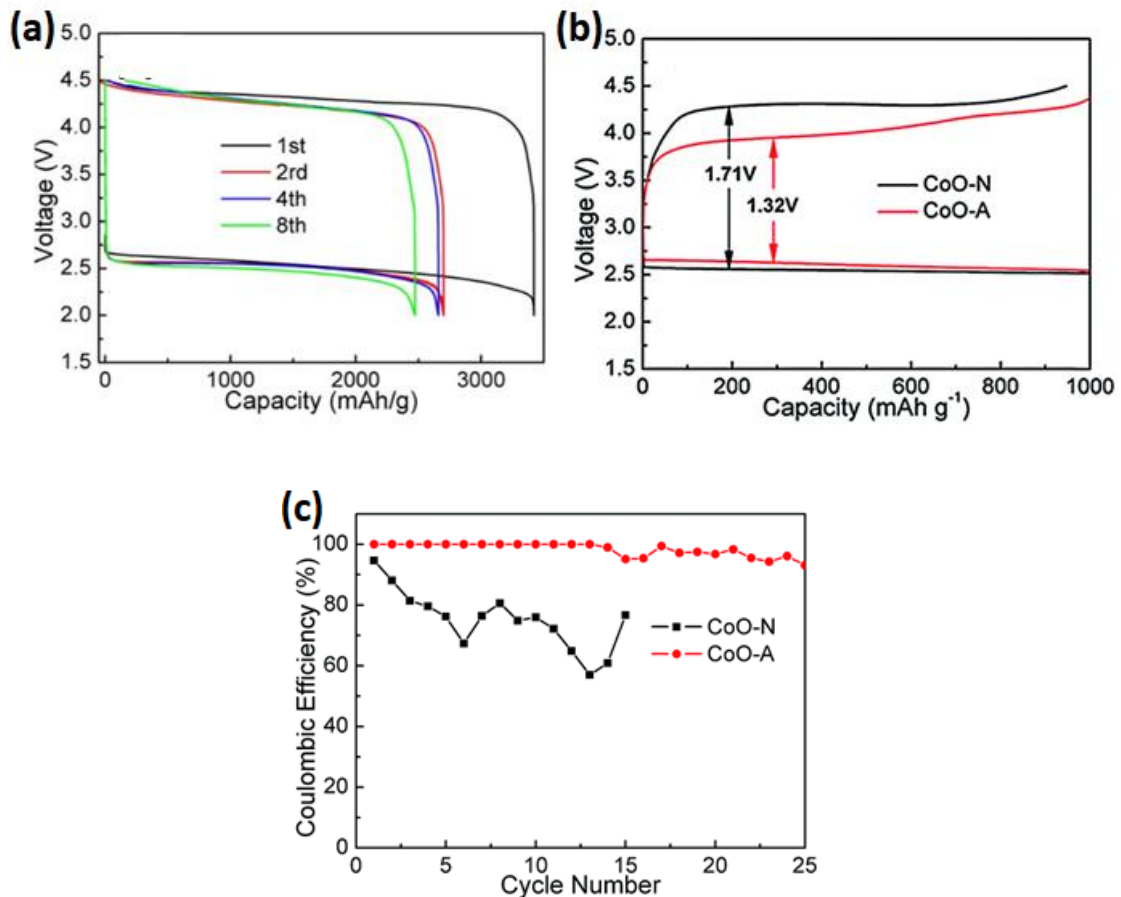


Figure I-21 : (a) The full discharge-charge profiles of CoO-A. (b) The first limited discharge-charge curves, and (c) the coulombic efficiency of CoO-A and CoO-N based cathodes with a cut-off capacity of 1000 mAh/g. The applied current densities are 200 mA/g [108].

Alternatively, manganese oxides have been studied intensively as air cathodes for Li-O₂ batteries due to their robust OER and ORR performances [109], [110]. MnO₂ crystallizes in various structures including three tunnel structures (α -, β -, γ -MnO₂) and a layered structure (δ -MnO₂). The addition of MnO₂ nanoparticles in carbon electrodes significantly increases the discharge capacity and the reduced discharge and charge overpotentials compared to bare carbon electrodes [111]. Figure I-22 shows the charge-discharge profile of Li-O₂ batteries with different MnO₂ cathodes as well as a KB carbon electrode. Both α -MnO₂ and δ -MnO₂ electrodes exhibit similar discharge (2.7 V vs. Li⁺/Li) and charge potentials (3.9 V vs. Li⁺/Li) [111]. The smaller overpotentials observed for MnO₂ demonstrate the better catalytic activity of MnO₂ compared to KB carbon. The α -MnO₂ electrode delivers a maximum discharge capacity of 6126 mAh/g which is more than 2000 mAh/g higher than δ -MnO₂ electrode, and 3-fold higher than the carbon KB electrode. The α -MnO₂ electrode promotes also a high charge capacity with 100 % coulombic efficiency [111].

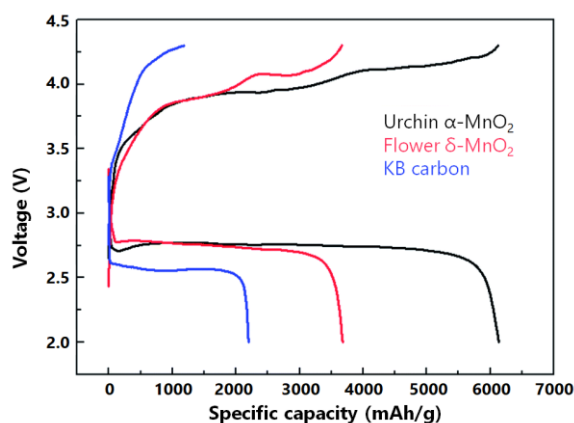


Figure I-22 : Charge-discharge profiles of α - and δ - MnO_2 nanomaterials. Reprinted from [111].

There are still various other transition metal oxides such as Co_3O_4 , NiO , Fe_3O_4 , Mn_3O_4 that have been studied as air cathode with efficient catalytic activity. Besides, some binary transition metals can provide better catalytic capacity than a single one [101].

However, the bulk transition metals / metal oxides particles suffer from particle aggregation and may decrease their active sites exposed to the air. The particle dispersion control of these compounds is key to their better catalytic performance in Li-O_2 batteries.

I.2.6. Reproducibility issue

The data reproducibility of Li-O_2 batteries is a big challenge in the community but it is not often reported or even discussed. In most reports, a single cycle is presented and reproducibility is not discussed. We give below the only few examples found in the literature.

Firstly, as shown in Figure I-23, a large discrepancy in both the discharge capacities and the overpotentials has been observed for cycled Li-O_2 batteries, even for homogenous electrode films [67], [112]. For example, a difference of discharge capacity close to 2000 mAh/g could be observed for two similar carbon-loaded DPB60 electrodes at a low rate of $50 \mu\text{A}$.

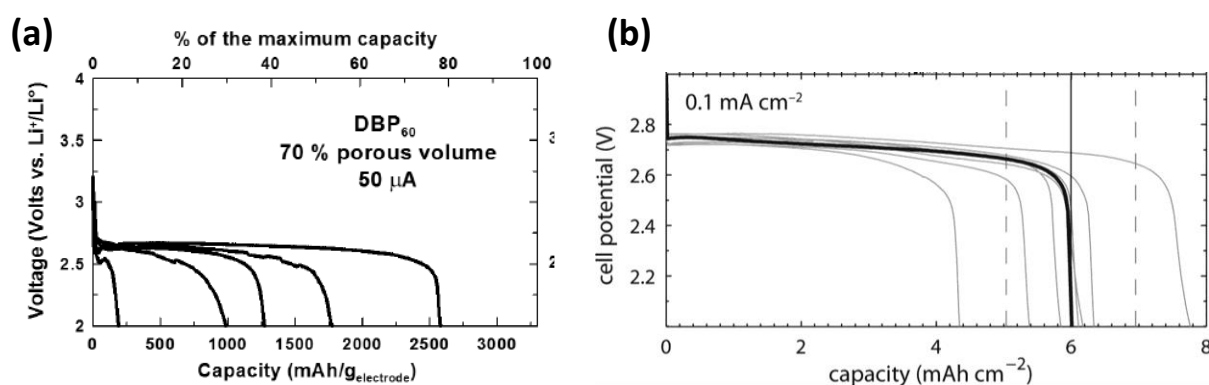


Figure I-23 : (a) First discharge curves in Li-O_2 battery for carbon-based DPB60 electrodes at $50 \mu\text{A}$ [112]. (b) Dependence of potential on specific capacity for carbon-based Li-O_2 cells discharged at 0.1 mA/cm^2 . Vertical solid lines show the average discharge capacity; vertical dashed lines indicate its standard deviation [67].

Besides, Read *et al.* revealed that the electrolyte volume is a critical parameter for obtaining reproducible results [113]. As shown in Figure I-24, the volume of the electrolyte influence the capacity : excess or small amount of electrolyte lead to a decrease of the capacity. With suitable volume electrolyte, the best capacity is obtained for the electrolyte-filling cathode while still having sufficient pores for the O₂ diffusion.

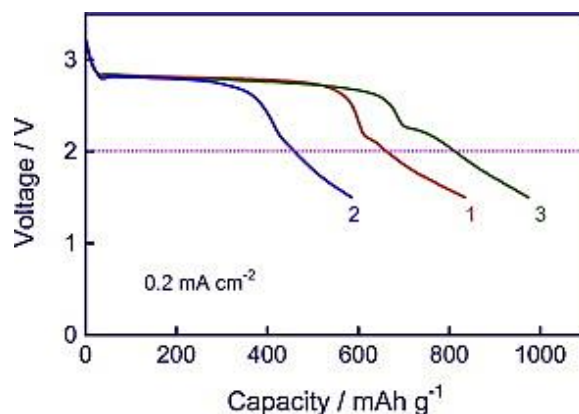


Figure I-24 : First discharge curves of three Li-O₂ cells with different electrolyte-filling statuses, recorded at 0.2 mA/cm². (1) With insufficient electrolyte, (2) with excess electrolyte, (3) with appropriate amount of electrolyte [113].

Overall, the largest discharge/charge capacities are often reached at the first full cycling (around several thousand mAh/g). As a consequence of reproducibility issue from full cycling, researches are usually cycling the Li-O₂ batteries with a cut-off capacity in order to increase the battery cyclability, for example 1000 mAh/g, which is still larger than that of Li-ion batteries. However, the true capacities depend on initial porosity and thus the discharge product-to-electrolyte ratio, the limited-capacity regimes are believed unsuitable to demonstrate the large reversible capacities for many cycles in the batteries [114].

I.3. Metal-Organic Frameworks

I.3.1. Definition

Metal-Organic Frameworks (MOFs) constitute a class of crystalline porous materials built up from inorganic and organic groups connected through covalent bonds to form multidimensional structures. As shown in Figure I-25, the inorganic moieties (also called Secondary Building Units – SBU) can be composed of metal ions or metallic clusters (dimer, trimer,...), chains, layers, or 3D-networks and define the dimensionalities of the sub-network [115]. The organic linker has generally one or more aromatic rings to provide a certain rigidity to the structure and at least two complexing functions to create self-assembly. The most popular organic ligand is based on carboxylate groups, such as benzene-1,4-dicarboxylic acid (BDC) or benzene-1,3,5-tricarboxylic acid (BTC). Others groups such as phosphonate, sulfonate, or imidazole are also being used [116], [117]. The combination of various metal centers and the wide variety of organic ligands available offers a large range of compositions and structures, leading to multiple applications.

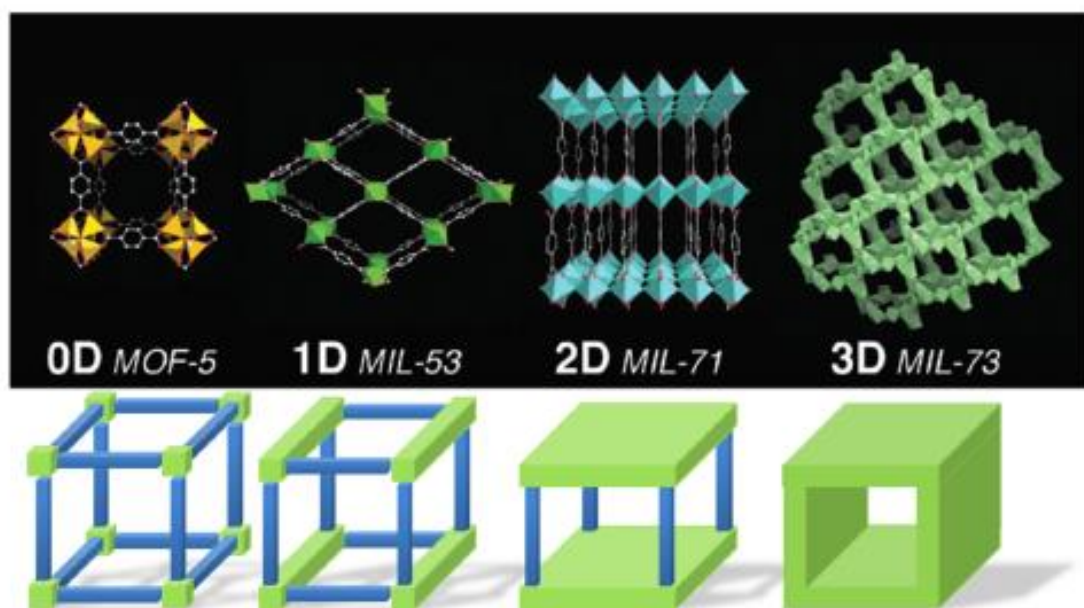


Figure I-25 : Examples of MOFs with different dimensionalities of the inorganic sub-network and their schematic representations (green: inorganic entities and blue organic linker). Reprinted from [115].

The term MOF was used for the first time by Li and Yaghi in 1995 [118]. However, other groups have chosen to identify their own materials using a short acronym related to the name of the institute or university where the new materials were synthesized, such as MIL for *Materials Institute Lavoisier* or HKUST for *Hong-Kong University of Science and Technology*. Sometimes, only the chemical formula is used to identify new materials. In 2013, the IUPAC (International Union of Pure and Applied Chemistry) defined the term MOF as a coordination network with organic ligands containing potential voids [119].

Depending on the size of the cavities or pores, porous materials can be classified as microporous (pore diameter < 2 nm), mesoporous (pore diameter in the range 2-50 nm), or macroporous (pore diameter > 50 nm) materials [120]. MOFs materials are often microporous or mesoporous materials. They exhibit a high specific surface exceeding by far other porous materials such as zeolites or activated carbon [121]. To our knowledge, the highest record of BET surface area (7839 m²/g) was reported by the group of Kaskel in 2018 [122]. However, this ambiguous value corresponds to the BET estimated from different linear regions.

As shown in Figure I-26, Kitagawa and coworkers have proposed a classification of porous solids (MOFs included) into three categories depending on their responses to guest molecules (gases, solvent molecules, drug, *etc.*) present inside the pores [123]:

- The 1st generation: materials have microporous frameworks but show irreversible framework collapse or removal of guest molecules;
- The 2nd generation: materials have robust and rigid porous frameworks and retain their crystallinity with any guest molecules in the pores;
- The 3rd generation: materials have flexible and dynamic porous frameworks, leading to a reversible structural transformation under external stimuli such as temperature, presence of guest molecules.

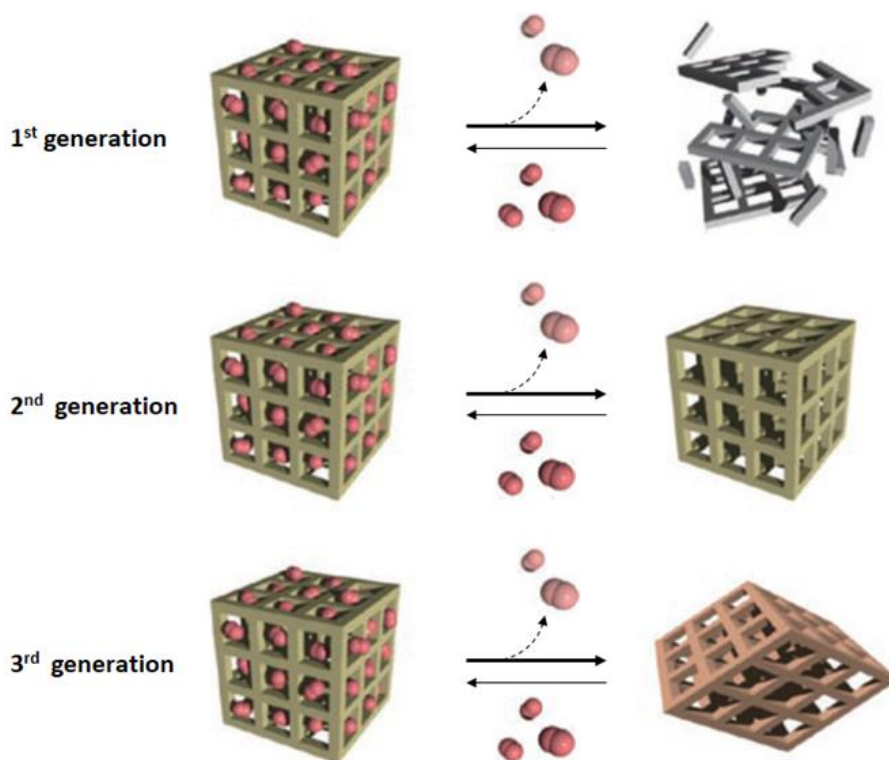


Figure I-26 : Schematic representation of the three generations of porous materials. Reprinted from [123].

I.3.2. Isoreticular chemistry and functionalization

To date, over 90 000 MOF materials have been synthesized [124]. Several approaches are developed to design new structures by replacing the original ligands with an organic ligand with different sizes or eventually functionalized, which increases the pore size while keeping the same inorganic network. Figure I-27 highlights the effects of increasing the length of the organic linker or introducing a functionalization on the pore volume. The IRMOF (isorecticular MOFs) series were reported by Yaghi and coworkers [125]. All IRMOFs have the cubic topology of the MOF-5 (also called IRMOF-1) in which an oxide-centered Zn_4O tetrahedron is edge-

bridged by six carboxylates (from organic linker) to form a 3D cubic structure. These structures differ in the nature of the functional groups decorating the pores and in the metrics of their pore structures. The pore size can be incrementally varied from 3.8 Å to 28.8 Å [125]. The functional groups that point towards the pore can affect the free pore size and thus properties such as polarity, hydrophobicity, adsorption property, flexibility, etc. [125]–[127]. Depending on the synthesis conditions (concentration of reactants, temperature, or other experimental conditions), a non-interpenetrated network can be obtained. The structure corresponds to two identical and independent network units thus forming a solid with different properties from the initial non-interpenetrating network solid. Although this formation is sometimes unwilling and is considered as a limit of isorecticular chemistry, it improves in certain cases the gas adsorption or selectivity properties (such as hydrogen, carbon dioxide, methane adsorptions), due to the pore volume reduction and the strengthening of the structure weakened during the departure of adsorbed solvent molecules. Besides, the extension of the linker length may generate interpenetration frameworks leading to less porous materials as expected [128].

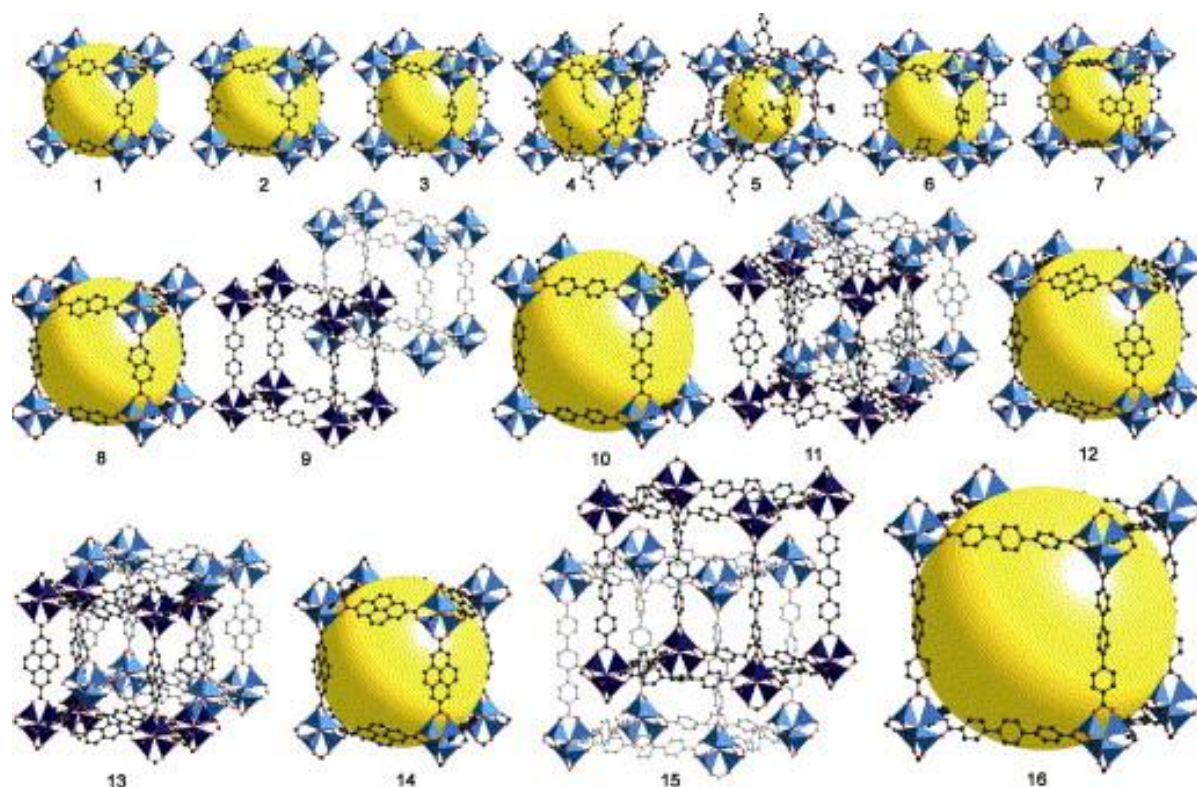


Figure I-27 : Structures of the IRMOF series. The number beside the structure corresponds to the name of the IRMOF-*n*. Blue: Zn, red: O, black: C, large yellow sphere: accessible pore based on the van der Waals sphere. When an interpenetrated structure is observed (*n*=9, 11, 13, and 15), no pore volume is available. Reprinted from [128].

I.3.3. Well-known MOFs

I.3.3.1. Rigid solids

Frameworks constructed with carboxylate group represent the large majority of MOFs. Among these materials, several MOFs are well known for their excellent thermal and chemical stabilities. We report here only the most studied MOFs that show good stability and remarkable properties.

In 1999, Williams *et al.* described firstly the structure of the solid **HKUST-1** or $\text{Cu}_3(\text{H}_2\text{O})_3(\text{BTC})_2$ [129] This compound is also called MOF-199 or Cu-BTC. It is composed of benzene-1,3,5-tricarboxylate (BTC) ligands coordinated by copper ions leading to a three-dimensional cubic structure, exhibiting large square-shaped pores of $9 \times 9 \text{ \AA}^2$ (Figure I-28). The copper is square-based pyramidal, with the axial positions being occupied by the other copper cations and a water molecule. These water molecules can be eliminated by simple heating, which promotes the creation of unsaturated metal centers necessary for physisorption. The solid has thus exceptional properties for gas sorption [130], [131]. The structure remains stable upon solvent sorption / desorption [132]. The solid achieves a BET surface area of $692.2 \text{ m}^2/\text{g}$.

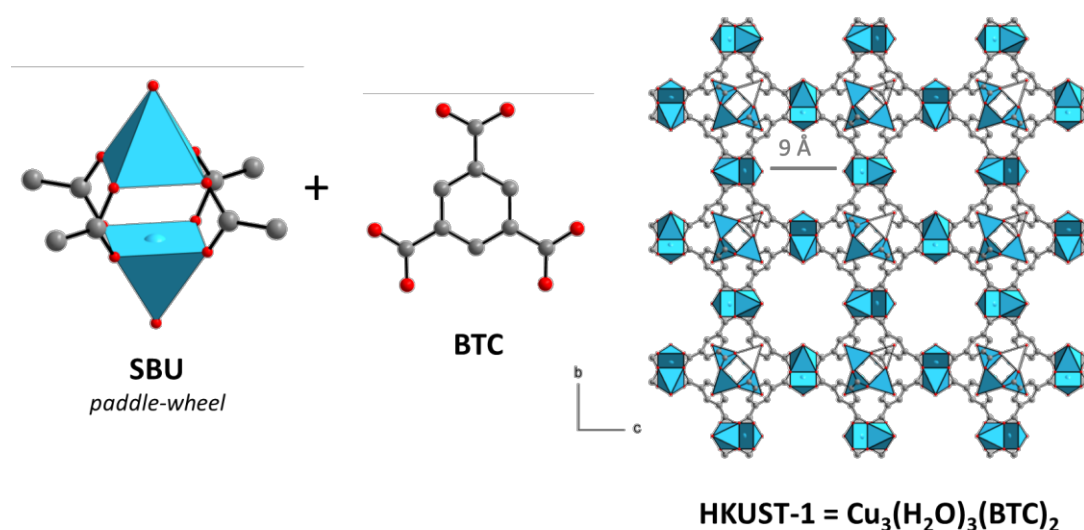


Figure I-28 : View of the SBU with Cu linked via the organic linker used and representation of the cubic structure of HKUST-1. Guest molecules have been removed for sake of clarity.

In the same year, Yaghi *et al.* reported the synthesis and the structure of **MOF-5** or $\text{Zn}_4\text{O}(\text{BDC})_3$, also known as IRMOF-1 [133]. Its three-dimensional cubic structure results from the connection of metal cluster Zn_4O by benzene-1,4-dicarboxylic acid (BDC) (Figure I-29). The metal cluster Zn_4O is built from four tetrahedrons ZnO_4 sharing a common oxygen atom, while the other oxygen atoms come from the carboxylate groups. It exhibits a high surface area of $2900 \text{ m}^2/\text{g}$ with a pore diameter of *ca.* 12 \AA . The structure remains crystalline and stable when fully desolvated or heated up to 300°C [133]. Since 1999, the solid is largely studied for its various applications such as gas storage [134], [135], catalysis [136], luminescence [137], electrochemistry [138], [139] *etc.* As illustrated in Section I.3.2, MOF-5 is the first of a series of

isorecticular MOFs sharing the same cubic topology. It is possible to modify its properties by increasing the organic ligand length or by decorating the pore volume.

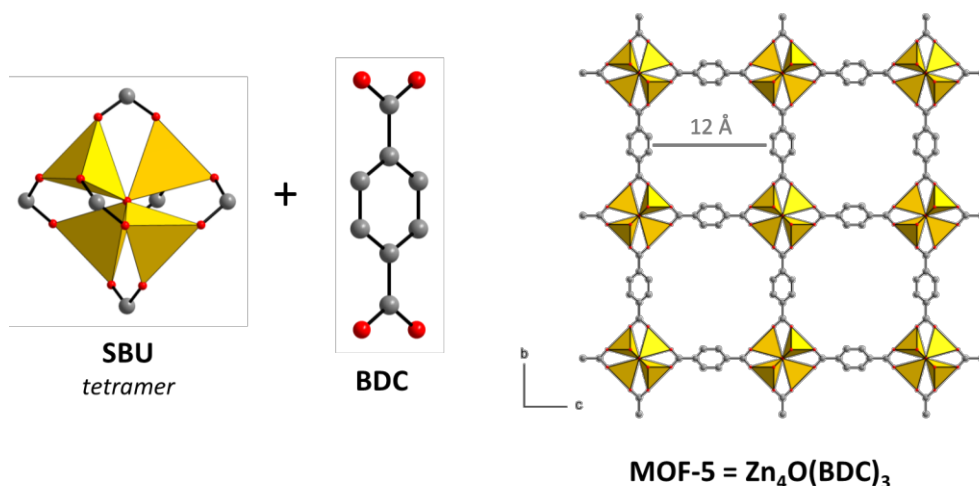


Figure I-29 : View of the SBU Zn linked via the organic linker used and representation of the cubic structure of MOF-5. Guest molecules have been omitted for sake of clarity.

Another crystallographic structure is obtained by replacing the benzene-1,4-dicarboxylic acid (BDC) with 2,5-dihydroxybenzene-1,4-dicarboxylic acid (DHBDC) [140]. The **MOF-74** structure is based on coordinated carboxyl and hydroxyl groups. Helical Zn–O–C rods of composition $[O_2Zn_2](CO_2)_2$ are constructed from 6-coordinated Zn(II) centers (Figure I-30). In addition, two hydroxyl groups are bound as doubly bridging. The structure exhibits 1D hexagonal channels, where free water molecules can be located. The group of Yaghi has reported the synthesis of an isorecticular series of M-MOF-74 with other metals (M=Mg, Co, Ni, Mn, etc.) [141]. Due to the presence of open metal sites, the M-MOF-74 are largely studied for gas adsorption, and as separator and catalyst [142].

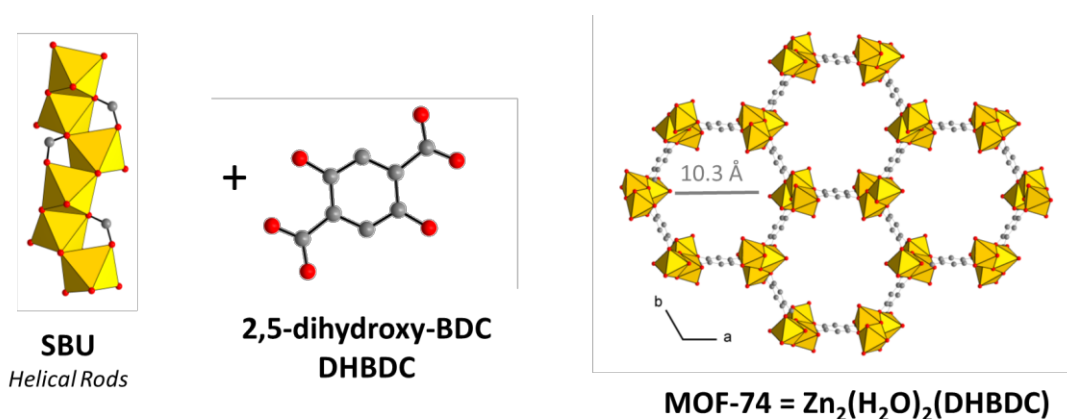


Figure I-30 : View of the SBU with Zn linked via the organic linker used and representation of the hexagonal structure of MOF-74. Guest molecules have been omitted for sake of clarity.

In the same period, the MIL-100 and MIL-101 solids with hybrid giant pores have been synthesized [143], [144]. Both solids crystallize in a three-dimensional cubic structure based on the connection of several super tetrahedrons (Figure I-31). These inorganic moieties are built up of inorganic trimers that consist of three chromium atoms in an octahedral environment with four oxygen atoms coming from the dicarboxylate groups (BTC and BDC for MIL-100 and MIL-101, respectively), sharing one common oxygen atom and the last oxygen atom comes from the terminal water. The super tetrahedrons are microporous and the resulting framework delimits two types of mesoporous cages with internal free diameters of 25 Å / 29 Å for MIL-100 and 29 Å / 34 Å for MIL-101. The large windows of both cages give access to very large molecules. The smaller cages exhibit pentagonal windows with a free opening of 12 Å and a hexagonal window of 14.7 - 16 Å. These solids have giant cell volumes (380 000 and 702 000 Å³) and exhibit high surface areas of 3100 m²/g and 5900 m²/g for MIL-100 and MIL-101 respectively. These solids are hence largely studied for their remarkable sorption properties. Especially the iron-based MIL-100 and MIL-101 show the advantages of being non-toxic and biocompatible carriers for the vectorization of drugs [145], [146].

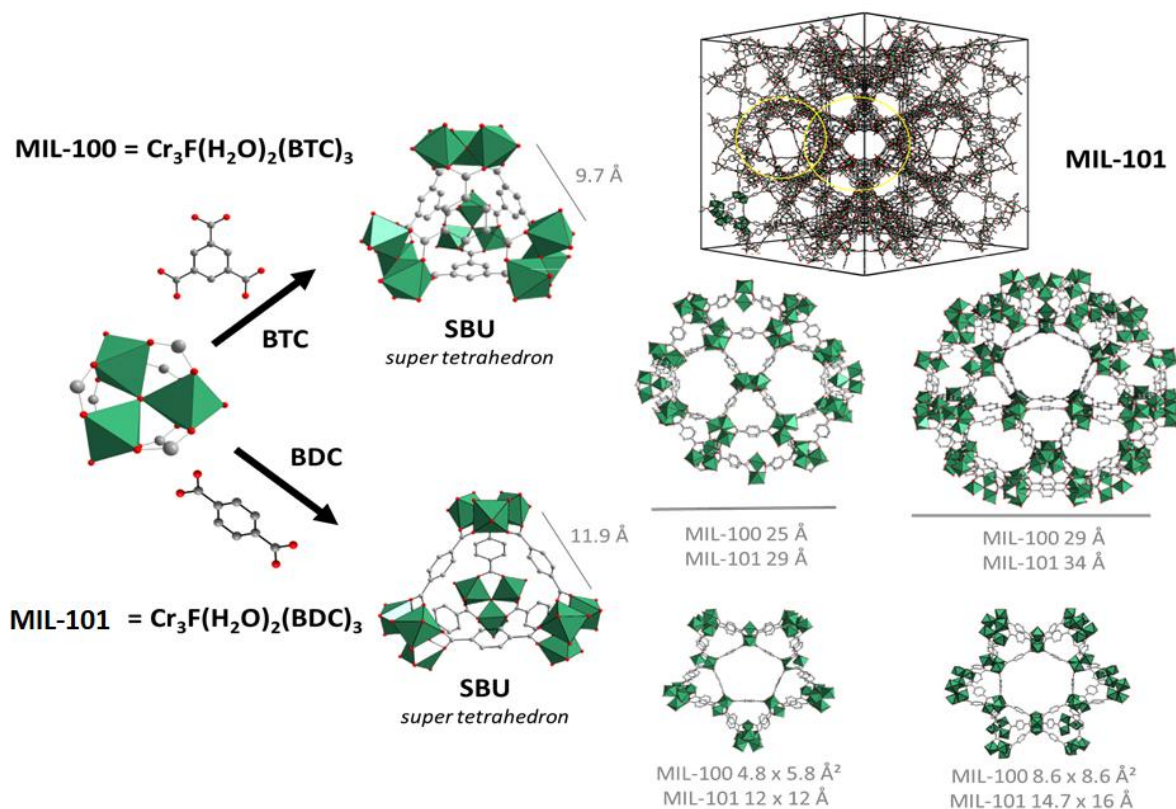


Figure I-31 : View of the SBU with Cr linked via the organic linker used and representation of the cubic structure of MIL-101. Guest molecules have been omitted for sake of clarity. Only the super tetrahedron of MIL-100(Cr) is shown.

A decade ago, Lillerud *et al.* have synthesized the zirconium-based MOF solid UiO-66 [147]. This compound consists of $Zr_6O_4(OH)_4$ hexamers coordinated with the dicarboxylate groups of BDC. Each $Zr_6O_4(OH)_4$ cluster is bridged with twelve BDC linkers, resulting in a face-centered cubic lattice. The framework features two types of cages: one is tetrahedral with a free diameter of 7 Å through trigonal windows and the other is octahedral with a free diameter of 9 Å (Figure I-32) [148]. The UiO-66 has a pore volume of 0.77 cm³/g and a BET surface area of 1160 m²/g [149]. The framework is stable until about 450°C. UiO-66 is the pioneer of Zr-based MOFs. Since the discovery of UiO-66, more than 40 analogues have been synthesized with functionalized BDC linkers or other organic linkers [150]. For example, among the isorecticular solids of UiO-66, the UiO-67 uses the 4,4'-biphenyl-dicarboxylate (BPDC) ligand, leading to a cage size up to 16 Å and a surface area of 3000 m²/g. Another isorecticular solid is the UiO-68 which uses the terphenyl-dicarboxylate (TPDC) ligand. This linker having a longer phenyl length than BDC and BPDC allows a larger cage size of 25.6 Å and a higher surface area of 4170 m²/g for UiO-68 [149]. Due to their stability in water, these Zr-based solids are largely studied towards water purification and hydrolysis [149].

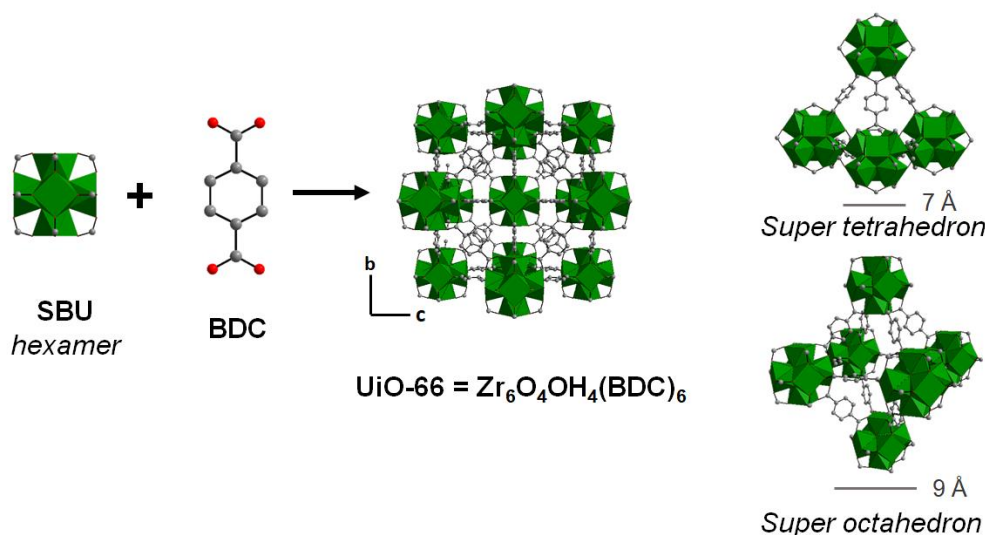


Figure I-32 : View of the SBU with Zr linked via the organic linker used and representation of the cubic structure of UiO-66. Guest molecules have been removed for sake of clarity.

I.3.3.2. Flexible solids

As defined by Kitagawa *et al.* [123], the third generation of MOFs is flexible: a reversible structural transformation occurs under external stimuli. These stimuli can be guest molecules adsorption / desorption [151], temperature [152], mechanical stress [153] or pressure [154]. The modification of the structure leads to drastic changes in its physical and chemical properties.

Flexibility generally depends upon metal nodes, the flexibility of ligands, and the connections between metal and ligands. It results from coordinative bonding / interactions between inorganic and organic components. The flexibility can be explained by different modes of transformation [154]. The flexibility can result from (i) breathing, (ii) swelling, (iii) linker rotation, and (iv) subnetwork displacement. Each mode is illustrated as below by an adequate example of MOF reported in the literature (Figure I-33).

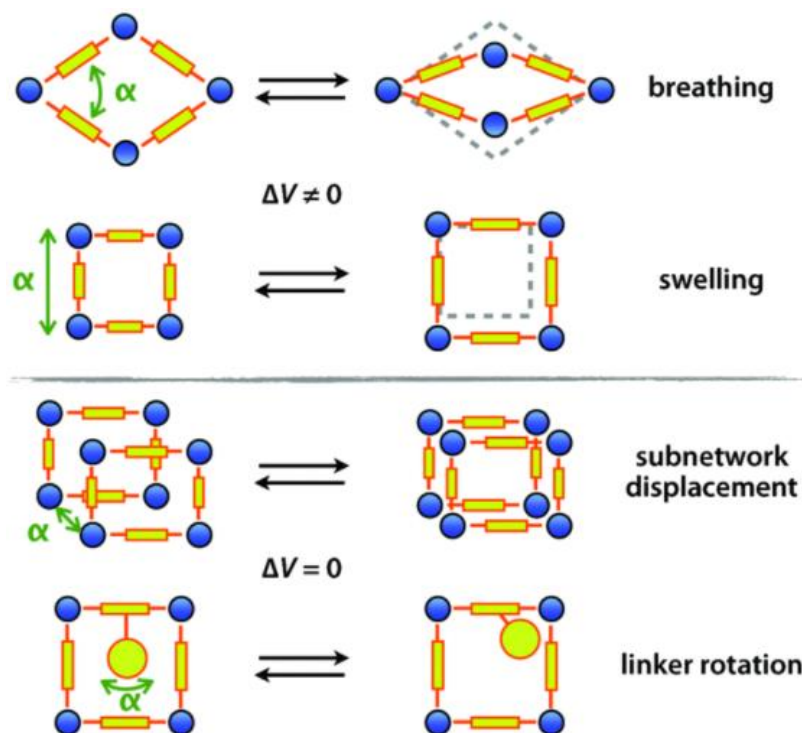


Figure I-33 : Schematic of the different modes of flexibility in porous materials. Reprinted from [154].

The **breathing mode** involves a reversible variation of the unit cell volume accompanied by a structural transformation. The well-known MIL-53 family illustrates these breathing transitions. MIL-53(Cr) is the first reported solid [155] whose structure is formed of unidimensional chains of corner-sharing $\text{CrO}_4(\text{OH})_2$ octahedra linked by benzene-1,4-dicarboxylate (BDC) ligands, which results in linear lozenge-shaped channels being large enough to accommodate small guest molecules (Figure I-34). A volume change up to 40% without loss of crystallinity is observed when the MIL-53(Cr) is dehydrated at 300°C and thus suggests fully open pores evolved. MIL-53(Cr)_{HT} (fully dehydrated) and MIL-53(Cr)_{LT} (fully hydrated) exhibit surface areas of 1500 m²/g and 1150 m²/g, respectively. Since then, isorecticular solids with a wide variety of metal cations (Al, Fe, Ga) and functional ligands have been investigated [156]. We will see in Chapter III that the breathing behaviors depend on the metal cation. In contrast to MIL-53(Cr), the pores of MIL-53(Fe) are fully open in the presence of free water molecules.

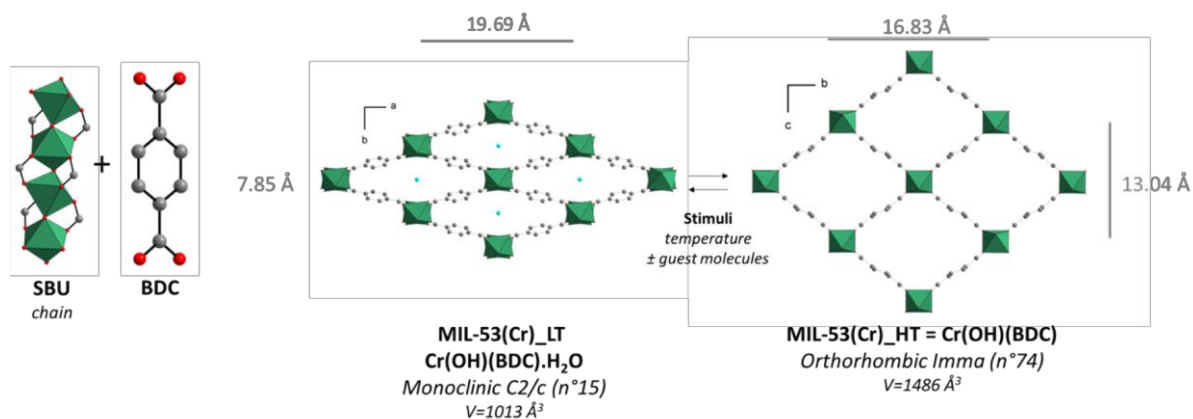


Figure I-34 : Representation of the breathing mode in the structure of MIL-53(Cr). View of the pore system upon hydration/dehydration.

The **swelling mode** is characterized by an enlargement of the MOF unit cell along with a change in the unit cell shape while maintaining the space group. The most representative material is MIL-88, which exhibits a large flexible behavior resulting from pore size change during solvation and desolvation (Figure I-35). Several isorecticular solids have been synthesized using various metals (Fe, Cr) and / or organic dicarboxylate linkers (fumaric acid, benzene-1,4-dicarboxylic acid, naphthalene-2,6-dicarboxylic acid...). The hexagonal structure consists of trimeric inorganic species (three octahedra sharing one oxygen atom) linked by dicarboxylic ligands. Upon immersion in solvents, a variation of the cell volume from 85% to 270% can be observed depending on the nature of the metal cation and organic moieties [157]–[159]. These systems are mostly studied for their adsorption properties [160] or drug delivery [161].

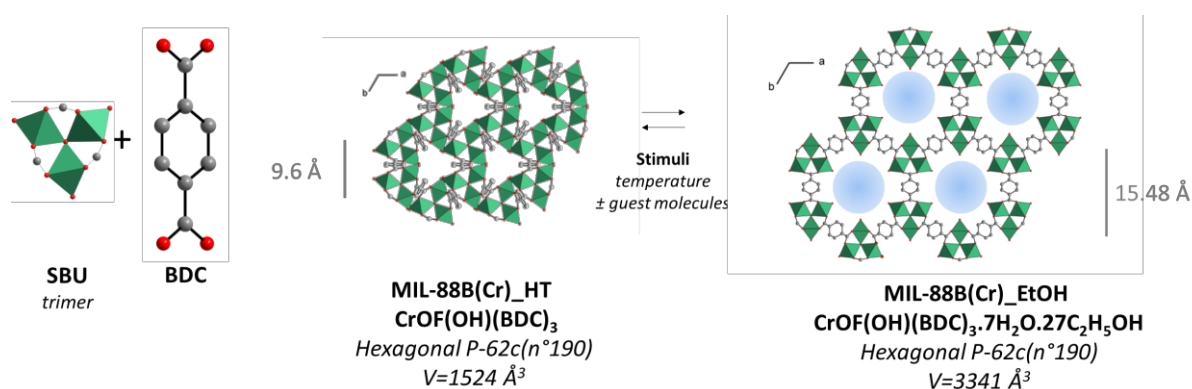


Figure I-35 : Representation of the swelling mode in the structure of MIL-88B(Cr). View of the pore system upon solvation, the blue spheres correspond to the solvent guests (here water and ethanol molecules).

The **subnetwork displacement** without changing in volume occurs generally in interpenetrated or interdigitated frameworks. Figure I-36 shows the example of InOF-23 (or $[\text{In}(\text{HL})_2]\text{Cl}\cdot 4\text{H}_2\text{O}$ with $\text{H}_2\text{L} = 6\text{-(4-carboxyphenyl) nicotinic acid}$) [161]. The orthorhombic structure can be simplified and described as a three-dimensional uninodal four-connected topological network. However, the indium atoms are in 8-coordinated geometry to give a tetrahedral four-connected node.

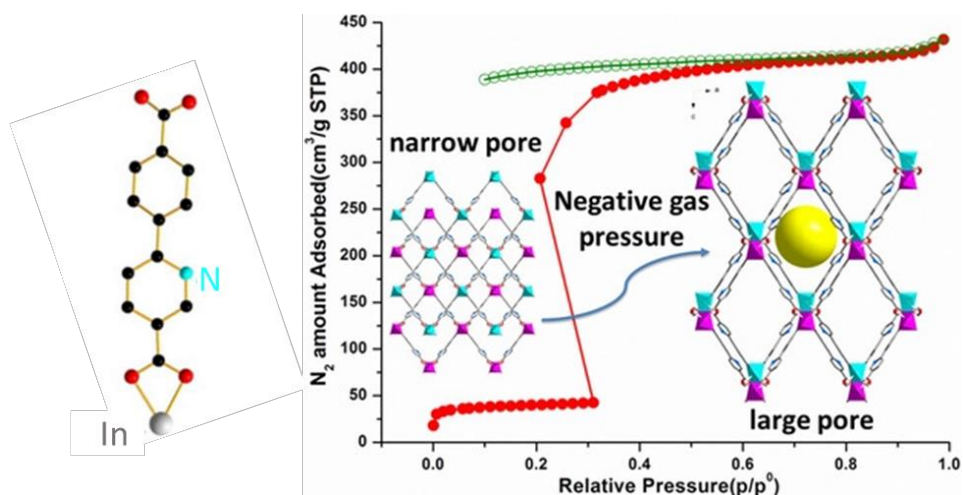


Figure I-36 : Representation of the structure of InOF-23 before and after adsorption of gases (N_2 , Ar, CO_2). Reprinted from [161].

The **linker rotation mode** or gate opening behavior is described as a transition where the linker can rotate around a certain axis without phase transitions to change the pore configuration. The gate opening of the ZIF-8 solid (zeolitic imidazolate framework) under N_2 adsorption is observed using inelastic neutron scattering (Figure I-37) [162]. The structure is isomorphic of zeolite compounds and is composed of zinc tetrahedrons connected by methylimidazolate linkers.

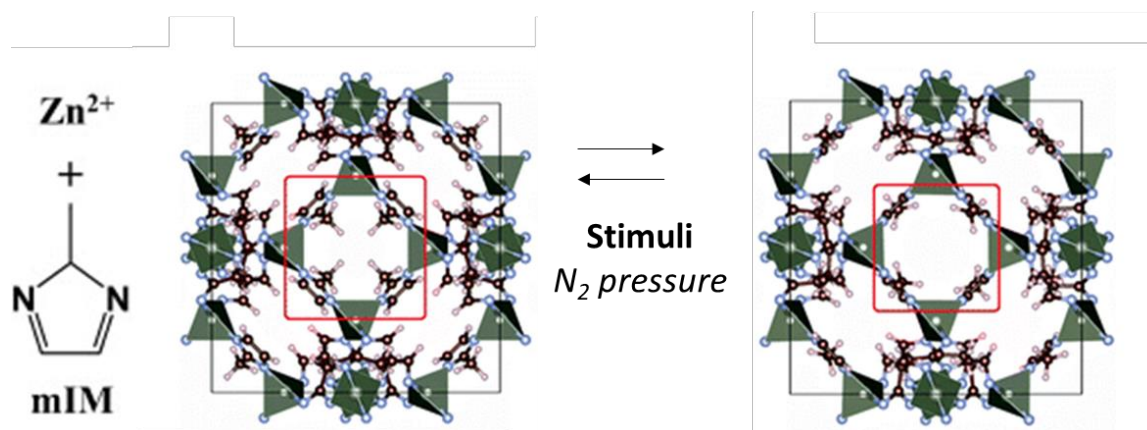


Figure I-37 : Representation of the structure of ZIF-8, view of the linker reorientation observed under N_2 adsorption. Reprinted from [162].

I.3.4. Overview of MOF applications

I.3.4.1. Generalities

MOFs have been investigated for numerous potential applications such as gas storage and separation processes, drug storage and delivery, sensors, catalysis, or energy [163]–[168]. The number of published articles involving the keyword “MOF” has increased with an exponential trend. MOF has also gained continuous interest in the field of energy since the last decade (Figure I-38). In addition to direct utilization of pristine MOF, MOFs have also been used to generate MOF composites or MOF derivatives or for energy applications. MOFs have been used as sacrificial templates for the synthesis of porous carbons / metal oxides. MOF derivatives thus benefit from the high electrical conductivities, hierarchical porous structure, and well-distributed catalysts. Besides, MOF composites are prepared by combining one MOF and one or more distinct constituent materials, including other MOFs, with properties noticeably differing from those of the individual components. They combine the advantages of both MOFs (flexibility, high porosity with ordered crystalline pores) and various kinds of functional materials (with electrical, magnetic, and catalytic properties). It can lead to composites with new physical and chemical properties and enhance performances that cannot be reached by the individual components [169].

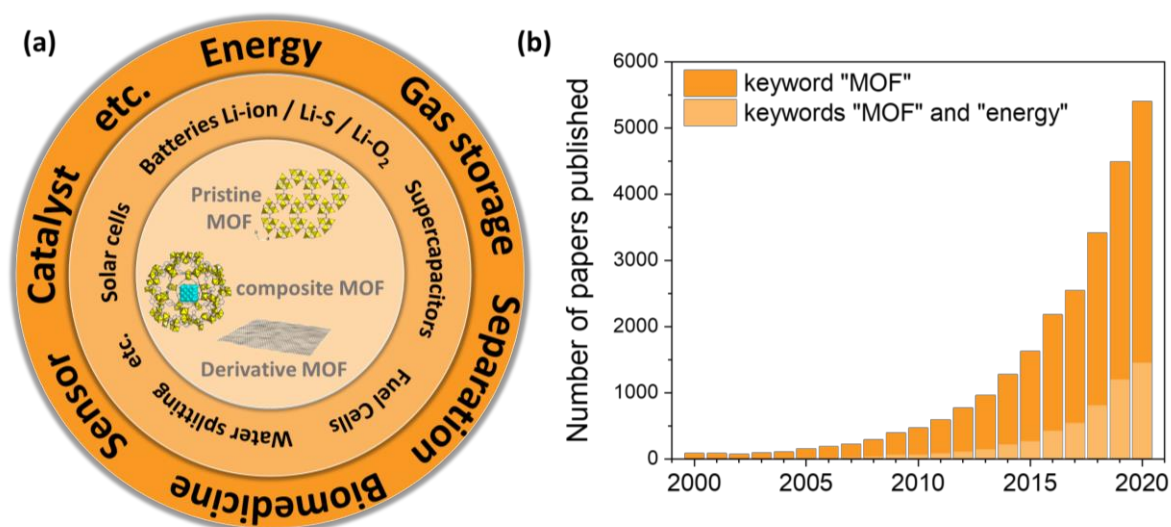


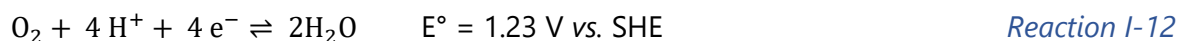
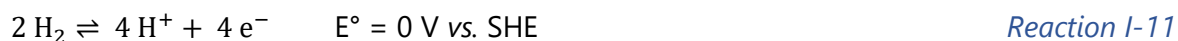
Figure I-38 : (a) Schematic representation of some MOF applications. (b) Number of publications with the keywords “MOF” and “MOF and energy” for the period 2000-2020 (data source: Web of Science).

I.3.4.2. MOFs for energy applications

Recently, MOFs have attracted many interests as electrocatalysts for the oxygen reduction reaction (ORR) and the oxygen evolution reaction (OER) [170], [171]. The ORR and OER are essential half-cell reactions to achieve energy storage and conversion through the transformation between chemical energy and electrical energy in many O₂-related energy devices, such as fuel cells and rechargeable metal-O₂ batteries, especially rechargeable Li-O₂ batteries.

a. Fuel cell

In a typical H₂-O₂ fuel cell (FC), H₂ molecules are electrochemically oxidized via the hydrogen oxidation reaction at the anode, while the O₂ are reduced to receive electrons through the oxygen reduction reaction (ORR) at the cathode. A four-electron transfer mechanism is involved as shown in Reaction I-11 and Reaction I-12 (the standard potential E° is reported in the reference to the standard hydrogen electrode (SHE) [171]):



Compared to the fast kinetics of hydrogen oxidation reaction, the kinetics of ORR is six times lower, leading to a high overpotential and a low energy efficiency in the H₂-O₂ fuel cells [172]. Therefore, efficient electrocatalysts for ORR are highly required.

The possibility of using pristine MOFs as ORR electrocatalysts for fuel cells (FC) is firstly investigated by Mao *et al.* [173]. In this study, two organic linkers are used to coordinate Cu²⁺ ions in Cu-bipy-BTC solid. The benzene-1,3,5-tricarboxylate (BTC) acts as the main linker while the 2,2'-bipyridine (bipy) serves as the auxiliary linker, which stabilizes the framework through stronger interaction of two linkers with the Cu²⁺ ions compared to the single-linker based Cu-BTC. The Cu-bipy-BTC is electrochemically active with one pair of redox waves at the formal potential of *ca.* -0.1 V vs. Ag/AgCl in the acid electrolyte, assigned to the redox process of Cu²⁺/Cu⁺. When used in an O₂-containing electrolyte, the Cu-bipy-BTC shows an obvious oxygen reduction peak during the CV scanning (Figure I-39). Moreover, the Cu-bipy-BTC electrode leads to a large positive shift of oxidation potential (*ca.* 0.4 V vs. Ag/AgCl) compared with the bare glassy carbon electrode, which reveals Cu-bipy-BTC is an efficient ORR catalyst. The Cu-bipy-BTC FC produces a power density of 126 mW/m², which is 5.4 times higher than the electrocatalyst-free FC but much lower than noble Pt FC [174].

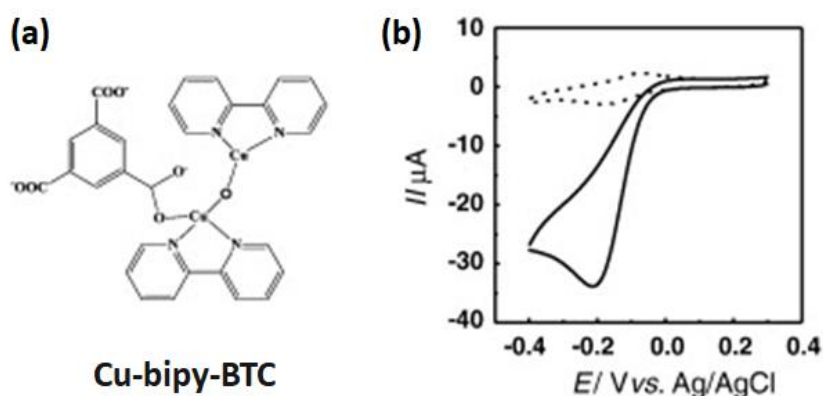


Figure I-39 : (a) Coordination geometry of Cu atoms in Cu-bipy-BTC. (b) CVs of Cu-bipy-BTC-modified GC electrodes in 0.1 M phosphate buffer solution (pH 6.0) saturated with N_2 (dotted curve) or O_2 (solid curve). Scan rate = 20 mV/s. Reprinted from [173].

Yin and co-workers have developed the BTC-based MOF(Fe) [175] as well as its bimetallic form MOF(Fe/Co) as ORR electrocatalysts in alkaline electrolyte [176]. Both these solids have high surface areas, good crystalline structures with micropores. The MOF(Fe) exhibits a good ORR activity with a current density of -0.93 mA/cm^2 at $-0.3 \text{ V vs. Ag/AgCl}$. The addition of Co into the MOF(Fe) enables MOF(Fe/Co) to enhance the ORR activity with an increased current density of -1.19 mA/cm^2 at the same potential. In comparison, a bare SP carbon electrode has a low ORR activity with a current density of only -0.08 mA/cm^2 at the same potential. It is found that the presence of both Fe and Co in MOF(Fe/Co) enhances the OER activity compared to the MOF(Fe) (Table I-7). The authors [176] attributed the good ORR/OER activities to the fast O_2 diffusion and the utilization of unsaturated metal sites as catalytic sites in MOF(Fe/Co), as a consequence of its high surface area and the microporous structure.

Table I-7 : Overview of MOF(Fe) and MOF(Fe/Co) ORR/OER catalytic activity [175], [176].

Active material	Surface area (m^2/g)	Average pore size (nm)	ORR activity	OER activity
MOF(Fe)	1600	1.2	-0.93 mA/cm^2 at $-0.3 \text{ V vs. Ag/AgCl}$	2.3 mA/cm^2 at $0.9 \text{ V vs. Ag/AgCl}$
MOF(Fe/Co)	1070	< 2	-1.19 mA/cm^2 at $-0.3 \text{ V vs. Ag/AgCl}$	2.97 mA/cm^2 at $0.9 \text{ V vs. Ag/AgCl}$
SP	-	-	-0.08 mA/cm^2 at $-0.3 \text{ V vs. Ag/AgCl}$	0.03 mA/cm^2 at $0.9 \text{ V vs. Ag/AgCl}$

Moreover, Dinca *et al.* have systematically investigated the charge conductive 2D $\text{Ni}_3(\text{HITP})_2$ (with HITP = 2, 3, 6, 7, 10, 11-hexaiminotriphenylene) as a ORR electrocatalyst [177]. This layered material has a high BET surface area of $630 \text{ m}^2/\text{g}$ along with a good electrical conductivity of 40 S/cm . Under the O_2 atmosphere, $\text{Ni}_3(\text{HITP})_2$ reduces oxygen with an onset potential of 0.8 V vs. RHE (Figure I-40). The measured ORR onset potential is competitive with the most active non-Pt group metal ORR electrocatalysts reported so far and sits at an overpotential of 0.18 V vs. RHE relative to Pt. $\text{Ni}_3(\text{HITP})_2$ retains 88 % of the initial current over 8 h electrochemical cycling. This study shows that the real electrocatalytic active site is not the Ni center but the organic linker HITP. A similar study has been reported by Bao *et al.* [178] for Ni-HAB (with HAB = hexaaminobenzene), where the organic linker HAB serves as active site and the Ni^{2+} ions help to modulate the linker sites' binding strength. These researches enlighten that not only the metal node but also the organic linker could be potential electrocatalytic sites for the oxygen reduction reaction.

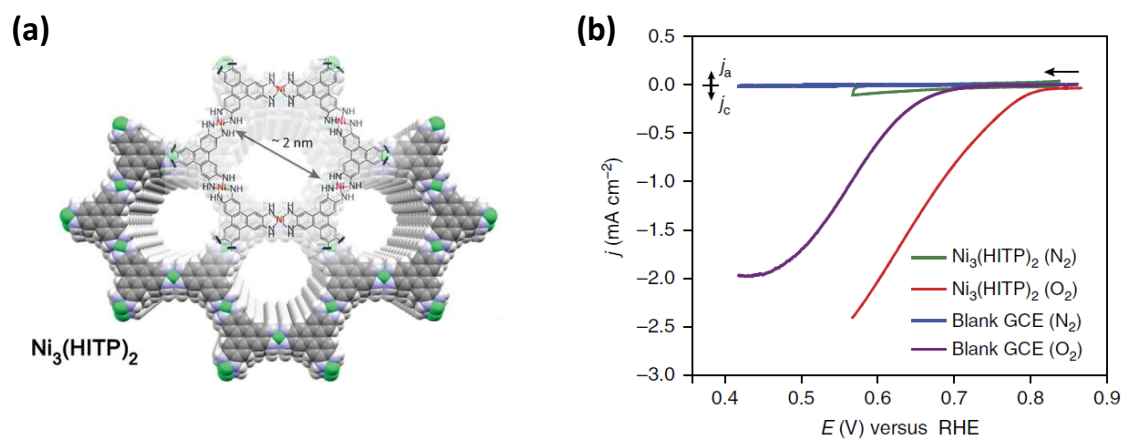


Figure I-40 : (a) View of the 2D layered structure of $\text{Ni}_3(\text{HITP})_2$. (b) Polarization curves of $\text{Ni}_3(\text{HITP})_2$ and the blank glassy carbon electrode under N_2 vs. O_2 atmosphere. Reprinted from [177], [179].

b. Li-ion battery

The MOFs and their derivatives have been also extensively studied for Li-ion battery applications. However, the pristine MOFs suffer generally from poor conductivity leading to poor cycling performance. MOF composites and MOF-derived metal oxide / carbon materials boost the research for Li-ion batteries.

In 2006, MOF-177 was first investigated as an anode material for Li-ion batteries [180]. Unfortunately, the sample exhibits an irreversible capacity loss at the first cycle and the MOF structure is destroyed after the first cycle (Figure I-41 (a-c)). However, this example shows that the porous framework of MOFs may be used for lithium insertion. In 2007, Tarascon *et al.* have investigated the electrochemical performance of MIL-53(Fe) as cathode material [181]. The authors show that lithium ions are inserted into the pores of MIL-53, leading to a reduction of Fe^{3+} to Fe^{2+} (formation of $\text{Li}_x\text{Fe}_x^{\text{II}}\text{Fe}_{1-x}^{\text{III}}(\text{OH})_{0.8}\text{F}_{0.2}$ (BDC)). A reversible capacity of 75 mAh/g was obtained (corresponding to the insertion of 0.6 moles of lithium per mole of iron) (Figure I-41

(d)). Meng and co-workers have investigated the possible insertion of lithium in MIL-101(Fe) [169]. The cathode can accommodate a similar amount of Li as MIL-53 (0.62 Li⁺/Fe upon initial lithiation). However the oxidation of Fe²⁺ to Fe³⁺ is irreversible, leading to a rapid loss of capacity (0.37 Li/Fe at the 5th charge-discharge cycle) (Figure I-41 (e)). The most promising material in which the conversion-reaction mechanism is reversible is the formate $Zn_3(HCOO)_6$, which exhibits a reversible capacity of 560 mAh/g (Figure I-41 (f)) [182].

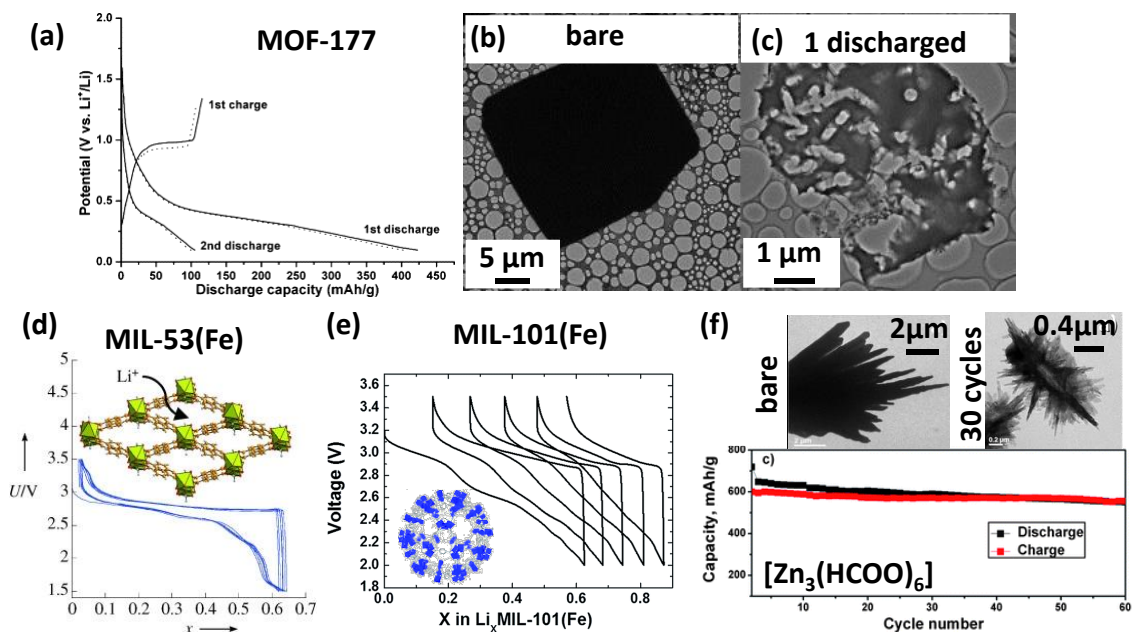


Figure I-41 : (a) Discharge–charge profiles of the microcubic MOF-177 anode (solid lines) at a current density of 50 mA/g. The TEM images of corresponding anode (b) before and (c) after 1 discharge [180]. (d) Discharge–charge profiles of the MIL-53(Fe) (inset) cathode at a current rate of C/40 [181]. (e) Discharge–charge performances of the MIL-101(Fe) (inset) cathode at a current rate of C/40 [169]. (f) Capacity vs. cycle number plot under the current density of 60 mA/g [182].

MOF-based materials have been also explored for sodium-ion batteries (SIBs) and potassium-ion batteries (PIBs). While the radius of Li⁺ ion (0.76 Å) is small enough to have suitable mobility, the larger radii of Na⁺ (1.06 Å) and K⁺ ions (1.38 Å) require thus a more open framework through which they could be inserted / extracted reversibly with acceptable mobility [183]. The BDC-based MIL-125(Ti) possesses a pore diameter *ca.* 1.6 nm, which is beneficial to the facile ion insertion and removal during the cycling process. The PIB based on the MIL-125(Ti) cathode exhibits an initial discharge capacity of 260 mAh/h at and a coulombic efficiency of 58.9% at current rate of 10 mA/g. Since the subsequent cycles, a coulombic efficiency close to 100% is maintained by MIL-125(Ti). Even after 2000 cycles at a high current density of 200 mA/g, there is almost no capacity loss, corresponding to a capacity retention of 90 %, which demonstrates its excellent cycling stability. In another study, a cobalt BDC-based layered MOF (L-Co₂(OH)₂BDC) has been tested as anode for a PIB, delivering a large capacity of 742 mAh/g at 50 mA/g. Even at 1 A/g, a capacity of 188 mAh/g can be achieved with almost 100% coulombic efficiency after 600 cycles [184]. However, compared to the LIBs, the research on the SIBs and PIBs are still limited due to the critical pore size requirement of large monovalent ionic radii.

Alternatively, MOF derivatives have been applied for increasing the capacity and rate performance of lithium-ion battery applications. For example, porous $Zn_xCo_{3-x}O_4$ material processed in a hollow structure allows a discharge capacity of 990 mAh/g after 50 cycles [185]. The sandwich-structured RGO¹/ZnCo₂O₄-ZnO-C/Ni electrode could reach a discharge capacity of 1184 mAh/g [186]. Even better performances are achieved by using MOF-derived metal oxide. The α -Fe₂O₃ produced by pyrolysis of Fe-MOF presents a reversible capacity of 1024 mAh/g [187]. Table I-8 summarizes the mentioned MOF derivatives' electrochemical performances in LIBs.

Table I-8 : Overview of MOF derivatives electrochemical performances in LIBs.

MOF derivatives	Potential window (V vs. Li ⁺ /Li)	Initial discharge capacity (mAh/g)	Reversible capacity (mAh/g)	Initial CE/cycled CE (%)	Ref.
Zn_xCo_{3-x}O₄	0.01-3	1272 @ 100 mA/g	990 @ 100 mA/g	76.2 % / -	[203]
RGO/ZnCo₂O₄-ZnO-C/Ni	0.01-3	930.3 @ 0.1 A/g	1184 @ 0.1 A/g	71.7 % / 99.1 @ 150 cycles	[204]
α-Fe₂O₃ nanospinel	0.005-3	1487 @ 100 mA/g	1024 @ 100 mA/g	68.8 % / 97 % @ 40 cycles	[205]

c. Li-S battery

Porous MOFs are also promising as cathode material for lithium-sulfur (Li-S) batteries. The Li-S system is also considered as one of the next-generation battery to its high theoretical capacity and energy density. One of the challenges in the development of the Li-S batteries is the irreversible energy loss due to the formation of soluble polysulfides in the reduction process of sulfur, and the poor electrical conductivity of sulfur.

Xiao *et al.* immobilized sulfur into the highly porous Ni-MOF based Ni₆(BTB)₄(BP)₃ (with BTB = benzene-1,3,5-tribenzoate and BP = 4,4'-bipyridyl) [188]. This framework provides two types of pore (with a free diameter of 13.8 Å and 27.6 Å, respectively) along with an impressive BET surface area of 5243 m²/g. At a low current rate of 0.1 C (168 mA/g), the Ni-MOF/S composite offers high-capacity retention of 89% after 100 cycles. The hierarchical porous structure of Ni-MOF and strong interactions between Ni metals and intermediate soluble polysulfides prevent their migrations out of the pores, thus leading to a high capacity retention of Ni-MOF/S composite. However, the insulating nature of MOFs and sulfur as well as the low content of carbon in the electrode (10 wt. %) results in a weak utilization of sulfur and a weak

¹ RGO = reduced graphene oxide

rate performance (Figure I-42). Similar studies have also been investigated with other MOF composites, such as MIL-100(Cr)/S [189], MIL-101(Cr)/S [190], [191], S/MIL-53(Al), S/NH₂-MIL-53(Al), and S/ZIF-8 [192].

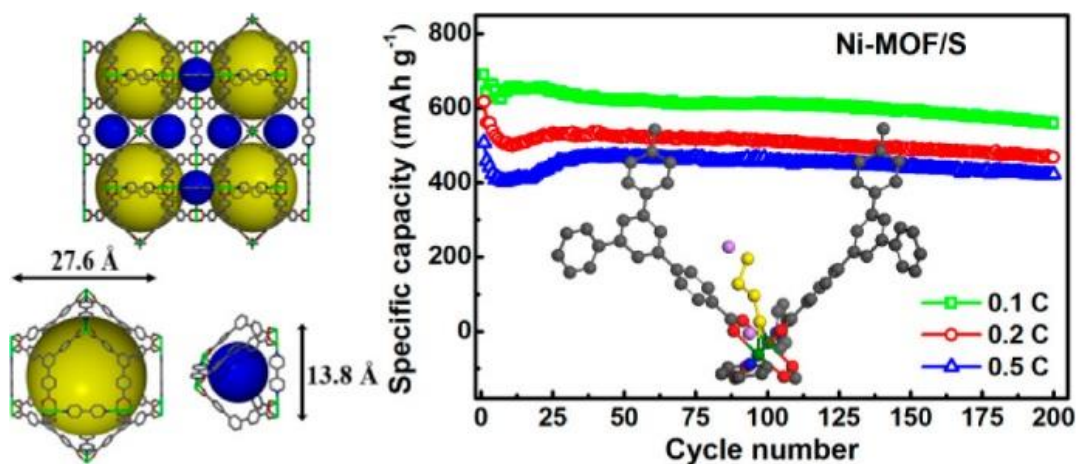


Figure I-42 : Crystal structure of $Ni_6(BTB)_4(BP)_3$, the corresponding cycling performance of Ni-MOF/S composite electrode at 0.1 C, 0.2 C, and 0.5 C current rates in a voltage range of 1.5 – 3.0 V vs. Li⁺/Li and schematic illustration of the interaction between polysulfides and Ni-MOF. With 1.0 C = 1685 mA/g. Reprinted from [188].

To tackle the poor electrical conductivity issue of pristine MOFs in Li-S batteries, an alternative investigation is to synthesize MOF-derived carbon material. Two MOF-derived carbons with different morphology have been synthesized from Cu-based MOF precursors [193]. The cross-linking hierarchical porous carbon fiber CHPCF is prepared from the Cu-BTC fiber precursor (Figure I-43), while the HKC with octahedral morphology is prepared from Cu₃(BTC)₂, also known as HKUST-1. Both MOF-derivative carbons exhibit high BET surface areas and large pore volumes (HKC: 1623 m²/g, 1.13 cm³/g; CHPCF: 1906 m²/g, 1.35 m³/g). After sulfur impregnation, it is noteworthy that the S/CHPCF composite provides more abundant micro-pores than S/HKC composite that help confining the diffusion of intermediate polysulfides. As a consequence, the S/CHPCF composite electrode provides a higher initial discharge capacity than S/HKC (1336 mAh/g vs. 1181 mAh/g at 1.0 C). Besides, after 100 cycles, the S/CHPCF still retains a discharge capacity of 904 mAh/g, which is 68 % of its initial discharge capacity and is 1.5-fold than that of S/HKC (599 mAh/g). The improved capacity and cyclability of S/CHPCF highlights the importance of hierarchical pore structure of MOF-derived materials for both the polysulfides confinement and Li⁺ migration.

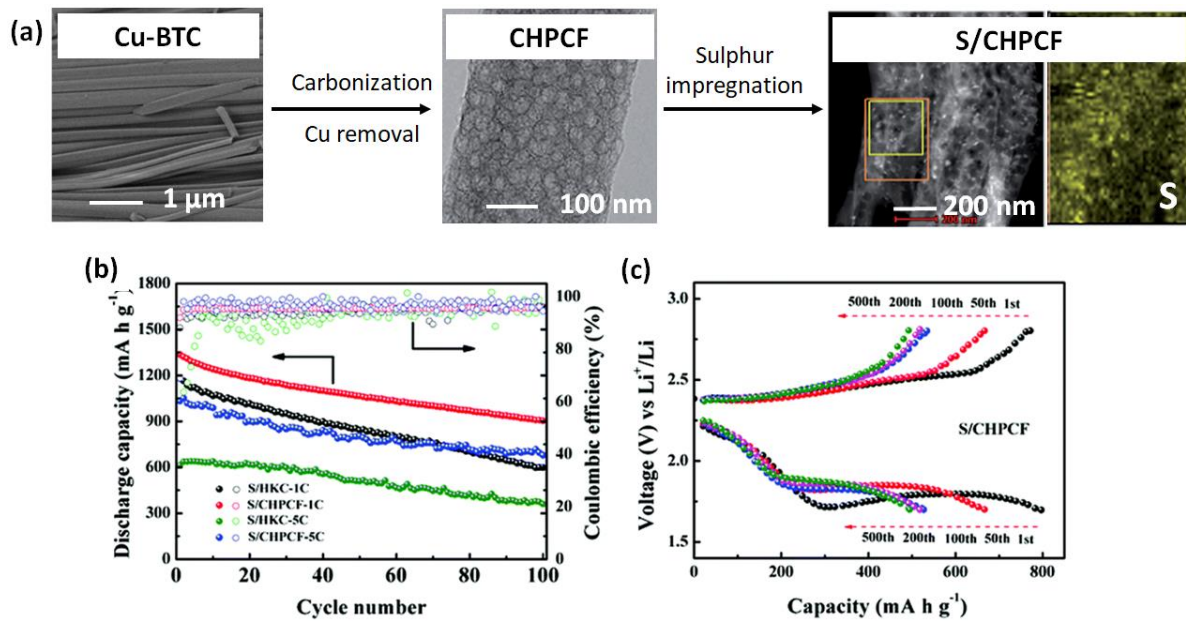


Figure I-43 : (a) Synthesis procedure of S/CHPCF composite (STEM image with sulfur mapping) from the 1D Cu-BTC fibers (SEM image) via the intermediate fibrous CHPCF (TEM image). (b) Cycling performance of S/HKC and S/CHPCF electrodes in a LiNO₃-free electrolyte. (c) Charge-discharge cycling of the S/CHPCF electrode at 5.0 C in the 1st, 50th, 100th, 200th, and 500th cycles with electrolyte LiNO₃ addition [193].

I.3.4.3. MOF for Li-O₂ battery applications

As we showed in Section I.3.1, metal-organic frameworks and their derivatives materials have a wide range of surface areas and different structures, they have gained interest in the field of energy, in particular as catalysts for ORR/OER reactions [172]. As cathode materials of the Li-O₂ battery application, MOFs may provide a host network for the mass transportation (diffusion of Li⁺ ions and O₂), accommodate the discharge products (such as Li₂O₂), and act as catalyst thanks to the open metal sites in the structure.

a. Pristine MOFs

Only few groups have reported the studies of pristine bulk MOFs as air cathode of Li-O₂ batteries [92], [194], [195]. At first, the group of Li has investigated five MOFs as air cathode material: MOF-5, HKUST-1, and M-MOF-74 (M=Mg, Mn, Co) [92]. The structures of these solids are described in Section I.3.3. They provide high surface areas in a wide range from 1213 to 3622 m²/g. A maximum initial discharge capacity of 9420 mAh/g is achieved with the Mn-MOF-74 electrode, which is more than four times higher than the corresponding Super P carbon electrode without MOF (Figure I-44 (a)). Their discharge performance is directly assigned to the O₂ enrichment of these MOF solids. The unsaturated metal coordination center could provide binding sites for O₂, thus increasing the amount of O₂ available for discharge in the Li-O₂ battery. As a result, despite MOF-5 exhibiting the highest surface area, both HKUST-1 and M-MOF-74, which are lined with open metal sites, show better O₂ uptakes, explaining the superior discharge capacities than the coordination-saturated MOF-5.

While the first discharge capacity is remarkable, significant discharge and charge capacity decays and electrode polarization are observed along with cycling. The Mn-MOF-74 retains a discharge capacity of *ca.* 1300 mAh/g after six full cycles at a high current of 200 mA/g (Figure I-44 (c)) [92]. The reversibility of Li-O₂ battery with Mn-MOF-74 might be impacted by the possible electrolyte decomposition; on the other hand, parasitic reactions might also affect electrode performance by diminishing the available porosity. However, an extended cyclability performance is achieved over 30 cycles with a cut-off capacity of 1000 mAh/g at a high current rate of 250 mA/g (Figure I-44 (b)). Besides, all the structures of these materials are still preserved after cycling. It is important to note that, while the first discharge capacities are impressive, the group of Li revealed only the first discharge capacities of all these MOFs. They showed only the cycling behavior along few cycles for Mn-MOF-74, while the cyclability data of the other MOFs are not provided nor discussed. Additionally, the MOF content in the electrode is quite low with 40wt. % of MOF and 40 wt. of carbon.

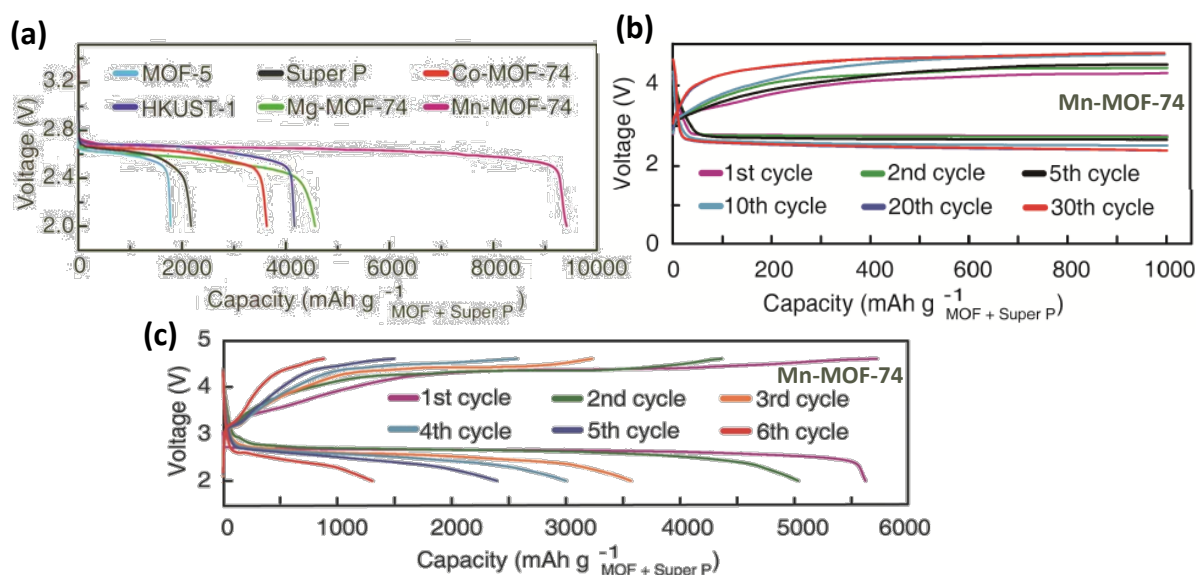


Figure I-44 : (a) Discharge profiles of Li-O₂ batteries with MOF-Super P composite electrodes or pure Super P cathodes. (b) Discharge-charge cycling response of the Mn-MOF-74 based battery with a capacity limited to 1000 mAh/g. Current: 250 mA/g. (c) Discharge-charge cycling response of the Mn-MOF-74 based battery. Current: 200 mA/g. Reprinted from [92].

The same group has also studied the electrochemical properties of Co-MOF-74 with distinct sizes and morphologies (homogeneous rod-shaped crystals with a width of \sim 1400 nm, nanorods with a width of \sim 1200 nm, and nanofibers with an average diameter of 20 nm) [196]. Downsizing the MOFs particles improve the electrochemistry performance. Figure I-45 (a) shows the first discharge curves of the different electrodes Co-MOF-n (with $n = 1400, 800,$ and 20 , n indicates the average length of the particle) in Li-O₂ batteries and the associated morphologies. Co-MOF-74-20 achieves a maximum notable discharge capacity of 11350 mAh/g. The deviation of the potential of 0.85 V vs. Li⁺/Li is much lower than the conventional value of 1.5 V from the carbon electrode. The capacity of the Li-O₂ cell decays rapidly with an

increase in the polarization (Figure I-45 (b)), similar to previous works [92]. The cycling stability of the Co-MOF-74-20 based Li-O₂ cell was also evaluated with a fixed capacity of 1000 mAh/g at a current density of 250 mA/g (Figure I-45 (c)). The discharge profiles of the first 8 cycles illustrate that the cell can operate efficiently with slightly lower voltage. A recent study reveals that a higher percentage of exposed metal sites on the surface of these nanocrystals might be responsible for the enhanced electrocatalytic behaviors compared to the bulk MOF [197]. However, the mass loading of Co-MOF-74 and Super P is 0.6 mg/cm², which is too low for MOF structure stability confirmation with XRD after cycling.

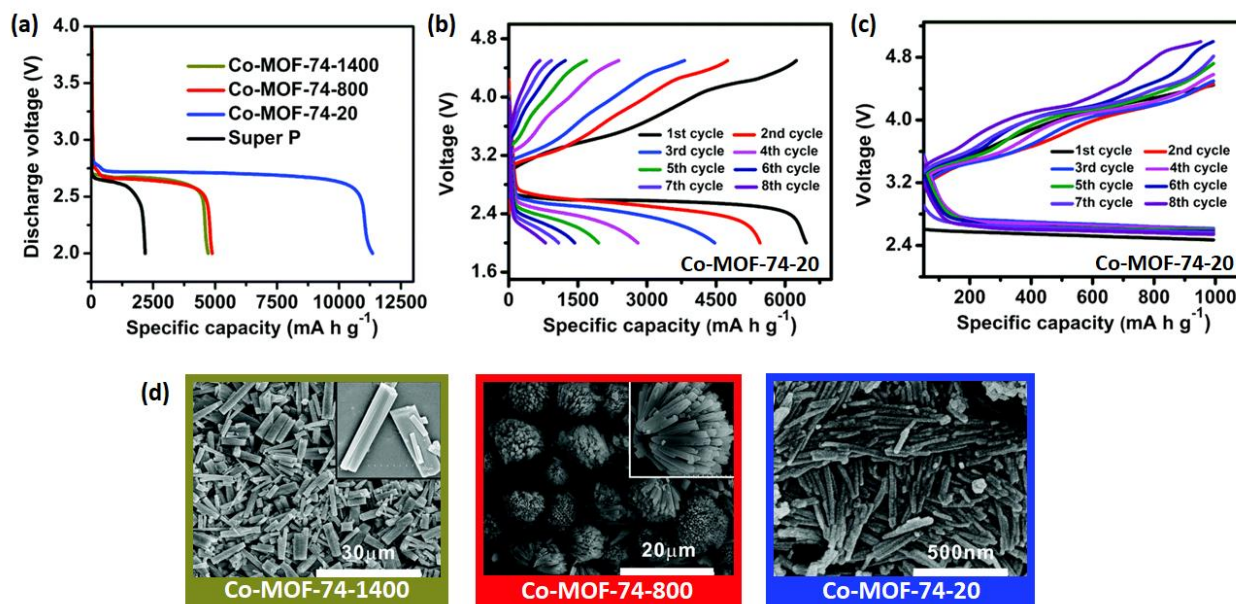


Figure I-45 : (a) Discharge profiles of Li-O₂ batteries with MOF-Super P composite electrodes or pure Super P cathodes at a current density of 100 mA/g. (b) Cycling response of the Co-MOF-74-20 based battery at a current of 500 mA/g. (c) The cycling performance of the Co-MOF-74-20 based Li-O₂ cell under a specific capacity limit of 1000 mAh/g at a current density of 250 mA/g. (d) SEM images of Co-MOF-74 (Co-MOF-74-1400 in olive green, Co-MOF-74-800 in red, and Co-MOF-74-20 in blue). Reprinted from [196].

Another group has studied the Ni-MOF (Ni(4,4'-bipy)(H₃BTC)) with 4-4'-bipy = 4-4'-bipyridine and H₃BTC = benzene-1,3,5-tricarboxylic acid [194]. The framework is constructed with two types of ligands of H₃BTC and 4,4'-bipy as well as Ni²⁺ centers. The honeycomb grid layers constructed by Ni²⁺ and H₃BTC are linked by 4,4'-bipy pillars to form a 3D structure (Figure I-46 (a)). This framework shows a high BET surface of 1225 m²/g and a bimodal pore-size distribution centered at ~ 7 and ~ 11 Å, which is believed to be large enough for the transfer of O₂ (3.46 Å) and Li⁺ electrolyte. Moreover, the Ni-MOF presents open metal sites, which favor the O₂ adsorption and enhance catalytic activities in Li-O₂ batteries. As shown in Figure I-46 (b), the Ni-MOF cathode exhibits either higher ORR (2.84 V vs. Li⁺/Li) potential or lower OER (3.84 V vs. Li⁺/Li) potential than corresponding potentials of pure VC-72 carbon electrode. Besides, a high discharge capacity of 9000 mAh/g is achieved with Ni-MOF at a low

rate of 0.12 mA/cm^2 . With a cut-off capacity of 600 mAh/g , the Li-O₂ battery with Ni-MOF electrode could maintain a capacity of 478 mAh/g over 170 cycles at a rate of 0.6 mA/cm^2 . A preliminary attempt for a plastic rechargeable Li-O₂ battery with Ni-MOF electrode delivers also an energy density of 537 Wh/kg at the 1st cycle and 239 Wh/kg at the 7th cycle.

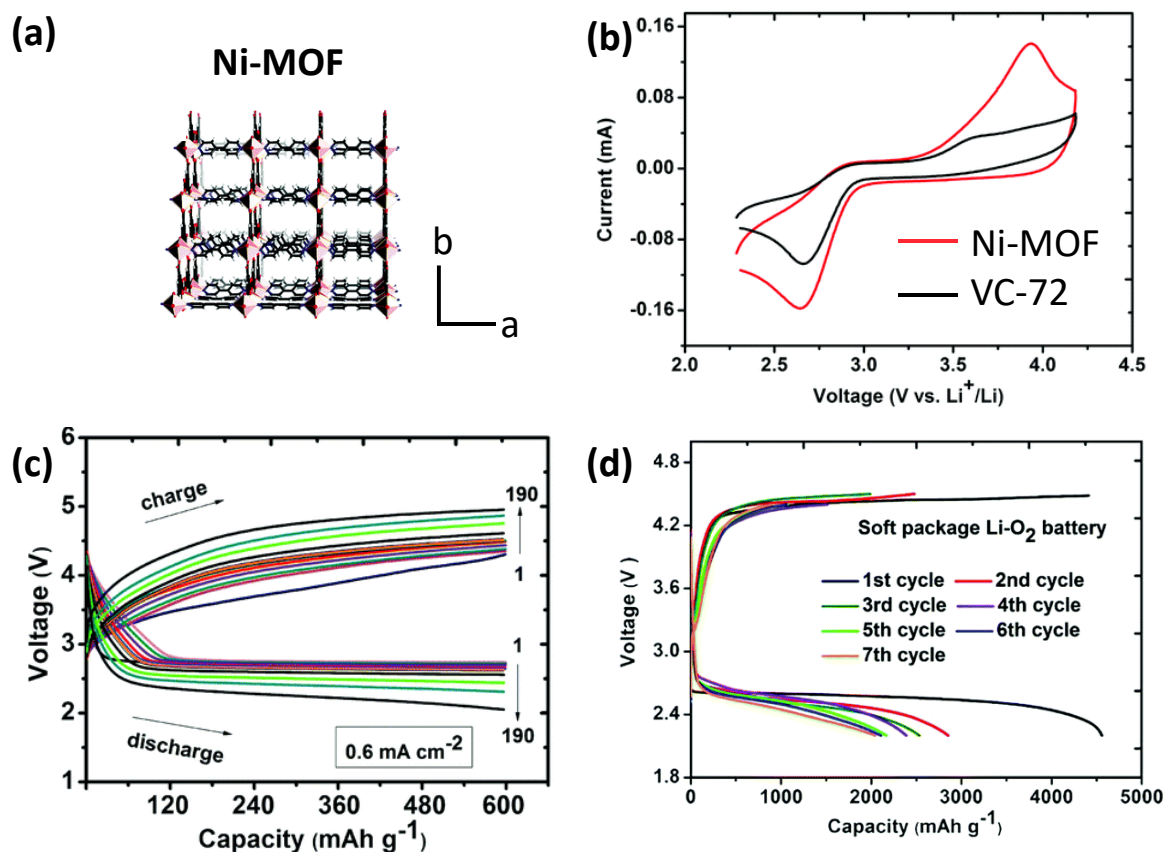


Figure I-46 : (a) Crystal structures of Ni-MOFs along the *c*-axis. (b) Cyclic voltammograms at 20 mV/s on rotating disk electrode. (c) Discharge–charge curves of Li–O₂ batteries (c) with a fixed capacity of 600 mAh/g at 0.6 mA/cm^2 and (d) cycling curves of a plastic Li–O₂ battery at 0.6 mA/cm^2 . Reprinted from [194].

The studies reported above show that the combination of pristine porous MOF and carbon as cathode can produce high discharge capacity. Specifically, the presence of open metal sites in the framework enhances significantly the electrochemical behaviors compared to the electrode without MOF in the Li-O₂ batteries. However, the pristine MOFs suffer from poor electronic conductivities, which could limit the capacities and increase polarization over cycling.

b. MOF derivatives and MOF composites

When pristine MOFs are used as sacrificial templates, metal-doped carbons or metal oxides can be generated by thermal treatment due to the collapse of coordination bonds and the carbonization of organic linkers. Since the low electrical conductivity of pristine MOFs and low kinetics of OER are detrimental factors for Li-O₂ batteries, the conversion from MOFs to MOF derivatives is an effective way to improve the electrical conductivities and catalytic activities while partially preserving the porous structures and active contents from MOF precursors.

Wu's group was the first to report nitrogen-iron graphene/graphene tube composite (N-Fe-MOF) derived from Co-MOFs containing dicyandiamide and Fe acetate (Figure I-47 (a)) [198]. The BET surface area changes from only 10 m²/g to 449 m²/g after the 1000°C pyrolysis of Co-MOF, as a result of the decomposition of N-C bonding and formation of porous carbon material. The authors proposed that the formation of Fe₃C promotes the growth of graphene tubes, while N-doping leads to the activation of adjacent carbon atoms and coordination with iron (Fe-N_x) which generates more active sites for O₂ binding and dissociation of O-O bonds. In addition, this composite favors the decomposition of Li₂O₂ and thus improves the OER catalytic performance. Compared with other derivatives prepared under different temperatures as well as other control samples including carbon black, Pt/C, and MOF-free N-Fe, the optimized N-Fe-MOF shows the best result with an onset potential around 3.2 V vs. Li⁺/Li in the non-aqueous electrolyte (0.1 mol/L LiPF₆ in tetramethylene glycol dimethyl ether) (Figure I-47(b)). Besides, the discharge capacity of N-Fe-MOF (~5300 mAh/g) is superior to other catalysts and it also shows a higher average voltage plateau at 50 mA/g. Moreover, the N-Fe-MOF-based cathode keeps stable discharge capacity for 16 cycles and exhibited 27% capacity loss at a high current density of 400 mA/g until the 50th cycle (Figure I-47(b-c)). The accumulated insoluble Li₂O₂ may block the catalyst sites and O₂ transfer channels in the electrodes, thereby leading to the observed degradation.

Tan and co-workers [199] published a biphasic nitrogen dopants N-doping Co@graphene derived from Co(mlm)₂ (with mlm = 2-methylimidazole) as the cathode catalyst for Li-O₂ batteries. The carbonization of this Co-MOF at 900°C leads to the formation of multiple core-shell nanocapsules, which are connected with each other through carbon networks (Figure I-47 (d)). This derived catalyst exhibits a BET surface area of 780 m²/g with an average pore size of 22 nm. During the thermal treatment, parts of nitrogen atoms from organic linkers are doped in the graphene shell, which creates defective sites, while some other nitrogen atoms take part in the association with cobalt atoms to form CoN. Both are the active sites for catalyzing redox reactions, while the multiple-nanocapsule heterostructure is the key to achieving a uniform distribution of those active sites, which leads to an initial discharge capacity of 3.63 mAh/cm² at 0.1 mA/cm² while maintaining a relatively stable performance in 30 cycles.

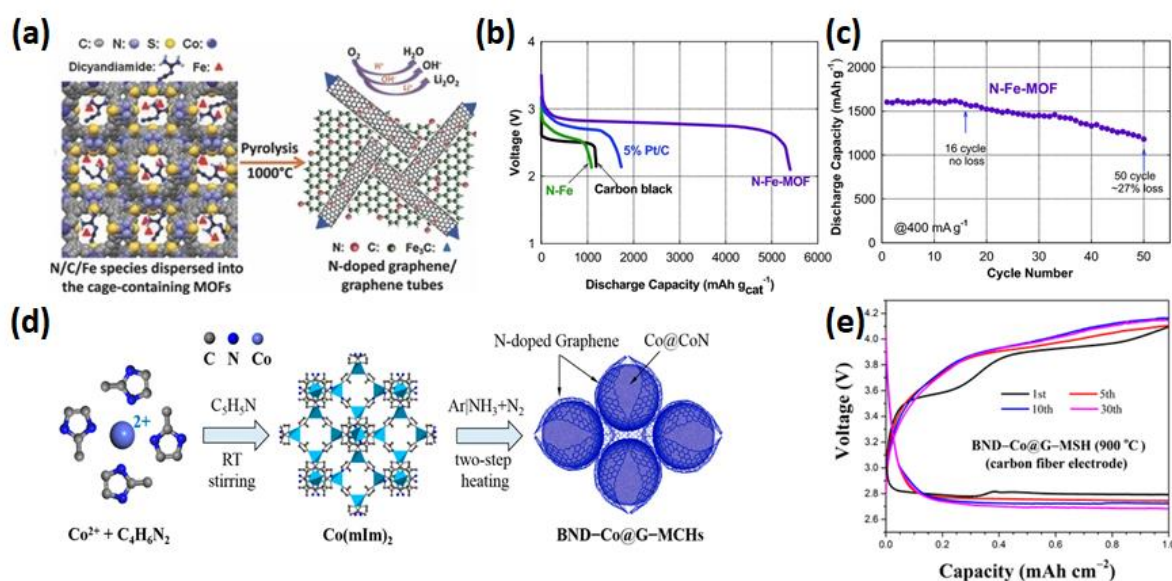


Figure I-47 : MOF-derived carbon catalysts for Li-O₂ batteries. Graphene/graphene tubes derived from Fe-modified Co-MOF (N-Fe-MOF) (a) schematic illustration of N-Fe-MOF formation; (b) the discharge profile of the N-Fe-MOF at the current density of 50 mA/g in comparison with those of 5% Pt/C, carbon black, and the controlled sample without MOF (N-Fe); (c) the discharge performance of N-Fe-MOF up to 50 cycles at the current density of 400 mA/g. N-doped Co@graphene derived from Co-MOF (BND-Co@G-MSH): (d) an illustration of synthesis procedure; (e) its discharge performance in 30 cycles at the current density of 0.1 mA cm⁻². Reprinted from [198], [199].

Transition metals oxides are well known as effective electrocatalysts for ORR and OER. Using MOFs as precursors to generate these oxides can lead to homogeneous distribution of catalytic sites, benefiting from the structural periodic arrangement of metal centers and organic linkers. Among all transition metals, cobalt has been largely studied [200]. Recently, Lyu *et al.* have reported the hierarchical 3D printed-nitrogen carbon-Co framework (denoted as 3DP-NC-Co) by calcinating the Co-MOF precursor [201]. This material displays a high discharge capacity of 1124 mAh/g. Moreover, the 3DP-NC-Co presents a lower overpotential and longer cycle ability than NC-Co/carbon paper electrode at a limited capacity of 1 mAh. The self-standing framework benefits not only from the intrinsic catalytic site and good electrical conductivity but also from the mechanical stability. This study provides new insight into the self-standing hierarchical porous architecture and electrode manufacturing method in developing advanced battery systems. Finally, we can mention the hierarchical nanocages of ZnO/ZnFe₂O₄ derived from Fe-MOF-5. They present discharge capacity over 11000 mAh/g at 300 mA/g and showed a stable reversibility of 15 cycles with a limited capacity of 5000 mAh/g [202]. In brief, the hierarchical porous material embedded with catalytic sites favors the efficient deposition of Li₂O₂ particles to enhance the discharge capacity and also facilitates the decomposition of insulating Li₂O₂, due to the confinement and the presence of catalyst within the hierarchical pores.

I.4. Conclusion

Up to now, the lithium-ion battery still holds a prominent place in the battery field since its first commercialization in 1991. This achievement could not have been possible without continuous improvements towards high-capacity electrodes and suitable electrolytes. Although its energy densities are still improving and its cycle life exceeds thousands of cycles, its specific capacity and energy density seem to reach their limits and will be insufficient in the long-term.

Among the “post lithium-ion” technologies, lithium-air batteries are the object of growing interest nowadays, owing to the high theoretical energy storage density of Li-O₂ systems compared to other technologies. However, the technology remains at the laboratory research stage for two decades due to the difficulty to master the chemistry and to find stable compounds under its oxidative environment. Numerous scientific and technical challenges must be overcome: capacity fading during cycling, electrolyte instability or large discharge and charge overpotentials, *etc.*

One of the challenges for the development of Li-O₂ batteries concerns the air cathode, where ORR and OER take place. The air cathode is exposed to ambient air, more specifically O₂, to store and convert energy. Major drawbacks of the air cathode include the sluggish kinetics of OER, high overpotentials, and pore clogging during the discharge process. Metal-Organic Frameworks (MOFs) appear as promising air cathode materials due to their high surface area, tunable pore size, and possible catalytic centers. Few pristine MOFs have been studied as air cathode materials for Li-O₂ batteries. These cathodes exhibit superior electrochemical performances to the corresponding electrodes without MOF. However, it is noteworthy that these high capacities are obtained with high content of carbon additives, which play an important role in increasing the electronic conductivity of air cathode. More efforts still need to be invested to determine the own performance of pristine MOF.

My PhD project focused on the development of new air cathode materials for Li-O₂ batteries based on the use of pristine MOF materials. Two analogues of flexible MIL-53 based on aluminum and iron were synthesized and used as air cathode materials. MIL-53(Al) and MIL-53(Fe) show different breathing transitions upon hosting guest molecules and may induce different behaviors upon charge-discharge cycles. A crucial point of this thesis is to study the impact of morphology and structure flexibility of the different MIL-53 compounds on the cathode performances. The work starts with the synthesis of MIL-53 and associated structural, physical, morphological characterizations. Before electrochemical tests, the framework flexibility of MIL-53 are explored against compounds used for electrode preparation. We then focus on the electrochemical behaviors of Li-O₂ batteries with MIL-53 cathodes. Battery using MOF-5 cathode is also studied for comparison as MOF-5 is a rigid structure. To complete the evaluation of the new materials, we applied *ex situ* structural and chemical characterizations in order to study the nature and the morphology of the discharge products and get better understanding of the cycling performance.

I.5. References

- [1] J.-M. Tarascon, "Histoire et évolution des technologies d'accumulateurs", 2011.
- [2] A. Coutts, "William Cruickshank of Woolwich", *Ann. Sci.*, vol. 15, n° 2, pp. 121–133, 1959.
- [3] T. M. Gür, "Review of electrical energy storage technologies, materials and systems: challenges and prospects for large-scale grid storage", *Energy Environ. Sci.*, vol. 11, no. 10, pp. 2696–2767, 2018.
- [4] M. S. Whittingham, "Electrical energy storage and intercalation chemistry", *Science*, vol. 192, n° 4244, pp. 1126–1127, 1976.
- [5] A. Yoshino, "The birth of the Lithium-ion battery", *Angew. Chem. Int. Ed.*, vol. 51, no. 24, pp. 5798–5800, 2012.
- [6] K. Mizushima, P. C. Jones, P. J. Wiseman, and J. B. Goodenough, "Li_xCoO₂ (0 < x ≤ 1): A new cathode material for batteries of high energy density", *Solid State Ion.*, vol. 3–4, pp. 171–174, 1981.
- [7] K. Ozawa, "Lithium-ion rechargeable batteries with LiCoO₂ and carbon electrodes: the LiCoO₂/C system", *Solid State Ion.*, vol. 69, n° 3, pp. 212–221, 1994.
- [8] "The Nobel Prize in Chemistry", 2019.
- [9] D. W. Murphy, J. Broadhead, and B. C. H. Steele, Eds., *Materials for Advanced Batteries*. Boston, MA: Springer US, 1980.
- [10] "Les batteries LMP (Lithium Métal Polymère), Bluecar", 2019.
- [11] J.-M. Tarascon and M. Armand, "Issues and challenges facing rechargeable lithium batteries", *Nature*, vol. 414, no. 6861, Art. n° 6861, 2001.
- [12] M. S. Whittingham, "Electrical energy storage and intercalation chemistry", *Science*, vol. 192, n° 4244, pp. 1126–1127, 1976.
- [13] A. Manthiram, "A reflection on lithium-ion battery cathode chemistry", *Nat. Commun.*, vol. 11, n° 1, p. 1550, 2020.
- [14] W. Li, E. M. Erickson, and A. Manthiram, "High-nickel layered oxide cathodes for lithium-based automotive batteries", *Nat. Energy*, vol. 5, n° 1, pp. 26–34, 2020.
- [15] P. K. Nayak *et al.*, "Review on challenges and recent advances in the electrochemical performance of high capacity Li- and Mn-Rich cathode materials for Li-ion batteries", *Adv. Energy Mater.*, vol. 8, n° 8, p. 1702397, 2018.
- [16] G. Assat and J.-M. Tarascon, "Fundamental understanding and practical challenges of anionic redox activity in Li-ion batteries", *Nat. Energy*, vol. 3, n° 5, Art. n° 5, 2018.
- [17] M. Sathiya *et al.*, "Reversible anionic redox chemistry in high-capacity layered-oxide electrodes", *Nat. Mater.*, vol. 12, n° 9, Art. n° 9, 2013.
- [18] M. M. Thackeray, W. I. F. David, P. G. Bruce, and J. B. Goodenough, "Lithium insertion into manganese spinels", *Mater. Res. Bull.*, vol. 18, n° 4, pp. 461–472, 1983.

- [19] M. M. Thackeray, P. J. Johnson, L. A. de Picciotto, P. G. Bruce, and J. B. Goodenough, "Electrochemical extraction of lithium from LiMn_2O_4 ", *Mater. Res. Bull.*, vol. 19, n° 2, pp. 179–187, 1984.
- [20] I. Saadoune and C. Delmas, " $\text{LiNi}_{1-y}\text{Co}_y\text{O}_2$ positive electrode materials: relationships between the structure, physical properties and electrochemical behaviour", *J. Mater. Chem.*, vol. 6, n° 2, pp. 193–199, 1996.
- [21] K. Amine, H. Tukamoto, H. Yasuda, and Y. Fujita, "Preparation and electrochemical investigation of $\text{LiMn}_{2-x}\text{Me}_x\text{O}_4$ (Me: Ni, Fe, and $x = 0.5, 1$) cathode materials for secondary lithium batteries", *J. Power Sources*, vol. 68, n° 2, pp. 604–608, 1997.
- [22] A. K. Padhi, K. S. Nanjundaswamy, and J. B. Goodenough, "Phospho-olivines as positive-electrode materials for rechargeable lithium batteries", *J. Electrochem. Soc.*, vol. 144, n° 4, p. 1188, 1997.
- [23] M. S. Islam and C. A. J. Fisher, "Lithium and sodium battery cathode materials: computational insights into voltage, diffusion and nanostructural properties", *Chem. Soc. Rev.*, vol. 43, n° 1, pp. 185–204, 2013.
- [24] D. W. Murphy, P. A. Christian, F. J. DiSalvo, and J. V. Waszczak, "Lithium incorporation by vanadium pentoxide", *Inorg. Chem.*, vol. 18, n° 10, pp. 2800–2803, 1979.
- [25] D. Huo *et al.*, "Understanding of the nanosize effect on the structure and electrochemistry of V_2O_5 obtained via fluorine chemistry", *Mater. Today Proc.*, vol. 5, n° 11, Part 1, pp. 22850–22858, 2018.
- [26] S. A. Hevia *et al.*, "High performance of V_2O_5 thin film electrodes for lithium-ion intercalation", *Appl. Surf. Sci.*, vol. 576, p. 151710, 2022.
- [27] H.-J. Kim *et al.*, "A Comprehensive review of Li-Ion battery materials and their recycling Techniques", *Electronics*, vol. 9, n° 7, Art. n° 7, 2020.
- [28] M. Rosa Palacín, "Recent advances in rechargeable battery materials: a chemist's perspective", *Chem. Soc. Rev.*, vol. 38, n° 9, pp. 2565–2575, 2009.
- [29] T. Ohzuku, A. Ueda, and N. Yamamoto, "Zero-strain insertion material of $\text{Li}[\text{Li}_{1/3}\text{Ti}_{5/3}]\text{O}_4$ for rechargeable lithium cells", *J. Electrochem. Soc.*, vol. 142, no. 5, p. 1431, 1995.
- [30] S. D. Beattie, D. Larcher, M. Morcrette, B. Simon, and J.-M. Tarascon, "Si electrodes for Li-ion batteries - a new way to look at an old problem", *J. Electrochem. Soc.*, vol. 155, n° 2, p. A158, 2007.
- [31] P. Poizot, S. Laruelle, S. Grugeon, L. Dupont, and J.-M. Tarascon, "Nano-sized transition-metal oxides as negative-electrode materials for lithium-ion batteries", *Nature*, vol. 407, n° 6803, Art. n° 6803, 2000.
- [32] D. Aurbach *et al.*, "Design of electrolyte solutions for Li and Li-ion batteries: a review", *Electrochimica Acta*, vol. 50, n° 2, pp. 247–254, 2004.
- [33] R. Fong, U. von Sacken, and J. R. Dahn, "Studies of lithium intercalation into carbons using nonaqueous electrochemical cells", *J. Electrochem. Soc.*, vol. 137, n° 7, p. 2009.

- [34] D. Guyomard and J. M. Tarascon, "Rechargeable $\text{Li}_{1+x}\text{Mn}_2\text{O}_4$ / carbon cells with a new electrolyte composition: potentiostatic studies and application to practical cells", *J. Electrochem. Soc.*, vol. 140, n° 11, p. 3071, 1993.
- [35] Y. Ein-Eli, S. R. Thomas, V. Koch, D. Aurbach, B. Markovsky, and A. Schechter, "Ethylmethylcarbonate, a promising solvent for Li-ion rechargeable batteries", *J. Electrochem. Soc.*, vol. 143, n° 12, p. L273, 1996.
- [36] D. Aurbach *et al.*, "The Study of electrolyte solutions based on ethylene and diethyl carbonates for rechargeable Li Batteries: II. Graphite electrodes", *J. Electrochem. Soc.*, vol. 142, n° 9, p. 2882, 1995.
- [37] E. Peled, "The Electrochemical Behavior of Alkali and Alkaline Earth Metals in nonaqueous battery systems - The solid electrolyte interphase model", *J. Electrochem. Soc.*, vol. 126, n° 12, p. 2047, 1979.
- [38] M. Nie, L. Madec, J. Xia, D. S. Hall, and J. R. Dahn, "Some lewis acid-base adducts involving boron trifluoride as electrolyte additives for lithium ion cells", *J. Power Sources*, vol. 328, pp. 433–442, 2016.
- [39] M. Ishikawa, H. Kawasaki, N. Yoshimoto, and M. Morita, "Pretreatment of Li metal anode with electrolyte additive for enhancing Li cycleability", *J. Power Sources*, vol. 146, n° 1, pp. 199–203, 2005.
- [40] P. V. Wright, "Electrical conductivity in ionic complexes of poly(ethylene oxide)", *Br. Polym. J.*, vol. 7, n° 5, pp. 319–327, 1975.
- [41] A. Manthiram, X. Yu, and S. Wang, "Lithium battery chemistries enabled by solid-state electrolytes", *Nat. Rev. Mater.*, vol. 2, n° 4, Art. n° 4, 2017.
- [42] K. Zhu *et al.*, "How far away are lithium-sulfur batteries from commercialization?", *Front. Energy Res.*, vol. 7, 2019, Accessed: Jan. 30, 2022.
- [43] W.-J. Kwak *et al.*, "Lithium–oxygen batteries and related Systems: potential, status, and future", *Chem. Rev.*, vol. 120, n° 14, pp. 6626–6683, 2020.
- [44] P. G. Bruce, S. A. Freunberger, L. J. Hardwick, and J.-M. Tarascon, "Li–O₂ and Li–S batteries with high energy storage", *Nat. Mater.*, vol. 11, n° 1, pp. 19–29, 2012.
- [45] D. Sharon, M. Salama, R. Attias, and D. Aurbach, "Electrolyte solutions for 'beyond Li-ion batteries': Li-S, Li-O₂, and Mg Batteries", *Electrochem. Soc. Interface*, vol. 28, n° 2, pp. 71–77, 2019.
- [46] Z. Yuan *et al.*, "Powering lithium–sulfur battery performance by propelling polysulfide redox at sulfiphilic hosts", *Nano Lett.*, vol. 16, n° 1, pp. 519–527, 2016.
- [47] X. Tao *et al.*, "Balancing surface adsorption and diffusion of lithium-polysulfides on nonconductive oxides for lithium–sulfur battery design", *Nat. Commun.*, vol. 7, n° 1, pp. 1–9, 2016.
- [48] X.-J. Hong *et al.*, "Confinement of polysulfides within bi-functional metal–organic frameworks for high performance lithium–sulfur batteries", *Nanoscale*, vol. 10, n° 6, pp. 2774–2780, 2018.

- [49] Industrie-techno, "https://www.industrie-techno.com/article/nous-voulons-creer-en-france-un-tesla-de-la-batterie-sodium-ion-affirme-laurent-hubard-directeur-de-tiamat-energy." 58344
- [50] K. Kubota, M. Dahbi, T. Hosaka, S. Kumakura, and S. Komaba, "Towards K-ion and Na-ion batteries as 'Beyond Li-ion'", *Chem. Rec.*, vol. 18, n° 4, pp. 459–479, 2018.
- [51] J. Ge, L. Fan, A. M. Rao, J. Zhou, and B. Lu, "Surface-substituted Prussian blue analogue cathode for sustainable potassium-ion batteries", *Nat. Sustain.*, pp. 1–10, 2021.
- [52] J. Muldoon, C. B. Bucur, and T. Gregory, "Quest for Nonaqueous multivalent secondary batteries: magnesium and beyond", *Chem. Rev.*, vol. 114, n° 23, pp. 11683–11720, 2014.
- [53] S. Dühnen, J. Betz, M. Kolek, R. Schmuck, M. Winter, and T. Placke, "Toward green battery cells: perspective on materials and technologies", *Small Methods*, vol. 4, n° 7, p. 2000039, 2020.
- [54] T. Liu, J. P. Vivek, E. W. Zhao, J. Lei, N. Garcia-Araez, and C. P. Grey, "Current challenges and routes forward for nonaqueous lithium–air batteries", *Chem. Rev.*, vol. 120, n° 14, pp. 6558–6625, 2020.
- [55] J. Fu, Z. P. Cano, M. G. Park, A. Yu, M. Fowler, and Z. Chen, "Electrically rechargeable Zinc–air batteries: progress, challenges, and perspectives", *Adv. Mater.*, vol. 29, n° 7, p. 1604685, 2017.
- [56] H.-F. Wang and Q. Xu, "Materials design for Rechargeable metal-air batteries", *Matter*, vol. 1, n° 3, pp. 565–595, 2019.
- [57] N. Chawla, "Recent advances in air-battery chemistries", *Mater. Today Chem.*, vol. 12, pp. 324–331, 2019.
- [58] K. M. Abraham and Z. Jiang, "A polymer electrolyte-based rechargeable lithium-oxygen battery", *J. Electrochem. Soc.*, vol. 143, n° 1, pp. 1–5, 1996.
- [59] J.-H. Kang *et al.*, "Lithium-air batteries: air-breathing challenges and perspective", *ACS Nano*, 2020.
- [60] J. Lu, L. Li, J.-B. Park, Y.-K. Sun, F. Wu, and K. Amine, "Aprotic and aqueous Li-O₂ batteries", *Chem. Rev.*, vol. 114, n° 11, pp. 5611–5640, 2014.
- [61] J. Lai, Y. Xing, N. Chen, L. Li, F. Wu, and R. Chen, "Electrolytes for rechargeable lithium-air batteries", *Angew. Chem. Int. Ed.*, vol. 59, n° 8, pp. 2974–2997, 2020.
- [62] C. O. Laoire, S. Mukerjee, K. M. Abraham, E. J. Plichta, and M. A. Hendrickson, "Influence of nonaqueous solvents on the electrochemistry of oxygen in the rechargeable lithium-air battery", *J. Phys. Chem. C*, vol. 114, n° 19, pp. 9178–9186, 2010.
- [63] S. J. Visco *et al.*, "Aqueous and nonaqueous lithium-air batteries enabled by water-stable lithium metal electrodes", *J. Solid State Electrochem.*, vol. 18, n° 5, pp. 1443–1456, 2014.
- [64] D. Aurbach, B. D. McCloskey, L. F. Nazar, and P. G. Bruce, "Advances in understanding mechanisms underpinning lithium-air batteries", *Nat. Energy*, vol. 1, n° 9, pp. 1–11, 2016.
- [65] Z. Lyu *et al.*, "Recent advances in understanding of the mechanism and control of Li₂O₂ formation in aprotic Li-O₂ batteries", *Chem. Soc. Rev.*, vol. 46, n° 19, pp. 6046–6072, 2017.

- [66] B. D. Adams, C. Radtke, R. Black, M. L. Trudeau, K. Zaghbi, and L. F. Nazar, "Current density dependence of peroxide formation in the Li-O₂ battery and its effect on charge", *Energy Environ. Sci.*, vol. 6, n° 6, pp. 1772–1778, 2013.
- [67] L. D. Griffith, A. E. S. Sleightholme, J. F. Mansfield, D. J. Siegel, and C. W. Monroe, "Correlating Li/O₂ cell capacity and product morphology with discharge current", *ACS Appl. Mater. Interfaces*, vol. 7, n° 14, pp. 7670–7678, 2015.
- [68] N. B. Aetukuri, B. D. McCloskey, J. M. García, L. E. Krupp, V. Viswanathan, and A. C. Luntz, "Solvating additives drive solution-mediated electrochemistry and enhance toroid growth in non-aqueous Li-O₂ batteries", *Nat. Chem.*, vol. 7, n° 1, pp. 50–56, 2015.
- [69] R. R. Mitchell, B. M. Gallant, Y. Shao-Horn, and C. V. Thompson, "Mechanisms of morphological evolution of Li₂O₂ particles during electrochemical growth", *J. Phys. Chem. Lett.*, vol. 4, n° 7, pp. 1060–1064, 2013.
- [70] N. B. Aetukuri, B. D. McCloskey, J. M. García, L. E. Krupp, V. Viswanathan, and A. C. Luntz, "On the origin and implications of Li₂O₂ toroid formation in nonaqueous Li-O₂ batteries", *Nat. Chem.*, vol. 7, n° 1, pp. 50–56, 2015.
- [71] R. R. Mitchell, B. M. Gallant, C. V. Thompson, and Y. Shao-Horn, "All-carbon-nanofiber electrodes for high-energy rechargeable Li-O₂ batteries", *Energy Environ. Sci.*, vol. 4, n° 8, p. 2952, 2011.
- [72] U. Schwenke, M. Metzger, T. Restle, M. Piana, and H. Gasteiger, "The influence of water and protons on Li₂O₂ crystal growth in aprotic Li-O₂ cells", *J. Electrochem. Soc.*, vol. 162, pp. A573–A584, 2015.
- [73] D. Zhai *et al.*, "Disproportionation in Li-O₂ batteries based on a large surface area carbon cathode", *J. Am. Chem. Soc.*, vol. 135, n° 41, pp. 15364–15372, 2013.
- [74] J. Read *et al.*, "Oxygen transport properties of organic electrolytes and performance of lithium-oxygen battery", *J. Electrochem. Soc.*, vol. 150, n° 10, p. A1351, 2003.
- [75] Handbook of batteries, 3rd Edition, "Handbook of batteries, 3rd Edition", 2001.
- [76] Z. Peng, S. A. Freunberger, Y. Chen, and P. G. Bruce, "A reversible and higher-ate Li-O₂ battery", *Science*, vol. 337, n° 6094, pp. 563–566, 2012.
- [77] E. Nasybulin *et al.*, "Effects of electrolyte salts on the performance of Li-O₂ batteries", *J. Phys. Chem. C*, vol. 117, n° 6, pp. 2635–2645, 2013.
- [78] L. Wang, Y. Zhang, Z. Liu, L. Guo, and Z. Peng, "Understanding oxygen electrochemistry in aprotic LiO₂ batteries", *Green Energy Environ.*, vol. 2, n° 3, pp. 186–203, 2017.
- [79] S. Oswald, D. Mikhailova, F. Scheiba, P. Reichel, A. Fiedler, and H. Ehrenberg, "XPS investigations of electrolyte/electrode interactions for various Li-ion battery materials", *Anal. Bioanal. Chem.*, vol. 400, n° 3, pp. 691–696, 2011.
- [80] P. Du *et al.*, "Compatibility of lithium salts with solvent of the non-aqueous electrolyte in Li-O₂ batteries", *Phys. Chem. Chem. Phys.*, vol. 15, n° 15, pp. 5572–5581, 2013.
- [81] Y.-C. Lu *et al.*, "Lithium–oxygen batteries: bridging mechanistic understanding and battery performance", *Energy Environ. Sci.*, vol. 6, n° 3, pp. 750–768, 2013.

- [82] M. Gauthier *et al.*, "Electrode-electrolyte interface in Li-ion batteries: current understanding and new insights", *J. Phys. Chem. Lett.*, vol. 6, n° 22, pp. 4653–4672, 2015.
- [83] Y. Liu *et al.*, "An artificial solid electrolyte interphase with high Li-ion Conductivity, mechanical strength, and flexibility for stable lithium metal anodes", *Adv. Mater.*, vol. 29, n° 10, p. 1605531, 2017.
- [84] J. Wandt, P. Jakes, J. Granwehr, H. A. Gasteiger, and R.-A. Eichel, "Singlet oxygen formation during the charging process of an aprotic lithium-oxygen battery", *Angew. Chem. Int. Ed.*, vol. 55, n° 24, pp. 6892–6895, 2016.
- [85] J. Wandt, A. T. S. Freiberg, A. Ogrodnik, and H. A. Gasteiger, "Singlet oxygen evolution from layered transition metal oxide cathode materials and its implications for lithium-ion batteries", *Mater. Today*, vol. 21, n° 8, pp. 825–833, 2018.
- [86] N. Mahne, S. E. Renfrew, B. D. McCloskey, and S. A. Freunberger, "Electrochemical oxidation of lithium carbonate generates singlet oxygen", *Angew. Chem. Int. Ed.*, vol. 57, n° 19, pp. 5529–5533, 2018.
- [87] N. Mahne *et al.*, "Singlet oxygen generation as a major cause for parasitic reactions during cycling of aprotic lithium-oxygen batteries", *Nat. Energy*, vol. 2, n° 5, pp. 1–9, 2017.
- [88] B. D. McCloskey *et al.*, "Combining accurate O₂ and Li₂O₂ assays to separate discharge and charge stability limitations in nonaqueous Li-O₂ batteries", *J. Phys. Chem. Lett.*, vol. 4, n° 17, pp. 2989–2993, 2013.
- [89] A. C. Luntz and B. D. McCloskey, "Li-air batteries: importance of singlet oxygen", *Nat. Energy*, vol. 2, n° 5, p. 17056, 2017.
- [90] Z. Ma *et al.*, "A review of cathode materials and structures for rechargeable lithium-air batteries", *Energy Environ. Sci.*, vol. 8, n° 8, pp. 2144–2198, 2015.
- [91] J.-W. Jung, S.-H. Cho, J. S. Nam, and I.-D. Kim, "Current and future cathode materials for non-aqueous Li-air (O₂) battery technology – a focused review", *Energy Storage Mater.*, vol. 24, pp. 512–528, 2020.
- [92] D. Wu *et al.*, "Metal–Organic Frameworks as Cathode Materials for Li-O₂ Batteries", *Adv. Mater.*, vol. 26, n° 20, pp. 3258–3262, 2014.
- [93] J. Kang, O. L. Li, and N. Saito, "Hierarchical meso–macro structure porous carbon black as electrode materials in Li-air battery", *J. Power Sources*, vol. 261, pp. 156–161, 2014.
- [94] N. Mahne, O. Fontaine, M. O. Thotiyl, M. Wilkening, and S. A. Freunberger, "Mechanism and performance of lithium-oxygen batteries – a perspective", *Chem. Sci.*, vol. 8, n° 10, pp. 6716–6729, 2017.
- [95] N. Ding, S. W. Chien, T. S. A. Hor, R. Lum, Y. Zong, and Z. Liu, "Influence of carbon pore size on the discharge capacity of Li-O₂ batteries", *J. Mater. Chem. A*, vol. 2, n° 31, pp. 12433–12441, 2014.
- [96] C. Shen *et al.*, "Influence of pore size on discharge capacity in Li-air batteries with hierarchically macroporous carbon nanotube foams as cathodes", *J. Electrochem. Soc.*, vol. 165, n° 11, p. A2833, 2018.

- [97] K. Sakai, S. Iwamura, and S. Mukai, "Influence of the porous structure of the cathode on the discharge capacity of lithium-air batteries", *J. Electrochem. Soc.*, vol. 164, pp. A3075–A3080, 2017.
- [98] S. B. Ma, D. J. Lee, V. Roev, D. Im, and S.-G. Doo, "Effect of porosity on electrochemical properties of carbon materials as cathode for lithium-oxygen battery", *J. Power Sources*, vol. 244, pp. 494–498, 2013.
- [99] F. Wang and X. Li, "Effects of the electrode wettability on the deep discharge capacity of Li-O₂ batteries", *ACS Omega*, vol. 3, n° 6, pp. 6006–6012, 2018.
- [100] X. Yang, P. He, and Y. Xia, "Preparation of mesocellular carbon foam and its application for lithium-oxygen battery", *Electrochem. Commun.*, vol. 11, n° 6, pp. 1127–1130, 2009.
- [101] C. Tran, X.-Q. Yang, and D. Qu, "Investigation of the gas-diffusion-electrode used as lithium/air cathode in non-aqueous electrolyte and the importance of carbon material porosity" *J. Power Sources*, vol. 195, no. 7, pp. 2057–2063, Apr. 2010, doi: 10.1016/j.jpowsour.2009.10.012.
- [102] C. Wang, Z. Xie, and Z. Zhou, "Lithium-air batteries: challenges coexist with opportunities", *APL Mater.*, vol. 7, n° 4, p. 040701, 2019.
- [103] Y.-C. Lu, H. A. Gasteiger, and Y. Shao-Horn, "Catalytic activity trends of oxygen reduction reaction for nonaqueous Li-air batteries", *J. Am. Chem. Soc.*, vol. 133, n° 47, pp. 19048–19051, 2011.
- [104] Y.-C. Lu, H. A. Gasteiger, M. C. Parent, V. Chiloyan, and Y. Shao-Horn, "The influence of catalysts on discharge and charge voltages of rechargeable Li-oxygen batteries", *MIT Web Domain*, Apr. 2010, Accessed: May 21, 2021 [Online].
- [105] Y.-C. Lu, H. A. Gasteiger, and Y. Shao-Horn, "Catalytic activity trends of oxygen reduction reaction for nonaqueous Li-air batteries", *J. Am. Chem. Soc.*, vol. 133, n° 47, pp. 19048–19051, 2011.
- [106] Y.-C. Lu, H. A. Gasteiger, M. C. Parent, V. Chiloyan, and Y. Shao-Horn, "The influence of catalysts on discharge and charge voltages of rechargeable Li-oxygen batteries", *Electrochem. Solid-State Lett.*, vol. 13, n° 6, p. A69, 2010.
- [107] F. Li *et al.*, "Ru/ITO: A carbon-free cathode for nonaqueous Li-O₂ battery", *Nano Lett.*, vol. 13, n° 10, pp. 4702–4707, 2013.
- [108] R. Gao *et al.*, "The role of oxygen vacancies in improving the performance of CoO as a bifunctional cathode catalyst for rechargeable Li-O₂ batteries", *J. Mater. Chem. A*, vol. 3, n° 34, pp. 17598–17605, 2015.
- [109] P. Zhang, D. Sun, M. He, J. Lang, S. Xu, and X. Yan, "Synthesis of porous δ -MnO₂ submicron tubes as highly efficient electrocatalyst for rechargeable Li-O₂ batteries", *ChemSusChem*, vol. 8, n° 11, pp. 1972–1979, 2015.
- [110] A. Débart, A. J. Paterson, J. Bao, and P. G. Bruce, " α -MnO₂ Nanowires: a catalyst for the O₂ electrode in rechargeable lithium batteries", *Angew. Chem. Int. Ed.*, vol. 47, n° 24, pp. 4521–4524, 2008.

- [111] A. Zahoor, H. S. Jang, J. S. Jeong, M. Christy, Y. J. Hwang, and K. S. Nahm, "A comparative study of nanostructured α - and δ -MnO₂ for lithium oxygen battery application", *RSC Adv.*, vol. 4, n° 18, pp. 8973–8977, 2014.
- [112] C. Gaya, A. A. Franco, C. Surcin, M. Courty, and D. Larcher, "Carbon-loaded flexible electrode films for Li-O₂ cells: Preparation, Porosity, Homogeneity and Electrochemical Characterization", 2020, doi: 10.26434/chemrxiv.13292759.v1.
- [113] S. S. Zhang, D. Foster, and J. Read, "Discharge characteristic of a non-aqueous electrolyte Li/O₂ battery", *J. Power Sources*, vol. 195, n° 4, pp. 1235–1240, 2010.
- [114] S. A. Freunberger, "True performance metrics in beyond-intercalation batteries", *Nat. Energy*, vol. 2, n° 7, pp. 1–4, 2017.
- [115] D. Foucher, "Impact de l'eau dans la flexibilité des MOFs", phd thesis, Université Paris-Saclay, 2016.
- [116] G. K. H. Shimizu, R. Vaidhyanathan, and J. M. Taylor, "Phosphonate and sulfonate metal organic frameworks", *Chem. Soc. Rev.*, vol. 38, n° 5, pp. 1430–1449, 2009.
- [117] D. G. Daraji, N. P. Prajapati, and H. D. Patel, "Synthesis and applications of 2-substituted imidazole and its derivatives: a review", *J. Heterocycl. Chem.*, vol. 56, n° 9, pp. 2299–2317, 2019.
- [118] O. M. Yaghi and H. Li, "Hydrothermal synthesis of a metal-organic framework containing large rectangular channels", *J. Am. Chem. Soc.*, vol. 117, n° 41, pp. 10401–10402, 1995.
- [119] S. R. Batten *et al.*, "Terminology of metal-organic frameworks and coordination polymers (IUPAC Recommendations 2013)", *Pure Appl. Chem.*, vol. 85, n° 8, pp. 1715–1724, 2013.
- [120] J. Rouquerol *et al.*, "Recommendations for the characterization of porous solids (Technical Report)", *Pure Appl. Chem.*, vol. 66, no. 8, pp. 1739–1758, 1994.
- [121] I. Senkovska and S. Kaskel, "Ultrahigh porosity in mesoporous MOFs: promises and limitations", *Chem. Commun.*, vol. 50, n° 54, pp. 7089–7098, 2014.
- [122] I. M. Hönicke *et al.*, "Balancing mechanical stability and ultrahigh porosity in crystalline framework materials", *Angew. Chem. Int. Ed.*, vol. 57, n° 42, pp. 13780–13783, 2018.
- [123] S. Horike, S. Shimomura, and S. Kitagawa, "Soft porous crystals", *Nat. Chem.*, vol. 1, n° 9, pp. 695–704, 2009.
- [124] S. M. Moosavi *et al.*, "Understanding the diversity of the metal-organic framework ecosystem", *Nat. Commun.*, vol. 11, n° 1, p. 4068, 2020.
- [125] M. Eddaoudi *et al.*, "Systematic design of pore size and functionality in isorecticular MOFs and their application in methane storage", *Science*, vol. 295, n° 5554, pp. 469–472, 2002.
- [126] A. C. Sudik, A. R. Millward, N. W. Ockwig, A. P. Côté, J. Kim, and O. M. Yaghi, "Design, synthesis, structure, and gas (N₂, Ar, CO₂, CH₄, and H₂) sorption properties of porous metal-organic tetrahedral and heterocuboidal polyhedra", *J. Am. Chem. Soc.*, vol. 127, n° 19, pp. 7110–7118, 2005.
- [127] H. Jiang *et al.*, "Metal-organic frameworks for high charge-discharge rates in lithium-sulfur batteries", *Angew. Chem. Int. Ed.*, vol. 57, n° 15, pp. 3916–3921, 2018.

- [128] J. L. C. Rowsell and O. M. Yaghi, "Metal-organic frameworks: a new class of porous materials", *Microporous Mesoporous Mater.*, vol. 73, n° 1–2, pp. 3–14, 2004.
- [129] S. S.-Y. Chui, S. M.-F. Lo, J. P. H. Charmant, A. G. Orpen, and I. D. Williams, "A chemically functionalizable nanoporous material $[\text{Cu}_3(\text{TMA})_2(\text{H}_2\text{O})_3]_n$ ", *Science*, vol. 283, n° 5405, pp. 1148–1150, 1999.
- [130] G. XJ, Z. D, D. LH, M. XH, and L. WJ, "Methane storage and synthesis of HKUST-1 prepared with different solvent", *China Pet. Process. Petrochem. Technol.*, vol. 21, n° 2, pp. 44–49, 2019.
- [131] Y. Chen, X. Mu, E. Lester, and T. Wu, "High efficiency synthesis of HKUST-1 under mild conditions with high BET surface area and CO_2 uptake capacity", *Prog. Nat. Sci. Mater. Int.*, vol. 28, n° 5, pp. 584–589, 2018.
- [132] K. A. Cychosz and A. J. Matzger, "Water stability of microporous coordination polymers and the adsorption of pharmaceuticals from water", *Langmuir*, vol. 26, n° 22, pp. 17198–17202, 2010.
- [133] H. Li, M. Eddaoudi, M. O’Keeffe, and O. M. Yaghi, "Design and synthesis of an exceptionally stable and highly porous metal-organic framework", *Nature*, vol. 402, n° 6759, pp. 276–279, 1999.
- [134] W. W. Lestari, A. H. Wibowo, S. Astuti, Irwinsyah, A. Z. Pamungkas, and Y. K. Krisnandi, "Fabrication of hybrid coating material of polypropylene itaconate containing MOF-5 for CO_2 capture", *Prog. Org. Coat.*, vol. 115, pp. 49–55, 2018.
- [135] H. Aykac Ozen and B. Ozturk, "Gas separation characteristic of mixed matrix membrane prepared by MOF-5 including different metals", *Sep. Purif. Technol.*, vol. 211, pp. 514–521, 2019.
- [136] B. Xiang, L. Fu, Y. Li, and Y. Liu, "A new $\text{Fe}^{(III)}$ /MOF-5(Ni) catalyst for highly selective synthesis of catechol from phenol and hydrogen peroxide", *ChemistrySelect*, vol. 4, n° 4, pp. 1502–1509, 2019.
- [137] V. Villemot, M. Hamel, R. B. Pansu, I. Leray, and G. H. V. Bertrand, "Unravelling the true MOF-5 luminescence", *RSC Adv.*, vol. 10, n° 31, pp. 18418–18422, 2020.
- [138] W. Kukulka, K. Cendrowski, and E. Mijowska, "Electrochemical performance of MOF-5 derived carbon nanocomposites with 1D, 2D and 3D carbon structures", *Electrochimica Acta*, vol. 307, pp. 582–594, 2019.
- [139] X. Wu *et al.*, "Metal-organic framework-derived, Zn-doped porous carbon polyhedra with enhanced activity as bifunctional catalysts for rechargeable zinc-air batteries", *Nano Res.*, pp. 1–11, 2017.
- [140] N. L. Rosi, J. Kim, M. Eddaoudi, B. Chen, M. O’Keeffe, and O. M. Yaghi, "Rod packings and metal-organic frameworks constructed from rod-shaped secondary building units", *J. Am. Chem. Soc.*, vol. 127, n° 5, pp. 1504–1518, 2005.
- [141] L. J. Wang *et al.*, "Synthesis and characterization of metal-organic framework 74 containing 2, 4, 6, 8, and 10 different Metals", *Inorg. Chem.*, vol. 53, n° 12, pp. 5881–5883, 2014.

- [142] T. Xiao and D. Liu, "The most advanced synthesis and a wide range of applications of MOF-74 and its derivatives", *Microporous Mesoporous Mater.*, vol. 283, pp. 88–103, 2019.
- [143] G. Férey *et al.*, "A hybrid solid with giant pores prepared by a combination of targeted chemistry, simulation, and powder diffraction", *Angew. Chem.-Int. Ed.*, vol. 43, n° 46, pp. 6296–6301, 2004.
- [144] G. Férey *et al.*, "A chromium terephthalate-based solid with unusually large pore volumes and surface area", *Science*, vol. 309, n° 5743, pp. 2040–2042, 2005.
- [145] G. Zhong, D. Liu, and J. Zhang, "Applications of porous metal-organic framework MIL-100(M) (M = Cr, Fe, Sc, Al, V)", *Cryst. Growth Des.*, vol. 18, n° 12, pp. 7730–7744, 2018.
- [146] M. Y. Zorainy, M. G. Alalm, S. Kaliaguine, and D. C. Boffito, "Revisiting the MIL-101 metal-organic framework: design, synthesis, modifications, advances, and recent applications", *J. Mater. Chem. A*, vol. 9, no. 39, pp. 22159–22217, 2021.
- [147] J. H. Cavka *et al.*, "A new zirconium inorganic building brick forming metal-organic frameworks with exceptional stability", *J. Am. Chem. Soc.*, vol. 130, n° 42, pp. 13850–13851, 2008.
- [148] S. Biswas *et al.*, "Enhanced selectivity of CO₂ over CH₄ in sulphonate-, carboxylate- and iodo-functionalized UiO-66 frameworks", *Dalton Trans.*, vol. 42, n° 13, pp. 4730–4737, 2013.
- [149] J. Winarta *et al.*, "A Decade of UiO-66 Research: A historic review of dynamic structure, synthesis mechanisms, and characterization techniques of an archetypal metal-organic framework", *Cryst. Growth Des.*, vol. 20, n° 2, pp. 1347–1362, 2020.
- [150] X. Liu, "Metal-organic framework UiO-66 membranes", *Front. Chem. Sci. Eng.*, vol. 14, n° 2, pp. 216–232, 2020.
- [151] L. Alaerts *et al.*, "Selective adsorption and separation of ortho-substituted alkylaromatics with the microporous aluminum terephthalate MIL-53", *J. Am. Chem. Soc.*, vol. 130, n° 43, pp. 14170–14178, 2008.
- [152] G. Férey and C. Serre, "Large breathing effects in three-dimensional porous hybrid matter: facts, analyses, rules and consequences", *Chem. Soc. Rev.*, vol. 38, n° 5, pp. 1380–1399, 2009.
- [153] A. Clearfield, "Flexible MOFs under stress: pressure and temperature", *Dalton Trans.*, vol. 45, n° 10, pp. 4100–4112, 2016.
- [154] D. Bousquet, F.-X. Coudert, A. G. J. Fossati, A. V. Neimark, A. H. Fuchs, and A. Boutin, "Adsorption induced transitions in soft porous crystals: an osmotic potential approach to multistability and intermediate structures", *J. Chem. Phys.*, vol. 138, n° 17, p. 174706, 2013.
- [155] C. Mellot-Draznieks, C. Serre, S. Surblé, N. Audebrand, and G. Férey, "Very large swelling in hybrid frameworks: a combined computational and powder diffraction study", *J. Am. Chem. Soc.*, vol. 127, n° 46, pp. 16273–16278, 2005.

- [156] F. Millange and R. I. Walton, "MIL-53 and its Isoreticular Analogues: a review of the chemistry and structure of a prototypical flexible metal-organic framework", *Isr. J. Chem.*, vol. 58, n° 9–10, pp. 1019–1035, 2018.
- [157] C. Mellot-Draznieks, C. Serre, S. Surble, N. Audebrand, and G. Férey, "Very large swelling in hybrid frameworks: A combined computational and powder diffraction study", *J. Am. Chem. Soc.*, vol. 127, n° 46, pp. 16273–16278, 2005.
- [158] C. Serre, F. Millange, S. Surble, and G. Férey, "A route to the synthesis of trivalent transition-metal porous carboxylates with trimeric secondary building units", *Angew. Chem.-Int. Ed.*, vol. 43, n° 46, pp. 6286–6289, 2004.
- [159] P. Horcajada *et al.*, "How linker's modification controls swelling properties of highly flexible iron(III) dicarboxylates MIL-88.", *J. Am. Chem. Soc.*, vol. 133, n° 44, pp. 17839–17847, 2011.
- [160] N. A. Ramsahye *et al.*, "Impact of the flexible character of MIL-88 iron(III) dicarboxylates on the adsorption of n-alkanes", *Chem. Mater.*, vol. 25, n° 3, pp. 479–488, 2013.
- [161] M. AL Haydar, H. R. Abid, B. Sunderland, and S. Wang, "Metal-organic frameworks as a drug delivery system for flurbiprofen", *Drug Des. Devel. Ther.*, vol. 11, pp. 2685–2695, 2017.
- [162] M. E. Casco *et al.*, "Gate-opening effect in ZIF-8: the first experimental proof using inelastic neutron scattering", *Chem. Commun.*, vol. 52, n° 18, pp. 3639–3642, 2016.
- [163] D. J. Tranchemontagne, K. S. Park, H. Furukawa, J. Eckert, C. B. Knobler, and O. M. Yaghi, "Hydrogen storage in new metal-organic frameworks", *J. Phys. Chem. C*, vol. 116, n° 24, pp. 13143–13151, 2012.
- [164] B. Chen *et al.*, "A microporous metal-organic framework for gas-chromatographic separation of alkanes", *Angew. Chem.*, vol. 118, n° 9, pp. 1418–1421, 2006.
- [165] Z. Messegee, J. Osborne, and T. M. Abdel-Fattah, "Green synthesis of nickel terephthalate MOF at room temperature for the catalysis of hydrogen generation", *ECS Trans.*, vol. 80, n° 10, pp. 1489–1493, 2017.
- [166] A. Sabetghadam *et al.*, "Influence of filler pore structure and polymer on the performance of MOF-based mixed-matrix membranes for CO₂ capture", *Chem. – Eur. J.*, vol. 24, n° 31, pp. 7949–7956, 2018.
- [167] McKinlay Alistair C. *et al.*, "BioMOFs: metal-organic frameworks for biological and medical applications", *Angew. Chem. Int. Ed.*, vol. 49, n° 36, pp. 6260–6266, 2010.
- [168] M. L. Aubrey, R. Ameloot, B. M. Wiers, and J. R. Long, "Metal-organic frameworks as solid magnesium electrolytes", *Energy Environ. Sci.*, vol. 7, n° 2, pp. 667–671, 2014.
- [169] J. Shin *et al.*, "MIL-101(Fe) as a lithium-ion battery electrode material: a relaxation and intercalation mechanism during lithium insertion", *J. Mater. Chem. A*, vol. 3, n° 8, pp. 4738–4744, 2015.
- [170] Y. Xue, S. Zheng, H. Xue, and H. Pang, "Metal-organic framework composites and their electrochemical applications", *J. Mater. Chem. A*, vol. 7, n° 13, pp. 7301–7327, 2019.

- [171] X. He, F. Yin, H. Wang, B. Chen, and G. Li, "Metal-organic frameworks for highly efficient oxygen electrocatalysis", *Chin. J. Catal.*, vol. 39, n° 2, pp. 207–227, 2018.
- [172] L. Li *et al.*, "Metal-organic frameworks: a promising platform for constructing non-noble electrocatalysts for the oxygen-reduction reaction", *J. Mater. Chem. A*, vol. 7, n° 5, pp. 1964–1988, 2019.
- [173] J. Mao, L. Yang, P. Yu, X. Wei, and L. Mao, "Electrocatalytic four-electron reduction of oxygen with Copper (II)-based metal-organic frameworks", *Electrochem. Commun.*, vol. 19, pp. 29–31, 2012.
- [174] L. Zhang, Y. Hu, J. Chen, W. Huang, J. Cheng, and Y. Chen, "A novel metal organic framework-derived carbon-based catalyst for oxygen reduction reaction in a microbial fuel cell", *J. Power Sources*, vol. 384, pp. 98–106, 2018.
- [175] G. Song, Z. Wang, L. Wang, G. Li, M. Huang, and F. Yin, "Preparation of MOF(Fe) and its catalytic activity for oxygen reduction reaction in an alkaline electrolyte", *Chin. J. Catal.*, vol. 35, n° 2, pp. 185–195, 2014.
- [176] H. Wang, F. Yin, G. Li, B. Chen, and Z. Wang, "Preparation, characterization and bifunctional catalytic properties of MOF(Fe/Co) catalyst for oxygen reduction/evolution reactions in alkaline electrolyte", *Int. J. Hydrog. Energy*, vol. 39, n° 28, pp. 16179–16186, 2014.
- [177] E. M. Miner, T. Fukushima, D. Sheberla, L. Sun, Y. Surendranath, and M. Dincă, "Electrochemical oxygen reduction catalysed by Ni₃(hexaiminotriphenylene)₂", *Nat. Commun.*, vol. 7, n° 1, Art. no. 1, 2016.
- [178] J. Park *et al.*, "Two-Dimensional conductive Ni-HAB as a catalyst for the electrochemical oxygen reduction reaction", *ACS Appl. Mater. Interfaces*, vol. 12, n° 35, pp. 39074–39081, 2020.
- [179] D. Sheberla *et al.*, "High Electrical Conductivity in Ni₃(2,3,6,7,10,11-hexaimino-triphenylene)₂, a semiconducting metam-organic graphene analogue", *J. Am. Chem. Soc.*, vol. 136, n° 25, pp. 8859–8862, 2014.
- [180] X. Li, F. Cheng, S. Zhang, and J. Chen, "Shape-controlled synthesis and lithium-storage study of metal-organic frameworks Zn₄O(1,3,5-benzenetribenzoate)₂", *J. Power Sources*, vol. 160, n° 1, pp. 542–547, 2006.
- [181] Férey Gérard *et al.*, "Mixed-valence Li/Fe-based metal-organic frameworks with both reversible redox and sorption properties", *Angew. Chem. Int. Ed.*, vol. 46, n° 18, pp. 3259–3263, 2007.
- [182] K. Saravanan, M. Nagarathinam, P. Balaya, and J. J. Vittal, "Lithium storage in a metal organic framework with diamondoid topology – a case study on metal formates", *J. Mater. Chem.*, vol. 20, n° 38, pp. 8329–8335, 2010.
- [183] R. D. Shannon, "Revised effective ionic radii and systematic studies of interatomic distances in halides and chalcogenides", *Acta Crystallogr. A*, vol. 32, n° 5, Art. n° 5, 1976.

- [184] C. Li, X. Hu, and B. Hu, "Cobalt(II) dicarboxylate-based metal-organic framework for long-cycling and high-rate potassium-ion battery anode", *Electrochimica Acta*, vol. 253, pp. 439–444, 2017.
- [185] R. Wu, X. Qian, K. Zhou, J. Wei, J. Lou, and P. M. Ajayan, "Porous spinel $Zn_xCo_{3-x}O_4$ hollow polyhedra templated for high-rate lithium-ion batteries", *ACS Nano*, vol. 8, n° 6, pp. 6297–6303, 2014.
- [186] Z. Li and L. Yin, "Sandwich-like reduced graphene oxide wrapped MOF-derived $ZnCo_2O_4$ - ZnO - C on nickel foam as anodes for high performance lithium ion batteries", *J. Mater. Chem. A*, vol. 3, n° 43, pp. 21569–21577, 2015.
- [187] A. Banerjee, V. Aravindan, S. Bhatnagar, D. Mhamane, S. Madhavi, and S. Ogale, "Superior lithium storage properties of α - Fe_2O_3 nano-assembled spindles", *Nano Energy*, vol. 2, n° 5, pp. 890–896, 2013.
- [188] J. Zheng *et al.*, "Lewis acid–base interactions between polysulfides and metal-organic framework in lithium sulfur batteries", *Nano Lett.*, vol. 14, n° 5, pp. 2345–2352, 2014.
- [189] R. Demir-Cakan *et al.*, "Cathode composites for Li–S batteries via the use of oxygenated porous architectures", *J. Am. Chem. Soc.*, vol. 133, n° 40, pp. 16154–16160, 2011.
- [190] Z. Zhao, S. Wang, R. Liang, Z. Li, Z. Shi, and G. Chen, "Graphene-wrapped chromium-MOF(MIL-101)/sulfur composite for performance improvement of high-rate rechargeable Li–S batteries", *J. Mater. Chem. A*, vol. 2, n° 33, pp. 13509–13512, 2014.
- [191] H. Wang *et al.*, "Graphene-wrapped sulfur particles as a rechargeable lithium-sulfur battery cathode material with high capacity and cycling stability", *Nano Lett.*, vol. 11, n° 7, pp. 2644–2647, 2011.
- [192] J. Zhou *et al.*, "Rational design of a metal–organic framework host for sulfur storage in fast, long-cycle Li–S batteries", *Energy Environ. Sci.*, vol. 7, n° 8, pp. 2715–2724, 2014.
- [193] X. Yang, Y. Yu, N. Yan, H. Zhang, X. Li, and H. Zhang, "1-D oriented cross-linking hierarchical porous carbon fibers as a sulfur immobilizer for high performance lithium-sulfur batteries", *J. Mater. Chem. A*, vol. 4, n° 16, pp. 5965–5972, 2016.
- [194] X. Hu, Z. Zhu, F. Cheng, Z. Tao, and J. Chen, "Micro-nano structured Ni-MOFs as high-performance cathode catalyst for rechargeable Li- O_2 batteries", *Nanoscale*, vol. 7, n° 28, pp. 11833–11840, 2015.
- [195] W. Yan, Z. Guo, H. Xu, Y. Lou, J. Chen, and Q. Li, "Downsizing metal–organic frameworks with distinct morphologies as cathode materials for high-capacity Li- O_2 batteries", *Mater. Chem. Front.*, vol. 1, n° 7, pp. 1324–1330, 2017.
- [196] W. Yan, Z. Guo, H. Xu, Y. Lou, J. Chen, and Q. Li, "Downsizing metal–organic frameworks with distinct morphologies as cathode materials for high-capacity Li- O_2 batteries", *Mater. Chem. Front.*, vol. 1, n° 7, pp. 1324–1330, 2017.
- [197] M. Yuan *et al.*, "Ultrathin two-dimensional metal-organic framework nanosheets with the inherent open active sites as electrocatalysts in aprotic Li- O_2 Batteries", *ACS Appl. Mater. Interfaces*, vol. 11, n° 12, pp. 11403–11413, 2019.

- [198] Q. Li *et al.*, "Graphene/graphene-tube nanocomposites templated from cage-Containing metal-organic frameworks for oxygen reduction in Li-O₂ Batteries", *Adv. Mater.*, vol. 26, n° 9, pp. 1378–1386, 2014.
- [199] G. Tan *et al.*, "Toward highly efficient electrocatalyst for Li-O₂ batteries using biphasic N-Doping cobalt@graphene multiple-capsule heterostructures", *Nano Lett.*, vol. 17, n° 5, pp. 2959–2966, 2017.
- [200] R. Zhao, Z. Liang, R. Zou, and Q. Xu, "Metal-organic frameworks for batteries", *Joule*, vol. 2, n° 11, pp. 2235–2259, 2018.
- [201] Z. Lyu *et al.*, "3D-printed MOF-derived hierarchically porous frameworks for practical high-energy density Li-O₂ batteries", *Adv. Funct. Mater.*, vol. 29, n° 1, p. 1806658, 2019.
- [202] W. Yin, Y. Shen, F. Zou, X. Hu, B. Chi, and Y. Huang, "Metal-organic framework derived ZnO/ZnFe₂O₄ /C nanocages as stable cathode material for reversible lithium-oxygen batteries", *ACS Appl. Mater. Interfaces*, vol. 7, n° 8, pp. 4947–4954, 2015.

Chapter II. Experimental procedures

This chapter is dedicated to the description of experimental procedures. We will first describe the synthesis processes used for the preparation of the MOF materials (solvothermal, microwave-assisted, or reflux methods). The electrochemical procedures will then be described in detail (from the preparation of electrodes and electrolyte until the electrochemical measurements). Then the dedicated apparatus used for the structural and physical characterizations of MOF powders and *ex situ* characterizations for electrodes will be presented.

The syntheses of MIL-53 materials and the corresponding structural / physical characterizations (XRD, BET, TGA and SEM) involved in this PhD work were performed in collaboration with Vanessa Pimenta at ESPCI.

II.1 Synthesis routes

Conventional solvothermal synthesis is one of the most popular methods to obtain Metal-Organic Framework (MOF) solids [1]. Alternatively, they can be prepared also with other methods, including microwave-assisted, ambient pressure, ionic liquids, mechanochemistry, ultrasound, electrochemistry methods, *etc.* [2].

The list of the chemical products used during this work is reported in Appendix 1. All chemicals were used as received without any purification.

II.1.1. Conventional solvothermal synthesis

The solvothermal synthesis of MOF materials consists of mixing metal precursors (acetate, chloride, or nitrate salts) and organic linkers with a solvent (deionized water, alcohols, pyridine, dimethylformamide ...). When water is used as solvent, the synthesis method is rather designated by the term hydrothermal synthesis. The inorganic/organic precursor mixture was introduced inside a Teflon liner and sealed in a stainless-steel autoclave (Figure II-1). When the autoclave was heated at moderate temperatures (80°C - 250°C), an autogenous high vapor pressure was generated, leading to crystalline powders. This commercial autoclave (also called Parr® Acid Digestion Vessel) is designed to prevent leakage thanks to the Teflon liner and to burst safely if the pressure in the liner becomes too high.

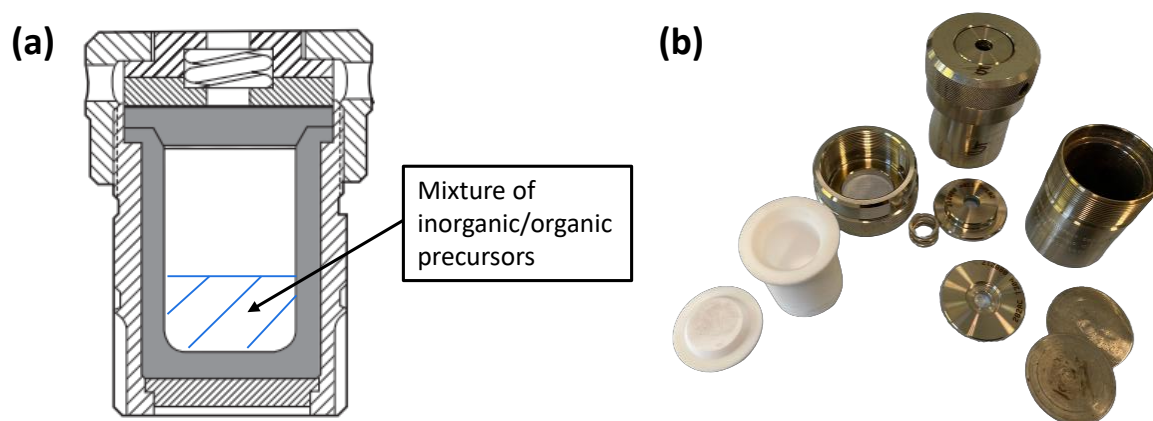


Figure II-1 : (a) Longitudinal schematic representation of a 4749-type Parr Teflon-lined autoclave assembly, and (b) a photograph of the Teflon container together with stainless-steel vessel (Parr Instrument Co.).

The composition and crystallinity of the final MOF depend on various parameters: nature of solvents and precursors (nitrate or chloride for metal salts), inorganic / organic materials ratio, pH of the reaction, temperature, *etc.* [3]–[10]. Figure II-2 lists the synthesis parameters of three well-known MOF materials by varying the solvent or the temperature.

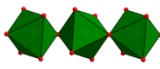
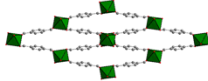
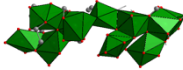
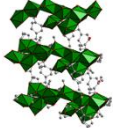
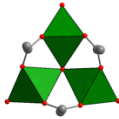
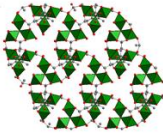
MOF	Synthesis conditions	SBU	Structure
MIL-53	Metal nitrate / 1,4-BDC / HF / H ₂ O 1:1:1:278 220°C 72 h		
MIL-85	Metal acetate / 1,4-BDC / NaOH / MeOH 1:3:1.5:1000 90°C 96 h		
MIL-88B	Metal nitrate / 1,4-BDC / HF/pyridine / H ₂ O 1:1:1:19:139 220°C 96 h		

Figure II-2 : MOF materials synthesized with solvothermal method and the related parameters [9], [11], [12].

II.1.2. Microwave-assisted solvothermal method

In the case of microwave-assisted synthesis, the inorganic/organic mixture is introduced into a Teflon vessel and heated at an intermediate temperature (up to 250°C), as in the conventional solvothermal method. However, in the microwave irradiation (microwave power in the few hundred Watt range), the heating of the starting mixture is generated by the use of the high-frequency wave. The heating mechanism can be explained by two processes: dipolar polarization and ionic conductivity. The nucleation process is favored instead of the growth of crystals as in the conventional route. This leads to short reaction times and therefore smaller particles than the conventional solvothermal route. Few minutes are sufficient to perform reactions which require several hours with conventional heating. Compared to the solvothermal synthesis, the microwave-assisted synthesis benefits also from an increased product yield and is a more energy-efficient process [13]–[15].

Figure II-3 presents the microwave Mars 6 synthesizer equipment used at ESPCI together with the multiple Teflon-lined vessels, where the sample temperature is probe-controlled [16].



Figure II-3 : Photograph of a single Teflon-lined reaction vessel (EasyPrep Plus) and the microwave synthesizer Mars 6 equipped with multiple vessels (Copyright CEM Corporation).

II.1.3. Reflux synthesis

Compared with the conventional solvothermal synthesis, the reflux synthesis – also called bottom-flask synthesis – benefits from better reproducibility, better safety (lower synthesis temperature and atmospheric pressure), and the possibility to scale up the synthesis in order to produce several kilograms of powder [17].

The initial inorganic / organic precursors were introduced in a round-bottom flask. A continuous stirring of precursor mixture was applied during the synthesis which limits the particle growth. Also, the inorganic / organic mixture could be heated at a moderate temperature at atmospheric pressure.

Figure II-4 illustrates the longitudinal schematic representation of the experimental setup. A three-necked round-bottom flask equipped with a thermometer and a water-cooled condenser was placed over a heating mantle with stirrer. The synthesis was carried out under stirring at room pressure and a thermo-controlled water circulator was connected to the condenser to maintain a 20°C-water-cooling of the condenser during the synthesis. To better isolate the system, we covered the area of the round-bottom flask exposed to the air with aluminum paper.

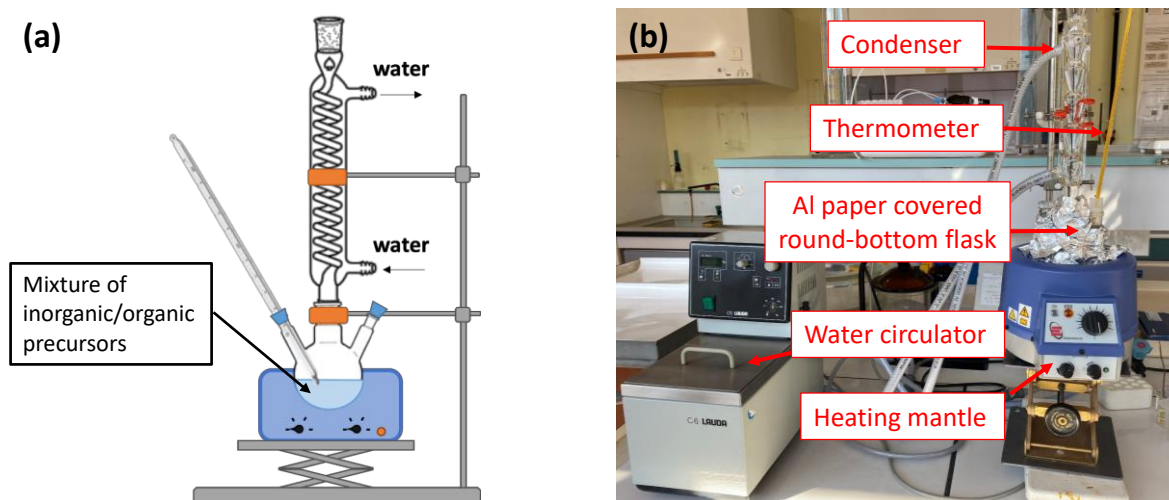


Figure II-4 : (a) Schematic representation of the reflux synthesis. (b) Photograph of the experimental reflux synthesis setup equipped with a water circulator (Lauda C6 CS). The round flask is covered with aluminum paper for better temperature isolation.

II.2 Electrochemical characterization

The ideal operating environment of practical Li-air batteries is ambient atmosphere, in which oxygen is the main contributing gas for the battery. However, some components of air, such as carbon dioxide, water, are also reactive with lithium. To avoid unnecessary parasitic reactions and the formation of byproducts, we performed the experiments with pure and dry O_2 . In this case, the tested batteries were hereafter denoted as Li- O_2 batteries.

The electrochemical parameters related to the air cathode, including the mass loading, current density, and capacity, are expressed herein gravimetrically with respect to the mass of MOF and C_{sp} . This implies that values reported in " mg/cm^2 ", " mA/g ", and " mAh/g " correspond to values in " $g_{(MOF+C)}/cm^2$ ", " $mA/g_{(MOF+C)}$ ", " $mAh/g_{(MOF+C)}$ " respectively.

II.2.1. Preparation of electrodes and electrolyte

II.2.1.1. Preparation of air cathode

An ideal air cathode for the aprotic Li- O_2 batteries needs to provide a good electronic conductivity, be porous to allow gas flow and to host discharge products. The porous air cathode is usually made up in the form of an ink printed on the current collector. The ink consists of a porous active material, carbon, and an appropriate solvent that dissolves a binder. The active material provides the porosity and acts as a potential catalyst for electrochemical reactions. Carbon is also porous but more importantly ensures a good electronic conductivity of the air cathode. Finally, the binder ensures the triple connection among powder components and also a good adhesion for the ink on the current collector. This later plays also a role in the diffusion of gas through the air cathode.

Figure II-5 illustrates a schematic representation of the MOF / carbon / PVDF composite air cathode used in this thesis. The mixture of porous MOF, carbon, and PVDF was deposited on the gas diffusion current collector. In this work, porous air cathodes were prepared by drop-casting the ink of MOF material, carbon black Super P (noted hereafter C_{sp}), and polyvinylidene fluoride (PVDF, Kynar 2801) mixed in N-methyl-2-pyrrolidone (NMP) over Toray carbon paper discs. Two formulations (expressed with respect to the weight ratio (wt. %)) for MOF / C_{sp} / PVDF electrodes were investigated in this work:

- (1) 65 / 25 / 10 wt. % of MOF / C_{sp} / PVDF;
- (2) 40 / 40 / 20 wt. % of MOF / C_{sp} / PVDF, which was the formulation reported in Li's work on MOF cathodes in Li-O₂ batteries [18].

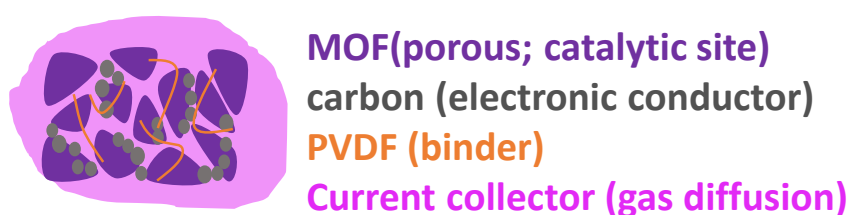


Figure II-5 : Schematic representation of MOF/carbon/PVDF composite air cathodes.

The porous air cathodes were prepared with a standardized procedure in order to ensure a good reproducibility between electrodes:

1. A suitable mass of PVDF was dissolved in around 600 μ L of NMP for 24 h at ambient temperature in order to get an adequate binder solution viscosity.
2. Secondly, the previous homogenous PVDF@NMP solution was mixed together with the anhydrous MOF and the C_{sp} powder in a 1.5 mL-Eppendorf equipped with stainless steel balls inside of the Ar glove box. These elements were then mixed using a vibratory grinding mixer (Mixer Mill MM400, Retsch) at 20 Hz for 10 minutes.
3. Thirdly, the homogenous ink was drop-casted vertically 2-3 cm in height over the \varnothing 18 mm Toray carbon discs (Figure II-6). We optimized the ink volume deposited for individual electrode with respect to the ink formulation in order to obtain a fully covered neat disc. Injected volumes of 100 μ L and 200 μ L were moderated for the 65 / 25 / 10 wt.% and 40 / 40 / 20 wt. % ink formulation for each electrode, respectively. Air cathodes were prepared one by one before use.

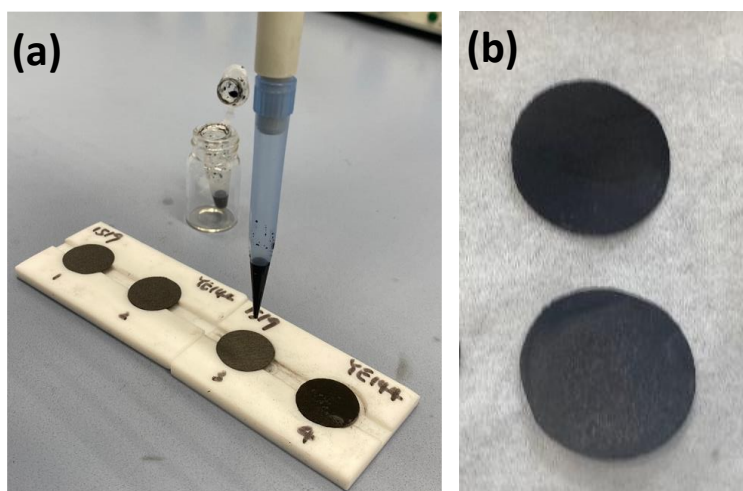


Figure II-6 : (a) Photograph of the drop-casting procedure. The support rack with cavity is used to hold individually Toray carbon discs. The micropipette filled with ink is held vertically 2-3 cm in height above the disc. (b) Photographs of the two sides of the dried MIL-53(Al) electrodes. Top: front side; Bottom: back side.

4. To prevent material loss while evaporating the NMP solvent, it was necessary to dry first the electrodes in ambient air for several hours (2-3 h) at 80°C on a heating plate so as to remove the majority of NMP. The wet electrodes were then dried under vacuum (Diaphragm Vacuum Pump Vaccubrand MD 1C) in a Büchi oven (Büchi Glass Oven B-585) at 80°C for 24 h. Then, the dried electrodes were transferred into the Ar glove box (Jacomex, H₂O < 1ppm) without any air exposure before further use.

The mass loading of MOF and C_{sp} per electrode was targeted at around 1 mg/cm².

For comparison with MOF electrodes, pure C_{sp} electrodes were also prepared as the procedure described above by replacing the MOF content with the C_{sp}, i.e. two formulations of C_{sp} / PVDF in respect of 90 / 10 wt. % and 80 / 20 wt. %.

II.2.1.2. Preparation of electrolyte

The electrolyte used for testing the Li-O₂ battery-cells was a solution of 1 M lithium bis(trifluoromethanesulfonyl)imide (LiTFSI) in 1,2-dimethoxyethane (DME). The commercial LiTFSI salt was dried at 150°C overnight under vacuum in a Büchi oven before the preparation of the electrolyte inside of the Ar glove box, while the commercial anhydrous DME was used without further treatment. The LiTFSI was quickly dissolved in DME inside of an Al bottle by hand-shaking. The electrolyte was then stored inside the Ar glove box without any exposure to the air atmosphere.

The water content of the electrolyte was measured with an automated Karl Fisher titrator (CEA/LISCEN): the amount of water in the electrolyte is 5 ppm.

II.2.2. Battery assembly

ECC-Air metal-oxygen electrochemical test cells (Figure II-7) were purchased from EL-CELL GmbH (Germany). Cells were assembled inside of the glove box under the Ar atmosphere containing less than 1 ppm of H₂O. The ECC-Air cell was dried in the oven for 2 h at 100°C before assembly. Figure II-7 (a) illustrates the schematic representation of the main components of the Li-O₂ battery assembly. The anode consisted of a Ø18 mm Li metal foil, and the porous air cathode was prepared as described previously in section II.2.1.1. The two electrodes were separated by two Ø18 mm electrolyte-impregnated glass fiber separators (Whatman glass microfiber filters, grade GF/A).

Figure II-7 (b) shows the disassembled parts of an ECC-Air test cell. This test cell consists mainly of a lid and a hollow base both in stainless steel, which ensures the electrical conduction between the potentiostat and the cell. In order to avoid short circuit issues, a cylindrical isolating sleeve is fixed inside the hollow base through a locking ring. Then we put inside the hollow base from the bottom to the top the Li anode, two electrolyte-impregnated separators (20 drops of electrolyte per cell), the porous air cathode, and a stainless steel perforated plate. Before covering the lid over the base, a stainless steel plunger and a golden spring were loaded successively over the perforated plate, which ensures the electrical conduction between the lid and the cathode and a suitable mechanical pressure in the cell once entirely mounted, respectively. Furthermore, an isolating seal inserted between the lid and the base ensured the tightness of the cell. The channel-containing lid was fitted from the side with two gas tubes with valves and below with a hollow isolating siphon, allowing a gas flow inside the cell. Eventually, the stacked assembly was tightly sealed with the help of a bracket with a wing nut before being taken out of the Ar glove box for testing.

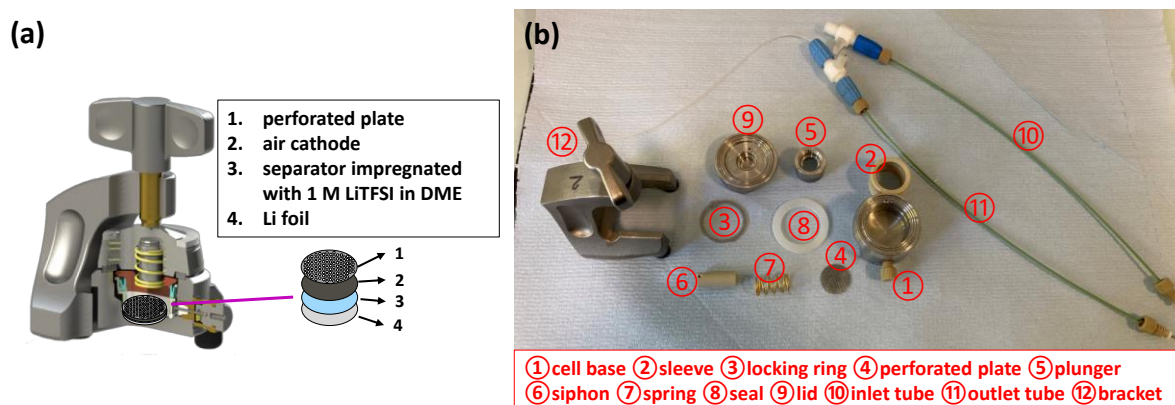


Figure II-7 : (a) Schematic representation of the Li-O₂ battery assembly. (b) Photograph of the unmounted Li-O₂ test cell.

After assembly, the tightened Li-O₂ cell was transported to an O₂-filling station (Figure II-8), and purged with pure and dry O₂ at 0.3 bar for 5 min using Omnifit[®] connectors. To obtain a slightly positive pressure inside the cell, the gas-inlet was maintained open for 10 s while the outlet was closed.

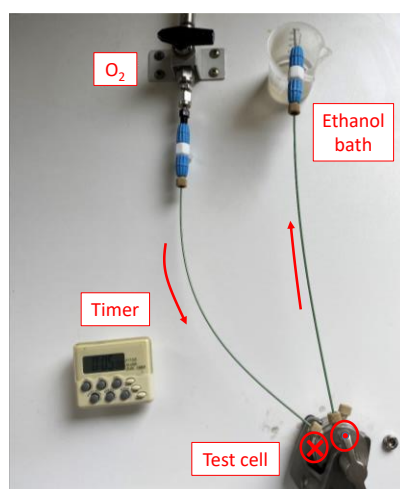


Figure II-8 : Oxygen-filling station showing the direction of the O_2 flow for the Li- O_2 battery.

II.2.3. Galvanostatic cycling with potential limitation

Galvanostatic cycling with potential limitation (GCPL) is a common electrochemical characterization method in the field of batteries. By using GCPL, the electrochemical characteristics of a battery, such as discharge / charge capacity, cycling stability, etc. are determined from the cycling profiles.

In this method, the current applied between the cathode and the anode is fixed at the same value but in the opposite direction for the discharge and charge regimes, while the potential is limited. A negative current is applied for the discharge while a positive current is applied for the charge. Figure II-9 represents a typical discharge-charge cycling profile of a battery at a fixed current. Both the discharge and the charge processes are characterized by potential plateaus at which the redox reactions occur.

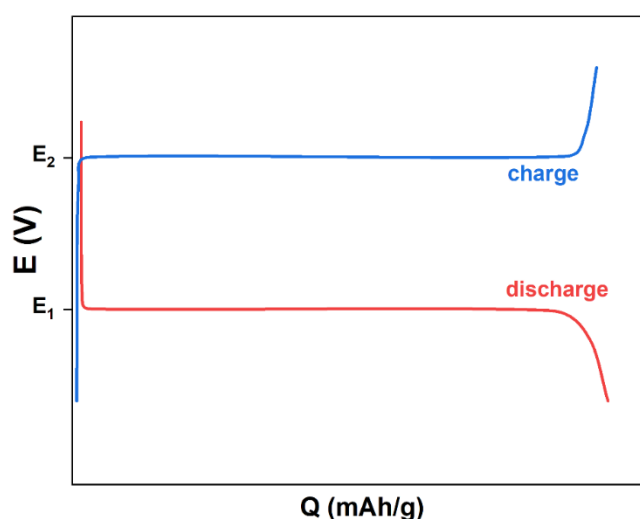


Figure II-9 : Schematic representation of the GCPL discharge-charge cycling profile for a battery at a constant current. The profile is characterized by a discharge potential (E_1) and a charge potential (E_2).

In this work, we allowed the O₂-filled cells to rest for 6 h at open circuit for the O₂ dissolution in the electrolyte as well as the impregnation of electrolyte in the air cathode before any GCPL test was performed. The electrochemical tests were carried out with a BioLogic VMP3 multichannel potentiostat. Galvanostatic discharge and charge cycling was applied at a current density of 50 mA/g between 2.0 V and 4.5 V vs. Li⁺ / Li [18]–[20].

All electrochemical tests in this work were reproduced several times in order to confirm the results. For sake of clarity, the reported voltages values of Li-O₂ batteries hereafter are expressed in “V”, corresponding to “V vs. Li⁺/Li”.

II.3 Structural and physical characterizations

We applied different analysis techniques for the characterization of the MOF materials and the *ex situ* MOF air cathodes. These latter electrodes were analyzed outside of the batteries where electrochemical tests originally takes place.

II.3.1. X-ray diffraction

X-ray diffraction (XRD) is the most common technique to investigate the structural properties of materials. This technique is non-destructive. We used XRD to check firstly the crystallinity and the purity of the synthesized MOF powders and to study the breathing transitions occurring in flexible MOF materials. The identification of the discharge products on cycled electrodes was also investigated by *ex situ* XRD.

II.3.1.1. X-ray basis: X-ray/material interactions

X-ray diffraction is based on constructive interference of monochromatic X-rays in a crystalline sample. The beam is generated by an anticathode (anode) ray tube filtrated to produce monochromatic radiation and collimated towards the sample. Since atoms are ordered in three spatial directions in the crystalline solid, the interaction between the incident X-ray photons with the sample produces diffracted constructive interference when the Bragg’s law (Equation II-1) condition is satisfied:

$$n \times \lambda = 2 \times d_{hkl} \times \sin \theta \quad \text{Equation II-1}$$

The Bragg’s law relates the wavelength of electromagnetic incident radiation (λ) to the inter-reticular distance between two crystal lattice planes (d_{hkl}) and the incident radiation angle of X-ray beam (θ). An effect of diffraction of the n^{th} order due to the reflection from lattice planes can always be interpreted as a reflection of the first order from the imaginary lattice planes ($h'k'l'$) with indices $h' = nh$, $k' = nk$, and $l' = nl$ and a spacing $d_{h'k'l'} = d_{hkl}/n$ [21]. The analysis is therefore based on the variations of intensity of the emerging X-rays according to crystal lattice planes orientation. These X-rays interfere with each other, resulting in maximal intensity for particular crystallographic directions.

II.3.1.2. Apparatus and experimental setup

a. MIL-53 materials and pristine electrode analyses

X-ray diffraction of starting MOF solids were performed on a powder sample with Bruker D8 Advance diffractometer operating at 40 kV and 40 mA (ESPCI, Paris) under Cu-K α radiation ($\lambda_{K\alpha_1} = 1.5406 \text{ \AA}$, $\lambda_{K\alpha_2} = 1.5444 \text{ \AA}$, with $K\alpha_1 / K\alpha_2$ ratio = 0.5) in the Bragg-Brentano geometry ($\theta - 2\theta$ mode). Analyses were performed here with a 2θ range of $1.6^\circ - 30^\circ$, a step size of 0.02° and a step time of 71.4 s.

The studies of the breathing transition for the flexible MOF materials and the identification of MIL-53 on pristine electrode were realized with a Siemens D5000 diffractometer at INSTN (Institut National des Sciences et Techniques Nucléaires), operating at 40 kV and 40 mA under Cu-K α radiation in the $\theta - 2\theta$ mode. Analyses were performed with a 2θ range of $5^\circ - 50^\circ$, a step size of 0.04° and a step time of 3.0 s.

b. *Ex situ* MIL-53 electrode analyses

The cycled MOF cathodes were analyzed in order to identify the discharge products formed during discharge of the Li-O₂ battery which are air-sensitive.

After electrochemical tests, the cycled cells were disassembled inside of the Ar glove box. A small piece of cycled air cathode (dimension $\sim 5 \times 5 \text{ mm}^2$) was sealed between two pieces of adhesive Kapton tape (polyimide, 0.07 mm thickness) to avoid air contact (Figure II-10). For comparison, the dried MOF electrode ink was also analyzed in order to verify the presence of MOF material.

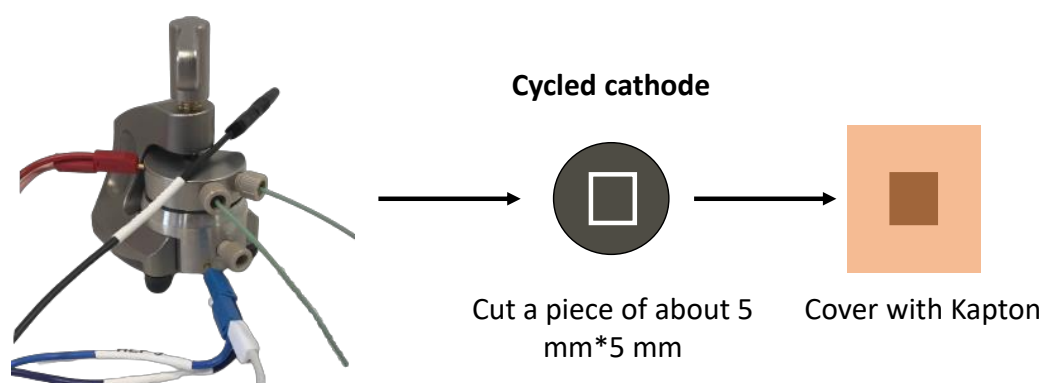


Figure II-10 : Schematic representation of *ex situ* XRD electrode sample preparation.

XRD patterns were collected using an RU-200B (Rigaku) rotating X-ray generator located at NIMBE/LAPA (CEA Saclay), equipped with a molybdenum (Mo) anode. The Mo beam was monochromatized ($\lambda_{K\alpha} = 0.70932 \text{ \AA}$) using a FOX-2D Mo 25-25 (Xenocs). The beam with a size of $100 \mu\text{m}$ and a photon flux of around $20 - 30 \times 10^6$ photons/s was focused on the sample. The sample holder is made of several holes with a diameter of a few millimeters in an Al foil

(0.5 mm in depth). Kapton tape (polyimide, 0.07 mm thickness) covered both sides of these slots to prevent material loss. The diffracted rays (Debye-Scherrer rings) were recorded for 10 min and collected by three different detectors in transmission geometry:

- a Pilatus 300K hybrid pixel detector (Dectris) with a 2θ range of $2^\circ - 35^\circ$;
- a two-dimension image plate detector (Fuji) with a 2θ range of $2^\circ - 35^\circ$. A Molecular Dynamics STORM 820 (GE Healthcare) scanner allowed pixelating the recorded images with a resolution of $100 \times 100 \mu\text{m}^2$;
- a Rebir-70S (Cegitek) hybrid pixel array detector with a 2θ range of $2^\circ - 35^\circ$.

Classical $I = f(2\theta)$ XRD patterns were obtained after circular integration using the fit2D (version 17.006) [22] and PyFAI (version 0.20.0) softwares [23]. The phase identification was performed with the Diffrac-EVA V5 software (Bruker) incorporating the ICDD references and the Crystallography Open Database [24].

II.3.2. Thermogravimetric analysis

Thermogravimetric analysis (TGA) is a thermal analysis in which the mass of the sample is monitored over a range of temperature or time after exposing the sample to a controlled temperature ramp in a controlled atmosphere. While heating, the mass can increase due to oxidation or absorption, or decrease due to decomposition, reduction, or evaporation. The temperatures at which these processes take place allow us to know the thermal stability and the volatility or the mass of adsorbed materials of the MOFs samples.

TG analyses were carried out at ESPCI. Few milligrams of powder were placed inside of a weighing alumina crucible. The measurements were operated by the thermogravimetric analyzer (Mettler Toledo TGA/DSC 2 STAR) with an air flow of $10 \text{ cm}^3/\text{min}$. The temperature was increased from 20°C to 800°C with a heating rate of $3^\circ\text{C}/\text{min}$.

II.3.3. Brunauer-Emmett-Teller measurement

Brunauer-Emmett-Teller (BET) theory is applied for measuring the surface area and the pore volume of porous materials by measuring the amount of physically adsorbed probing gas (such as N_2 , CO_2). The most common gas used is N_2 . In this work, we performed our analysis under N_2 gas at its boiling point (77 K). At this temperature, the N_2 molecules condense on the surface of the material as the temperature of the material is below its critical point. The BET theory extends the mono-layer (Langmuir theory) to multi-layer adsorption, relating the multi-layer adsorption of probing gas molecules onto the solid surface to the gas pressure at a fixed temperature [25]. Three assumptions are considered: (a) gas molecules physically adsorb on the solid in layers infinitely; (b) different layers do not interact; (c) the Langmuir theory can be applied to each layer.

Since the N₂ molecule size is known, N₂ gas is assumed to have access to the entire surface of the solid. The amount of adsorbed gas is correlated to the total surface area of the solid. The total surface area (S_{total}) for a known mass (m) of solid and the specific BET surface area (S_{BET}) can be expressed as follows in Equation II-2 and Equation II-3:

$$S_{\text{total}} = \frac{V_0 N_a s}{M_v} \quad \text{Equation II-2}$$

$$S_{\text{BET}} = \frac{S_{\text{BET}}}{m} \quad \text{Equation II-3}$$

where V_0 is the monolayer volume of gas adsorbed at standard temperature and pressure (273K and 1 atm), N_a is the Avogadro's number, s is the cross-sectional area of the adsorbed gas and equals 0.162 nm² for an adsorbed N₂ molecule, M_v is the molar volume and equals 22414 mL [26].

In this work, we used an advanced six-port Smart VacPreP™ 067 apparatus to heat and degas (or called activate) samples at 200°C for 12 h. The N₂ adsorption isotherm of the dehydrated MOF solid samples was then measured by N₂ porosimetry using a Micromeritics Tristar II Plus instrument at 77 K and the results were analyzed with the Microactive software.

II.3.4. Scanning electron microscopy

Scanning electron microscopy (SEM) allows observing the morphology and texture of samples by scanning the sample surface with a focused electron beam which interacts with atoms in various depths of the sample. Different types of radiation can be emitted from the probed sample, such as secondary electrons, backscattered electrons, characteristic X-rays and cathodoluminescence photons, and transmitted electrons. These radiations are then collected by selective detectors and form the SEM image of the sample.

In this work, two microscopes equipped with a field emission gun and a secondary electron detector were used to observe the morphology of the MOF solids and discharge products on the cycled MOF cathodes:

- A FEI Magellan 400 equipped with Everhart-Thornley detector (ESPCI Paris), operated at 15 kV with a beam current of 50 pA, is used for the morphology characterization for the MOF solids.
- A SEM-FEG Carl Zeiss Ultra 55 equipped with InLens detector (CEA/LEDNA) was used in order to study the morphology of the discharge products on the cycled MOF electrodes. Cells were disassembled in the Ar glove box after cycling. The electrodes were quickly transferred into the microscope chamber with an exposure to air for less than two minutes. As the MOF electrodes are very sensitive to the electron beam, two beam acceleration potentials were moderated (1.5 kV and 3.0 kV) to record the SEM images.

II.3.5. X-ray photoelectron spectroscopy

X-ray photoelectron spectroscopy (XPS) is a surface-sensitive quantitative spectroscopic technique. XPS can identify the chemical elements within the given sample surface as well as their oxidation states and offers information about the chemical bonding based on the photoelectric effect. XPS analysis is based on the electron binding energy (BE) analysis by irradiating the sample with an X-ray beam. According to the kinetic energies of emitted electrons from the surface (below 50 Å [27]), the binding energy of core-level electron of each atom on the surface can be determined by using the photoelectric effect equation (Equation II-4):

$$E_{\text{binding}} = E_{\text{photon}} - (E_{\text{kinetic}} + \emptyset) \quad \text{Equation II-4}$$

where E_{binding} is the electron binding energy relative to the core-level electron, E_{photon} is the energy of the incident X-ray photon, E_{kinetic} is the kinetic energy of the electron measured by the analyzer and \emptyset is a constant of the instrument.

An XPS spectrum exhibits a number of peaks for detected electrons at specific BEs. Basically, each element could produce a set of characteristic XPS peaks. These peaks correspond to different electron configurations within the atom, 1s, 2s, 2p, 3s for instance. The number of detected electrons in each peak is directly related to the number of elements within the analyzed sample volume.

The pure MOF solid, pristine and cycled electrode samples were analyzed with XPS using a Kratos Analytical Axis Ultra DLD equipped with a monochromatic Al K α excitation (1486.7 eV) and a charge neutralizer (CEA/LISCEN).

After the electrochemical tests, we washed the cycled electrodes with few drops of DME in order to remove the remaining electrolyte. The liquid in excess was gently absorbed with a Kimtech wiper.

An isolating tape was used to fix the powder / electrode sample to avoid the overcharging with X-ray beam. The sample was loaded into the XPS apparatus without exposure to ambient air using a dedicated sample transfer vessel. All spectra were recorded with a pass energy of 40 eV.

The quantification was explored using the CasaXPS (version 2.3.23 PR1.0) software [28]. The position, width, and area of peak spectra were fitted using a Gaussian-Lorentzian (GL) fitting function [29] and a non-linear Shirley background [30]. All spectra were calibrated according to the C 1s photoemission peak of the adventitious carbon at 284.4 eV [31].

II.4 References

- [1] R. I. Walton, "Subcritical solvothermal synthesis of condensed inorganic materials", *Chem. Soc. Rev.*, vol. 31, n°4, pp. 230–238, 2002.
- [2] M. Rubio-Martinez, C. Avci-Camur, A. W. Thornton, I. Imaz, D. Maspocho, and M. R. Hill, "New synthetic routes towards MOF production at scale," *Chem. Soc. Rev.*, vol. 46, n° 11, pp. 3453–3480, 2017.
- [3] N. Stock and S. Biswas, "Synthesis of metal-organic frameworks (MOFs): routes to various MOF topologies, morphologies, and composites", *Chem. Rev.*, vol. 112, n° 2, pp. 933–969, 2012.
- [4] Y.-K. Seo, G. Hundal, I. T. Jang, Y. K. Hwang, C.-H. Jun, and J.-S. Chang, "Microwave synthesis of hybrid inorganic–organic materials including porous $\text{Cu}_3(\text{BTC})_2$ from $\text{Cu}(\text{II})$ -trimesate mixture", *Microporous Mesoporous Mater.*, vol. 119, n° 1, pp. 331–337, 2009.
- [5] G. Férey, "Hybrid porous solids: past, present, future," *Chem. Soc. Rev.*, vol. 37, n° 1, pp. 191–214, 2007.
- [6] D. Riou and G. Férey, "Hybrid open frameworks (MIL-n). Part 3 Crystal structures of the HT and LT forms of MIL-7: a new vanadium propylenediphosphonate with an open-framework. Influence of the synthesis temperature on the oxidation state of vanadium within the same structural type", *J. Mater. Chem.*, vol. 8, n° 12, pp. 2733–2735, 1998.
- [7] C. Livage, C. Egger, M. Nogues, and G. Férey, "Hybrid open frameworks (MIL-n). Part 5 Synthesis and crystal structure of MIL-9: a new three-dimensional ferrimagnetic cobalt(II) carboxylate with a two-dimensional array of edge-sharing Co octahedra with 12-membered rings", *J. Mater. Chem.*, vol. 8, n° 12, pp. 2743–2747, 1998.
- [8] S. Bauer *et al.*, "High-Throughput Assisted Rationalization of the Formation of Metal Organic Frameworks in the Iron(III) Aminoterephthalate Solvothermal System", *Inorg. Chem.*, vol. 47, n° 17, pp. 7568–7576, 2008.
- [9] S. Surblé, C. Serre, C. Mellot-Draznieks, F. Millange, and G. Férey, "A new isorecticular class of metal-organic-frameworks with the MIL-88 topology", *Chem. Commun.*, n° 3, pp. 284–286, 2006.
- [10] U. Mueller, M. Schubert, F. Teich, H. Puetter, K. Schierle-Arndt, and J. Pastré, "Metal–organic frameworks - prospective industrial applications", *J. Mater. Chem.*, vol. 16, n° 7, pp. 626–636, 2006.
- [11] C. Serre *et al.*, "Very large breathing effect in the first nanoporous chromium(III)-based solids: MIL-53 or $\text{Cr}^{\text{III}}(\text{OH})\cdot\{\text{O}_2\text{C}-\text{C}_6\text{H}_4-\text{CO}_2\}_x\{\text{HO}_2\text{C}-\text{C}_6\text{H}_4-\text{CO}_2\text{H}\}_y\text{H}_2\text{O}$ ", *J. Am. Chem. Soc.*, vol. 124, n° 45, pp. 13519–13526, 2002.
- [12] P. Serra-Crespo, E. V. Ramos-Fernandez, J. Gascon, and F. Kapteijn, "Synthesis and characterization of an amino functionalized MIL-101(Al): separation and catalytic properties", *Chem. Mater.*, vol. 23, n° 10, pp. 2565–2572, 2011.

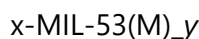
- [13] C.-M. Lu, J. Liu, K. Xiao, and A. T. Harris, "Microwave enhanced synthesis of MOF-5 and its CO₂ capture ability at moderate temperatures across multiple capture and release cycles", *Chem. Eng. J.*, vol. 156, n° 2, pp. 465–470, 2010.
- [14] C. McKinstry, E. J. Cussen, A. J. Fletcher, S. V. Patwardhan, and J. Sefcik, "Scalable continuous production of high quality HKUST-1 via conventional and microwave heating", *Chem. Eng. J.*, vol. 326, pp. 570–577, 2017.
- [15] J. Gordon, H. Kazemian, and S. Rohani, "Rapid and efficient crystallization of MIL-53(Fe) by ultrasound and microwave irradiation", *Microporous Mesoporous Mater.*, vol. 162, pp. 36–43, 2012.
- [16] "iWave." <https://cem.com/iwave>.
- [17] J. Kim, S.-H. Kim, S.-T. Yang, and W.-S. Ahn, "Bench-scale preparation of Cu₃(BTC)₂ by ethanol reflux: synthesis optimization and adsorption/catalytic applications", *Microporous Mesoporous Mater.*, vol. 161, pp. 48–55, 2012.
- [18] D. Wu *et al.*, "Metal-organic frameworks as cathode Materials for Li-O₂ Batteries", *Adv. Mater.*, vol. 26, n° 20, pp. 3258–3262, 2014.
- [19] X. Guo and N. Zhao, "The role of charge reactions in cyclability of lithium-oxygen Batteries", *Adv. Energy Mater.*, vol. 3, n° 11, pp. 1413–1416, 2013.
- [20] B. M. Gallant, D. G. Kwabi, R. R. Mitchell, J. Zhou, C. V. Thompson, and Y. Shao-Horn, "Influence of Li₂O₂ morphology on oxygen reduction and evolution kinetics in Li-O₂ batteries", *Energy Environ. Sci.*, vol. 6, n° 8, pp. 2518–2528, 2013.
- [21] D. D. Le Pevelen, "Small molecule X-Ray crystallography, theory and workflow", in *Encyclopedia of Spectroscopy and Spectrometry (Second Edition)*, J. C. Lindon, Ed. Oxford: Academic Press, pp. 2559–2576, 2010..
- [22] A. P. Hammersley, S. O. Svensson, M. Hanfland, A. N. Fitch, and D. Hausermann, "Two-dimensional detector software: From real detector to idealised image or two-theta scan", *High Press. Res.*, vol. 14, n° 4–6, pp. 235–248, 1996
- [23] J. Kieffer and D. Karkoulis, "PyFAI, a versatile library for azimuthal regrouping", *J. Phys. Conf. Ser.*, vol. 425, n° 20, p. 202012, 2013.
- [24] S. Gražulis *et al.*, "Crystallography Open Database – an open-access collection of crystal structures", *J. Appl. Crystallogr.*, vol. 42, n° 4, Art. n° 4, 2009.
- [25] S. Brunauer, P. H. Emmett, and E. Teller, "Adsorption of gases in multimolecular layers", *J. Am. Chem. Soc.*, vol. 60, n° 2, pp. 309–319, 1938.
- [26] "BET surface area analysis of nanoparticles", *Chemistry LibreTexts*, 13, 2016.
- [25] S. Brunauer, P. H. Emmett, and E. Teller, "Adsorption of gases in multimolecular layers", *J. Am. Chem. Soc.*, vol. 60, n° 2, pp. 309–319, 1938.

- [26] "BET surface area analysis of nanoparticles", *Chemistry LibreTexts*, 13, 2016.
- [27] H. Bryngelsson, M. Stjerndahl, T. Gustafsson, and K. Edström, "How dynamic is the SEI?," *J. Power Sources*, vol. 174, n° 2, pp. 970–975, 2007.
- [28] "CasaXPS Software." <http://www.casaxps.com>.
- [29] "Line Shapes." http://www.casaxps.com/help_manual/line_shapes.htm.
- [30] "Peak Fitting in XPS."
http://www.casaxps.com/help_manual/manual_updates/peak_fitting_in_xps.pdf<http://www.casaxps.com>
- [31] K. N. Wood and G. Teeter, "XPS on Li-battery-related compounds: analysis of inorganic SEI phases and a methodology for charge correction", *ACS Appl. Energy Mater.*, vol. 1, n° 9, pp. 4493–4504, 2018.

Chapter III. Synthesis and characterizations

We will present in this chapter the synthesis and the characterizations of two analogues of the flexible MIL-53 materials. MIL-53(Al) was synthesized using two methods: conventional hydrothermal and microwave-assisted hydrothermal syntheses, while MIL-53(Fe) was obtained through reflux synthesis. These materials were characterized by different techniques, including XRD, TGA, BET, and SEM. The last section will be devoted to the study of the flexibility of both MIL-53 when impregnated with the solvents used for the Li-O₂ electrochemical tests.

Reminder for readers: for sake of clarity, the MIL-53s were studied under various experimental conditions. As the denomination of this flexible material diverges according to the authors, a nomenclature inspired by the existing one is defined for this work. The general formula for these materials is defined as:



where $x = \text{H, MW, or R}$ indicates the synthesis method, $M = \text{Al or Fe}$, and y represents the guest molecule inside of the pores, such as BDC, H_2O , DMF, or empty when no molecules fill the pores. For example, the $\text{H-MIL-53(Al)}_{\text{empty}}$ formula represents the anhydrous form of hydrothermal synthesized MIL-53(Al), the $\text{R-MIL-53(Fe)}_{\text{DMF}}$ formula represents the reflux synthesized MIL-53(Fe) with pores occupied by DMF. $\text{H-MIL-53(Al)}_{\text{PVDF@NMP}}$, $\text{H-MIL-53(Al)}_{\text{PVDF}}$, $\text{H-MIL-53(Al)}_{\text{empty}}$ designate the MIL-53(Al) solid synthesized through the hydrothermal route when the pores are filled with the PVDF@NMP, with the PVDF (we suppose that the NMP molecules are removed after drying) and when the pores are empty, respectively.

However, we will keep the notation of the literature when we will describe the state of the art of the flexibility occurring in the isoreticular MIL-53 materials *i.e.* HT (high temperature) and LT (low temperature) to designate the anhydrous solid – without solvent molecules in the pores – and fully hydrated solid (free water molecules in the pores).

III.1 The flexibility of MIL-53

As mentioned in Chapter I, the MIL-53(Cr) was the first MIL-53 compound reported in the literature [1]. The structure consists of infinite corner-sharing metal chains of $\text{CrO}_4(\text{OH})_2$ octahedra bridged by the linear organic linker (benzene-1,4-dicarboxylic acid or BDC), which results in large lozenge-shaped channels (Figure III-1). In response to adsorption of gas/solvent molecules or temperature, the structure evolves: the low temperature form (MIL-53(Cr)_{LT} , the solid is fully hydrated) presents a contracted or “closed” pore, while in the high temperature form (MIL-53(Cr)_{HT}), the pores are open.

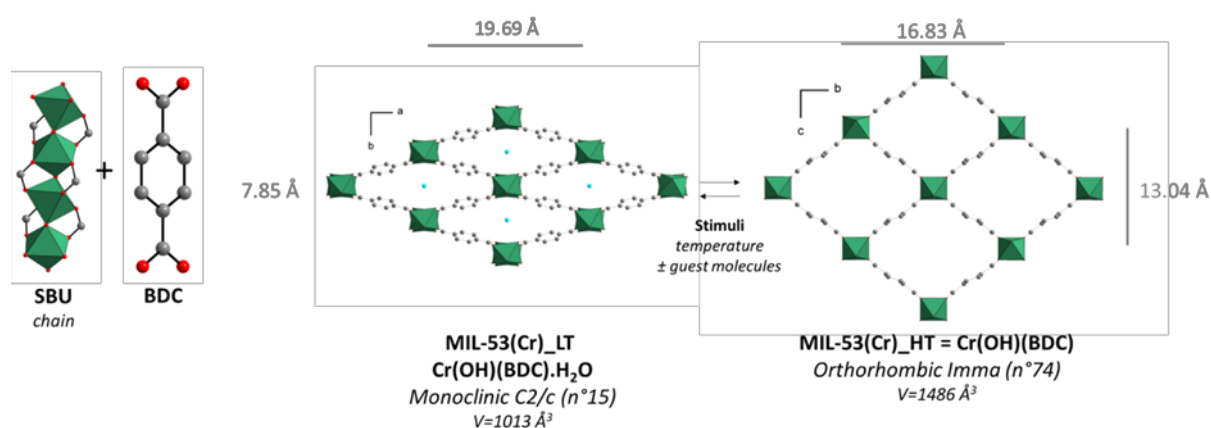


Figure III-1 : Representation of the breathing effect of MIL-53(Cr). View of the pore system upon hydration/dehydration.

Until now, isorecticular solids with a wide variety of metal cations (Al, In, Fe, Ga, Sc ...) and functional ligands (-NH₂, NO₂, F...) have been investigated [2]. Similar structures are observed with different cation valence, the neutrality of the framework being compensated by the bridging group shared by the metal octahedra (μ_2 -O, μ_2 -OH, or DMF) (Figure III-2).

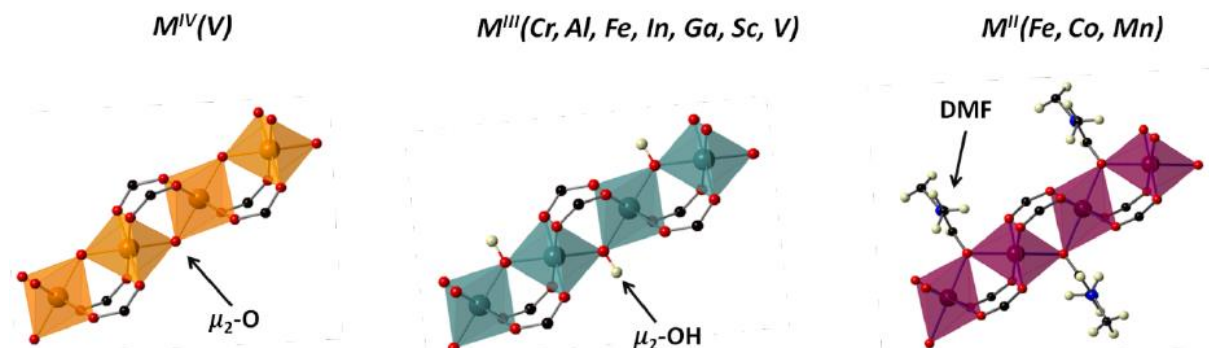


Figure III-2 : Representation of different groups bridging the cations in the metal chains of MIL-53 depending on metal valence states (tetravalent, trivalent, bivalent). Reprinted from [3].

Except for the vanadium analogue (also called MIL-47) [2], the breathing effect is observed for all MIL-53 analogues. However, the nature of the metal influences drastically the breathing behavior. Férey and Serre demonstrated that the hydroxyl groups (μ_2 -OH) play a role in the flexibility [4]. The rigidity of MIL-47(V) can be explained by the presence of a μ_2 -O instead of a μ_2 -OH [5]. The breathing magnitude depends mainly on the existence of weak points (here the connections between the inorganic chains and the carboxylate groups) which allow the flexibility by a possible rotation around the O-O axis of the two plans O-Cr-Cr-O and O-C-O (Figure III-3). The guest-guest (molecules or gas inside the pores) and host-guest interactions are also decisive for the breathing behaviors.

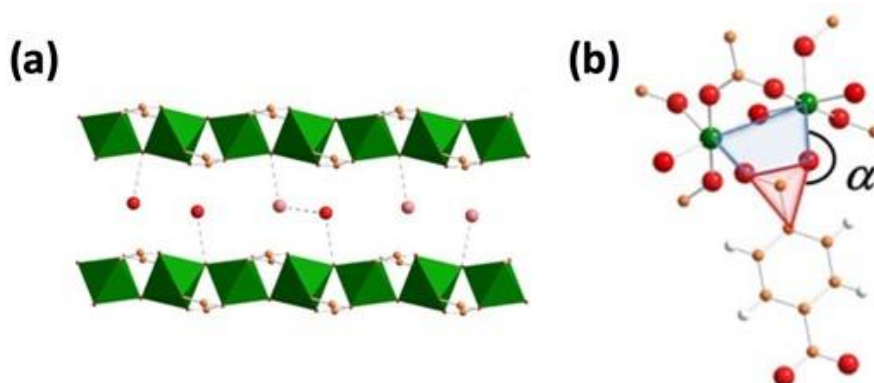


Figure III-3 : Breathing of MIL-53 (Cr) - (a) hydrogen bonding interactions between water molecules and between water molecules and the hydroxide framework. (b) Mode of connection between a dicarboxylate and Cr centers illustrating the flexible part of the structure, with α indicating the variable inter-plane angle with the dicarboxylate oxygens forming the hinge. CrO₆ octahedral are green with benzene-1,4-dicarboxylate atoms colored: oxygen red, carbon orange, hydrogen atoms white. Reprinted from [2].

The flexibility of the structure is activated by the presence of molecules inserted in the pores and the creation of weak bonds between the guest and the skeleton. Similar to the parent MIL-53(Cr), in the as-synthesized form of MIL-53 analogues, the pores (in form of tunnels) are occupied by free BDC or solvent molecules (H₂O, DMF). Simple heating at a high temperature (up to 300°C) removes the guest molecules and creates a structure (often called MIL-53_{HT}) with empty tunnels. By cooling in ambient air, the structure MIL-53_{HT} evolves to MIL-53_{LT} and the pores are filled with water molecules. The transition $HT \rightleftharpoons LT$ is fully reversible. Only the structure of the as-synthesized form for MIL-53(In) has been reported [6], but no report mentions a possible activation of the solid to obtain the form with open pores. After activation of MIL-53(Ga), a mixture of LT and HT forms persists until the point of thermal decomposition [7]. In contrast with MIL-53(Cr), the In- Ga- Sc- and Fe-analogues (MIL-53(Fe)) present another breathing transition behavior. The anhydrous forms of MIL-53(Sc) and MIL-53(Fe) show a contraction of the pore after activation (while MIL-53(Cr) presents open pores) and the pores open when guests are inserted (Figure III-4).

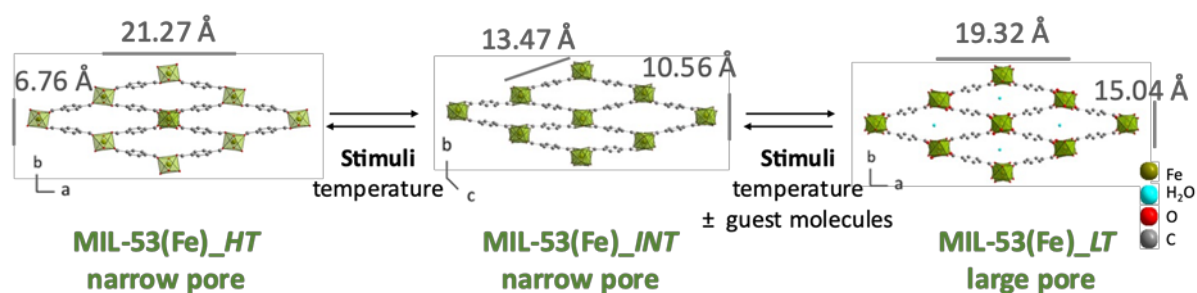


Figure III-4 : Flexibility behaviors of MIL-53(Fe).

In this work, we investigated the influence of such flexibility on the electrochemical performance of two MIL-53 analogues (MIL-53(Al) and MIL-53(Fe)). MIL-53(Al) has a similar breathing behavior to the MIL-53(Cr). The anhydrous form presents pores fully open while the pores are contracted in the presence of guest molecules (H₂O, gas, solvent molecules). Furthermore, the Al-analogue has a very high thermal stability (decomposition at ~500°C compared to ~400°C with Cr or < 350°C with Fe). In contrast, the pores of MIL-53(Fe) are open in the presence of guest molecules.

III.2 Synthesis and characterizations

III.2.1. Synthesis

Both MIL-53 samples were synthesized using previous syntheses described in the literature [8]–[10]. MIL-53(Al) solids were synthesized using two synthesis routes: conventional hydrothermal synthesis and microwave-assisted hydrothermal synthesis (H-MIL-53(Al) and MW-MIL-53(Al) respectively). The MIL-53(Fe) solid was obtained by reflux synthesis.

For each synthesis, metal precursor (aluminum nitrate nonahydrate and iron chloride hexahydrate) and organic ligand (BDC) were first mixed and prepared in water or DMF (MIL-53(Al) and MIL-53(Fe), respectively) according to the molar ratio mentioned in Figure III-5. The mixtures were then heated at 220°C for both H-MIL-53(Al) and MW-MIL-53(Al) for 72 hours or 30 minutes (hydrothermal or microwave routes), and 150°C for R-MIL-53(Fe) for 48 hours. The as-synthesized form of MIL-53 sample was filtered using a Büchner for H-MIL-53(Al) or centrifuged for MW-MIL-53(Al) and R-MIL-53(Fe) in order to separate the solid and the surfactant. In each case, the as-synthesized solids were washed several times with deionized water and dried under air.

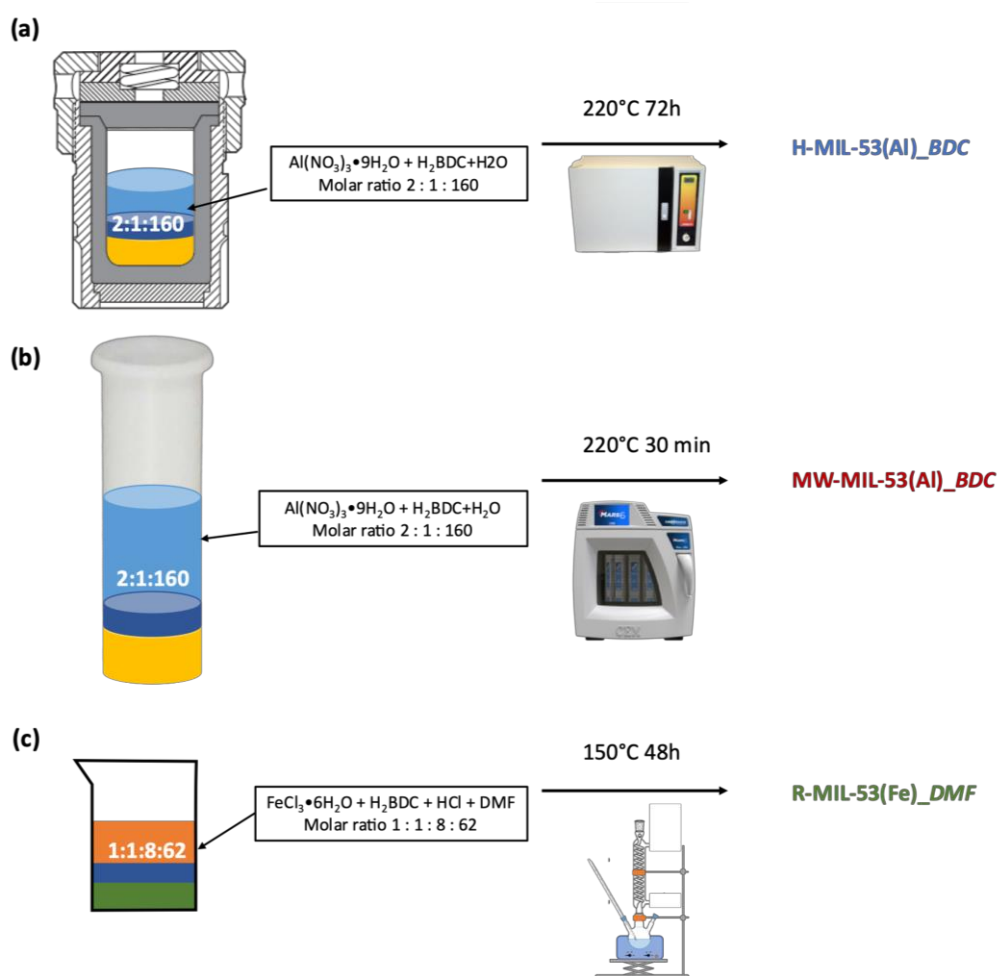


Figure III-5 : Schematic representation of (a) the synthesis of H-MIL-53(Al), (b) MW-MIL-53(Al), and (c) R-MIL-53(Fe).

III.2.2. Structure characterizations

In all as-synthesized solids, the pores are filled by benzene-1,4-dicarboxylic acid (BDC) for both MIL-53(Al), or by solvent molecules (DMF) for MIL-53(Fe) (the solids are called hereafter MIL-53(Al)_{BDC} or MIL-53(Fe)_{DMF}). MIL-53(Al) solids were heated at 360°C in order to remove the free acid and obtain the anhydrous forms MIL-53(Al)_{empty}; whereas the DMF

molecules were first exchanged by methanol molecules and then by deionized H₂O following the scheme MIL-53(Fe)_{DMF} → MIL-53(Fe)_{MeOH} → MIL-53(Fe)_{H₂O}. The anhydrous form was obtained after a heat treatment at 100°C in order to remove the water molecules inserted in the pores. However, when the solids were exposed to ambient air, they reabsorbed instantaneously water molecules, it was thus not possible to isolate the anhydrous form.

Figure III-6 shows the X-ray diffraction patterns of the as-synthesized and fully hydrated samples corresponding to the forms reported in the literature [8], [10]. As the solids reabsorbed instantaneously water molecules from ambient air, it was thus not possible to record the XRD patterns of the anhydrous forms; we obtained a mixture of MIL-53_{H₂O} and MIL-53_{empty}. By comparing the XRD of the as-synthesized phase of both MIL-53(Al), we observe an additional peak around $2\theta = 17.5^\circ$, which is more intense for the H-MIL-53(Al)_{BDC} than MW-MIL-53(Al)_{BDC} and corresponds to the free acid.

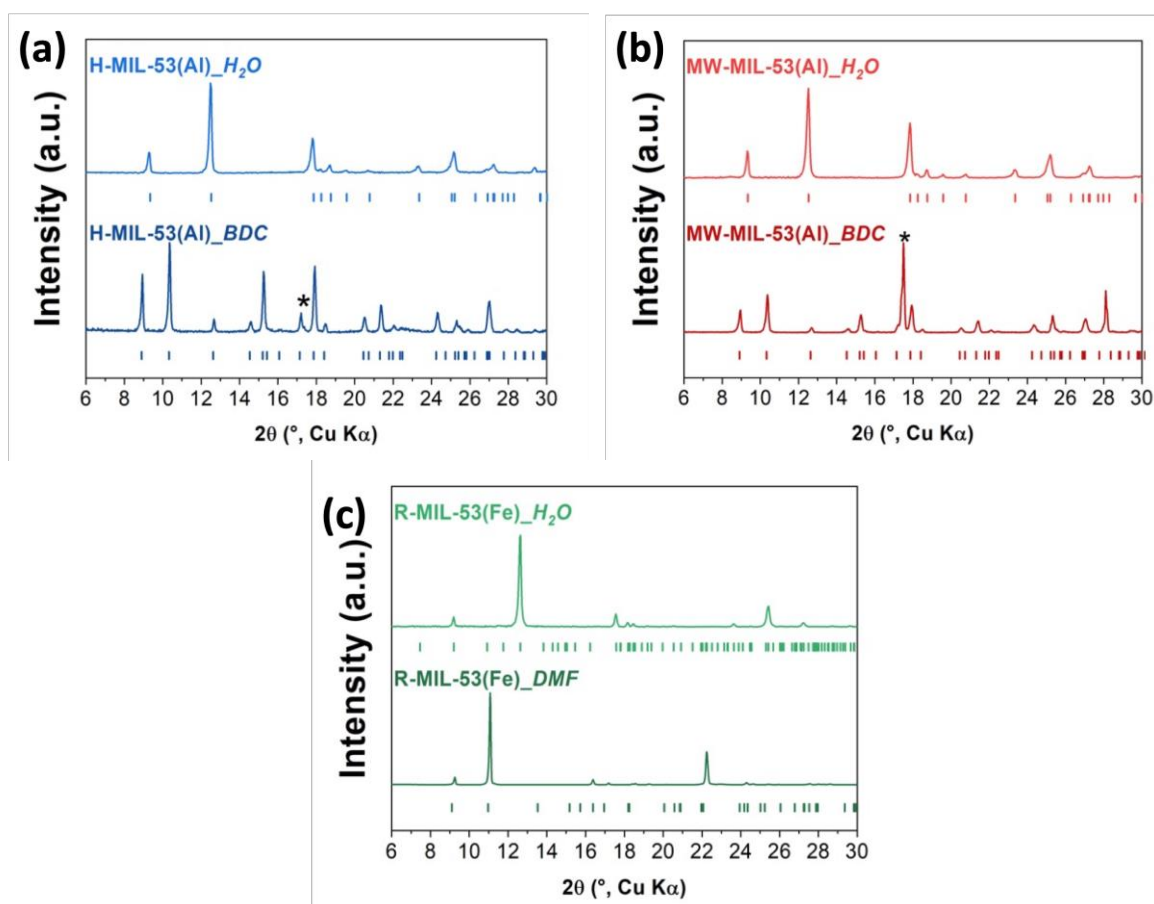


Figure III-6 : XRD patterns of MIL-53(Al)_{BDC}, MIL-53(Al)_{H₂O} for (a) H-MIL-53(Al), (b) MW-MIL-53(Al), and (c) of R-MIL-53(Fe)_{DMF} and R-MIL-53(Fe)_{H₂O}. Bragg positions of the as-synthesized and hydrated forms described in the literature are indicated by tick marks [8], [10]. The star mark indicates the presence of disordered free acid trapped inside the pores of MIL-53(Al).

TGA measurements confirm the persistence of benzene-1,4-dicarboxylic acid (BDC) or DMF molecules inserted in the pores for the as-synthesized samples (Figure III-7). Furthermore, we observe more content of BDC with the microwave route than the hydrothermal one. We have also successfully removed BDC or exchanged DMF and reabsorbed water molecules in order to obtain the fully hydrated samples.

Table III-1 gives the chemical formula of as-synthesized and hydrated forms for both MIL-53(Al) and MIL-53(Fe).

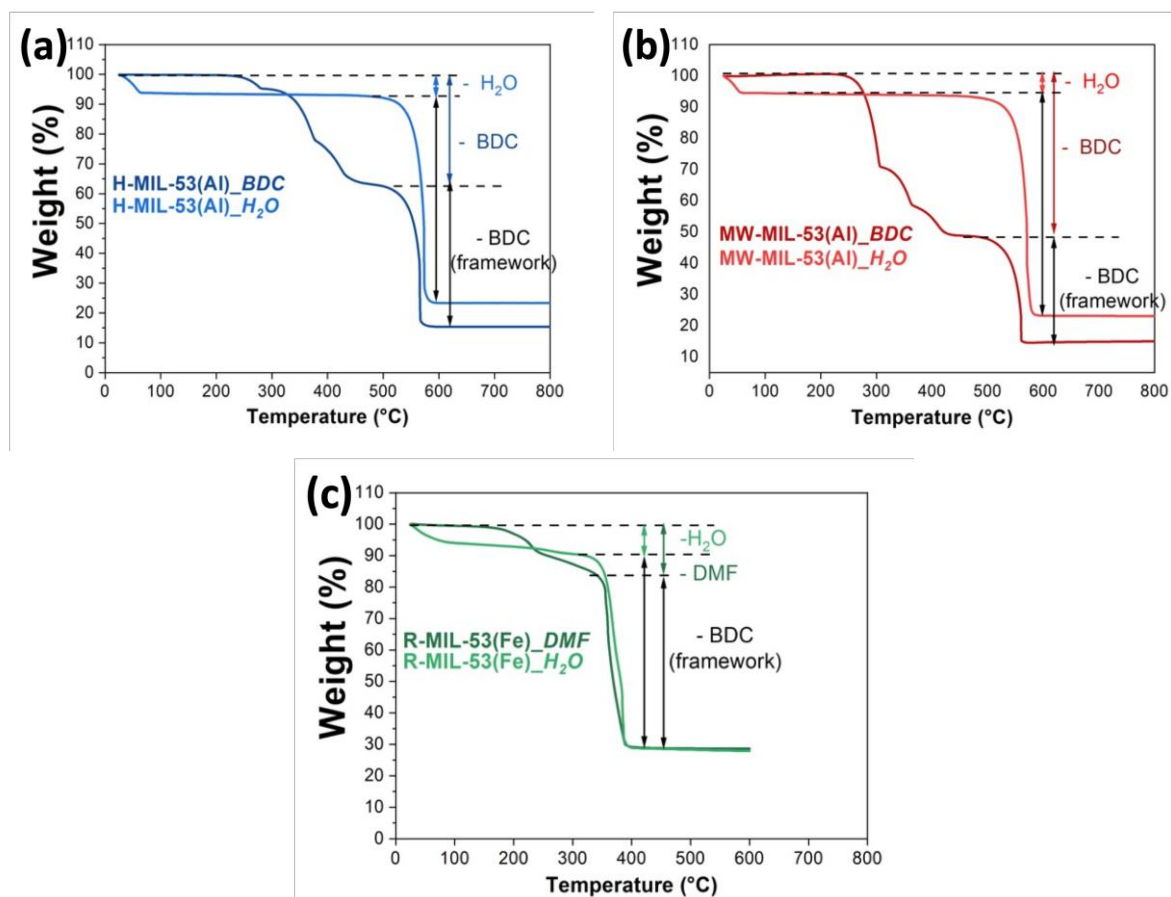


Figure III-7 TGA curves of as-synthesized and fully hydrated forms of (a) H-MIL-53(Al), (b) MW-MIL-53(Al), and (c) R-MIL-53(Fe).

Table III-1 : Experimental and calculated losses observed on TGA curves for all as-synthesized and hydrated MIL-53. We report the chemical formula deduced from these analyses.

Abbr.	H_MIL-53(Al)_BDC	MW_MIL-53(Al)_BDC	R_MIL-53(Fe)_DMF
Formula	Al(OH)(BDC)•0.7(BDC)	Al(OH)(BDC)•1.3(BDC)	Fe(OH)(BDC)•0.7(DMF) ¹
Loss 1	250-450°C – BDC pore exp. 36.6% calc. 35.9%	250-450°C – BDC pore exp. 51.5% calc. 52.1%	250-350°C – DMF pore exp. 15.8% calc. 15.6%
Loss 2	470-560°C BDC framework exp. 14.9% calc. 16.2% final product Al ₂ O ₃	470-560°C BDC framework exp. 14.3% calc. 11.9% final product Al ₂ O ₃	320-400°C BDC framework exp. 55.3% calc. 55.9% final product Fe ₂ O ₃
Abbr.	H_MIL-53(Al)_H ₂ O	MW_MIL-53(Al)_H ₂ O	R_MIL-53(Fe)_H ₂ O
Formula	Al(OH)(BDC)•0.7H ₂ O	Al(OH)(BDC)•0.7H ₂ O	Fe(OH)(BDC)•1.4H ₂ O
Loss 1	up to 100°C – H ₂ O pore exp. 6.0% calc. 5.7%	up to 100°C – H ₂ O pore exp. 5.5% calc. 5.7%	up to 100°C – H ₂ O pore exp. 9.9% calc. 9.6%
Loss 2	500°C BDC framework exp. 70.9% calc. 70.6% final product Al ₂ O ₃	500°C BDC framework exp. 71.3% calc. 70.6% final product Al ₂ O ₃	320°C BDC framework exp. 61.4% calc. 55.9% final product Fe ₂ O ₃

(1) The DMF molecules may be also coordinated to the iron octahedra if one considers the two-step of loss of DMF : $Fe(OH)_{0.67}(DMF)_{0.33}(BDC) \cdot 0.37(DMF)$.

III.2.3. Other characterizations

The morphology and particle size of MIL-53 were investigated by scanning electron microscopy (SEM) for all the hydrated samples. SEM images are illustrated in Figure III-8. Clearly, the microwave route leads to a smaller particle size than other routes (hydrothermal or reflux synthesis) due to the time involved for the synthesis (30 minutes instead of 2 or 3 days). For the H-MIL-53(Al) solid, micrometer-sized platelet crystallites are observed with an average crystal length of ~ 2 μm, while smaller pseudo-spherical crystallites with an average crystal diameter ~ 500 nm are observed for the MW-MIL-53(Al) solid, about 4-times-smaller than H-MIL-53(Al). The length-width or aspect ratio of the particles is smaller with the MW synthesis method.

As the MIL-53(Fe) samples are unstable under the electron beam irradiations, a shorter time of exposition leads also to a degradation of the MOF. However, the main particles seem to be micrometer-sized platelet crystallites like H-MIL-53(Al) with a length of 1 - 3 μm .

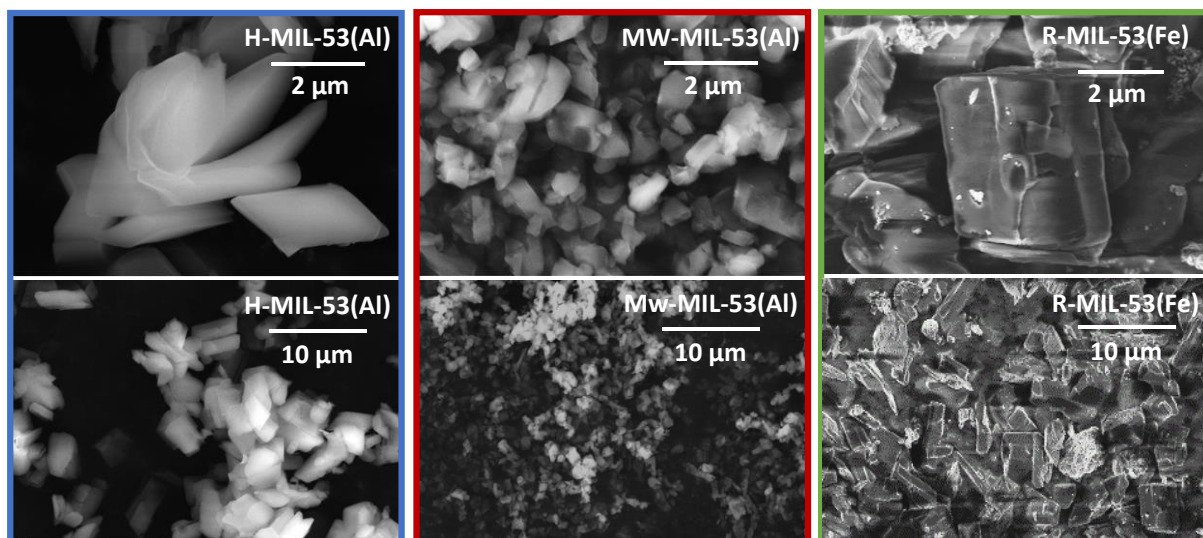


Figure III-8 : SEM images of H-MIL-53(Al)_{H₂O} (blue), MW-MIL-53(Al)_{H₂O} (red), and R-MIL-53(Fe)_{H₂O} (green).

The surface areas of both MIL-53(Al), determined by Brunauer–Emmett–Teller (BET) method (Appendix 3), and the external surfaces obtained by Harkins-Jura equation, are summarized in Table III-2. The MIL-53(Al) solids were first dried overnight at 100°C in order to obtain the anhydrous form. Both MIL-53(Al) compounds display a high surface area, MW-MIL-53 having a slightly higher value, certainly related to the smaller particle size. These values are in agreement with those already reported [12]. As the anhydrous MIL-53(Fe) is in the contracted form, we expect that no porosity could be measured.

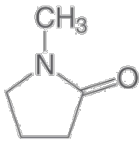
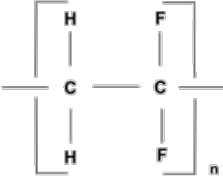
Table III-2 : BET surface area (S_{BET}) and external surface area (S_{ext}) of MIL-53(Al) solids.

Material	S_{BET} (m^2/g)	S_{ext} (m^2/g)
H-MIL-53(Al)	1240.46 ± 2.51	52.13
MW-MIL-53(Al)	1390.72 ± 0.43	48.31

III.3 Studies of the breathing transition

Breathing transitions occur in both MIL-53 solids (Al- or Fe-analogues) upon absorption of guest molecules (such as gases, solvent molecules) [14], [15]. Moreover, size effect in flexible MOFs is known to strongly impact the physical and structural properties of the material [16]. Downsizing the particles size directly influences the breathing effect of the framework, usually making it easier once the particle size decreases, enhancing the diffusion of the trapped species in the pores. In addition, flexibility is also influenced by the framework interaction with solvents [17]. For the electrochemical studies, the cathode materials were prepared by mixing MIL-53 materials with carbon black and a binder composed of PVDF in a NMP solution (10 wt. % in NMP, noted PVDF@NMP). Table III-3 sums up the developed formula of NMP and PVDF.

Table III-3 : Name of the solvent NMP and binder PVDF and their developed formula.

Abbreviation	NMP	PVDF
Name	N-Methyl-2-pyrrolidone	polyvinylidene fluoride
Developed formula		
Molar mass (g/mol)	99.13	534 (n=8.34)

For this purpose, the anhydrous form of both solids MIL-53(Al) and MIL-53(Fe) were impregnated with an excess of NMP solvent (MIL-53_NMP) or PVDF@NMP (MIL-53_PVDF@NMP). Then the solids were dried under vacuum at 80° C in order to simulate the drying of the electrodes, 80°C being the usual temperature to remove the NMP solvent without destroying the electrode structure [18], [19]. Figure III-9 shows the evolution of XRD patterns as a function of the guest molecules. None of the recorded XRD patterns correspond to the anhydrous form fingerprint, which implies that the guest molecules are confined in the pores. Unsurprisingly, MIL-53(Al) and MIL-53(Fe) show different behaviors. For both MIL-53(Al), the insertions of solvent molecules are quite similar. First, the NMP molecules are inserted in the pores and produce a MIL-53(Al)_NMP phase. Additional Bragg peaks are observed when the anhydrous solids are impregnated by the PVDF@NMP solution. These peaks seem to remain at approximately the same 2θ position after drying at 80°C under vacuum (MIL-53(Al)_PVDF). Similar XRD patterns are observed for the MIL-53(Fe) materials. Furthermore, we observe some similarities between the three XRD patterns related to the PVDF forms of all samples. The first peak at $2\theta = 9.14^\circ$ is common to all powders.

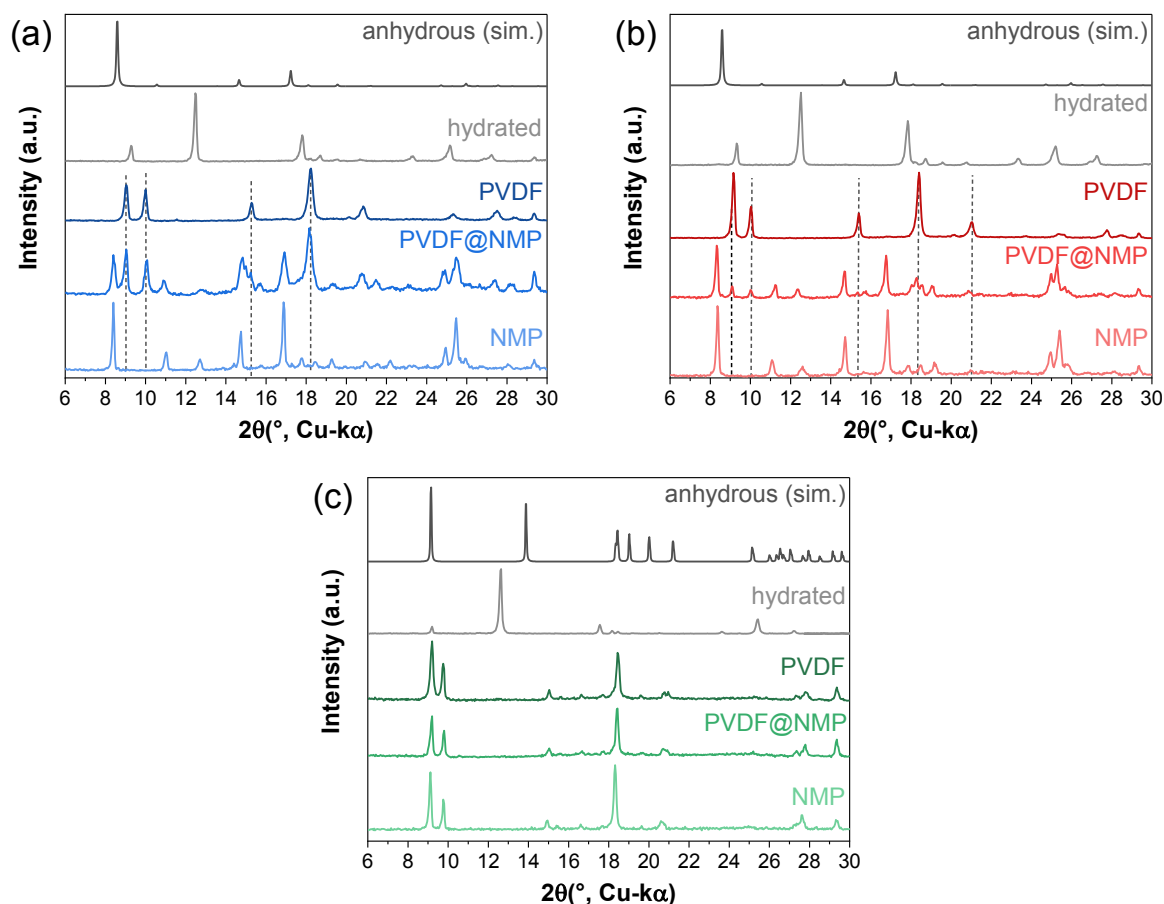


Figure III-9 : Evolution of XRD patterns as a function of the molecules guests inside the pores of (a) H-MIL-53(Al) (blue), (b) MW-MIL-53(Al) (red), and (c) R-MIL-53(Fe) (green). The colors for the guest molecule are light color (NMP), medium color (PVDF@NMP), and dark colors (PVDF). The dash lines highlight the additional Bragg peaks observed as soon as the MIL-53(Al) powders are in contact with a solution of PVDF@NMP.

Despite the low quality of XRD patterns, we tried to determine the cell parameters of both MIL-53(Al)_{PVDF} and MIL-53(Fe)_{PVDF}. XRD patterns were indexed using Dicvol program [20] and pattern matching refinements were performed with Fullprof Software [21]. Table III-4 gives the crystal systems and the cell parameters. We assume for the pattern matching refinements that the space group remained C2/c – like for the hydrated forms. The unit cells for H-MIL-53(Al)_{PVDF} and MW-MIL-53(Al)_{PVDF} are quite similar: no effects of the particle size or aspect ratio are observed on the breathing transition as expected. These results should be taken carefully as drastic conditions were used to limit the number of possibilities ($a < 25 \text{ \AA}$, b and $c < 10 \text{ \AA}$, $90^\circ < \beta < 110^\circ$). By comparing the cell parameters with those of the anhydrous and the hydrated MIL-53(Al)/MIL-53(Fe) solids (Table III-5), we find that the pores are closed upon absorption of guest molecules for MIL-53(Al)_{PVDF} and opened for the MIL-53(Fe)_{PVDF}.

Table III-4 : Cell Parameters of both MIL-53(Al)_PVDF and MIL-53(Fe)_PVDF.

Form * _PVDF	* = H-MIL-53(Al)	* = MW-MIL-53(Al)	* = R-MIL-53(Fe)
Figure of Merit - dicvol	34.2	48.1	24.1
System	monoclinic	monoclinic	monoclinic
Space group	C2/c (n°15)	C2/c (n°15)	C2/c (n°15)
a (Å)	19.619(1)	19.484(5)	18.526(4)
b (Å)	8.813(3)	8.808(3)	11.329(2)
c (Å)	7.703(2)	7.667(2)	8.535(2)
β (°)	98.46(3)	98.56(3)	101.69(3)
V (Å ³)	1317.6(8)	1301.1(6)	1754.1(6)

Table III-5 Cell parameters of anhydrous and hydrated forms of MIL-53(Al) and MIL-53(Fe).

Powder	MIL-53(Al)_empty	MIL-53(Al)_H ₂ O	MIL-53(Fe)_empty	MIL-53(Fe)_H ₂ O
System	orthorhombic	monoclinic	monoclinic	monoclinic
Space group	Imma (n°74)	Cc (n°9)	C2/c (n°15)	C2/c (n°15)
a (Å)	16.675(3)	19.513(2)	21.269(3)	19.319(2)
b (Å)	12.813(2)	7.612(1)	6.758(1)	15.036(2)
c (Å)	6.608(1)	6.576(1)	6.884(2)	6.835(6)
β (°)	-	104.24(1)	114.62(2)	96.31(1)
V (Å ³)	1411.9(4)	946.7(2)	899.6(3)	1973.5(3)

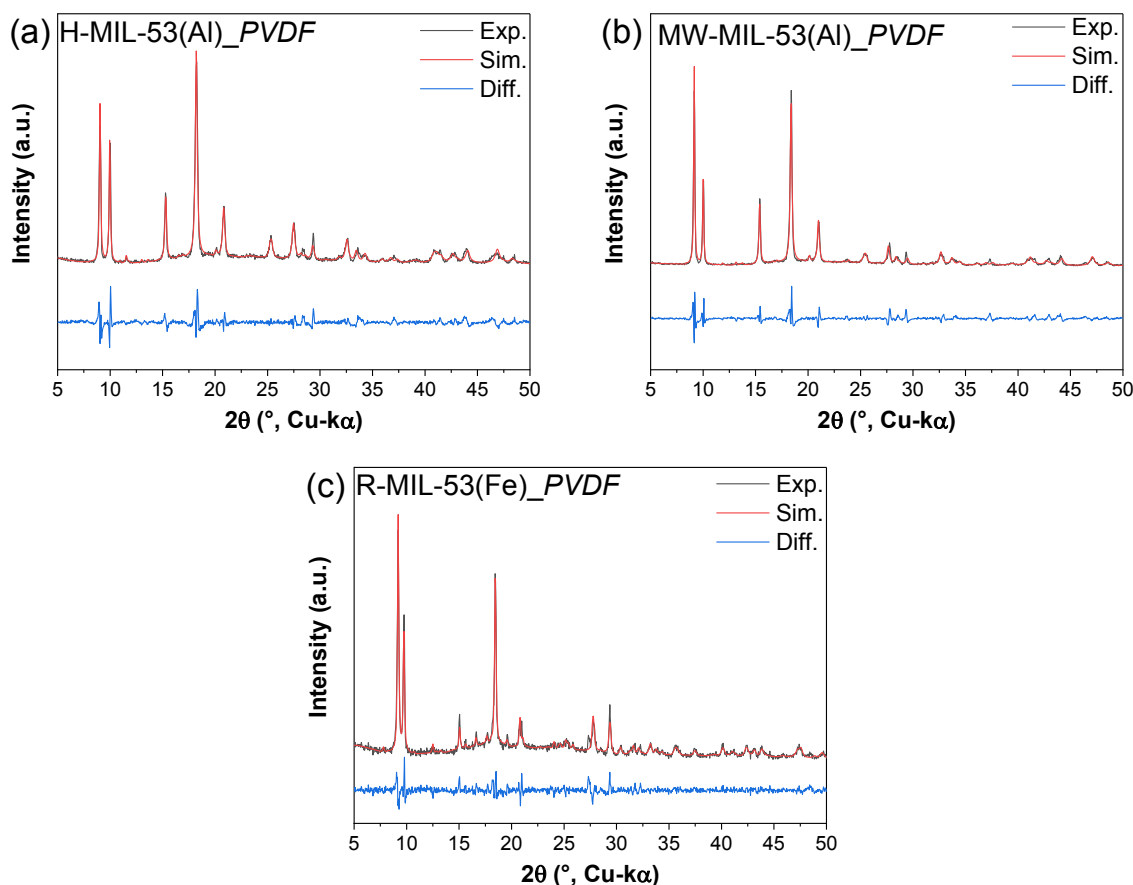


Figure III-10 : Pattern matchings of both MIL-53(Al)_PVDF and MIL-53(Fe)_PVDF. The difference between calculated (red line) and experimental profiles (black line) is given by the blue solid line.

III.4 Conclusion

MIL-53(Al) compounds were successfully synthesized through hydrothermal and microwave-assisted routes (H-MIL-53(Al) and MW-MIL-53(Al), respectively) in order to investigate the potential impact of the particle size / aspect ratio on their electrochemical behavior. The particle sizes of MW-MIL-53(Al) were found 4 times lower than H-MIL-53(Al) (500 nm vs. 2 μm). We also synthesized the Fe-analogue with the reflux method (R-MIL-53(Fe)). In the anhydrous form, MIL-53(Al) exhibits fully open pores. Both MIL-53(Al) have high BET surface and internal surface (up to 1240 and 1390 m^2/g for H-MIL-53(Al)_{empty} and MW-MIL-53(Al)_{empty}, respectively). As the MIL-53(Fe) solid has narrow pores, no porosity could be measured.

In order to study the flexibility of these materials occurring during the preparation of the cathode materials, we investigated how the structure evolved when adding NMP solvent and PVDF@NMP binder solution and after drying at 80°C under vacuum. Based on qualitative results, two phases seem to coexist when the MIL-53 powders are in contact with the PVDF@NMP solution: a form with NMP and a second which corresponds to the initial powder. The pattern matching refinements were performed on the later solids (MIL-53_PVDF). They confirmed that the pores had been contracted for both MIL-53(Al) and opened for MIL-53(Fe).

Several porous flexible MIL-53 materials were successfully synthesized and characterized. These flexible materials will be studied in the next chapter as the active material of air cathodes of Li-O₂ batteries.

III.5 References

- [1] F. Millange, C. Serre, and G. Férey, "Synthesis, structure determination and properties of MIL-53as and MIL-53ht: the first Cr^{III} hybrid inorganic-organic microporous solids: Cr^{III}(OH)·{O₂C–C₆H₄–CO₂}·{HO₂C–C₆H₄–CO₂H}_x", *Chem. Commun.*, n° 8, pp. 822–823, 2002.
- [2] F. Millange and R. I. Walton, "MIL-53 and its Isoreticular analogues: a review of the chemistry and structure of a prototypical flexible metal-organic framework", *Isr. J. Chem.*, vol. 58, n° 58, pp. 1019-1035, 2018.
- [3] D. Foucher, "Impact de l'eau dans la flexibilité des MOFs," phdthesis, Université Paris-Saclay, 2016.
- [4] G. Férey and C. Serre, "Large breathing effects in three-dimensional porous hybrid matter: facts, analyses, rules and consequences", *Chem. Soc. Rev.*, vol. 38, n° 5, pp. 1380–1399, 2009.
- [5] J. Wieme, L. Vanduyfhuys, S. M. J. Rogge, M. Waroquier, and V. Van Speybroeck, "Exploring the flexibility of MIL-47(V)-Type materials using force field molecular dynamics simulations", *J. Phys. Chem. C*, vol. 120, n°27, pp. 14934–14947, 2016.
- [6] E. V. Anokhina, M. Vougo-Zanda, X. Wang, and A. J. Jacobson, "In(OH)BDC-0.75BDCH₂ (BDC = Benzenedicarboxylate), a hybrid inorganic-organic vernier structure", *J. Am. Chem. Soc.*, vol. 127, n° 43, pp. 15000–15001, 2005.
- [7] A. Boutin *et al.*, "Temperature-induced structural transitions in the gallium-based MIL-53 metal-organic framework", *J. Phys. Chem. C*, vol. 117, n°16, pp. 8180–8188, 2013.
- [8] A. Boutin *et al.*, "Breathing transitions in MIL-53(Al) metal-organic framework upon xenon adsorption", *Angew. Chem.*, vol. 121, n°44, pp. 8464–8467, 2009.
- [9] M. Taddei, D. A. Steitz, J. A. van Bokhoven, and M. Ranocchiari, "Continuous-flow microwave synthesis of metal-organic frameworks: a highly efficient method for large-scale production", *Chem. – Eur. J.*, vol. 22, n°10, pp. 3245–3249, 2016.
- [10] A. S. Munn, A. J. Ramirez-Cuesta, F. Millange, and R. I. Walton, "Interaction of methanol with the flexible metal-organic framework MIL-53(Fe) observed by inelastic neutron scattering", *Chem. Phys.*, vol. 427, pp. 30–37, 2013.
- [11] T. Loiseau, C. Mellot-Draznieks, H. Muguerra, G. Férey, M. Haouas, and F. Taulelle, "Hydrothermal synthesis and crystal structure of a new three-dimensional aluminum-organic framework MIL-69 with 2,6-naphthalenedicarboxylate (ndc), Al(OH)(ndc)·H₂O", *Comptes Rendus Chim.*, vol. 8, n°3, pp. 765–772, 2005.
- [12] T. Loiseau *et al.*, "A Rationale for the large breathing of the porous aluminum terephthalate (MIL-53) upon hydration", *Chem. – Eur. J.*, vol. 10, n° 6, pp. 1373–1382, 2004.
- [13] T. R. Whitfield, X. Wang, L. Liu, and A. J. Jacobson, "Metal-organic frameworks based on iron oxide octahedral chains connected by benzenedicarboxylate dianions," *Solid State Sci.*, vol. 7, n° 9, pp. 1096–1103, 2005.

- [14] L. Alaerts *et al.*, "Selective adsorption and separation of ortho-Substituted alkylaromatics with the microporous aluminum terephthalate MIL-53," *J. Am. Chem. Soc.*, vol. 130, n°43, pp. 14170–14178, 2008.
- [15] F. Millange *et al.*, "Selective sorption of organic molecules by the flexible porous hybrid metal-organic framework MIL-53(Fe) controlled by various host-guest interactions," *Chem. Mater.*, vol. 22, n°4, pp. 4237–4245, 2010.
- [16] O. M. Linder-Patton *et al.*, "Particle size effects in the kinetic trapping of a structurally-locked form of a flexible MOF," *CrystEngComm*, vol. 18, n° 22, pp. 4172–4179, 2016.
- [17] S. Leubner *et al.*, "Solvent Impact on the properties of benchmark metal-organic frameworks: acetonitrile-based synthesis of CAU-10, Ce-UiO-66, and Al-MIL-53," *Chem. Weinh. Bergstr. Ger.*, vol. 26, n°7, p. 3877, 2020.
- [18] C.-H. Jo and S.-T. Myung, "Efficient recycling of valuable resources from discarded lithium-ion batteries," *J. Power Sources*, vol. 426, pp. 259–265, 2019,.
- [19] W. Xu *et al.*, "Investigation on the charging process of Li₂O₂ based air electrodes in Li-O₂ batteries with organic carbonate electrolytes," *J. Power Sources*, vol. 196, n° 8, pp. 3894–3899, 2011.
- [20] A. Boultif and D. Louër, "Powder pattern indexing with the dichotomy method," *J. Appl. Crystallogr.*, vol. 37, n°5, Art. n°5, 2004.
- [21] J. Rodriguez-Carvajal, "Fullprof: A Program for Rietveld Refinement and Pattern Matching Analysis," *Abstract of the Satellite Meeting on Powder Diffraction of the XV Congress of the IUCr*, Toulouse, France, p. 127, 1990.

Chapter IV. MOF electrode cycling performances

This chapter will present the electrochemical properties of both flexible MIL-53(Al) and MIL-53(Fe) materials. We will compare first the effect of the structure and morphology on the electrochemical performance by comparing MW-MIL-53(Al) and H-MIL-53(Al). Then, we will investigate the electrochemical properties of R-MIL-53(Fe) in order to identify the role of the breathing effect of flexible materials. We will end the chapter by comparing the flexible MIL-53 structure with a rigid structure MOF-5. The capacities of MOF electrodes will also be compared with the ones of pure carbon black electrodes and also with literature. Finally, the reproducibility of the cycling performances of these particular materials will be discussed.

Reminder for readers: for sake of clarity, the reported capacity values in this chapter are expressed with respect to the weight of MOF together with Super P carbon black (C_{sp}). This implies that values reported in “mAh/g” correspond to values in “mAh/g_(MOF+C_{sp})”. All voltages are given versus Li^+/Li .

IV.1 Flexible MOF

IV.1.1. MIL-53(Al)

The porous MIL-53(Al) structure is predicted to be able to store the discharge products formed in Li-O₂ batteries. The effect of size in flexible MOFs is known to strongly impact the physical and structural properties of the material [1]. Downsizing the particles size directly influences the breathing effect of the framework, usually making it easier once the particle size decreases, enhancing the diffusion of the trapped species in the pores [2]. In addition, the structure and the morphology of the cathode materials can influence the capacity of the Li-O₂ batteries [3]–[6].

In this work, the MIL-53(Al) material is obtained with two different morphologies: homogenous small particles generated by microwave irradiation (500 nm) and heterogeneous large particles obtained by the conventional hydrothermal method (2 μ m) (Section III.2.3). Surprisingly, same breathing transitions occur on both samples. Here we will first present separately the electrochemical performances of MW-MIL-53(Al) and H-MIL-53(Al), while their performances will be compared to pure C_{sp} electrodes. Then, the effect of the morphology of MIL-53(Al) on the electrochemical performances of cathodes for Li-O₂ batteries will be discussed. We may expect better discharge capacities with MIL-53(Al) compounds compared to the pure C_{sp} due to their higher surface area (1240 and 1390 m²/g for H-MIL-53(Al) and MW-MIL-53(Al)), 52.52 m²/g for C_{sp}).

IV.1.1.1. MW-MIL-53(Al) electrochemical behavior and performances

To evaluate the performance of the MW-MIL-53(Al) compound, a series of independent Li-O₂ cells with MW-MIL-53(Al) electrodes were cycled. We report here the results of seven successful tests with MW-MIL-53(Al) for sake of reproducibility.

The first discharge profiles of Li-O₂ batteries with MW-MIL-53(Al) cathodes are shown in Figure IV-1. For all electrochemical tests, we observe a wide range of initial discharge capacities, from limited or no capacity to 1200 mAh/g. The discharge profiles are characterized by monotonic plateaus / slopes followed by an abrupt drop in potential, which is assigned to the end of the discharge process. The potentials of these plateaus are however different and seem to determine the value of the initial discharge capacity.

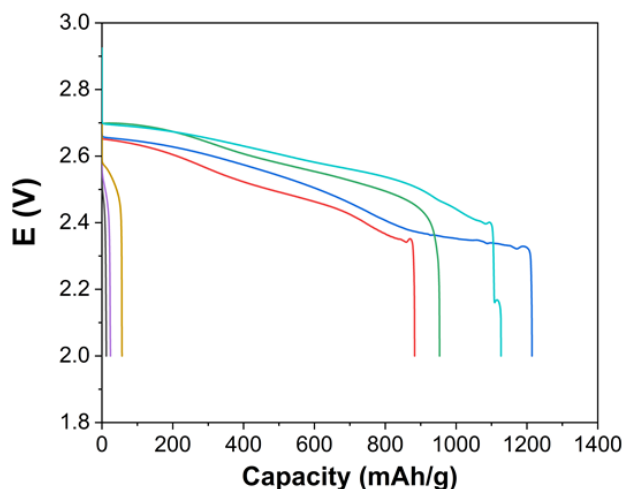


Figure IV-1 : First discharge profiles of Li-O₂ batteries with seven similar MW-MIL-53(Al) cathodes.

As shown in Figure IV-2 (a), two behaviors are observed: (case1) a high potential plateau (>2.6 V) associated with a gradual decrease of discharge capacity upon cycles and (case 2) a low potential plateau (<2.6 V) associated with low or no initial discharge capacity.

For 60 % of the electrodes (case 1), the initial discharge capacities are in the range 800 - 1200 mAh/g. The corresponding discharge potentials are around 2.6 - 2.7 V, which correspond well with the value expected for the formation of Li₂O₂ [7]. No charge capacity is observed, indicating that the OER process does not occur for these electrodes. The charge profile reaches quickly the potential limit (4.5 V) fixed by the stability window of the LiTFSI/DME electrolyte, thus preventing a complete OER. It is important to note that the high overpotential observed in charge may, in turn, trigger electrolyte decomposition. The discharge capacities decrease quickly over cycles (Figure IV-2(a)), as we may expect that Li₂O₂ products from the first discharge block the pores, preventing the next deposition. In the same time, the potential of the discharge plateau slowly decreases to 2.5 V upon cycling due to the increase of the insulating Li₂O₂ discharge products. Moreover, the insulating Li₂O₂ limits electron transfer and leads to an increase of overpotentials. The presence of these agglomerates at the cathode will lead to greater resistance values due to the reduction of active cathode pore / area, limiting the ORR. In addition, the low conductivity of Li₂O₂ will also limit the reduction kinetics of ORR [8].

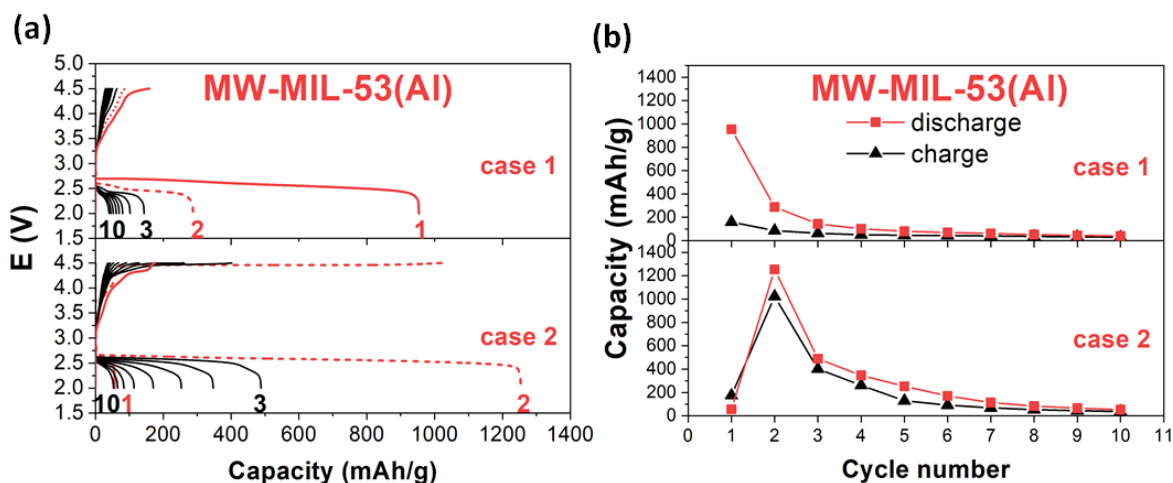


Figure IV-2 : (a) The discharge-charge cycling profiles for Li-O_2 batteries with MW-MIL-53(Al) electrodes. Cycles 1 and 2 are represented respectively in solid and dash red lines while cycles 3 to 10 are represented in black solid lines. (b) Discharge (square) and charge (black triangle) capacities as a function of the cycle number for Li-O_2 batteries with MW-MIL-53(Al) electrodes.

For other electrodes (40%, case 2), no capacity is delivered at the initial discharge (<100 mAh/g), while the second discharge capacities are higher than the first ones (Figure IV-2(b)), denoting a possible activation process during the first cycle. We observe a “sustainable” discharge capacity until the fourth cycle (<400 mAh/g). These electrodes display large inclines with an onset of the first discharge potential between 2.4 – 2.5 V, which are slightly lower than the values reported for the formation of Li_2O_2 [7]. After the first cycle, the discharge plateau potentials are higher (2.6 – 2.7 V) and the discharge process occurs, leading most probably to the formation of Li_2O_2 . The lower discharge potential at the first discharge may suggest some limitations in the transfer of species inside the electrodes. Some reports reveal that a suitable tri-phase boundary between electrode / O_2 / electrolyte could ensure good performance [9], [10]. The liquid covers the active area with a thin film ensuring the ionic transport to the active sites, while the non-wetted regions ensure proper gas transport to the active areas. Not enough or over-wetted electrodes could reduce the Li^+ diffusion or O_2 diffusion respectively, thus diminishing the battery cycle performance. Consequently, the limited first capacities may be explained by an electrode wetting issue. The open circuit voltage (OCV) values are lower for the electrodes which need “an activation process” (OCV~2.8 V, case 2) than for the electrodes which have a constant decrease of capacity over cycles (OCV~2.9 V, case 1). These observations are in favor of a lack of wettability of the electrode. We can also infer that an initial activation cycle is occasionally necessary to reorganize or remove some solvent molecules or PVDF inside the pores, which may at first prevent the nucleation of the discharge products. In contrast to the first case, we observe a high charge capacity until the second cycle, meaning that the decomposition of Li_2O_2 through the OER occurs. Yet, after the fourth cycle, a severe drop in capacity occurs.

IV.1.1.2. H-MIL-53(Al) electrochemical behavior and performances

The large micro-sized H-MIL-53(Al) is synthesized through the traditional hydrothermal heating method (Section III.2.1). Ten individual Li-O₂ batteries with H-MIL-53(Al) electrodes are evaluated here.

Figure IV-3 illustrates the first discharge and cycling profiles of H-MIL-53(Al) electrodes. These discharge profiles are also characterized by monotonic plateaus / slopes followed by an abrupt drop in potential. We observe also a large dispersion of the initial discharge capacities from close to null to 1200 mAh/g. Compared with MW-MIL-53(Al) electrodes, one additional behavior (case 3) is observed where the discharge capacities are in a medium range (700 – 900 mAh/g).

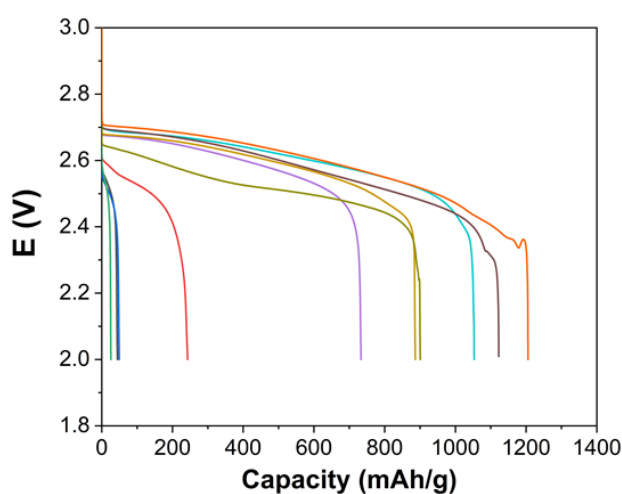


Figure IV-3 : First discharge profiles of Li-O₂ batteries with ten similar H-MIL-53(Al) cathodes.

An overview of the three cases obtained with H-MIL-53(Al) electrode is shown in Figure IV-4. Like for the MW-MIL-53(Al) electrodes, the first case (high initial discharge capacity (900 – 1200 mAh/g) is observed for 30% of electrodes. The discharge capacities are higher at the first cycle and quickly decrease over cycles. The potentials of the plateau start at ~2.7 V and then slowly decrease to 2.4 V due to the increase of insulating discharge product Li₂O₂. No charge capacity is observed for these electrodes, thus no OER occurs. For the next cycles (2 - 10), limited discharge capacities are obtained due to the low discharge plateau potentials (<2.5 V) which disfavor the formation / growth of Li₂O₂. The second case is characterized by a low initial discharge capacity (<250 mAh/g for 40% of the electrodes), associated with a low discharge plateau potential (<2.5 V) that may account for the limited growth of discharge products such as Li₂O₂. For these later electrodes, the open circuit voltages (OCV) are also lower than for the case 1 (~2.8 V vs ~2.9V), like for MW-MIL-53(Al) electrodes. We can again suggest that an activation process is necessary to reorganize the pore configuration or wet the whole electrode volume. After this step, the cells are quite reversibly cycling but the capacities are limited after the fourth cycle, probably as a consequence of the high charge plateau potential (~4.4V).

The last case concerns the electrode with a medium initial discharge capacity (700 – 900 mAh/g; 30 % of the electrodes). The discharge plateau starts from 2.7 V and decreases slightly to 2.5 V, before collapsing and signifying the end of the discharge. The OER process is observed for these electrodes from the first cycle, denoting the decomposition of Li_2O_2 . The cells are reversible for the first three cycles, denoting efficient ORR and OER processes. We can suppose that if the pores are not fully blocked by Li_2O_2 in the first discharge, it decomposes more easily during the charge process (OER) and allow a new formation / growth of Li_2O_2 during the next discharge. Unfortunately, all capacities fade after the fourth cycle, suggesting a poor cycling behavior of the MOF.

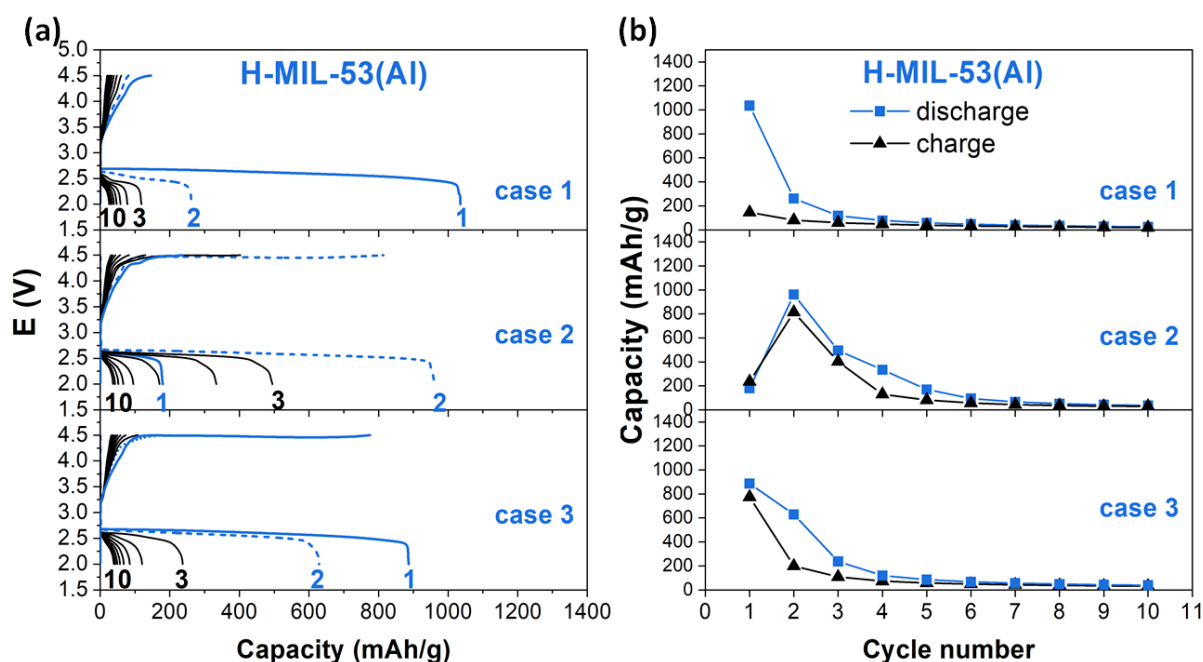


Figure IV-4 : (a) The discharge-charge cycling profiles for Li-O₂ batteries with H-MIL-53(Al) electrodes. Cycles 1 and 2 are represented respectively in solid and dash blue lines while cycles 3 to 10 are represented in black solid lines. Case 1 : $Q_1 = \text{maximum}$. Case 2 : $Q_1 = \text{minimum}$. Case 3 : $Q_1 = \text{medium}$. Batteries were cycled at a current density of 50 mA/g. (b) Discharge (square) and charge (black triangle) capacities as a function of the cycle number for Li-O₂ batteries with H-MIL-53(Al) electrodes.

IV.1.1.3. Effect of morphology

The morphologies of both MW-MIL-53(Al) and H-MIL-53(Al) have been already illustrated in Chapter III. As a quick reminder, nanometer-sized pseudo-spherical crystallites are observed (with an average crystal length of ~ 500 nm) for the MW-MIL-53(Al), while micrometer-sized platelet crystallites (with an average crystal diameter ~ 2 μm) are obtained for H-MIL-53(Al) solid. Besides, the length-width or aspect ratio of the particles is smaller for these latter particles (Section III.2.3). The breathing transitions occurring when the solids are fully impregnated with the PVDF solution (10 wt. % PVDF salt in NMP solvent) are in the same amplitude for both MIL-53(Al) solids (monoclinic cell with a volume of 1302 \AA^3 and 1318 \AA^3 for MW-MIL-53(Al) and H-MIL-53(Al), respectively).

However, the expected impact of the morphology on the electrochemical performance of Li-O₂ batteries is negligible for our MIL-53(Al) materials. Figure IV-5 illustrates the first two discharge behaviors of both MIL-53(Al) electrodes studied. The top figure illustrates the first and the second discharge capacities of the Li-O₂ batteries obtained with H-MIL-53(Al) or MW-MIL-53(Al). With some electrodes, the first discharge capacities are in the range 700 - 1200 mAh/g, while other capacities are limited (< 250 mAh/g). In the latter case, the second discharge capacities are higher than the first discharge capacities, denoting a possible activation process during the first cycle, as discussed previously. Despite the activation process, the discharge capacities still fade rapidly in a few cycles, and no charge capacities are obtained. This stresses the absence of OER reactions with both MIL-53(Al) and the lack of reversibility of these materials. Noteworthy, both MIL-53(Al) samples have similar BET surface areas and external surfaces. As the surface area is in part responsible for the accommodation of guest molecules, this may explain the similar electrochemical performances observed with MIL-53(Al).

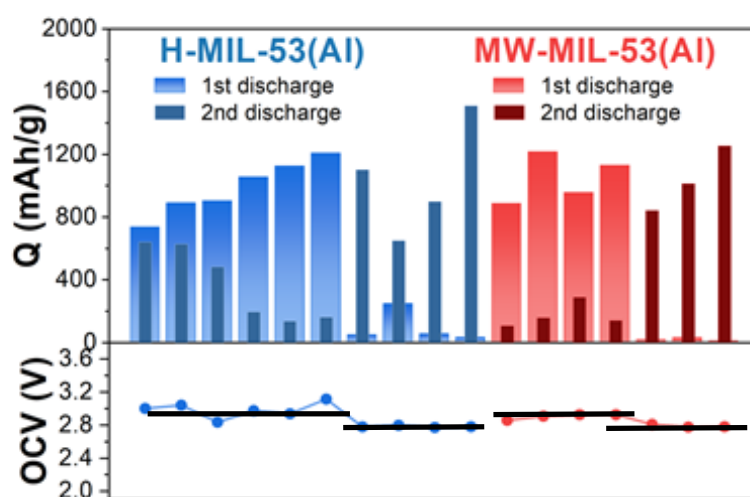


Figure IV-5 : Top: discharge capacities at the first (gradient) and second (uniform) cycles for Li-O₂ batteries at a current of 50 mA/g with H-MIL-53 (blue) and MW-MIL-53 (red) electrodes. Bottom: associated open-circuit voltages (V) for each cell. The black lines indicate the tendency.

Same overpotentials for charge and discharge are observed for both MIL-53(Al) electrodes. Moreover, higher overpotentials for charge and discharge are observed for both MIL-53(Al) electrodes compared to the Super P carbon ones (Appendix 4). The accumulation of insulating Li₂O₂ limits the electron transfer through the electrode and increases the internal battery resistance. The Li₂O₂ and possible other parasitic products may block the surface area, and no more porosity is available for the next deposition of the discharge product. As a result, severe capacities are lost over deep cycling. As both MIL-53(Al) have similar surface areas, their capacities fade both quickly with few cycles.

Overall, compared to pure C_{sp} electrodes (Appendix 4) the values of the discharge potentials for MIL-53(Al) are slightly lower than for pure C_{sp} electrodes (~ 2.60 V vs. ~ 2.72 V for MOF and C_{sp} electrodes, respectively). Besides, the charge potentials (~ 4.5 V) are higher for MW-MIL-53(Al) electrodes compared to C_{sp} electrodes (~ 4.3 V, Appendix 4). Moreover, the best discharge capacity of MIL-53(Al) electrodes is about three times lower than C_{sp} electrodes (~ 3300 mAh/g, Appendix 4). Both the lower potential and discharge capacities reached for MOF materials suggest some limitations in the transfer of species inside the electrodes or obstruction of catalytic sites, if any, by the discharge products. While the overpotential is larger for MOF electrodes, the polarization is still limited with regard to the thermodynamic potential for the formation of Li_2O_2 ($E_{Li_2O_2} = 2.96$ V) [11]. The poor electric conductivity of MOF may cause high overpotentials, leading to unsatisfactory ORR and OER reactions [12].

To conclude on the MIL-53(Al) solids, we first expected a high-capacity delivery owing to the high surface area of MIL-53(Al) compared to the C_{sp} . But in contrast, we observe lower capacities with both H-MIL-53(Al) and MW-MIL-53(Al) (average discharge capacity at the first cycle: 1000 mAh/g) which is certainly due to the poor electric conductivity of insulating MOF. Concerning the size of the starting MOF, the smaller crystal sizes of MIL-53(Al) with microwave irradiation compared to the hydrothermal does not result in different electrochemical behaviors as expected. Such a difference in particle size / porosity of both MIL-53(Al) seems not sufficient for battery performance improvement. Moreover, an activation process is necessary for some electrodes so as to remove some guest solvent or PVDF molecules inside of the pores. A further study on the porosity of pristine MOF electrodes could be helpful to confirm our assumption for the activation step. Despite the activation process, the discharge capacities still fade rapidly in a few cycles, and no charge capacities are obtained. This stresses the absence of OER reactions with the MIL-53(Al) and the lack of reversibility of these materials. The low performance of MIL-53(Al), compared to the pure C_{sp} electrode, is also impacted by the lack of active open metal sites within the MIL-53 structure. Moreover, it is also possible that the MIL-53(Al) pores are clogged while accommodating the discharge products, and hardly reverse the pore opening for the decomposition of discharge products (OER) during the charge process. This quasi-irreversible pore closure during the accommodation of discharge products may prevent deep accessibility of pores and lead to a low cyclability. A less closed structure or even opened pores, in reverse, might be key for achieving a better battery performance.

IV.1.2. MIL-53(Fe)

IV.1.2.1. Introduction

Inspired by the assumption that the poor reversibility observed with MIL-53(Al) electrodes is probably related to the pore closure, we then investigated the flexible MIL-53(Fe), expected to better accommodate the discharge products in the Li-O₂ batteries. As described earlier in Chapter III, MIL-53(Fe) exhibits opposite breathing transitions while adsorbing / releasing guest molecules compared to MIL-53(Al). When the pores are empty, MIL-53(Al) has

a fully open framework while the pores of MIL-53(Fe) are closed. In contrast, when the pores are filled with guest molecules (for example water molecules), the pores are narrow for MIL-53(Al) but open for MIL-53(Fe). Thus, we expect a better capacity for MIL-53(Fe), for which the discharge products can be stored in the open pores. We present hereafter the electrochemical performances of the micrometer-sized R-MIL-53(Fe) synthesized by reflux in the Li-O₂ batteries.

IV.1.2.2. Electrochemical behavior and performance of MIL-53(Fe)

Six independent Li-O₂ cells with R-MIL-53(Fe) electrodes were cycled for sake of reproducibility. For all electrodes, the open circuit voltage (OCV) of R-MIL-53(Fe) cells is up to 2.8 V, which is comparable to the calculated OCV [13]. The first discharge-charge profiles and corresponding capacities are illustrated in Figure IV-6 (a). The MIL-53(Fe) delivers an initial high discharge capacity in a range of 1500 – 2200 mAh/g, which is higher than the capacities of MIL-53(Al) electrodes (700-1200 mAh/g). The capacity deviation is similar that the one observed on MIL-53(Al) cells. The discharge profile is characterized by two distinct plateaus. The first discharge plateau (2.53 - 2.63 V) corresponds to the formation of Li₂O₂ [14], while the second plateau at a lower potential (2.33 - 2.41 V) may refer to the formation of Li₂O [15] or Li₂CO₃ [16]. The abrupt drop of potential between the two plateaus is related to the nucleation of first grains and the growth of particles. Compared to the C_{sp} electrode (2.72 V, Appendix 4), the Li₂O₂ formation on R-MIL-53(Fe) electrode occurs at a lower discharge potential. This confirms our previous assumption on the better electronic conductivity for the C_{sp} electrode compared with the more insulating MOF-based electrodes.

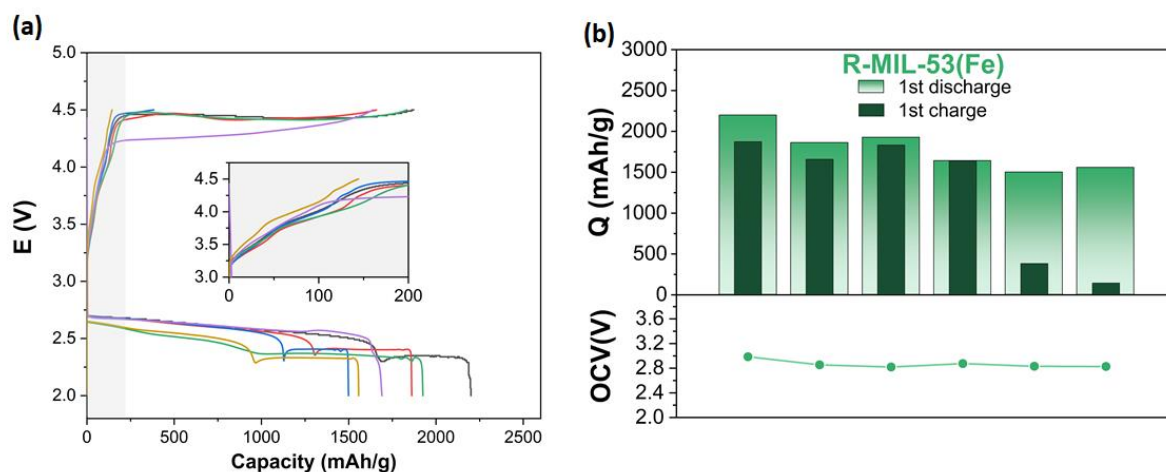


Figure IV-6 : (a) First discharge-charge profiles of Li-O₂ batteries with six similar R-MIL-53(Fe) electrodes. The inset illustrates the onset process of the charge. (b) (Top) First discharge (gradient) and charge (uniform) capacities and (bottom) the associated open-circuit voltage of Li-O₂ batteries with R-MIL-53(Fe) electrodes.

Contrary to Al-analogues, a wide range of first charge capacities is observed with the MIL-53(Fe) and can be declined into two trends: either a low charge capacity (case 1, 140 - 390 mAh/g for 33% of all experiments) or a high charge capacity (case 2, 1630 - 1880 mAh/g for 67% of all experiments), as illustrated in Figure IV-6 (b). The charge potentials of the cells

are nearly the same as pure C_{sp} electrodes (~ 4.3 V). Such a high charge potential of MIL-53(Fe) denotes a lack of catalytic site within the framework. The low charge capacity obtained in case 1 implies that pores of R-MIL-53(Fe) are clogged by Li_2O_2 at the end of the charge, then no more porosity is available for the next deposition of the product. Lack of porosity or thick deposition of insulating Li_2O_2 is supposed to impact the next deposition.

Starting from the second cycle, the discharge profile turns again into a typical monotonical plateau, ending with a sharp decline (Figure IV-7). The transformation from Li_2O_2 into Li_2O may require too high overpotentials out of the electrolyte stability window, as accumulated Li_2O_2 or other decomposed byproducts limit the charge transfer in the electrode [17]. Interestingly, the two behaviors observed on the initial charge impact the performance of the second cycle. For the electrodes presenting low first charge capacities at the first cycle (case 1) the second discharge voltage is centered at 2.5 V ($\sim 2.49 - 2.53$ V), ~ 0.1 V below their first discharge potentials. In contrast, the electrodes delivering high charge capacities at their first cycles (case 2) exhibit a second discharge plateau at around 2.6 V. This observation could confirm our previous assumption about the residual Li_2O_2 in the pores due to the inefficient OER. The lack of porosity left due to the presence of residual Li_2O_2 prevents the deposition of the product in the next discharge. The residual Li_2O_2 increases also the discharge overpotential for the next cycles, as the charge transfers are limited through the insulating Li_2O_2 [16]. After the second discharge, the restructuring of pore allows an intense removal of discharge products at the second charge, followed by an increase of the discharge potential at the third cycle up to 2.60 V (case 1). This higher discharge potential confirms the foregoing deep decomposition of insulating Li_2O_2 , which reduces the polarization and decreases the discharge overpotential of the cell.

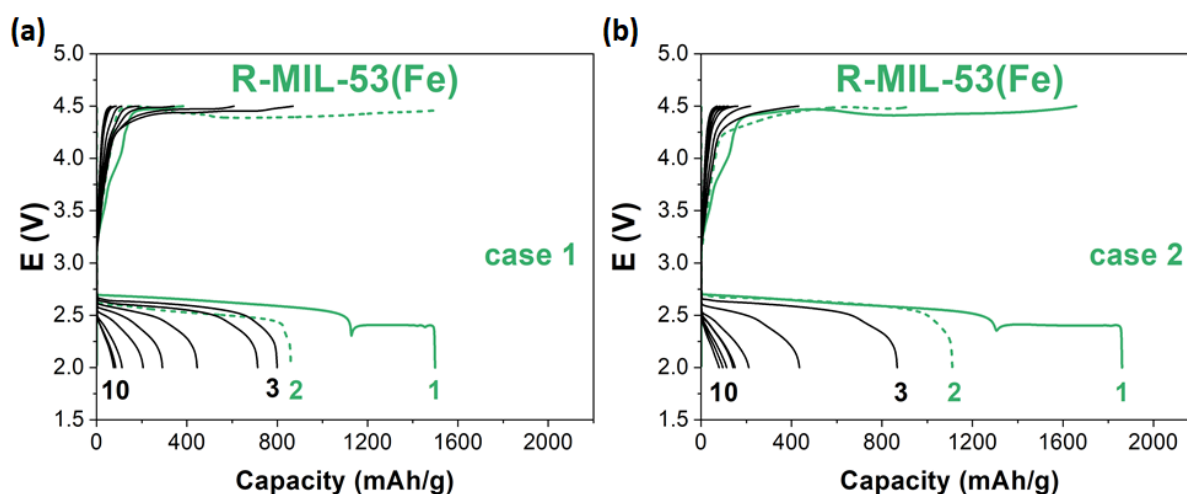


Figure IV-7 Discharge-charge cycling profiles of $Li-O_2$ batteries with R-MIL-53(Fe) electrodes. (a) Case 1: low first charge capacity. (b) Case 2 : high first charge capacity. Cycle 1 and cycle 2 are represented respectively in green solid and dash lines while cycles 3 to 10 are represented in black solid lines.

Figure IV-8 shows the R-MIL-53(Fe) discharge and charge capacities as a function of cycle number. This illustrates again the two trends upon cycling for the R-MIL-53(Fe) electrodes. For the first group (case 1), the low charge capacity delivered at the first cycle induces a medium value in the second discharge capacity. Yet, after the removal of species in the pores, similar or even higher charge capacities are delivered at the second cycle compared to the first cycle. Thereby, a CE over 100 % is obtained. This CE should not be considered as meaningful as it could benefit from the decomposition of Li_2O_2 produced on the first cycle or from parasitic reactions from electrolyte decomposition [11]. For the other group (case 2), efficient OER occurs with a high CE maintained between 80 – 94 % until the second cycle. Since then, the charge capacity has faded more significantly than the discharge, but still, with a CE of around 50 % retained at the fourth cycle. Some electrodes still deliver ~ 200 mAh/g discharge capacity at the sixth cycle. Overall, in both cases, the charge and discharge capacities decrease rapidly over cycles.

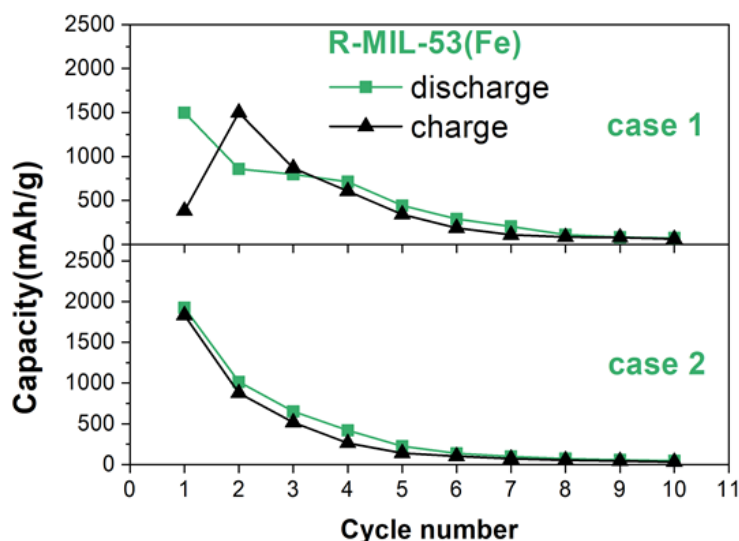


Figure IV-8 : Discharge (green square) and charge (black triangle) capacities of Li-O_2 batteries with R-MIL-53(Fe) electrodes as a function of the cycle number.

As mentioned in the literature [18], the capacity fading at deep discharge / charge is related to inefficient deposition and decomposition of Li_2O_2 or decomposition of electrolyte. The main discharge product Li_2O_2 or other byproducts due to the electrolyte decomposition could block the air cathode over full cycling [19]. While the presence of the insulating Li_2O_2 results in limited electron transfer at the cathode / Li_2O_2 interface, the absence of porosity left for the deposition of the discharge products affects also the performance of the battery. This is what the electrochemical response suggests here for the MIL-53(Fe) material. In addition, the charge potential of R-MIL-53(Fe) electrodes reaches the limits of the stability window of the DME solvent, which results in a risk for electrolyte decomposition and Li_2CO_3 formation. The byproduct might also impact the accessible surface of the framework for the main discharge product.

IV.1.3. Conclusion on the pore opening effect

The two analogues MIL-53(Al) and MIL-53(Fe) show different breathing behaviors against guest molecules. Upon adsorbing PVDF, the MIL-53(Al) presents a narrow-pore form with the dimension of contracted diamond-like pore; while the MIL-53(Fe) presents an open pore form with the same shaped-pore expanded. As shown earlier in Chapter III, the final MIL-53_PVDF has both larger unit cell volume and pore size for the Fe analogue than for the Al analogue (1754 \AA^3 vs. 1318 \AA^3 and $18.5 \text{ \AA} \times 11.3 \text{ \AA}$ vs. $19.6 \times 8.8 \text{ \AA}$, for MIL-53(Fe)_PVDF and MIL-53(Al)_PVDF respectively). The open pores of MIL-53(Fe) are more accessible to the discharge products than the narrowed pores of MIL-53(Al), explaining the improved capacity obtained with the MIL-53(Fe). An almost two-fold higher initial discharge capacity is delivered by MIL-53(Fe) compared to MIL-53(Al) ($\sim 2000 \text{ mAh/g}$ for R-MIL-53(Fe) vs. $\sim 1000 \text{ mAh/g}$ for MW-MIL-53(Al) / H-MIL-53(Al)). The enlargement of pore size also ensures a more efficient decomposition of discharge products during the charge process, leading to higher charge capacities. As the ORR / OER occurs on each full cycle with MIL-53(Fe), it leads to better capacities and a better battery cyclability than with both MIL-53(Al) compounds. Although the capacity fades significantly over cycling, for most of the cases, a charge capacity over 300 mAh/g is maintained by the MIL-53(Fe) material until the fourth cycle while only less than 100 mAh/g is reached at the third cycle by the MIL-53(Al) compound. The pore might be gradually blocked by the Li_2O_2 discharge product or parasitic species derived from electrolyte decomposition during the discharge-charge cycling. At a high voltage, ether-based electrolyte might decompose. The concerned parasitic species might be gradually accumulating inside of the pores, thus leading to a rapid capacity fading over the ten cycles. Without efficient OER catalysts in MIL-53(Fe), Li_2O_2 could not be completely decomposed due to the sluggish kinetics of the OER process. The accumulation of insulating products on the cathode may also lead to the gradual capacity fading upon cycling. Among most of the cells, the OER reactions occur efficiently with a CE of *ca.* 85 % for MIL-53(Fe) for all cycles. Overall, such differences in discharge / charge capacities, CE, and capacity retention with R-MIL-53(Fe) and MIL-53(Al) highlight the importance of the pore opening on the performance of flexible MOF materials for Li-O₂ batteries.

IV.2 Rigid vs. flexible MOF

To evaluate the effect of flexibility on the electrochemical performance, we compare here the flexible MIL-53 to a rigid MOF. Several rigid MOF materials with a wide range of surface areas in diverse structural topologies have been studied as active materials of air cathode in Li-O₂ batteries by Li *et al.* [20]. We select the rigid solid MOF-5 that has the same organic linker as MIL-53, *i.e.* the benzene-1,4-dicarboxylic acid (BDC). Although the MIL-53(Fe) shows better performance, we select the H-MIL-53-(Al), as its electrochemical behavior with the monotonic plateau is simpler.

IV.2.1. Electrochemical behavior and performance of R-MOF-5

The solid R-MOF-5 is first synthesized using the reflux method as previously reported by Yaghi *et al.* [21]. The procedure and the XRD characterizations are given in Appendix 2. MOF-5 consists of zinc clusters linked by the BDC leading to a 3D channel system with 12.9 Å spacing between the centers of adjacent clusters [22] (Figure IV-9). Note that the pore size of MOF-5 is comparable to the anhydrous MIL-53(Al) with a large pore (16.7 Å × 12.8 Å).

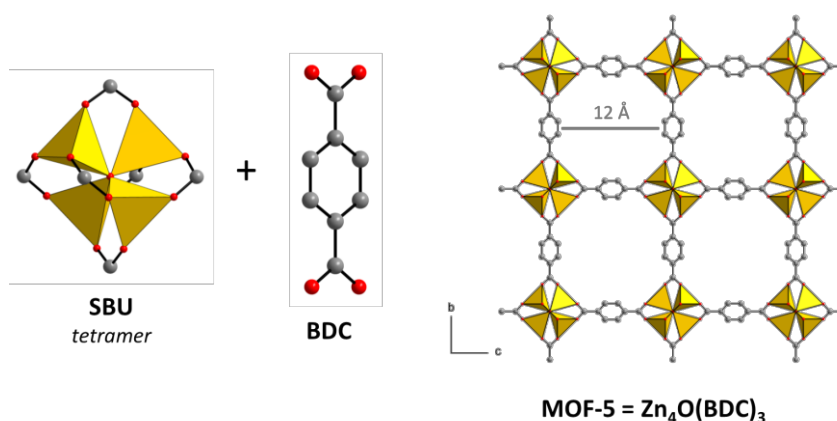


Figure IV-9: View of the SBU with Zn with the organic linker used and representation of the cubic structure of MOF-5. Guest molecules have been omitted for sake of clarity.

MOF-5's electrochemical behavior is already reported in the literature by Li *et al.* [20]. Their electrodes formulation consists of MOF-5/C_{sp}/PVDF in a wt. % of 40/40/20 with the Toray carbon paper as the gas diffusion layer. The 1M LiTFSI in TEGDME (tetraethylene glycol dimethyl ether) is used as electrolyte. Moreover, all their batteries are tested in an O₂-filled glove box. The cell with MOF-5 electrode reported by Li *et al.* delivers a first discharge capacity of 1780 mAh/g [20]. They showed that the MOF-5 structure remains intact after the first discharge by XRD. However, the authors did not investigate the following discharge-charge cycles and showed only the initial discharge profile of MOF-5 cathode. We thus investigated here the electrochemical properties along few cycles of this material using the same formulation in order to have a point of comparison with the literature. Note however that our sealed battery assembly are filled with O₂ out of glove box prior to the tests. Besides, the electrolyte used consists of 1 M LiTFSI in DME.

The first discharge profiles of five similar R-MOF-5 cathodes are shown in Figure IV-10. Despite the rigid structure with constant pore opening, we effectively observe a wide range of initial discharge capacities among the different R-MOF-5 cathode samples from 393 mAh/g to 1390 mAh/g. Only the best capacity value that we obtained is in the same order as the result obtained by Li *et al.* (1780 mAh/g). However, it is worth mentioning that Li *et al.* [20] did not address the reliability of the reported capacity. It is unclear if the reported capacity corresponds to the optimal result or to a reproducible one. In our case, the R-MOF-5 cathodes provide an onset discharge plateau voltage of 2.7 V and the discharge potentials of 2.6 V, which is similar to the reported result of Li *et al.* [20].

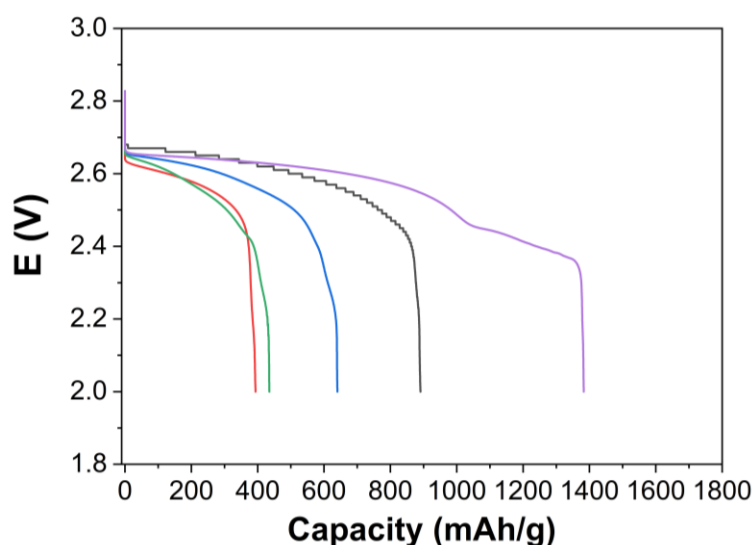


Figure IV-10 : First discharge profiles of Li-O₂ batteries with five similar R-MOF-5.

Figure IV-11 illustrates the cycling performance of R-MOF-5 electrodes. Upon galvanostatic cycling, a maximal discharge capacity is reached at the second cycle for four of the cells. A possible activation seems also necessary at the first cycle for the R-MOF-5, following the MIL-53 cases. The discharge capacity fades gradually over cycling and the charge provides a plateau at ~ 4.4 V, especially at the first two cycles. Discharge and charge capacities fade quickly starting from the second cycle. An increase of polarization appears during the cycling of R-MOF-5 electrodes. CE maintains a level of 80% from the fourth cycle, but it does not imply a great reversibility of the ORR / OER processes. Indeed, the difference between charge and discharge capacities on these cycles becomes less important as a result of significant capacity fading ahead. At the end of the 10th cycle, the remaining discharge capacity accounts for only less than 100 mAh/g.

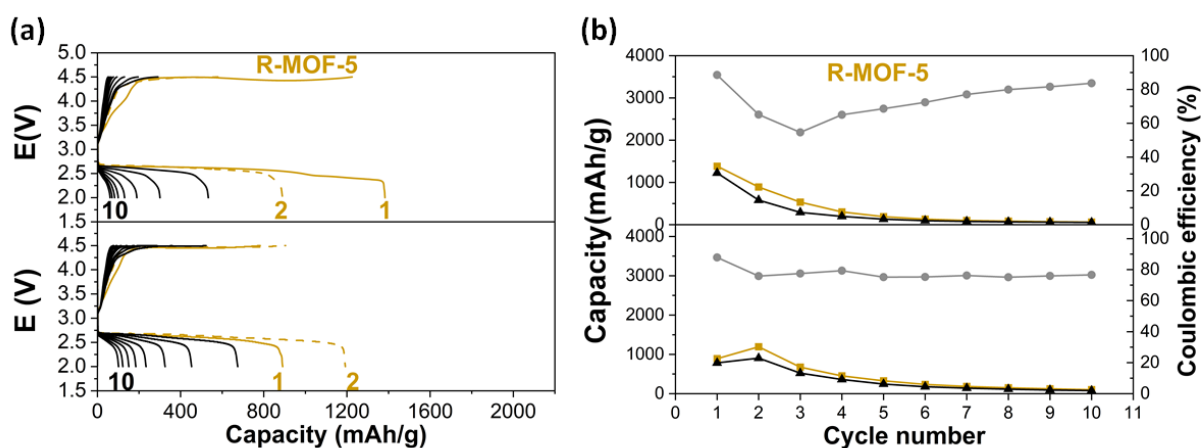


Figure IV-11 : (a) Galvanostatic discharge-charge cycling profiles of Li-O₂ batteries with R-MOF-5 electrodes. The first and second cycles are respectively represented in yellow solid and dash lines, while cycles 3 to 10 are represented in black solid lines. (b) R-MOF-5 discharge (yellow square) and charge (black triangle) capacities along with the coulombic efficiency (grey circle) in Li-O₂ batteries as a function of the cycle number.

IV.2.2. Comparison with MIL-53(Al) and effect of flexibility

In order to have a point of comparison with R-MOF-5, we explored the flexible H-MIL-53(Al) in the same conditions, i.e with a low MOF content (40% MOF / 40% C_{sp} / 20% PVDF). We now compare the results of the flexible structure H-MIL-53(Al) with R-MOF-5. We will then discuss the effect of pore flexibility on the Li-O₂ battery cycling performance.

Three individual tests with H-MIL-53(Al) electrodes were performed with the same formulation as R-MOF-5 (40/40/20 wt.%). Figure IV-12 compares the first and the second discharge capacities of H-MIL-53(Al) and R-MOF-5 electrodes in the Li-O₂ batteries. Similarly to the results obtained earlier with high MIL-53(Al) content (65 wt.%) electrodes in Section IV.1, two behaviors are observed for H-MIL-53(Al): for two-thirds of electrodes, the activation process occurs at the first cycles while the remaining one-third of electrodes delivers a maximum capacity at the first cycle. The discharge capacity distribution is in a wide range of 1000 - 3390 mAh/g. For the electrodes submitted to an activation process (discharge capacity $Q_1 < Q_2$), the cells deliver first discharge capacities approximatively in the same magnitude as the rigid R-MOF-5. However, after activation, the corresponding second discharge capacities of H-MIL-53(Al) could even reach over 3000 mAh/g, which is almost twice higher than the R-MOF-5 electrode. Such improvement in the discharge capacity might be triggered by the flexible pores of H-MIL-53(Al) upon activation. The MOF-5 structure has in contrast small pore size variation as adsorbent [23]. Thus, the pore size of R-MOF-5 remains still while accommodating the discharge product. In contrast, the H-MIL-53(Al) structure remains flexible even though it reveals a narrow pore during electrode preparation. It is possible that the pore breathes during the activation, leading to an enhanced accommodation of discharge products. The OCV for H-MIL-53(Al) is approximatively in the same order as R-MOF-5 (2.80 - 2.87 V for MIL-53(Al) and 2.79 - 2.83 V for R-MOF-5).

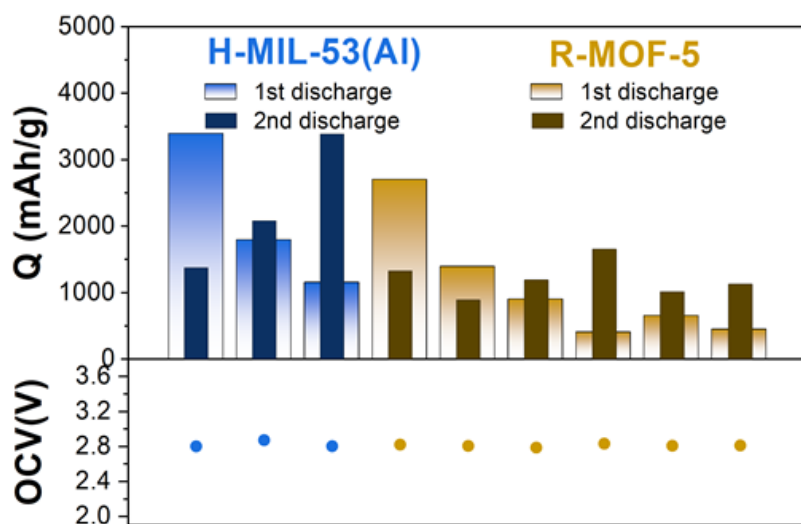


Figure IV-12 Discharge capacities at the first and second cycles for Li-O₂ batteries with H-MIL-53(Al) (blue) and R-MOF-5 electrodes (brown) and associated open-circuit voltages.

Figure IV-13 illustrates the discharge and charge capacities evolution of H-MIL-53(Al) electrodes. H-MIL-53(Al) can deliver a high discharge capacity of 3390 mAh/g at the first cycle. Despite this promising feature, only half of the initial discharge capacity remains at the second discharge. For the H-MIL-53(Al) electrodes submitted to the activation process at the first cycle (discharge capacity between 1143 - 1786 mAh/g), a higher discharge capacity (from 2000 mAh/g up to 3500mAh/g) could be reached at the second cycle. Similarly to the R-MOF-5 electrode, the activation process at the first cycle allows a higher discharge capacity delivery at the second cycle with a good coulombic efficiency maintained over 80 % during the first four cycles. For the electrodes reaching the highest discharge capacity at the first cycle, an efficient charge leading to a CE of *ca.* 80 % occurs. We may attribute this quite high efficiency to the good electric conductivity ensured by the high carbon content (40 wt. %) in the electrode formulation. However, a severe drop in capacities still happens since the second cycle. A discharge capacity of *ca.* 1500 mAh/g is maintained at the second cycle, while a CE less than 40 % is reached. Similarly to previous observations with other MOFs electrodes of this work, the decomposition of insulating Li_2O_2 remains incomplete due to the lack of catalyst in H-MIL-53(Al). The pores are clogged by the discharge products or parasitic products accumulated along cycling, and less porosity is available for the next deposition of Li_2O_2 . However, compared to the R-MOF-5 with the robust pore size, the flexible H-MIL-53(Al) provides better capacities at a first glance. The flexible structure seems thus predominant for accommodating Li_2O_2 . Yet, both H-MIL-53(Al) and MOF-5 show quick capacity fading upon cycling, meaning that the opening of the pore does not improve the capacity retention of the battery.

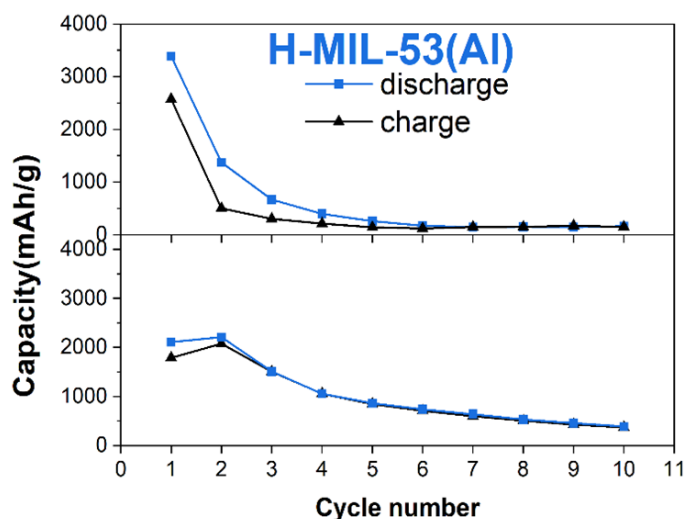


Figure IV-13 : Discharge (square) and charge (triangle) capacity evolutions of the $\text{Li}-\text{O}_2$ batteries with H-MIL-53(Al) low content electrode as a function of the cycle number Case 1: $Q_1 < Q_2$. Case 2: $Q_1 > Q_2$. Electrode formulation : MOF/ C_{sp} /PVDF = 40/40/20 wt. %.

For comparison purposes, we also prepared the pure C_{sp} electrodes with the formulation 80/20 wt. % (for C_{sp} and PVDF respectively). Figure IV-14 compares the discharge and charge profiles at the 1st and the 2nd cycle of R-MOF-5 and H-MIL-53(Al) electrodes and pure C_{sp} electrodes. The discharge / charge profiles are in agreement with the reported carbon electrode in the literature [17]. Compared to the pure C_{sp} electrode, both R-MOF-5 and H-MIL-

53(Al) electrodes with low MOF content show polarizations as high as with the high MOF content electrodes (Section IV.1). Both R-MOF-5 and H-MIL-53(Al) show not only lower discharge potentials but also higher charge potentials than carbon electrodes (discharge potential: ~ 2.63 V vs. ~ 2.66 V and charge potential ~ 4.5 V vs. ~ 4.3 V, for MOF and C_{sp} respectively). This may again be due to the lower conductivity of the MOF materials. Even with a lower MOF content (40 %), the conductivity is still too low compared to the pure C_{sp} .

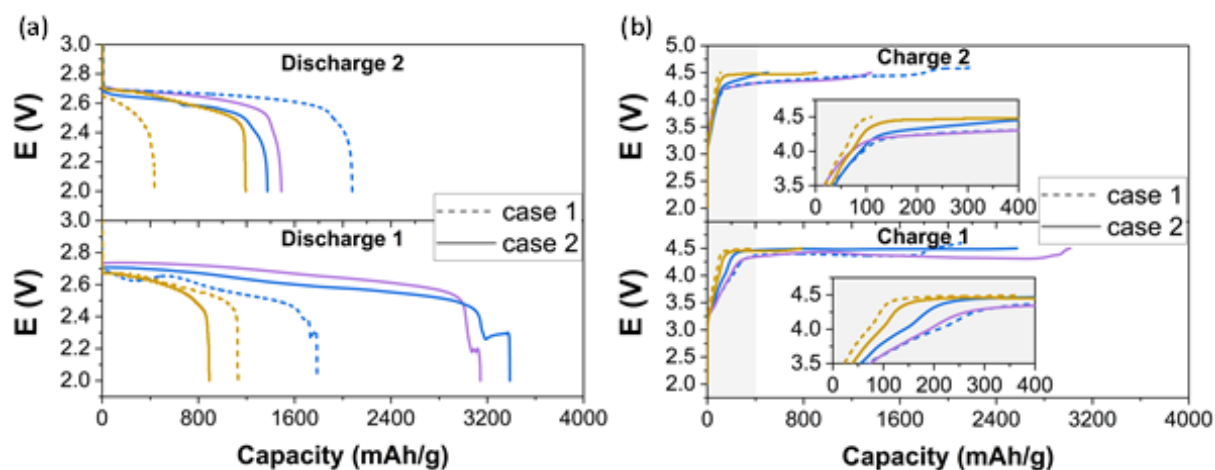


Figure IV-14 : Comparison of (a) discharge and (b) charge profiles at the 1st and 2nd cycles of Li-O₂ batteries with low R-MOF-5 or H-MIL-53(Al) weight content electrode. The electrode formulation is 40/40/20 wt.% for MOF/ C_{sp} /PVDF. Yellow/blue solid lines: $Q_1 < Q_2$ (case 1), yellow/blue dash lines: $Q_1 > Q_2$ (case 2) for R-MOF-5/MIL-53(Al). Purple solid lines: pure C_{sp} electrode in an electrode formulation of C_{sp} /PVDF = 80/20 wt. %.

To conclude, the flexible H-MIL-53(Al) appears as a promising cathode material with a better first discharge capacity than the rigid R-MOF-5, as the flexible framework could accommodate the discharge products in the pore volume. The PVDF in rigid R-MOF-5 occupies part of the porosity, while the rigid framework of R-MOF-5 limits the insertion of discharge products. In turn, the H-MIL-53(Al) can deliver higher discharge capacities than the rigid R-MOF-5, however the capacity retention is poor. Finally, it is noteworthy that these better performances are obtained with low MOF content electrodes. The high content of carbon may also favor a better electronic conductivity and better performance of these MOF/C/PVDF composite electrodes.

IV.3 Discussion

As described in Chapter I, the cathode plays a crucial role as it hosts the essential ORR / OER processes of the Li-O₂ battery. The design of air cathode materials follows essentially three key rules. At first, a high porosity is mandatory for the storage of the Li₂O₂ discharge products. The porosity guarantees also the Li⁺ ion and O₂ diffusions and electrolyte penetration. Secondly, a good electronic conductivity is required for the fast electron supply for both ORR

/ OER. Finally, as these reactions are sluggish, a catalyst in the cathode is highly desirable so as to reduce the overpotential of the battery.

In this work, we investigated the flexible MIL-53(Al) and MIL-53(Fe) as cathode material in Li-O₂ batteries. The structural flexibility of MIL-53 implies the potential to accommodate / remove guest molecules. During electrode processing, the polymeric binder PVDF is adsorbed by the anhydrous MIL-53, resulting in MIL-53_PVDF form, while the electronic conductor C_{sp} remains intact in the cathode. We will discuss the global performance of the MOFs materials in comparison to the literature and discuss the effect of porosity and pore-opening on the MIL-53 electrode performances. Moreover, even if several studies addressed reproducibility issues of the Li-O₂ system based on carbon cathode [7], [24], there is still a lack of deep understanding of the reproducibility of pristine MOF cathodes. At the end of this section, we will discuss this issue related to the MIL-53 electrodes.

IV.3.1. Comparison with literature

Apart from the porosity, there are also two other crucial factors for the design of efficient cathodes for Li-O₂ batteries: guaranteeing the electronic conductivity and presenting catalytic sites to improve the sluggish ORR / OER. Inspired by all these requirements, various types of cathode materials have been developed, including the MOF-based electrodes. MOF materials are known for their porous structures and high surface areas. The MOFs having open metal sites (OMSs) could also act as catalysts for the ORR / OER.

Table IV-1 summarizes the physical and electrochemical properties of C_{sp} electrodes, some reported rigid MOFs, the H-MIL-53(Al) and MOF-5, all reported with a low MOF content.

Table IV-1 : BET, mass loading of both MOF and C_{sp}, and corresponding first discharge capacities of Li-O₂ battery with low MOF content electrode and related electrodes.

Materials	BET (m ² /g)	External surface (m ² /g)	MOF+C _{sp} mass loading (mg/cm ²)	Formulation (wt. %)	Capacity (mAh/g)	Ref.
MOF-5	3622	-	0.56	40/40/20	1780	[20]
Mn-MOF-74	1213	-	0.56	40/40/20	9420	[20]
C_{sp}	87.6	-	0.56	80/20	2170	[20]
C_{sp}	52.5	39.65	1.1	80/20	3327	This work
MOF-5	-	-	0.8 – 0.9	40/40/20	1390(max.)/ 750(mean)	This work
H-MIL-53(Al)	1240	52.13	0.9 – 1.0	40/40/20	3387(max.) / 2106 (mean)	This work

Li *et al.* reported in a pioneering work several benchmark MOFs (HKUST-1, MOF-5, and M-MOF-74 with M = Mg, Co, Mn) as cathodes for Li-O₂ batteries in 2014 [20]. These porous materials have high BET surfaces within a large range. The authors have shown that the presence of open metal sites (OMS or coordinatively unsaturated sites) in MOF materials can improve the capacity compared to the corresponding electrode without MOF. The OMSs are beneficial to bind with O₂. They also participate in the cleavage of the O₂ intermolecular bond during the discharge, as well as the O-O reformation during the charge [16]. For instance, the porous OMS-containing Mn-MOF-74 shows a high discharge capacity of 9420 mAh/g. The initial discharge capacity of a similar structure Mn-MOF-74 without accessible OMS (terminal water on metal cluster) is 30% lower than with the accessible OMS [20]. Besides, the Mn-MOF-74 solids show a gain of polarization of 0.62 V compared to the carbon black electrode [25]. This evidences the contributions of OMS to the capacity as well as to the reduction of overpotentials in a MOF-based Li-O₂ battery.

We have reproduced Li's experiment with MOF-5 and C_{sp} electrodes, and studied the MIL-53(Al) performance under similar conditions (with low MOF content electrode formulation). Li *et al.* reported only one capacity value for each material studied without mentioning the reproducibility [20]. When looking at our best result with MOF-5 electrodes, we are indeed approaching the value of Li *et al.*. We however in our case bring more with reproducibility experiments which show lower mean value, while it is unclear if Li's data is the best they obtained or a reliable result. Besides, our C_{sp} electrode delivers a capacity of *ca.* 3300 mAh/g, which is 1200 mAh/g superior to Li's work. It is possible that the higher mass loading used here contributes to the improvement of capacity [26]. Otherwise, this difference in capacity may be also attributed to the Li₂O₂ growth mechanism ensured by solvent. Following the model proposed by McCloskey *et al.* [27], the DME we used here with higher DN than TEGDME used by Li *et al.* [20] favors the stable solvation of Li⁺ and intermediate O₂⁻ species, thus inducing an increased capacity.

When looking at the performance of the flexible H-MIL-53(Al) electrodes, we show that it presents a high initial discharge capacity with an average of 2106 mAh/g and a maximum up to 3387 mAh/g, which is comparable with the discharge capacities obtained for MOF-5 and C_{sp}. Although the external surface areas of both compounds are in the same range, we can note that the overall surface area is much higher for H-MIL-53(Al) compared to C_{sp}. Regarding our present result, a high surface area is not sufficient to enhance the electrochemical performance.

While the best or the mean initial discharge capacity of H-MIL-53(Al) is over 2-fold higher than the MOF-5, the uptake of O₂ of MIL-53(Al) is similar to the coordination-saturated MOF-5 (5.5 mg/g at 288K for MIL-53(Al) [28] and 6.6 mg/g at 273 K for MOF-5 [20]). Thus, the superior performance of MIL-53(Al) compared to MOF-5 in the Li-O₂ battery is most probably promoted by the flexible structure. In other words, the flexible structure is beneficial for the accommodation of discharge products in Li-O₂ batteries.

Upon exploring MIL-53(Al) electrodes, we have assumed that the flexibility of the framework may hinder their performance in the Li-O₂ batteries, explaining the lower capacities obtained in comparison to MOF reported by Li et al. At first, the narrow pore limits the storage capacity of the Li₂O₂, its deposition could quickly fill entirely the pores. Besides, it may also prevent the decomposition of Li₂O₂ during the charge, as these particles might be held tight by the narrow pores for MIL-53(Al). While for the alternative MIL-53(Fe), the pores are fully open upon absorption of solvent molecules. A higher initial discharge capacity is delivered (~2000 mAh/g). This pore-opening is believed to facilitate the deposition / decomposition of Li₂O₂, thus resulting in the improved initial discharge capacity. Yet the capacities are still far from the 9420 mAh/g obtained with an OMS-based MOF [20]. Moreover, the MIL-53(Fe) shows a charge potential of near 4.3 V, as high as with the pure C_{sp} electrode, illustrating a lack of OER catalytic activity for the framework. As a result, such high charge potential may lead to electrolyte decomposition [16]. In turn, the deposition of parasitic products, as well as the residual Li₂O₂, may thus increase the internal battery resistance, and cause a higher polarization over cycling. Thus, the absence of catalytic sites in the MIL-53 series partly explains the more modest capacities obtained in comparison to the literature. The use of efficient electrocatalysts for OER, especially, is mandatory for better Li-O₂ performance.

IV.3.2. Reproducibility issues

Overall, in this thesis, numerous independent cells with MIL-53(Al) / MIL-53(Fe) cathodes have been meticulously cycled targeting reproducible results to estimate the average capacity of each system. However large discrepancies in initial discharge capacities have been observed with MIL-53 electrodes.

In the case of a high MIL-53(Al) content electrode, a large discrepancy in discharge capacity of MIL-53(Al) has been observed from 12 mAh/g to 1214 mAh/g (Figure IV-15). We cannot attribute directly this large discrepancy to the failure of the flexible MIL-53 material, as this phenomenon has been already reported with other carbon-based electrodes [7], [29]. In contrast, several trends in capacity evolution over cycling are observed with MIL-53(Al) and MIL-53(Fe) electrodes. In general, at the initial cycle, two-thirds of all tests are able to deliver high discharge capacities, while the rest could only deliver a low discharge capacity with MIL-53(Al) or a low charge capacity with MIL-53(Fe). Noteworthy, the reproducibility issue is inherent in the Li-O₂ system, as described notably by Larcher *et al.* [29] For example, they showed that initial discharge capacity ranges from 2 to 87 mAh/g for six individual cells with homogenous carbon-fiber gas diffusion layer electrodes. Critical parameters of the cathode may thus impact the reliability of the electrochemical performances. We are giving below some possible insights.

At first, a non-uniform electrode distribution may affect the variation of capacity. In our case, we have developed a standardized drop-casting procedure (Chapter II.2.1.1) for a reliable mass loading preparation around 1 mg/cm² for both MOF and C_{sp} electrodes. The final specific mass loading of (MIL-53+C_{sp}) are achieved between 0.8 to 1.5 mg/cm², *i.e.* 2.0 – 3.7 mg per

electrode. This value of active material loading mass is widely used for air cathodes [30]–[32]. Figure IV-15 illustrates the initial discharge capacities of high MIL-53 content electrodes as well as their specific loading mass. The results are plotted with the evolution of capacity. It indicated clearly that there is no direct relationship between the capacities obtained and the specific loading mass deviating around 1.0 mg/cm^2 . Even having the same mass loading, electrodes capacities could vary. For instance, for the four electrodes with the same loading of 1.1 mg/cm^2 with MIL-53(Al) (Figure IV-15 (a)), a large discrepancy in their first capacities exists, ranging from 700 to 1200 mAh/g. One possible hypothesis to these scattered results is the inhomogeneous distribution of electrode components during electrode processing. According to Lestriez *et al.* [33], not-well dispersed formulation and / or improper electrode processing might result in inhomogeneous ink deposition from one electrode to another, such as the agglomeration of the polymeric binder, excess of binder, or lack of conductive additives, *etc.* However, the latter assumption seems untenable in our case. For the electrodes delivering discharge capacities lower than 300 mAh/g at the first cycle, a large capacity up to 1000 mAh/g can still be reached at the second cycle, except if the first cycle contributes to redistribution and homogenization of species.

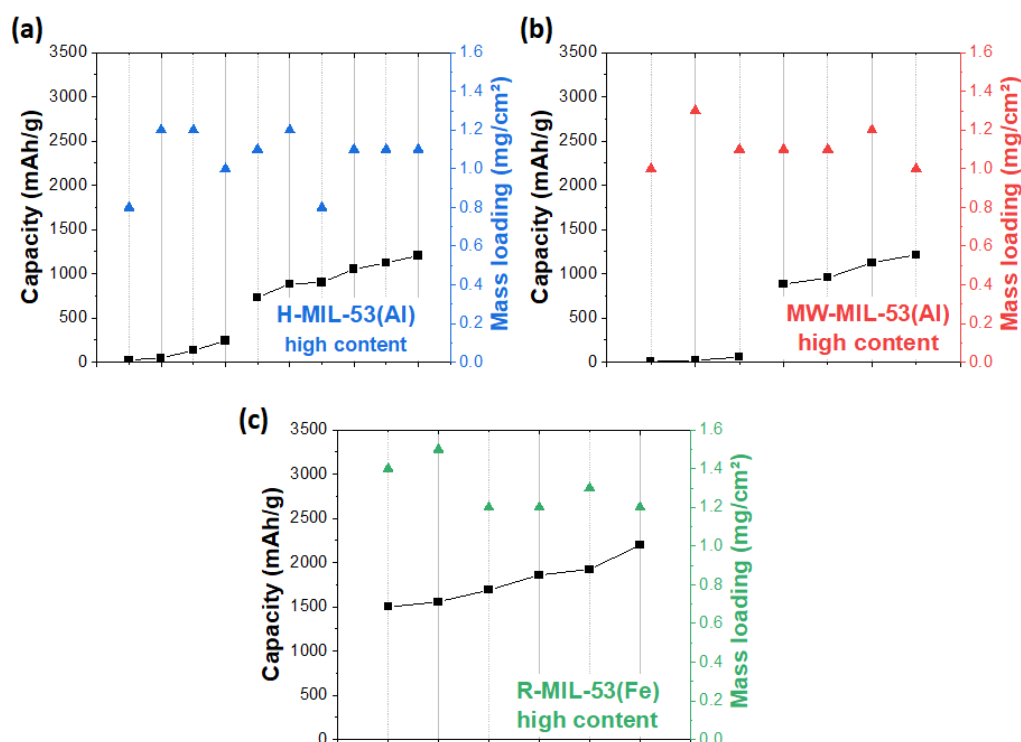


Figure IV-15 : First discharge capacities of Li-O₂ battery (black lined square) with the corresponding specific mass loading for (a) H-MIL-53(Al), (b) MW-MIL-53(Al), and (c) R-MIL-53(Fe) electrodes. The capacities are measured with 23 similar cells in total. For MIL-53(Al) electrodes, two behaviors are observed: capacities less than 300 mAh/g, and large capacities with more than 700 mAh/g. The results of each behavior are lined up. For MIL-53(Al) electrode, the capacities are more centered at 2000 mAh/g.

Apart from the specific mass loading of active material, another crucial parameter is the accessible porosity, *i.e.* the active surface and pore size of the cathode material. As mentioned in Chapter I, a larger pore size accommodates more Li_2O_2 during the discharge process, while the pore's entrance easily clogs if the pore size is too small, preventing access to the inner pore volume. The MIL-53(Al) samples present a type I N_2 adsorption isotherm (Appendix 3, Figure A.-4), denoting that they are microporous materials. According to the IUPAC classification, microporous materials have pore diameters up to 2 nm [34]. Based on previous research [35], a pore size less than 10 nm might be too narrow for O_2 diffusion and might easily be blocked during the cathode processing despite the use of a low binder content. Indeed, the XRD patterns of both MIL-53(Al) pristine electrodes confirm the pore occupation by PVDF. While for the anhydrous MIL-53(Al) the pores are open, they shrink upon adsorbing the PVDF molecules, resulting in narrow pores (pore size = $19.6 \text{ \AA} \times 8.8 \text{ \AA}$). This contraction may further deteriorate the pore accessibility. Especially, the "sudden death" with a low discharge capacity may be induced by several possible cloggings: the encapsulated PVDF, or also some electrolyte, or degradation products, or the generated discharge product Li_2O_2 . At the initial discharge, if PVDF or electrolyte clog completely the pores, they thus impede the deposition of Li_2O_2 discharge products and lead to an abrupt voltage drop and an early end of discharge [9]. Upon recharging, a possible activation process removing PVDF or the passivation layer may allow the reopening of the pores, which facilitates the future accommodation of Li_2O_2 and O_2 diffusion. As we observed earlier in Section IV.1.1, these latter electrodes allow to chase up discharge capacities at the second cycle as high as other electrodes delivering their highest capacity at the initial cycle. It may be possible that the PVDF-containing pores are unevenly distributed between electrodes. Some electrodes may have more accessible pores and are therefore able to show medium or high discharge capacity at the first cycle. This phenomenon may explain the two trends observed and the lack of reproducibility of the MIL-53.

In the case of MIL-53(Fe), the anhydrous MIL-53(Fe) analogue allows, in contrast, an enlargement of the pore dimension from its anhydrous form by adsorbing PVDF, with a pore size of $18.5 \text{ \AA} \times 11.3 \text{ \AA}$ (Chapter III.3). It may explain why we do not have any reproducibility issues at the first discharge with the Fe analogue. However, some of these electrodes exhibit limited charge capacities at the first cycle. This early "sudden death" is probably related to interface phenomena. The gradual shrinkage of Li_2O_2 particles upon charging may induce a disconnection of the Li_2O_2 from the substrate. Consequently, the lack of interface contact blocks the electron transfer pathway, leading to the end of the charge. Still, the following discharge process with new Li_2O_2 formation rebuilds up the better Li_2O_2 / electrode, Li_2O_2 / electrolyte interfaces, thus allowing a deep second charge.

For all MIL-53 electrodes, we have hardly observed reproducible capacities when comparing electrodes at the same cycling number. Considering all aforementioned potential impacts, the accessible porosity for Li_2O_2 deposition still needs to be further controlled for reliable results. It is worthy to measure the porosity of MIL-53_PVDF to further understand the mechanism of Li_2O_2 accommodation inside the pore of MIL-53 electrodes.

Finally, we should keep in mind the intrinsic issue about the insulating Li_2O_2 . Studies have illustrated that a crucial Li_2O_2 thickness of 5-10 nm could also impulse the “sudden death” of discharge even on the glassy carbon electrode, as the Li^+ ion and electron transport through the insulating Li_2O_2 layer is too small to support equivalent electrochemical current [11]. Its deposition strongly influences capacity. Thus, a suitable optimization between the deposited Li_2O_2 thickness and the capacity might be a key for achieving a long-life battery.

IV.4 Conclusion

In this chapter, we studied the electrochemical properties in Li-O₂ batteries with MIL-53 electrodes. The effect of several factors related to the MOF electrodes properties was discussed, including the crystal size and flexibility. We investigated three flexible MIL-53 materials based on Al and Fe metal sites as the active material of air cathode in the Li-O₂ batteries and we compared their behaviors with a rigid MOF and pure super P carbon (C_{sp}) electrodes.

Due to their high surface area, both porous MIL-53(Al) electrodes were expected to deliver higher capacity compared to the C_{sp} . An average discharge capacity at the first discharge of 1000 mAh/g is obtained for both MIL-53(Al), denoting their potential as cathodes for Li-O₂ batteries. However, the highly porous MIL-53(Al) does not show superior capacities and capacity retention than the pure C_{sp} electrode. This is mainly related to the poor electric conductivity of insulating MOFs and to the pore size reduction upon adsorbing polymeric binder during electrode preparation, which prevents the accommodation of the discharge products. Interestingly, the discharge capacities for some electrodes are really low at the first cycle compared to the second cycle. An activation process is then necessary in that case so as to remove the possible passivation layer or the guest PVDF from the pores. Finally, we discovered that the decomposition of discharge products in charge (OER) is almost completely impeded in MIL-53(Al), as shown by the very limited charge capacities observed. Lack of catalytic sites explains the poorly efficient OER, explaining the rapid capacity fading and limited cyclability observed. As previously shown in Chapter III, the MIL-53(Al) presents closed pores when impregnated with solvent. We suggest that the closed pores in MIL-53(Al) could be hardly reopened for the decomposition of discharge products (OER) during the charge process. Concerning the effect of morphology, we showed that the particle sizes of MIL-53(Al) compounds (500 nm – 2 μm) do not play a role in the capacity delivery, as similar capacities are reached with both synthesis methods.

Based on the poor charge capacity obtained with closed pores MIL-53(Al), we then investigated the flexible R-MIL-53(Fe) showing opened pores with PVDF. Enhancements in both discharge/charge capacities were obtained for R-MIL-53(Fe). The expansion in volume with R-MIL-53(Fe) favors the accommodation of discharge products. The different breathing behaviors result in higher discharge capacity deliveries with R-MIL-53(Fe) than MIL-53(Al) (in average ~2000 mAh/g for R-MIL-53(Fe) vs. ~1000 mAh/g for MIL-53(Al)). Better ORR / OER performances and cyclability could be obtained with the opened pore R-MIL-53(Fe). However,

for some R-MIL-53(Fe) electrodes, a delay in charge capacity delivery is observed due probably to the clogging of the pore volume or obstruction of reaction sites while charging.

We finally compared the effect of the flexibility on the performance of the MOFs cathodes by comparing two compounds with similar pore sizes: the flexible MIL-53(Al) and the rigid structure MOF-5. As the PVDF is already occupied part of the pore volume of the MOF material, the rigid MOF-5 has a restricted volume for accommodating discharge products. After the activation process, the flexible MIL-53(Al) electrodes show higher discharge capacity than MOF-5 electrodes (300 – 2000 mAh/g improvement in discharge capacities compared to MOF-5 at the second cycle). The activation process allows an expansion in MIL-53(Al) pore volume thus favoring a higher discharge capacity at the second cycle compared with the robust framework MOF-5. This highlights the importance of porosity in promoting the Li-O₂ battery performance. The flexible MIL-53 structure is promising for improving the Li-O₂ battery performance compared to the rigid structure. Note that in this case high capacities above 1000 mAh/g are reached for MIL-53(Al) but with a formulation containing only 40 wt. % of MOF instead of 65 wt. % when MIL-53(Al) and MIL-53(Fe) were compared. This appears promising but deviates from our initial intent of using MOF as the major active material in the Li-O₂ battery. Compared to either C_{sp} or porous rigid MOF-5, the flexible porous structure of MIL-53(Al) is beneficial for the good capacity in Li-O₂ batteries. Furthermore, thanks to the pore-opening, the MIL-53(Fe) provides better capacities than MIL-53(Al).

Overall, the poor electronic conductivity of all aforementioned MOF materials results in a high polarization. The absence of catalytic sites contributes also to the high overpotentials, leading to unsatisfactory ORR and OER in the Li-O₂ batteries. A general activation process in the first cycle is assumed to be necessary for almost all porous MOF electrodes to remove the possible passivation layer or the guest PVDF from the pores. The poor electronic conductivity of insulating MOF makes the electrodes still less competitive than the pure C_{sp} carbon electrode in terms of cyclability and delivered capacity. It is thus necessary to reduce the polarization of MOF electrodes. Alternative catalytic additives, such as metal oxide or open metal site in the framework, *etc.*, will be interesting to improve the Li-O₂ battery performance.

Finally, we observed that our results (capacity, CE...) are highly scattered whatever the considered MOF. Although this is a relatively common observation in Li-O₂ battery investigation, and also not systematically addressed, we emitted some hypotheses for the reproducibility issue. At first, non-uniform ink contents could lead to an inhomogeneous distribution of porosity, which we proved to be indispensable for the air cathode. Besides, a non-reversible pore opening, such as MIL-53(Al) with narrow pores, diminishes the reversible charge process. This could cause a pore-clogging and a higher polarization by the insulating Li₂O₂ or parasitic products. Moreover, the loss of triple points during the cycling may lead to sudden death in capacities. Further investigations are needed to address these issues and improve the global performances of such electrodes.

IV.5 References

- [1] O. M. Linder-Patton *et al.*, "Particle size effects in the kinetic trapping of a structurally-locked form of a flexible MOF," *CrystEngComm*, vol. 18, n° 22, pp. 4172–4179, 2016.
- [2] Y. Zhang *et al.*, "MIL-53 Metal-Organic Framework as a flexible cathode for lithium-oxygen batteries," *Materials*, vol. 14, n°16, Art. n°16, 2021.
- [3] Y. Hu, T. Zhang, F. Cheng, Q. Zhao, X. Han, and J. Chen, "Recycling application of Li–MnO₂ batteries as rechargeable lithium-air batteries," *Angew. Chem.*, vol. 127, n°14, pp. 4412–4417, 2015.
- [4] F. Cheng *et al.*, "Facile controlled synthesis of MnO₂ nanostructures of novel shapes and their application in batteries," *Inorg. Chem.*, vol. 45, n°5, pp. 2038–2044, 2006.
- [5] A. Débart, A. J. Paterson, J. Bao, and P. G. Bruce, "α-MnO₂ Nanowires: a Catalyst for the O₂ electrode in rechargeable lithium batteries," *Angew. Chem.*, vol. 120, n°24, pp. 4597–4600, 2008.
- [6] W. Yan, Z. Guo, H. Xu, Y. Lou, J. Chen, and Q. Li, "Downsizing metal–organic frameworks with distinct morphologies as cathode materials for high-capacity Li–O₂ batteries," *Mater. Chem. Front.*, vol. 1, n°7, pp. 1324–1330, 2017.
- [7] L. D. Griffith, A. E. S. Sleightholme, J. F. Mansfield, D. J. Siegel, and C. W. Monroe, "Correlating Li/O₂ cell capacity and product morphology with discharge current," *ACS Appl. Mater. Interfaces*, vol. 7, n°14, pp. 7670–7678, 2015.
- [8] I. Landa-Medrano, I. Ruiz de Larramendi, N. Ortiz-Vitoriano, R. Pinedo, J. Ignacio Ruiz de Larramendi, and T. Rojo, "In situ monitoring of discharge/charge processes in Li–O₂ batteries by electrochemical impedance spectroscopy," *J. Power Sources*, vol. 249, pp. 110–117, 2014.
- [9] C. Xia, C. L. Bender, B. Bergner, K. Peppler, and J. Janek, "An electrolyte partially-wetted cathode improving oxygen diffusion in cathodes of non-aqueous Li–air batteries," *Electrochem. Commun.*, vol. 26, pp. 93–96, 2013.
- [10] A. Kube, F. Bienen, N. Wagner, and K. A. Friedrich, "Wetting behavior of aprotic Li–air battery electrolytes," *Adv. Mater. Interfaces*, vol. 9, n°4, p. 2101569, 2022.
- [11] A. C. Luntz and B. D. McCloskey, "Nonaqueous Li–air batteries: a status report," *Chem. Rev.*, vol. 114, n°23, pp. 11721–11750, 2014.
- [12] D. Geng *et al.*, "From lithium-oxygen to lithium-air batteries: challenges and opportunities," *Adv. Energy Mater.*, vol. 6, n°9, p. 1502164, 2016.
- [13] Y.-C. Lu, H. A. Gasteiger, M. C. Parent, V. Chiloyan, and Y. Shao-Horn, "The influence of catalysts on discharge and charge voltages of rechargeable Li-oxygen batteries," *MIT Web Domain*, Apr. 2010, A.
- [14] B. M. Gallant, D. G. Kwabi, R. R. Mitchell, J. Zhou, C. V. Thompson, and Y. Shao-Horn, "Influence of Li₂O₂ morphology on oxygen reduction and evolution kinetics in Li–O₂ batteries," *Energy Environ. Sci.*, vol. 6, n°8, pp. 2518–2528, 2013.

- [15] J. Read, "Characterization of the lithium-oxygen organic electrolyte battery," *J. Electrochem. Soc.*, vol. 149, n°9, p. A1190, 2002.
- [16] T. Liu, J. P. Vivek, E. W. Zhao, J. Lei, N. Garcia-Araez, and C. P. Grey, "Current challenges and routes forward for nonaqueous lithium-air batteries," *Chem. Rev.*, vol. 120, n°14, pp. 6558–6625, 2020.
- [17] S. S. Zhang, D. Foster, and J. Read, "Discharge characteristic of a non-aqueous electrolyte Li/O₂ battery," *J. Power Sources*, vol. 195, n°4, pp. 1235–1240, 2010.
- [18] A. Débart, A. J. Paterson, J. Bao, and P. G. Bruce, "α-MnO₂ nanowires: a catalyst for the O₂ Electrode in Rechargeable Lithium Batteries," *Angew. Chem. Int. Ed.*, vol. 47, n°24, pp. 4521–4524, 2008.
- [19] T. Zhang and H. Zhou, "A reversible long-life lithium-air battery in ambient air," *Nat. Commun.*, vol. 4, n°1, Art. n° 1, 2013.
- [20] D. Wu *et al.*, "Metal-organic frameworks as cathode materials for Li-O₂ batteries," *Adv. Mater.*, vol. 26, n°20, pp. 3258–3262, 2014.
- [21] D. J. Tranchemontagne, J. R. Hunt, and O. M. Yaghi, "Room temperature synthesis of metal-organic frameworks: MOF-5, MOF-74, MOF-177, MOF-199, and IRMOF-0," *Tetrahedron*, vol. 64, n°36, pp. 8553–8557, 2008.
- [22] M. Eddaoudi, H. Li, and O. M. Yaghi, "Highly porous and stable metal-organic frameworks: structure design and sorption properties," *J. Am. Chem. Soc.*, vol. 122, n°7, pp. 1391–1397, 2000.
- [23] S. M. Mirsoleimani-azizi, P. Setoodeh, S. Zeinali, and M. R. Rahimpour, "Tetracycline antibiotic removal from aqueous solutions by MOF-5: Adsorption isotherm, kinetic and thermodynamic studies," *J. Environ. Chem. Eng.*, vol. 6, n°5, pp. 6118–6130, 2018.
- [24] H. Cheng and K. Scott, "Carbon-supported manganese oxide nanocatalysts for rechargeable lithium-air batteries," *J. Power Sources*, vol. 195, n°5, pp. 1370–1374, 2010.
- [25] S. H. Kim, Y. J. Lee, D. H. Kim, and Y. J. Lee, "Bimetallic Metal-Organic Frameworks as efficient cathode catalysts for Li-O₂ batteries," *ACS Appl. Mater. Interfaces*, vol. 10, n°1, pp. 660–667, 2018.
- [26] M. Carboni, A. G. Marrani, R. Spezia, and S. Brutti, "Degradation of LiTfO/TEGME and LiTfO/DME electrolytes in Li-O₂ batteries," *J. Electrochem. Soc.*, vol. 165, n°2, p. A118, 2018.
- [27] C. M. Burke, V. Pande, A. Khetan, V. Viswanathan, and B. D. McCloskey, "Enhancing electrochemical intermediate solvation through electrolyte anion selection to increase nonaqueous Li-O₂ battery capacity," *Proc. Natl. Acad. Sci.*, vol. 112, n°30, pp. 9293–9298, 2015.
- [28] P. Rallapalli, K. P. Prasanth, D. Patil, R. S. Somani, R. V. Jasra, and H. C. Bajaj, "Sorption studies of CO₂, CH₄, N₂, CO, O₂ and Ar on nanoporous aluminum terephthalate [MIL-53(Al)]," *J. Porous Mater.*, vol. 18, n° 2, pp. 205–210, 2011.
- [29] C. Gaya, A. A. Franco, C. Surcin, M. Courty, and D. Larcher, "Carbon-loaded flexible electrode films for Li-O₂ cells: preparation, porosity, homogeneity and electrochemical characterization," 2020, doi: 10.26434/chemrxiv.13292759.v1.

- [30] N. Feng *et al.*, "A multi-layered Fe₂O₃/graphene composite with mesopores as a catalyst for rechargeable aprotic lithium–oxygen batteries," *Nanotechnology*, vol. 27, n°36, p. 365402, 2016.
- [31] C. Shang *et al.*, "Fe₃O₄@CoO mesospheres with core-shell nanostructure as catalyst for Li-O₂ batteries," *Appl. Surf. Sci.*, vol. 457, pp. 804–808, 2018.
- [32] N. Mahne *et al.*, "Singlet oxygen generation as a major cause for parasitic reactions during cycling of aprotic lithium–oxygen batteries," *Nat. Energy*, vol. 2, n°5, pp. 1–9, 2017.
- [33] S. J. Tambio, F. Cadiou, E. Maire, N. Besnard, M. Deschamps, and B. Lestriez, "The concept of effective porosity in the discharge rate performance of high-density positive electrodes for automotive application," *J. Electrochem. Soc.*, vol. 167, n° 16, p. 160509, 2020.
- [34] F. Ambroz, T. J. Macdonald, V. Martis, and I. P. Parkin, "Evaluation of the BET theory for the characterization of meso and microporous MOFs," *Small Methods*, vol. 2, n°11, p. 1800173, 2018.
- [35] O. L. Li and T. Ishizaki, "Chapter 4 - Development, challenges, and prospects of carbon-based electrode for lithium-air batteries," in *Emerging Materials for Energy Conversion and Storage*, K. Y. Cheong, G. Impellizzeri, and M. A. Fraga, Eds. Elsevier, 2018, pp. 115–152..

Chapter V. *Ex situ* characterizations

This chapter will present the *ex situ* analyses realized on discharged MIL-53 electrodes to understand the electrochemical behavior of these materials. Various characterization techniques are applied, including *ex situ* XRD, SEM, and XPS. The lithium peroxide (Li_2O_2) is identified as the main discharge product on MIL-53 electrodes. Depending on the state of discharge of each MIL-53 electrode, different Li_2O_2 morphologies are observed, including platelets, toroids and pseudo-spheres.

V.1 Nature and morphology of discharge products

To perform *ex situ* characterizations on cycled MIL-53 electrodes, similar individual Li-O₂ batteries with MIL-53 electrodes were galvanostatically cycled for 1 discharge or for 10 discharges. The electrodes were immediately recovered at the end of discharge. Each electrode was sectioned into small samples pieces for both XRD and SEM analyses. The discharge products and active materials are easily removed by gentle DME rinsing. Hence, no rinsing was applied on samples for XRD and SEM analyses to avoid discharge product loss. However, rinsing was found mandatory for XPS measurements.

V.1.1. *Ex situ* X-ray diffraction

In order to identify the nature of the discharge products, the MIL-53 electrodes before and after cycling were investigated by XRD. As the discharged products are highly air-sensitive, it is necessary to record XRD diffractograms using an adequate sample protection. In this work, we used a Kapton tape. Unfortunately, this tape gives a signal in Bragg-Brentano geometry (with the Cu anode) which masks a non-negligible part of the signal from the electrodes. We alternatively used the Mo anode diffractometer in transition geometry, whose incident source allows us to go through the whole sample and the two Kapton tape layers, generating viable diffraction signals. Figure V-1 illustrates the XRD patterns as a function of reciprocal lattice distance $1/d_{hkl}$ with both Mo and Cu anodes. The resolution with the Mo anode was not as good as with the Cu anode; for example, the two first peaks for R-MIL-53(Fe) cannot be separated. Yet we can still identify some peaks of the MIL-53 compound. The MIL-53 ink powder samples reveal diffraction peaks for crystalline MIL-53, while C_{sp} and PVDF are amorphous. An additional peak at $1/d_{hkl} = 0.30 \text{ \AA}^{-1}$ is observed for all electrodes, corresponding to the Toray carbon paper. Above all, we can hardly observe changes in MIL-53 on the patterns acquired with Mo radiation but at least it is sufficient to identify the formation of discharge products on the Kapton protected electrodes.

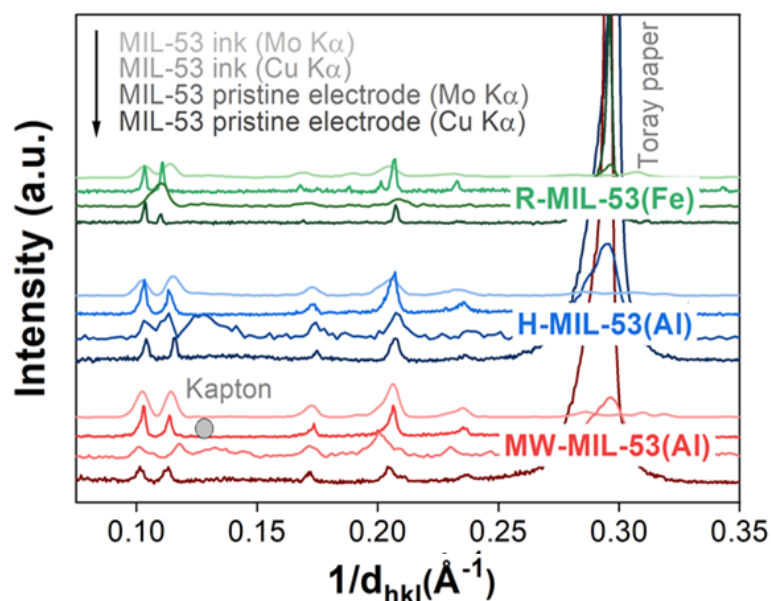


Figure V-1 : XRD patterns as a function of reciprocal lattice distance $1/d_{hkl}$ for all MIL-53 electrodes, ink powder, and MIL-53 pristine electrodes with Cu and Mo radiations. The Kapton tape results in a large peak at $1/d_{hkl} = 0.17 \text{ \AA}^{-1}$. The Toray carbon paper results in a large intense peak at $1/d_{hkl} = 0.30 \text{ \AA}^{-1}$.

Figure V-2 shows the *ex situ* XRD patterns collected after the first and the tenth discharge for MIL-53(Al) electrodes along with XRD on pristine electrodes with or without electrolyte soaking. By comparing the XRD patterns of pristine MIL-53(Al) electrodes and C_{sp} electrodes, we can attribute the first 2θ peak to the MIL-53. After discharge, we observe a shift in the 2θ value of this peak (from 4.17° to 3.85° for pristine and discharged electrodes, respectively), which evidences an evolution of the pore configuration of the MIL-53(Al) when the discharge products are inserted inside the pores. Upon adding electrolyte on the pristine electrodes, we observe additional peaks corresponding to the electrolyte (by comparison with C_{sp} electrode), meanwhile no MIL-53 peak evolution is observed, denoting the stability of the MOF in the electrolyte solution.

After discharging the cells, lithium peroxide Li_2O_2 is found as the main discharge product for all MIL-53(Al) electrodes (Figure V-2). The diffraction peaks at $2\theta = 14.8^\circ$, 15.7° , and 26.1° correspond respectively to the (100), (101), and (110) Bragg peaks of crystalline Li_2O_2 [1]. The intensity of the main peak at 15.7° significantly increases with the number of discharges for MIL-53(Al) electrodes, denoting a large accumulation of crystalline Li_2O_2 products upon cycling. As noted in Chapter IV.1, charge capacities are found very low in these electrodes due to the limited OER reactions. Hence, the accumulation of Li_2O_2 products on the electrode is explained by the absence of Li_2O_2 decomposition during the charge. Thus, the Li_2O_2 observed at the 10th discharge does not only arise from the Li_2O_2 formed solely on the 10th discharge but to the Li_2O_2 products accumulated all along the ten cycles. XRD patterns were also recorded at the end of the 10th charge. The main peak of Li_2O_2 at 15.7° remains after the 10th charge, again confirming the incomplete OER reaction, i.e. the incomplete decomposition of Li_2O_2 . This is in agreement with the evolution of the discharge and charge profiles upon cycling (Figure V-3).

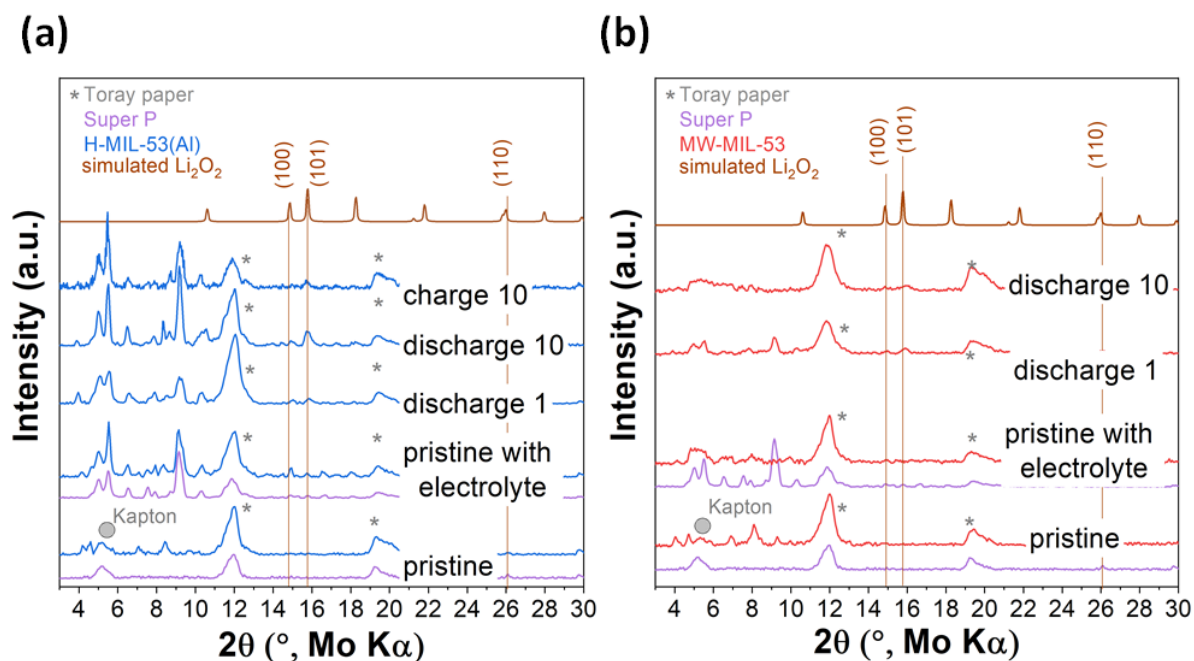


Figure V-2 : Ex situ XRD patterns of (a) H-MIL-53(Al) (blue) and (b) MW-MIL-53(Al) (red) after 1 discharge, 10 discharges, and 10 charges, as well as a comparison with C_{sp} pristine electrode, and the pristine electrode impregnated with 1M LiTFSI in DME electrolyte. The grey star marks indicate the contributions from the Toray paper. The Li_2O_2 is simulated according to crystal data PDF 01-074-0115. To visualize the evolution of the Li_2O_2 discharge product, solid lines represent the (100), (101), and (110) Li_2O_2 Bragg positions.

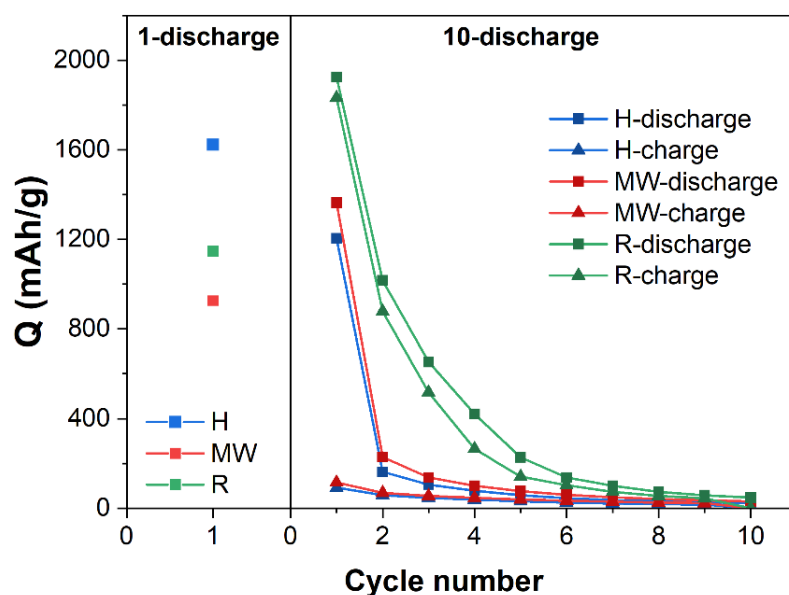


Figure V-3 : Capacity evolution as a function of cycle number for Li- O_2 batteries with (left) 1-discharged and (right) 10-discharged H-MIL-53(Al) (blue), MW-MIL-53(Al) (red) and R-MIL-53(Fe) (red) electrodes. The discharge and charge capacities are shown with square and triangle, respectively.

The same studies were also performed for R-MIL-53(Fe) electrodes. By comparing the XRD pattern of R-MIL-53(Fe) pristine electrode with the C_{sp} electrodes (Figure V-4), we can deduce that the first peak at $2\theta = 4.5^\circ$ is attributed to the R-MIL-53(Fe). After introducing the electrolyte, we observe a new peak at $2\theta = 3.8^\circ$, denoting a significant structure transition of the R-MIL-53(Fe). In contrast to the MIL-53(Al), guest molecules can fully open the pores of the R-MIL-53(Fe) structure (e.g. this is the case of water molecules). When adding electrolyte solution at the surface of the R-MIL-53(Fe) electrodes, we observe an evolution of the XRD pattern, showing another breathing transition. After discharge, two additional peaks are observed on both peaks at $2\theta = 3.8^\circ$ and 4.5° positions. As a result, not only the LiTFSI in DME electrolyte but also the discharge products influence the pore configuration of the R-MIL-53(Fe). The characteristic peaks for crystalline Li_2O_2 [1] are found on the electrode at first discharge at $2\theta = 14.8^\circ$, 15.7° , and 26.1° . Meanwhile, these peaks become hardly visible after ten discharges, which is in agreement with the low discharge capacity obtained at the 10th cycle (Figure V-3, $Q_{10th} = 47.6$ mAh/g). While the second plateau observed on the discharge of R-MIL-53(Fe) electrodes is attributed to Li_2O (see IV.1.2), no crystalline Li_2O is detected here. This suggests the absence of Li_2O or its formation in an amorphous state. As shown in Figure V-3, R-MIL-53(Fe) presents a good reversibility with a deep OER during the charge process. In contrast to MIL-53(Al), high charge capacities denote the decomposition of Li_2O_2 at each cycle. However, almost no capacity is delivered at the 10th cycle leading to few amounts of Li_2O_2 discharge product formed. It is possible that the growth of Li_2O_2 at deep discharge causes the expansion of the R-MIL-53(Fe), resulting in a loss of contact between electrode particles or even a deformation of the R-MIL-53(Fe) structure [2]. However, no significant structure evolution of R-MIL-53(Fe) between the first and the tenth discharge electrodes is observed with XRD (Figure V-4).

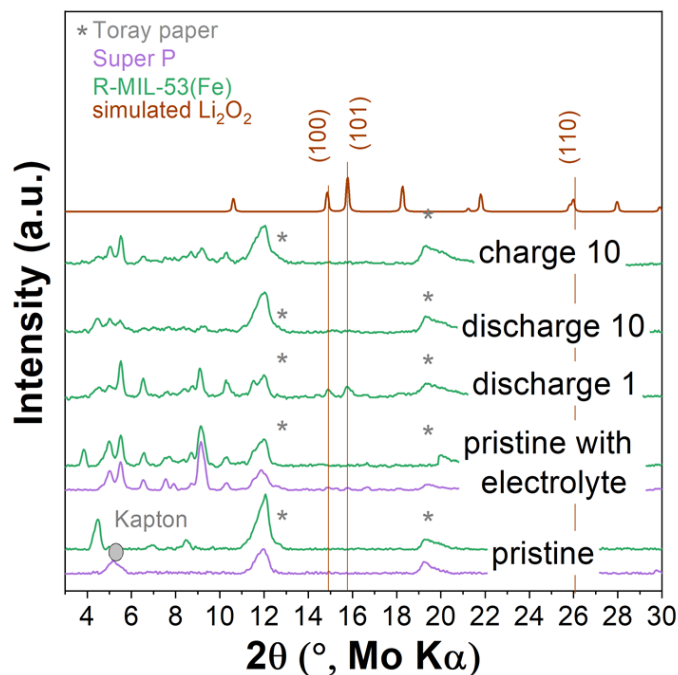


Figure V-4 : Ex situ XRD patterns (Mo-K α) of the R-MIL-53(Fe) (green) and C_{sp} (purple) electrodes after 1, 10 discharges and 10 charges, as well as a comparison with C_{sp} pristine electrode, and the pristine electrode impregnated with 1M LiTFSI in DME electrolyte. The grey star marks indicate the Toray paper. The Li_2O_2 is simulated according to crystal data PDF 01-074-0115. To visualize the evolution of the discharge product Li_2O_2 , solid lines represent the Li_2O_2 Bragg positions (100), (101), and (110).

Above all, the lithium peroxide Li_2O_2 is successfully identified by *ex situ* XRD as the main discharge product on MIL-53 electrodes in the Li- O_2 batteries, showing that the MIL-53 series is a promising cathode material for Li- O_2 batteries. The inefficient OER with the MIL-53(Al) compound implies no Li_2O_2 decomposition during the charge and a significant accumulation of Li_2O_2 over cycles. The MIL-53(Fe) in turn has open pores transition upon adsorbing guests, favoring deep OER on each cycle. However, the deep discharge may lead to the contact loss of electrode particles or the deformation MIL-53(Fe), resulting in the rapid fading in capacity after 10 cycles. As suggested in Chapter IV, the poor electronic conductivity and the absence of catalytic sites in the electrodes may also explain the capacity fading.

V.1.2. Ex situ scanning electronic microscopy

The morphology of the Li_2O_2 discharge product on MIL-53 electrodes was investigated with SEM on the samples already analyzed by XRD in Chapter V.1.1. After disassembling the batteries, these electrodes were quickly transferred into the analysis chamber of the microscope, with an air exposure of less than one or two minutes. As the Li_2O_2 discharge product is unstable under the electron beam, the acquisition time was shortened to prevent Li_2O_2 from collapsing under the beam.

Interestingly, different morphologies of the Li_2O_2 discharge product are observed on MIL-53 electrodes. The Li_2O_2 forms vary among the MIL-53 series and also with the discharge cycle number. Figure V-5 shows the SEM images of MIL-53 electrodes discharged once and ten times.

After the first discharge, we observe toroidal (yellow circled) and thin platelet (pink circled) Li_2O_2 products for H-MIL-53(Al) and MW-MIL-53(Al) electrodes, respectively. Few Li_2O_2 toroids are also observed with the MW-MIL-53(Al). Some Li_2O_2 particles are isolated while others are partially overlapping. The morphology of the Li_2O_2 products is well reported in the literature and is in fact dependent on current density [3], electrolyte [4], and capacity [1]. The nature of the cathode also plays a role as different Li_2O_2 morphologies can also be observed across different reports with similar battery cycling conditions. For example, plate-like Li_2O_2 is observed on a XC 72 carbon electrode [5] while a crescent-like Li_2O_2 is identified on the carbon paper without loading active carbon [6]. Here, knowing that the cycling conditions are similar for both MIL-53(Al) compounds, the difference of Li_2O_2 morphology observed seems to be related to the MIL-53(Al) particles size or morphology. Consequently, the synthesis route of the MIL-53(Al) influences the Li_2O_2 formation mechanism. After 10 discharges, we observe an evolution of the morphologies for both MIL-53(Al) electrodes. We observe toroids presenting a shape close to Li_2O_2 spheres and few small toroids for H-MIL-53(Al) electrodes, while in contrary small toroids are observed for MW-MIL-53(Al) with few Li_2O_2 spheres.

Compared to the Li_2O_2 particles observed on MIL-53(Al) discharged electrodes, smaller Li_2O_2 particles are observed with R-MIL-53(Fe) discharged electrodes (Figure V-5). In this case, the discharge products edges are not well defined compared with MIL-53(Al), which is probably due to the presence of Li_2O on the particles' surface [5]. Besides, as the Li_2O_2 is unstable under the electron beam, the small toroids after one discharge collapse rapidly during the observation (beam focusing on the sample). After ten discharges, tiny Li_2O_2 toroids and bare R-MIL-53(Fe) crystallites are visible. Besides, the electrode surface of R-MIL-53(Fe) is covered with crumpled products that might arise from incompletely decomposed Li_2O_2 toroids (brown circled in Figure V-5) upon OER [5]. We can infer that these crumpled undecomposed discharge products gradually accumulate and clog the pores, leading to the fading of the discharge capacity upon cycling. At the end of the tenth discharge, only few Li_2O_2 particles could form due to the lack of remaining porosity.

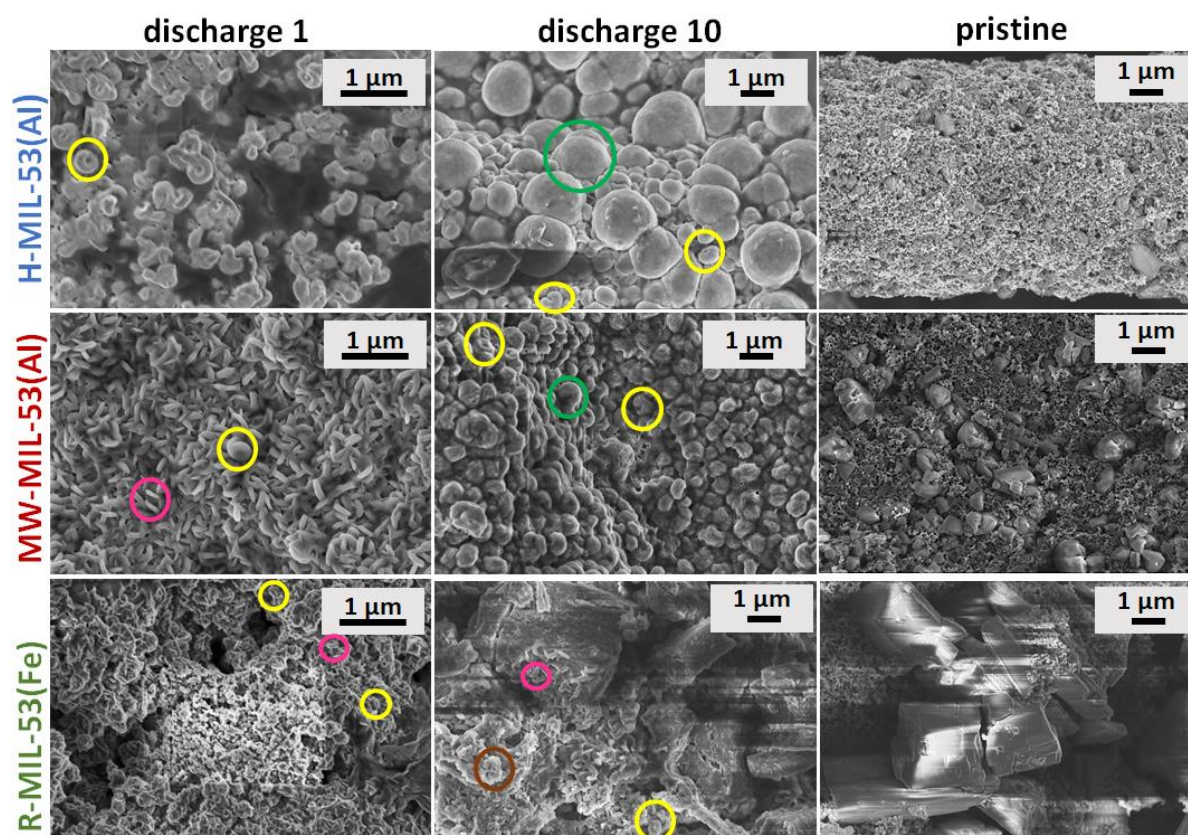


Figure V-5 : SEM images of pristine electrodes and different discharge product morphologies deposited on the separator side of MIL-53 electrodes cycled at 50 mA/g after one discharge and ten discharges. The SEM images for the first discharge H-MIL-53(Al) and R-MIL-53(Fe) electrodes are obtained under an acceleration voltage of 1.5 kV, the other images are obtained under an acceleration voltage of 3.0 kV.

In order to qualitatively compare the sizes of the Li_2O_2 discharge products obtained for the MIL-53 electrodes, we measured the discharge particle length for Li_2O_2 particles with the ImageJ software. All visible individual discharge products (around 80-90 individuals for both H-MIL-53(Al) / MW-MIL-53(Al) and 40-50 for R-MIL-53(Fe) on each image) were measured. Figure V-6 shows the histogram of discharge particle size distribution of Li_2O_2 particles. For the H-MIL-53(Al), the small toroid diameter distribution at the end of the first discharge is found at 358 ± 42 nm. These Li_2O_2 particle sizes are in the same order as Li_2O_2 toroid size (300 – 400 nm) reported in the literature [6]. The toroid size largely evolves after ten discharges, where particles grow into pseudo-spheres and their diameters are more widely dispersed from 520 nm to 2.2 μm .

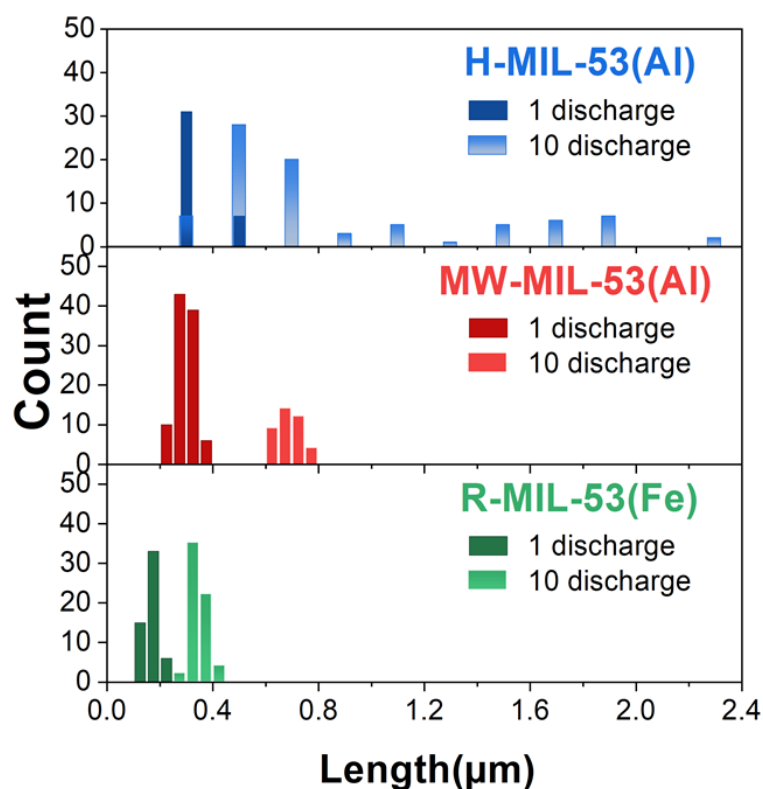


Figure V-6 : Particle length distribution of the Li_2O_2 discharge products measured on MIL-53 electrodes after one or ten discharges.

Different morphologies are observed with the MW-MIL-53(Al) electrodes. A homogenous Li_2O_2 particle morphology evolution is observed with MW-MIL-53(Al). After one discharge, the electrode surface is covered with a homogenous discharge product deposition. We observe two forms of Li_2O_2 products in similar length sizes: almost all of them are platelet-like while a few are toroidal. The Li_2O_2 platelets and toroids have lengths concentrated at 299 ± 41 nm. After ten discharges, the surface deposition is still homogenous but almost all Li_2O_2 particles are toroidal (random pseudo-spherical) with a diameter ranging from 550 nm to 1 μm .

The size evolution of Li_2O_2 is actively related to the discharge capacity [1]. Some reports have illustrated that the toroids evolve from disk-like to spherical-like when increasing the depth of discharge [1], [7]. At a low current density, the solution-mediate mechanism of Li_2O_2 growth is dominant, as the solvation of intermediate LiO_2 molecules occurs at a faster rate than the direct electron transfer to the cathode surface, leading to the disproportionation of LiO_2 to Li_2O_2 in solution [8]. Upon exceeding its limited solubility (order of 10^{-17}M) [9], the Li_2O_2 precipitates directly on the surface of the electrode at the nucleation site. In our case, no efficient OER occurs with MIL-53(Al), thus Li_2O_2 is retained on the electrode upon charging. As a result, these residual Li_2O_2 particles could serve as nucleation sites to generate larger particles upon further cycling.

Table V-1 presents the cumulated discharge and charge capacities for both H-MIL-53(Al) and MW-MIL-53(Al) electrodes discharged ten times. We also calculated the difference between the cumulated discharge capacities and the cumulated charge capacities of each electrode. We consider that the discharge/charge capacities are directly related to the quantity of Li_2O_2 formed / decomposed. As shown in Table V-1, 80% of the discharge capacity obtained along the 10 cycles is not reversibly reached on charge (ratio of the difference of the cumulated discharge and charge capacities to the discharge capacities). Li_2O_2 discharge products are thus not degraded and accumulate inside the pores during the charge.

By combining these findings with the observed morphologies, we could predict a possible Li_2O_2 growth mechanism related to the morphology of MIL-53(Al), (Figure V-7). We propose that for the H-MIL-53(Al), Li_2O_2 grows first on the surface of the MIL-53(Al) electrode upon the first discharge. The platelet Li_2O_2 forms for low discharge capacity and grows up into toroids with the increasing of discharge capacity (926.4 mAh/g-platelet vs 1622.7 mAh/g-toroid). In subsequent cycles, both Li_2O_2 toroids accumulated during the first discharge and the large H-MIL-53(Al) particles (2 μm) act as nucleation sites for the following Li_2O_2 products deposition. The deposition of new Li_2O_2 on the toroids finally leads to the large Li_2O_2 pseudo-spheres (Figure V-7). In the case of MW-MIL-53(Al), the mechanism is similar, Li_2O_2 grows on accumulated Li_2O_2 platelets together with homogenous smaller MW-MIL-53(Al) particles (500 nm) into homogenous toroids.

Table V-1 : Cumulated discharge/charge capacities ($Q_{\text{discharge}}/Q_{\text{charge}}$) over 10 cycles and the difference between them for MIL-53 electrodes observed with SEM. 10D corresponds to 10 discharges.

Electrode	H-10D	MW-10D	R-10D
Total cumulated discharge capacities ($Q_{\text{discharge}}$)	1771	2122	4659
Total cumulated charge capacities (Q_{charge})	347	435	3910
Cumulated $Q_{\text{discharge}} - Q_{\text{charge}}$	1424	1687	749
$\%(Q_{\text{discharge}} - Q_{\text{charge}})/Q_{\text{discharge}}$	80%	80%	16%
Li_2O_2 morphology	Pseudo-sphere & toroid (minor)	Toroid & pseudo-sphere (minor)	Platelet & toroid

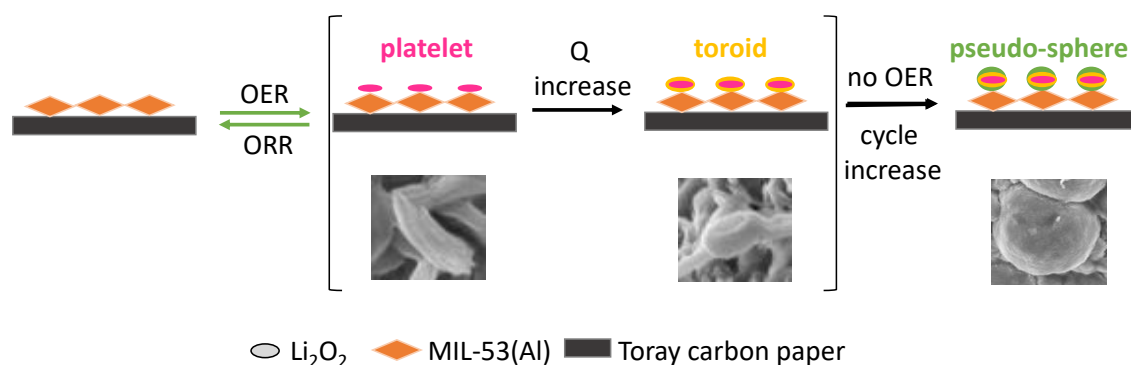


Figure V-7 : Proposed Li_2O_2 growth mechanism on MIL-53(Al) electrode. The SEM images of Li_2O_2 are obtained in this work.

In contrast, the Li_2O_2 particle size evolution is different with R-MIL-53(Fe). Only nano-sized Li_2O_2 platelets and toroids are found on both 1-discharged and 10-discharged electrodes. The Li_2O_2 size after one discharge is centered at 171 ± 25 nm, which is much smaller than with any other MIL-53(Al) electrodes. Even after ten discharges, the average Li_2O_2 size is still smaller than those observed on MIL-53(Al) electrodes (351 nm vs. 762 nm). As discussed in Chapter IV.2, R-MIL-53(Fe) delivers advanced charge capacity during OER due to its open pores configuration compared to the MIL-53(Al). This is illustrated in Table V-1, where only 16% of the cumulated discharge capacities are not reversible. The satisfying ORR / OER favored a reversible formation / decomposition process of Li_2O_2 particles on the first cycles. A large part of Li_2O_2 is thus decomposed and not accumulated during the charge, as illustrated in Figure V-8. In contrast to the close pores configuration in MIL-53(Al), the open pores of R-MIL-53(Fe) ensure the accommodation of Li_2O_2 . Even at the external surface of R-MIL-53(Fe) crystallites, new Li_2O_2 grows on each discharge on almost “fresh” surfaces, as confirmed by the SEM images. As shown in Table V-1, the total charge capacity is higher for R-MIL-53(Fe) electrodes than for MIL-53(Al) electrodes, certainly due to the difference of pore opening between the two MIL-53 analogues. However, and even if the removal of Li_2O_2 is substantial, we still observe crumpled toroidal particles on the 10-discharged R-MIL-53(Fe) electrode, denoting some irreversibility in the OER process.

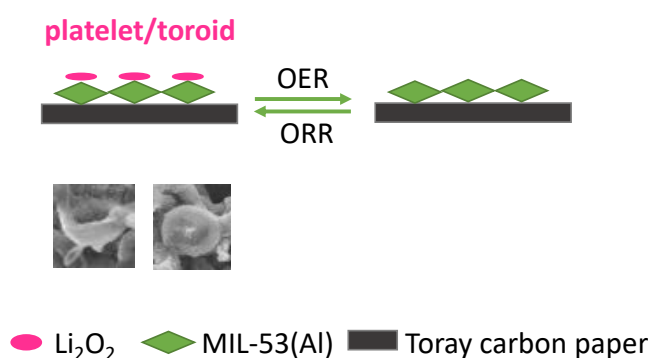


Figure V-8 : Proposed Li_2O_2 growth mechanism on R-MIL-53(Fe) electrode. The SEM images of Li_2O_2 were obtained in this work.

To conclude, we thus propose two distinct growth routes of Li_2O_2 related to the MIL-53(Al) and R-MIL-53(Fe) materials in the DME-based Li-O₂ battery. For MIL-53(Al) electrodes, platelet Li_2O_2 particles are firstly formed with low discharge capacity. With the increase in cumulated discharge capacity, Li_2O_2 platelets grow into toroids. As the OER is not efficient in MIL-53(Al) electrodes, the Li_2O_2 toroids are not decomposed on charge. In the following discharges, Li_2O_2 still accumulates on the electrode. The pseudo-spheres morphology suggests that Li_2O_2 on further discharges nucleates on the existing toroids from the first discharge. When no Li_2O_2 decomposition during OER exists (MIL-53(Al)), the morphology evolution of Li_2O_2 particles is directly related to the morphology of the MIL-53(Al) crystallites. Homogenous Li_2O_2 toroids form with MW-MIL-53(Al) crystallites while Li_2O_2 particles with large dispersion in size are observed with H-MIL-53(Al).

For the R-MIL-53(Fe) electrode, only small Li_2O_2 platelets and toroids are observed. The pores of the framework open while accommodating electrolyte and Li_2O_2 discharge products which may allow the formation of triple points. Li_2O_2 largely decomposes at the charge in contrast to MIL-53(Al). Thus, on further discharges, only small Li_2O_2 particles are formed on bare R-MIL-53(Fe) crystals as previous Li_2O_2 particles are degraded.

V.2 X-ray photoelectron spectroscopy investigations

A deeper study of discharge products was performed for H-MIL-53(Al) electrodes with X-ray photoelectron spectroscopy. XPS analyses were conducted on the same electrodes studied with XRD and SEM. Figure V-9 shows an overview of XPS survey spectra for all electrodes.

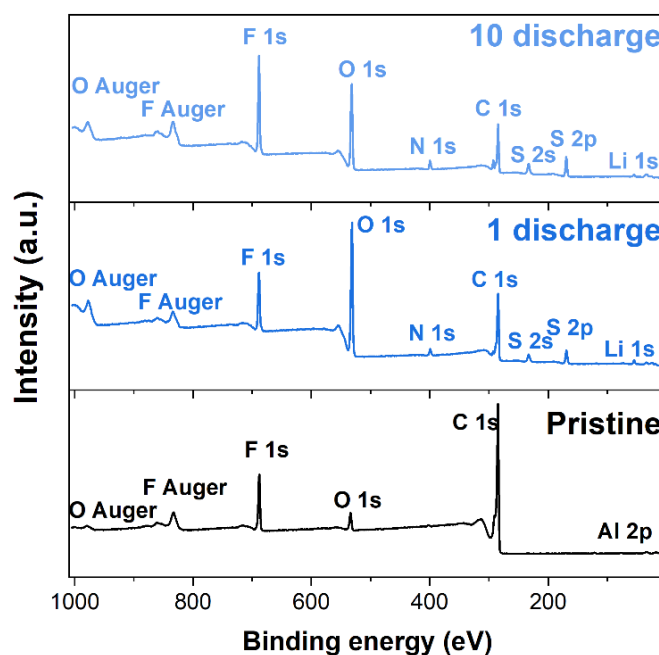


Figure V-9 : XPS spectra (Al K α) for the pristine H-MIL-53(Al) electrode, and similar electrodes after 1 discharge and 10 discharges in 1 M LiTFSI in DME.

Figure V-10 shows the high-resolution fitted XPS spectra for pristine and discharged H-MIL-53(Al) electrodes after one and ten discharges. For the pristine electrode in the C 1s region, the contribution at approximately 285 eV is fitted into two contributions from the sp^2 C=C bond (284.4 eV) and the sp^3 C-C bond (284.8 eV) in the benzene ring of the dicarboxylate linker of the framework. The latter peak might also come from the adventitious carbon on the surface. Peaks at 286.5 eV and 288.6 eV binding energies are indexed to C-O and C=O bonds, respectively. The C-O and the C=O bonds are also indexed by the peaks at 534.4 eV and 533.4 eV in the O 1s spectrum. These peaks are in accordance with the reported organic linker of the MIL-53 compound in the literature [10]. Besides, one more peak is observed for the pristine electrode and is attributed to the C-F bond (291.2 eV) from the $-CF_2$ group of PVDF binder. After 1 or 10 discharges, lithium peroxide Li_2O_2 is clearly confirmed as the main discharge product, as shown by the peaks at 54.8 eV and 531.5 eV in the Li 1s region and the O 1s region, respectively. Even though the discharged electrodes are rinsed with a few drops of DME solvent to remove the electrolyte in excess, we still see some contributions from the LiTFSI salt (at 56.1 eV in the Li 1s region, at 293.0 eV in the C 1s region, at 688.3 eV in the F 1s region, and the doublet peaks at 169.3 eV and 170.5 eV in the S 2p region assigned to S 2p_{3/2} and S 2p_{1/2} of the LiTFSI salt) [11]. Interestingly, additional doublet peaks (167.2 eV and 168.4 eV) are observed in the S 2p region for the discharged electrodes, corresponding to the S=O bond, most probably arising from the decomposition products of the electrolyte salt [11], [12]. The peak at 56.1 eV in the Li 1s region could be attributed to the byproduct Li_2CO_3 as its relative intensity towards the Li_2O_2 increases over cycles [13].

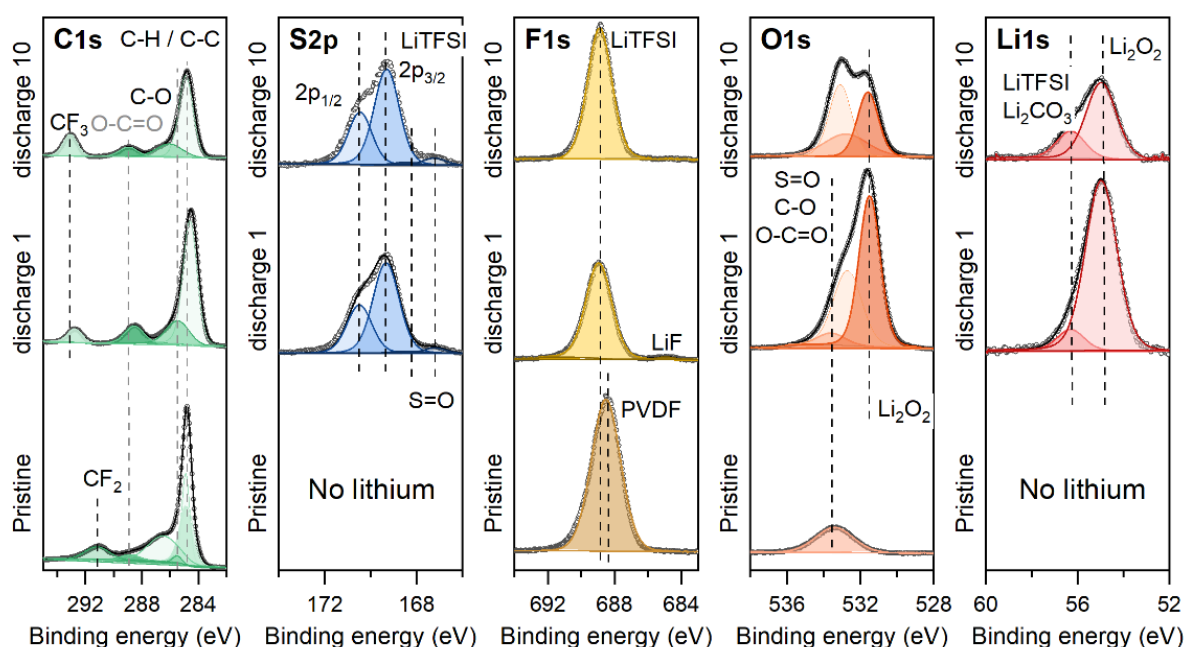


Figure V-10 : High resolution *ex situ* XPS spectra of C 1s, S 2p, F 1s, O 1s, and Li 1s for pristine, and 1 and 10-discharged H-MIL-53(Al) electrodes.

Table V-2 summarizes the characteristic peak binding energies and the assignments of the principal elements: C 1s, O 1s, F 1s, S 2p, and Li 1s.

Overall, the XPS characterization confirms again the presence of Li_2O_2 on H-MIL-53(Al) electrodes over cycles. Additionally, XPS evidenced the LiTFSI salt decomposition since the first discharge in the DME-based Li- O_2 batteries. This side-reaction needs to be considered for further developments of the Li- O_2 batteries.

Table V-2 : Binding energies (eV) and assignments from XPS peaks of the MIL-53 pristine electrode, electrode after 1 discharge and after 10 discharges.

Peak	BE (eV)	Assignment	BE (eV)	Assignment	BE (eV)	Assignment
	pristine		1 discharge		10 discharges	
C 1s	284.4	C=C	284.8	C-C	284.8	C-C
	284.8	C-C	285.7	C-O	286.1	C-O
	286.5	C-O	288.8	C=O	288.9	C=O
	288.6	C=O	293.0	CF_3 (LiTFSI)	293.1	CF_3 (LiTFSI)
	291.2	CF_2 (PVDF)				
O 1s	533.4	C=O	531.5	Li_2O_2	531.6	Li_2O_2
	534.4	C-O	532.4	C=O/C-O	533.1	C=O/C-O
F 1s	688.3	CF_2 (PVDF)	684.9	Li-F	688.9	CF_2 (LiTFSI)
			688.9	CF_2 (LiTFSI)		
S 2p	No signal		167.2	S=O	167.2	S=O
			168.4	S=O	168.4	S=O
			169.3	LiTFSI	169.3	LiTFSI
			170.5	LiTFSI	170.5	LiTFSI
Li 1s	No signal		54.8	Li_2O_2	54.1	Li_2O_2
			55.6	LiTFSI	56.1	LiTFSI
			56.1	LiF/ Li_2CO_3		

V.3 Conclusion

In this chapter, we explored with *ex situ* analysis (XRD, SEM and XPS) the H-MIL-53(Al), MW-MIL-53(Al), and R-MIL-53(Fe) electrode behaviors after the first and the tenth discharge in the Li- O_2 batteries in a typical ether electrolyte (1 M LiTFSI in DME).

The structural characterization evidenced the continuous formation of crystalline particles of Li_2O_2 as the main discharge product on both MIL-53(Al) electrodes according to the XRD and SEM. A complementary chemical study with XPS revealed also the presence of Li_2O_2 on the MIL-53(Al) electrodes. Due to the lack of OER efficiency, Li_2O_2 accumulated during

the discharges and subsequent cycles, leading to an increase in the crystal size from nano- to micro-sized Li_2O_2 and a more densely packed layer of Li_2O_2 with MIL-53(Al) electrodes. We assumed that the Li_2O_2 discharge product grows with the number of cycles on MIL-53(Al) electrodes from platelets, to toroids, until pseudo-spheres, with the first discharge Li_2O_2 products acting as nucleation sites for the pseudo-spheres. It seems also that the homogeneity of the Li_2O_2 particles is directly linked to the homogeneity of the MIL-53(Al) crystallites. After 10 discharges, larger pseudo-spherical Li_2O_2 were obtained with micro-sized H-MIL-53(Al) while homogenous toroids were observed with nano-sized MW-MIL-53(Al).

Conversely, the pore opening in R-MIL-53(Fe) probably favored the formation of triple points thus allowing efficient decomposition of Li_2O_2 during the charge process. As deep OER occurred, almost no Li_2O_2 residues accumulate during the charge, and Li_2O_2 is formed mainly as nano-sized platelets or toroids. This confirms that the R-MIL-53(Fe) is the best of the MOFs materials studied in this work.

Finally, the surface analysis on the MIL-53 electrodes highlighted the LiTFSI electrolyte decomposition starting from the first discharge. This side-reaction needs thus to be considered for further development of the Li- O_2 batteries.

V.4 References

- [1] D. Zhai *et al.*, "Disproportionation in Li–O₂ Batteries based on a large surface area carbon cathode," *J. Am. Chem. Soc.*, vol. 135, n°41, pp. 15364–15372, 2013.
- [2] A. Débart, A. J. Paterson, J. Bao, and P. G. Bruce, "α-MnO₂ nanowires: a catalyst for the O₂ electrode in rechargeable lithium batteries," *Angew. Chem. Int. Ed.*, vol. 47, n° 24, pp. 4521–4524, 2008.
- [3] B. Horstmann, B. Gallant, R. Mitchell, W. G. Bessler, Y. Shao-Horn, and M. Z. Bazant, "Rate-dependent morphology of Li₂O₂ growth in Li–O₂ batteries," *J. Phys. Chem. Lett.*, vol. 4, n°. 24, pp. 4217–4222, 2013.
- [4] B. Liu *et al.*, "Enhanced cycling stability of rechargeable Li–O₂ batteries using high-concentration electrolytes," *Adv. Funct. Mater.*, vol. 26, n°4, pp. 605–613, 2016.
- [5] L. Luo, B. Liu, S. Song, W. Xu, J.-G. Zhang, and C. Wang, "Revealing the reaction mechanisms of Li–O₂ batteries using environmental transmission electron microscopy," *Nat. Nanotechnol.*, vol. 12, n°6, pp. 535–539, 2017.
- [6] R. R. Mitchell, B. M. Gallant, Y. Shao-Horn, and C. V. Thompson, "Mechanisms of morphological evolution of Li₂O₂ particles during electrochemical growth," *J. Phys. Chem. Lett.*, vol. 4, n° 7, pp. 1060–1064, 2013.
- [7] C. Xia, M. Waletzko, L. Chen, K. Pepler, Peter. J. Klar, and J. Janek, "Evolution of Li₂O₂ Growth and its effect on kinetics of Li–O₂ batteries," *ACS Appl. Mater. Interfaces*, vol. 6, n° 15, pp. 12083–12092, 2014.
- [8] B. D. Adams, C. Radtke, R. Black, M. L. Trudeau, K. Zaghbi, and L. F. Nazar, "Current density dependence of peroxide formation in the Li–O₂ battery and its effect on charge," *Energy Environ. Sci.*, vol. 6, n°6, pp. 1772–1778, 2013.
- [9] L. Cheng, P. Redfern, K. C. Lau, R. S. Assary, B. Narayanan, and L. A. Curtiss, "Computational studies of solubilities of LiO₂ and Li₂O₂ in aprotic solvents," *J. Electrochem. Soc.*, vol. 164, n°11, p. E3696, 2017.
- [10] A. Khodayari and S. Sohrabnezhad, "Fabrication of MIL-53(Al)/Ag/AgCl plasmonic nanocomposite: an improved metal organic framework based photocatalyst for degradation of some organic pollutants," *J. Solid State Chem.*, vol. 297, p. 122087, 2021.
- [11] A. Guéguen, P. Novák, and E. J. Berg, "XPS study of the interface evolution of carbonaceous electrodes for Li–O₂ batteries during the 1st Cycle," *J. Electrochem. Soc.*, vol. 163, n°13, p. A2545, 2016.
- [12] V. Sharova, A. Moretti, T. Diemant, A. Varzi, R. J. Behm, and S. Passerini, "Comparative study of imide-based Li salts as electrolyte additives for Li-ion batteries," *J. Power Sources*, vol. 375, pp. 43–52, 2018.
- [13] D. Enslin, M. Stjern Dahl, A. Nyttén, T. Gustafsson, and J. O. Thomas, "A comparative XPS surface study of Li₂FeSiO₄/C cycled with LiTFSI- and LiPF₆-based electrolytes," *J. Mater. Chem.*, vol. 19, n°1, pp. 82–88, 2008.

General conclusion

Energy storage will be more essential in the future than it has never been in the past. The development of alternative energy is of the utmost importance because our society needs to produce, transport, consume and store energy to keep its high technological level and well-being. Lithium-ion battery holds in this area a prominent place on the market. Nevertheless, its specific capacity and energy density seem to reach their limits and they will be insufficient for the long-term needs of our society. It is therefore necessary to develop a new technology of batteries offering new prospects for capacity storage and safety, particularly in the automotive field. The Li-air batteries are receiving intense interest today due to potentially much higher gravimetric energy storage density compared to other technologies (1700 Wh/kg vs. 160 Wh/kg for current Li-ion batteries, in practice). However, there are numerous scientific and technical challenges of Li-air batteries to overcome, such as the rapid loss of electrochemical performance after only few cycles and the issue of reproducibility. Metal-Organic Frameworks (MOF) compounds have low density, high surface area, and high porosity. Their open structure provides a host network for lithium ion and oxygen diffusions and can potentially hosts catalytic sites. A sufficient space is also available for the discharge products. Their practical use for electrochemical applications and particularly for Li-air batteries should constitute a breakthrough; several MOFs have shown promising first discharge capacities in Li-air batteries[1], however, since 2014 no major studies have been reported regarding MOF performance and cyclability in Li-air batteries.

The objective of the thesis was to study two flexible MOF materials - MIL-53(Al) and MIL-53(Fe) - as potential active materials of air cathode in non-aqueous Li-O₂ batteries.

Different methods were used for the syntheses of MIL-53 materials. The electrochemical performances of MIL-53 electrodes were investigated with discharge-charge cycling and the performances were related to several properties of MIL-53: particle morphology, pore opening, and flexibility behavior. A combination of conventional characterization techniques was implemented on the starting MIL-53 materials as well as on *ex situ* electrodes after cycling in order to identify the discharge products.

The downsizing of particles was at first supposed to improve material properties, such as already reported for adsorption ability and for catalysis. The MIL-53(Al) was obtained through both microwave-assisted hydrothermal and conventional hydrothermal routes (MW-MIL-53(Al) and H-MIL-53(Al), respectively). Both MIL-53(Al) materials have high BET (1390 m²/g for MW-MIL-53(Al) and 1240 m²/g for H-MIL-53(Al)) and low external surface areas (48 m²/g for MW-MIL-53(Al) and 52 m²/g for H-MIL-53(Al)). The microwave irradiation favored a homogenous particle size and small crystallite formation while the conventional heating promoted the growth of larger crystallites.

We showed that the downsizing of MIL-53(Al) did not improve as expected the initial discharge capacity of the MOF electrodes in Li-O₂ batteries, but seemed to influence the morphology of the main discharge product, Li₂O₂. Li₂O₂ was indeed confirmed as the main discharge product on the MIL-53 electrodes by XRD, SEM, and XPS. The MIL-53(Al) is known for its narrow pores configuration while adsorbing guest molecules. We found that the PVDF binder was confined in the pores of MIL-53(Al) during electrode preparation, which restricted the pore re-opening of the framework for hosting the discharge products. We observed two discharge-charge cycling behaviors for both MIL-53(Al). For some electrodes, a first discharge capacity in a range of 700 – 1200 mAh/g (at a current density of 50 mA/g) was obtained but no charge capacity was delivered maybe due to the narrowed pore configuration of the MOF. The accumulation of Li₂O₂ or parasitic products prevented the next deposition of Li₂O₂, thus a rapid fading in discharge capacity was observed. For other electrodes, very limited discharge and charge capacities were delivered at the first cycle (less than 250 mAh/g), and an activation process in the first cycle seemed to be necessary to reorganize the guest molecules inside the pore and then wet the whole electrode. After the activation, a high discharge capacity (700 – 1600 mAh/g) was delivered at the 2nd cycle. As the Li₂O₂ did not decompose efficiently during the charge, the Li₂O₂ gradually accumulated over cycles. We visualized this accumulation through *ex situ* XRD and SEM. With the increase of discharge capacity and cycle number, the Li₂O₂ evolved from nano-sized platelets to nano-sized toroids, to finally micro-sized pseudo-spheres, which nucleated directly on the Li₂O₂ formed initially on the first discharge. Besides the rapid capacity fading behavior, starting from the first discharge, the decomposition of the LiTFSI-based electrolyte was revealed by XPS, which could also decrease the battery performance.

Inspired by the narrowed pore behavior for MIL-53(Al), we then investigated the MIL-53(Fe), whose pores are in contrast opened by the guest molecules (and here the PVDF binder). The MIL-53(Fe) was synthesized with the reflux method. MIL-53(Fe) delivered first discharge capacities of around 2000 mAh/g, which is almost two times higher than MIL-53(Al). We thus deduced that the pore opening favored the accommodating of Li_2O_2 . Moreover, MIL-53(Fe) allowed deep OER on each cycle, with few Li_2O_2 remaining after the charge. However, certain MIL-53(Fe) electrodes suffered from limited initial charge capacities. It seems that the MIL-53(Fe) cathodes have limitations in charge transfer or obstruction of active sites. Moreover, the capacity still faded upon few cycles. During the charge, pores shrank with the Li_2O_2 decomposition, and the possible tri-phase boundary might be lost during this process, leading to a decrease of charge capacity. We could observe some coverage of crumpled discharge products formed during charging after 10 discharges, denoting still some irreversibility in the OER.

We finally compared the effect of flexibility and rigidity of MOF materials on their electrochemical performances by comparing the flexible H-MIL-53(Al) and an already reported rigid MOF with the same organic linker (MOF-5) [1]. A low MOF content was used for both materials to allow a direct comparison with the literature. We found a median initial discharge capacity of MOF-5 around 750 mAh/g and a maximum of 1390 mAh/g. The median is approximately 2-fold lower while the maximum is approaching the capacity obtained with MOF-5 in the literature (1780 mAh/g) [1]. In the same way as MIL-53(Al), an activation behavior at the first cycle was also observed with the MOF-5 despite the rigid structure. Even though we found previously that MIL-53(Al) was less competitive than the MIL-53(Fe) as air cathode, we demonstrated here that the flexibility of MIL-53(Al) still allowed enhanced electrochemical performance compared to the rigid MOF-5, especially for the MOF electrodes that underwent the activation process. However, we cannot attribute the elevated capacity observed in this case solely to the MIL-53(Al), as the electronic conductivity was also improved with the increased C_{sp} content in the electrode formulation.

In comparison, all involved MIL-53 materials suffered from higher charge and discharge overpotentials compared to a C_{sp} electrode. These behaviors suggest a limited electronic conductivity of MIL-53 or some limits in species transport inside the cathode. The low performance of the high MIL-53 content electrode could be explained by two factors: one is the low electronic conductivity of the MIL-53 electrode, and another is the lack of catalytic site within the framework.

Above all, our work demonstrated that the pore opening ability associated with flexibility is a key feature for high-performance MOF-based Li-O₂ battery cathode materials. This property improved the capability to accommodate and decompose the Li₂O₂ products. Nonetheless, to overcome the MOFs' low conductivity drawback, we envision the design of new materials, in particular the synthesis of MOF/C composites including highly conductive agents such as Ketjenblack or graphene oxide[2], [3]. Combining the high conductivity of carbon with the high porosity and flexibility of the MOF could be an efficient way to enhance the electrochemical properties of MIL-53 electrodes for Li-O₂ batteries. For the most optimal components, high-rate cycling and cyclability investigations will provide significant insights on their electrochemical behavior. Beyond MIL-53s, other flexible porous materials hosting catalytic sites are also worthy to investigate targeting to improvement in OER and cyclability, such as MIL-101 [4]. The presence of catalytic sites may decrease the overpotentials in Li-O₂ batteries compared to MIL-53.

As only few pristine MOFs were reported as air cathode material in Li-O₂ batteries, there is still a lack of understanding in ORR / OER mechanisms involved in these materials. Apart from the *ex situ* SEM and XPS used in this work, complementary characterization techniques, such as FTIR, mass spectroscopy, online electrochemical mass spectrometry, electron paramagnetic resonance spectroscopy, or *operando* NMR, are potential techniques to implement to get a clearer view of the reaction mechanisms as well as the comprehension of the rapid capacity fading behavior [4,5]. Finally, the activation process needs to be investigated and rationalized. For example, one possible way is to examining the available porosity probe the available porosity by pulsed field gradient NMR [5].

References

- [1] D. Wu *et al.*, "Metal–Organic Frameworks as Cathode Materials for Li–O₂ Batteries," *Adv. Mater.*, vol. 26, n°20, pp. 3258–3262, 2014.
- [2] M. Muschi *et al.*, "Metal–organic framework/graphene oxide composites for CO₂ capture by microwave swing adsorption," *J. Mater. Chem. A*, vol. 9, n° 22, pp. 13135–13142, 2021.
- [3] M. Muschi and C. Serre, "Progress and challenges of graphene oxide/metal-organic composites," *Coord. Chem. Rev.*, vol. 387, pp. 262–272, 2019.
- [4] G. Li, X. He, F. Yin, B. Chen, and H. Yin, "Co-Fe/MIL-101(Cr) hybrid catalysts: Preparation and their electrocatalysis in oxygen reduction reaction," *Int. J. Hydrog. Energy*, vol. 44, n° 23, pp. 11754–11764, 2019.
- [5] A. Torayev *et al.*, "Probing and interpreting the porosity and tortuosity evolution of Li-O₂ cathodes on discharge through a combined experimental and theoretical approach," *J. Phys. Chem. C Nanomater. Interfaces*, vol. 125, n° 9, pp. 4955–4967, 2021.

Appendixes

Appendix 1- List of chemical products

Product	Brand	Purity
$\text{Al}(\text{NO}_3)_3 \cdot 9\text{H}_2\text{O}$	Sigma-Aldrich	99.99 %
Ar	Air Products	BIP X50S H_2O < 20 ppb, O_2 < 10 ppb
BDC	Sigma-Aldrich	99+ %
CHCl_3	Carbo Erba	For analysis
Deionized H_2O	Direct-Q 3 UV	18.2 M Ω .cm at 25°C
DME	Acros Organics	99.50 %
DMF	Carlo Erba	For analysis
EtOH	Carlo Erba	Pure
$\text{FeCl}_3 \cdot 6\text{H}_2\text{O}$	Sigma-Aldrich	≥ 99 %
HCl	VMR	37 % analytic
Li	Sigma-Aldrich	99.90 %
LiTFSI	Solvionic	99.90 %
MeOH	VWR	For analysis
NMP	Acros Organics	99 %, extra pure
O_2	Air Products	Ultrapure X20S, H_2O < 1ppm
PVDF	Arkema	Kynar 2801
C_{sp}	Alfa Aesar	100 %
TEA	Sigma-Aldrich	For synthesis
Toray carbon paper	Alfa Aesar	TGH-H-60
$\text{Zn}(\text{OAc})_2$	Sigma-Aldrich	99.99 %

Appendix 2- Synthesis and characterization of MOF-5

1.a. Synthesis procedure

The synthesis of MOF-5 is performed via reflux synthesis at room temperature in N,N-dimethylformamide (DMF), according to the procedure described by Yaghi *et al.* [1]. with a mass scale-down of reagents by half. The synthesis precursors are shown in Figure A.-1. Typically, a mixture of benzene-1,4-dicarboxylic acid (H_2BDC) and trimethylamine (TEA) with a molar ratio of 1:2 are dissolved in 100 mL DMF (named as organic solution). A 2.5 equivalent of zinc acetate ($Zn(OAc)_2$) salt is dissolved in 125 mL of DMF (named as zinc solution). Each solution is agitated for 30 min. The zinc solution is added to the organic solution and the global mixture is stirred for 3 h (Figure A.-1). A white precipitation is observed immediately after mixing the two solutions.

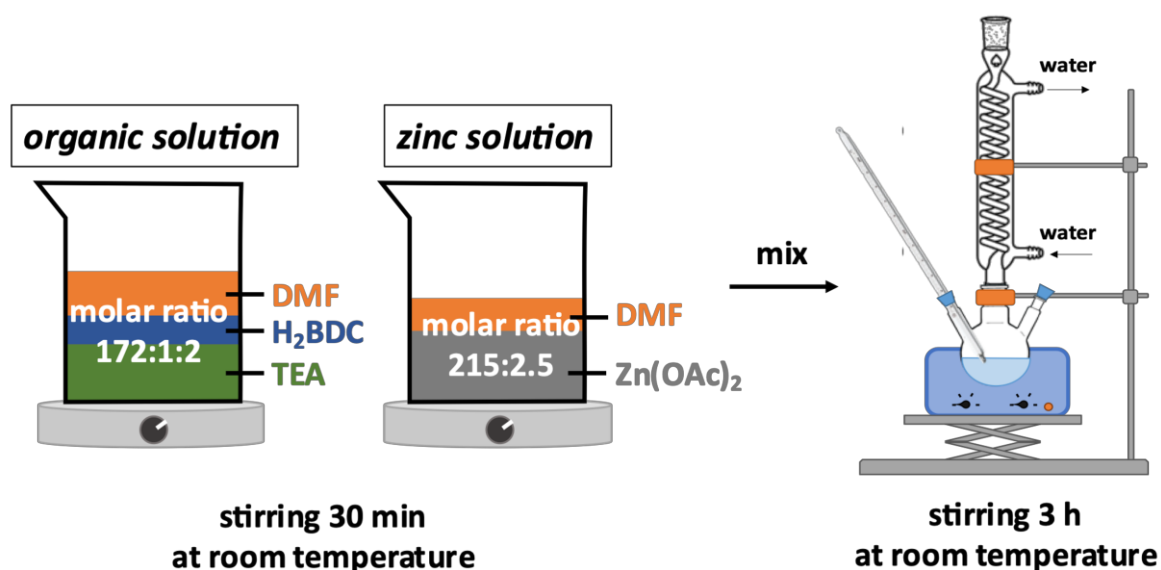


Figure A.-1 : Schematic representation of reflux MOF-5 synthesis. The organic and zinc solutions were stirred separately for 30 min. They were then mixed under stirring for 3 h with reflux.

The precipitate is centrifuged and immersed with 60 mL of DMF overnight in order to remove the unreacted acid. The DMF inside the pores is exchanged in multiple steps with DMF and chloroform (CHCl_3). After the last filtration, the DMF in MOF-5 is exchanged 4 times over 7 days with 90 mL of chloroform. The obtained residue is activated at 120 °C in a Büchi oven under vacuum for 48 h and then transferred into the Ar glove box without air exposure. We obtained a white powder (Figure A.-2) with a yield of 53.5 % regarding the molar mass of zinc salt.



Figure A.-2 : Photograph of the activated MOF-5. The activated sample was stored in the Ar glove box without any exposure to the air.

1.b. Structural characterization

XRD analysis of the activated MOF-5 is performed with Kapton tape protection in transmission mode with the Mo anode ($\lambda_{\text{K}\alpha} = 0.70932 \text{ \AA}$). The XRD pattern confirms that the activated solid corresponds to the MOF-5 solid as reported in the literature [1]. It matches with the MOF-5 Bragg positions (Figure A.-3). It is known that MOF-5 is water-sensitive, leading to an irreversible formation towards a new phase - MOF-69c [2], [3]. An additional peak at $2\theta = 8.9^\circ$ rises during the XRD acquisition with Cu-K α irradiation in air (less than 5 min) (Figure A.- 4). As we have limited access to a suitable sample protection for the Cu-sourced diffractometer, we then repeat the acquisition with the Kapton protection under Mo irradiation, which is less sensitive to the Kapton tape. This time we could only observe a tiny hump with Mo irradiation, which cannot significantly tell the impurity's presence. Considering the hydroreactivity of MOF-5 and a quick irreversible phase transition from MOF-5 towards MOF-69c in air, the dried MOF-5 powder has been stored in the Ar glove box without exposure to air. No more other physical characterizations are performed for MOF-5 powder, especially BET measurement, and

TGA, that requires preparation in air for a certain period of time (longer than 10 min) before analysis.

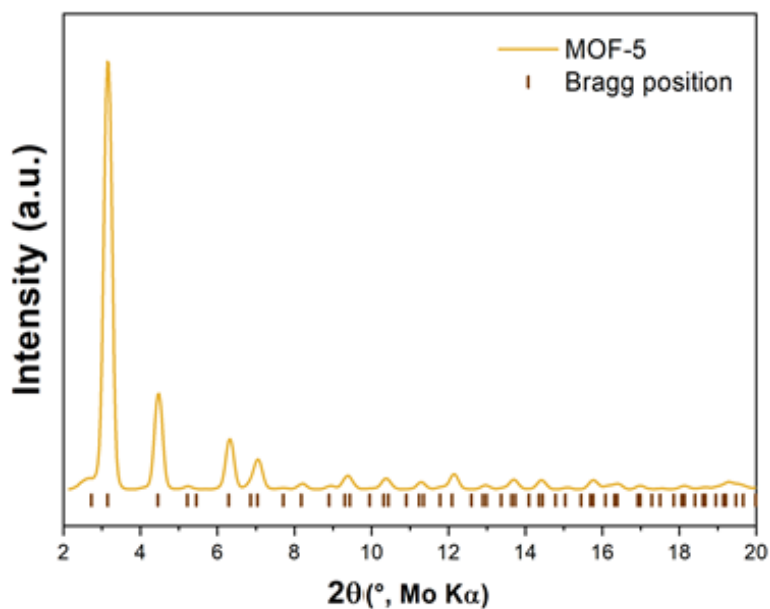


Figure A.-3 : XRD pattern of the MOF-5. The tic marks indicate the Bragg position of the MOF-5 [4]. The sample is protected with a Kapton layer.

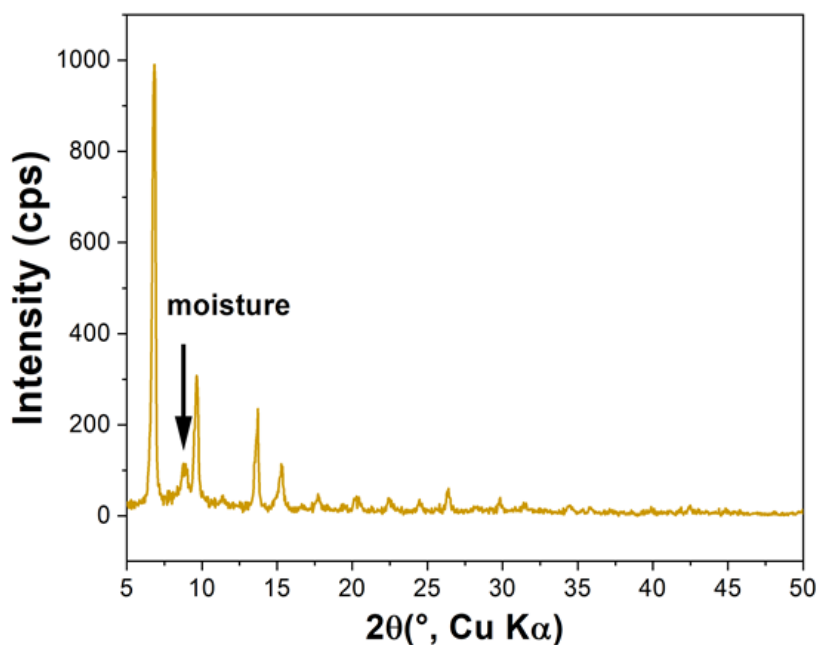


Figure A.- 4 : XRD pattern of MOF-5. The sample is exposed to air during the acquisition (5 min). Additional peak at $2\theta = 8.9^\circ$ is attributed to the new phase MOF-69c upon hydration [3].

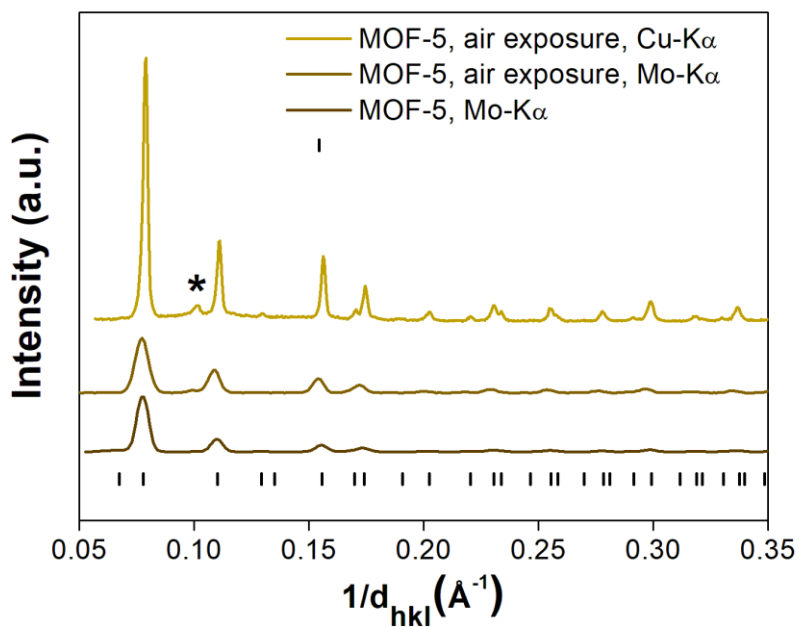


Figure A.- 5 : Comparison of XRD patterns for MOF-5 fresh-synthesized with Mo K α irradiation and MOF-5 exposed to air with both Mo- and Cu-K α irradiations.

1.c. References

- [1] D. J. Tranchemontagne, J. R. Hunt, and O. M. Yaghi, "Room temperature synthesis of metal-organic frameworks: MOF-5, MOF-74, MOF-177, MOF-199, and IRMOF-0," *Tetrahedron*, vol. 64, n°36, pp. 8553–8557, 2008.
- [2] L. Lu, X. Li, X.-Q. Liu, Z.-M. Wang, and L.-B. Sun, "Enhancing hydrostability and catalytic performance of metal-organic frameworks by hybridizing with attapulgite, a natural clay," *J. Mater. Chem. A*, vol. 3, 2015.
- [3] S. S. Kaye, A. Dailly, O. M. Yaghi, and J. R. Long, "Impact of preparation and handling on the hydrogen storage properties of $Zn_4O(1,4\text{-benzenedicarboxylate})_3$ (MOF-5)," *J. Am. Chem. Soc.*, vol. 129, n°46, pp. 14176–14177, 2007.
- [4] M. Eddaoudi *et al.*, "Modular chemistry: secondary building units as a basis for the design of highly porous and robust metal-organic carboxylate frameworks," *Acc. Chem. Res.*, vol. 34, n°4, pp. 319–330, 2001.

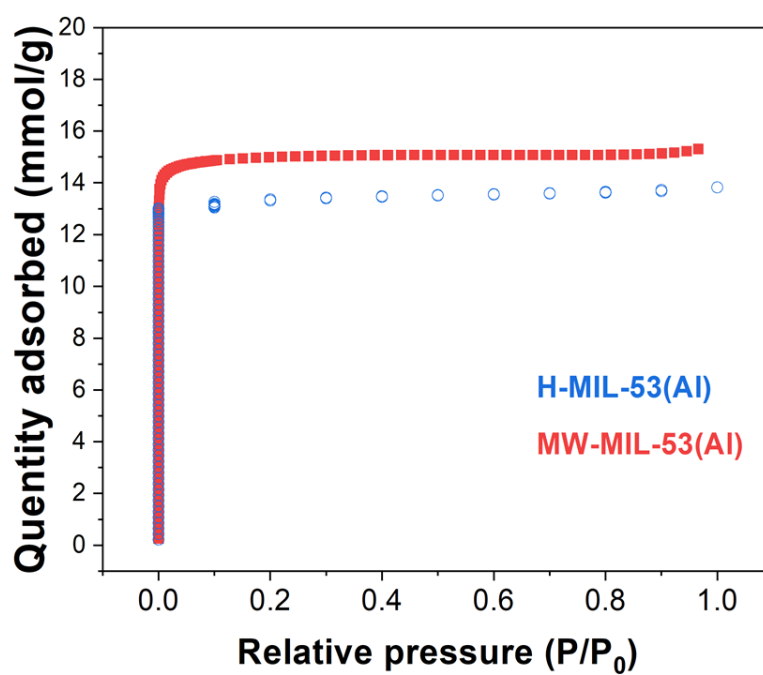
Appendix 3- Nitrogen adsorption isotherm of MIL-53(Al)

Figure A.-6 : Nitrogen adsorption isotherm of H-MIL-53(Al) and MW-MIL-53(Al) at 77 K.

Appendix 4- C_{sp} cathode electrochemical performance

For comparative investigation of MIL-53 and MOF-5 cathode performance in Li-O₂ batteries, similar batteries based on the pure carbon (C_{sp}) cathode are investigated. The electrode processing procedure is described in Chapter II.2. Two C_{sp} electrode formulations are prepared:

- (1) in 80/20 wt. % of C_{sp}/PVDF; and
- (2) in 90/10 wt. % of C_{sp}/PVDF.

The C_{sp} electrode in formulation (1) is considered as a comparison for the reported low MOF-5 content electrode [1], and the C_{sp} electrode in formulation (2) is used as a comparison for the high MIL-53 content electrode. The mass loading of C_{sp} on each electrode is about 1.0 mg/cm² for both formulations. To reproduce the results for each formulation, three individual batteries are cycled according to the conditions described in Chapter II.2. Here we present the cycling performance of C_{sp} electrode.

Prior to the discharge – charge cycling, all Li – O₂ batteries with C_{sp} electrodes are rest at open circuit to ensure the electrode wetting and diffusion of O₂ within the C_{sp} cathode. The open circuit voltage is stabilized at about 2.8 to 2.9 V, which is close to the theoretical value (2.96 V) [2].

1.a. Formulation (1) : 80 / 20 wt.% of C_{sp} / PVDF

The discharge – charge profiles of C_{sp} in formulation (1) are illustrated in Figure A.- 7 (a). The first discharge profile of C_{sp} electrode is characterized by a plateau at *ca.* 2.7 V, which corresponds to the formation of Li₂O₂ [3]. The first discharge capacity is *ca.* 3300 mAh/g between (3292 - 3327 mAh/g). Our capacities are about 1000 mA/g higher than the work of Li (2170 mAh/g) [1]. It is possible that our higher mass loading contributes to the improvement of capacity (1 mg/cm² vs. 0.5 mg/cm²). Otherwise, this difference in capacity may be also attributed to the Li₂O₂ growth mechanism ensured by solvent [4]. Following the model proposed by McCloskey *et al.* [5], the DME with higher DN than TEGDME favors the stable solvation of Li⁺ and intermediate O₂⁻ species, thus inducing an increased capacity. The first charge profile of C_{sp} electrode starts from a slope followed by a plateau at *ca.* 4.3 V. The charge

voltage corresponds to the reported value for C_{sp} electrode [6]. Such a high overpotential in charge, *idem.* 1.4 V, is actively related to the sluggish OER of the Li-O₂ batteries [2]. The first charge capacity of over 3000 mAh/g is delivered, with a coulombic efficiency of *ca.* 100%.

We notice that the charge profile at the first cycle is slightly different from the rest cycles, the slope at the low overpotential becomes less mild over cycling. Shao-Horn *et al.* suggest that the slope-stage is responsible for the surface decomposition and the plateau stage represents the bulk decomposition of Li₂O₂ at high overpotential [7]. According to their study, we may deduce that smaller Li₂O₂ particles (*i.e.* sphere), which have a larger surface / volume ratio are generated at the end of the first discharge, which accounts for a larger fraction of the lower overpotential surface delithiation. And since the second discharge, larger Li₂O₂ particles (*i.e.* toroid) are generated and less surface delithiation is performed.

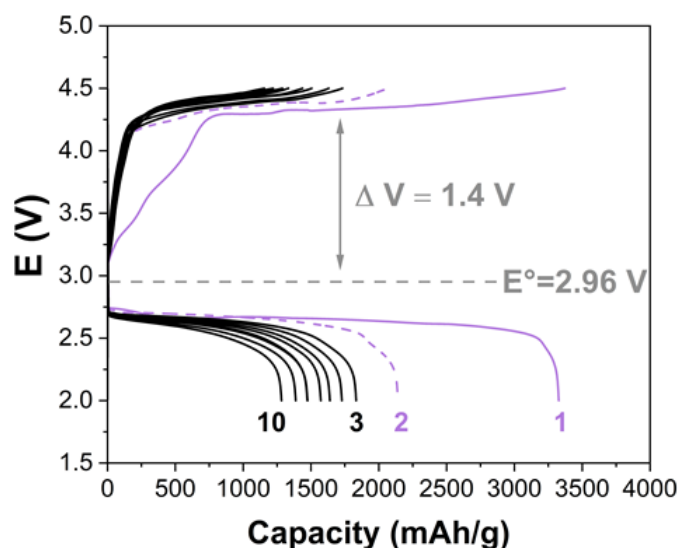


Figure A.- 7: (a) Discharge - charge cycling profiles of the Li-O₂ battery with C_{sp} electrode (in 80 / 20 wt. % of C_{sp} / PVDF). The first and the second cycle profiles are represented respectively in purple solid and dash lines, while cycles 3 to 10 are represented in black solid lines.

For the sake of clarity, we plot the discharge / charge capacities of C_{sp} electrode over cycling as a function of cycling number (Figure A.- 8). At the second cycle, there is a significant capacity fading of about 1000 mAh/g in both discharge and charge. We observe In the next cycles, although the capacity does fade, the rate of fade slows. A discharge capacity of *ca.* 1250 mA·h/g is still obtained after 10 cycles. The overpotentials of discharge / charge increase gradually over cycles. At the tenth cycle, we observe a variation of *ca.* 0.1 V in both overpotentials. Similar C_{sp} cycling behaviors are also observed by Bruce *et al.* with ether-based

electrolytes [6]. The rising overpotential in charge / discharge results actively from the limitation of charge transfer across insulating Li₂O₂ on the C_{sp} electrode [8]. Moreover, additive contribution may be the possible formation of side products (*i.e.* Li₂CO₃) [8]. These latter species require high potential to decompose, which in turn destabilize the electrolyte and cause also parasitic products [8]. As a result, they could not be deeply removed due to the potential barrier. Their accumulation may decrease the tri-phase boundary hence limiting the diffusion of Li⁺ ions and O₂, thus diminishing the ORR / OER [9]. A less active surface is available for the next deposition of Li₂O₂.

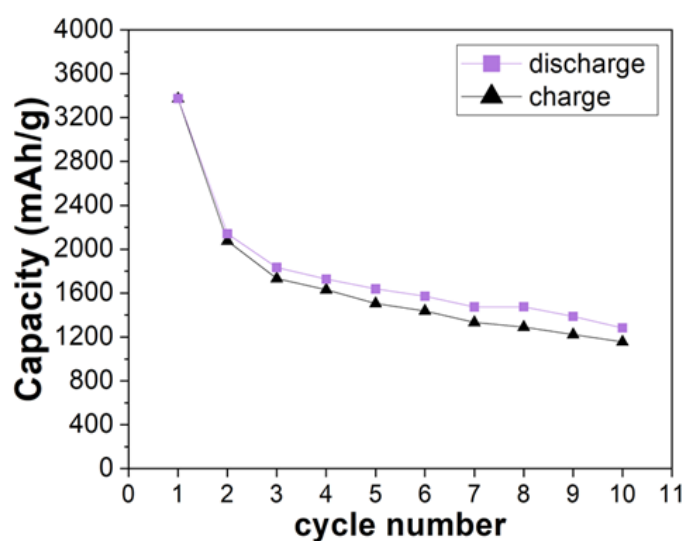


Figure A.- 8 : (a) Discharge - charge capacities of the Li-O₂ battery as a function of cycle number with C_{sp} electrode (in 80 / 20 wt. % of C_{sp} / PVDF).

1.b. Formulation (2) : 90 / 10 wt. % C_{sp} / PVDF

The higher C_{sp} content electrodes behave the same at the first cycle as those lower C_{sp} content electrodes (80 / 20 wt.%). The initial discharge capacities are dispersed between 3143 – 3551 mAh/g. We present here the example discharge – charge profiles of the C_{sp} electrode with the median initial capacities in Figure A.-9 (a). This C_{sp} electrode formulation shares the same initial discharge and charge potentials (*idem.* 2.7 V and 4.3 V, respectively) with the last formulation. It seems that such a difference in C_{sp} content does not affect their initial cycle performance. However, we notice a quicker capacity fading within the high C_{sp} content electrodes. For example, the example shown here in Figure A.-9 (b) results in a discharge capacity of less than 150 mAh/g. Even for the highest-discharge-capacity electrode, it remains

ca. 610 mAh/g at the tenth discharge, which is still twice less than the low C_{sp} content electrode. This difference capacity fading evolution may suffer from two factors. The first is the electrode wetting issue related to the binder content [10]. Besides, high C_{sp} content might be responsible for a larger fraction of side reactions compared to the formulation, especially, the side products could diminish the electrochemical behaviors as early mentioned in last section. Further quantification is required to understand this issue. However, this deviates from the main subject of the work. We keep focusing on the performance of MOF as active material performance in the main text. But this point of investigation keeps an open door for battery performance optimization.

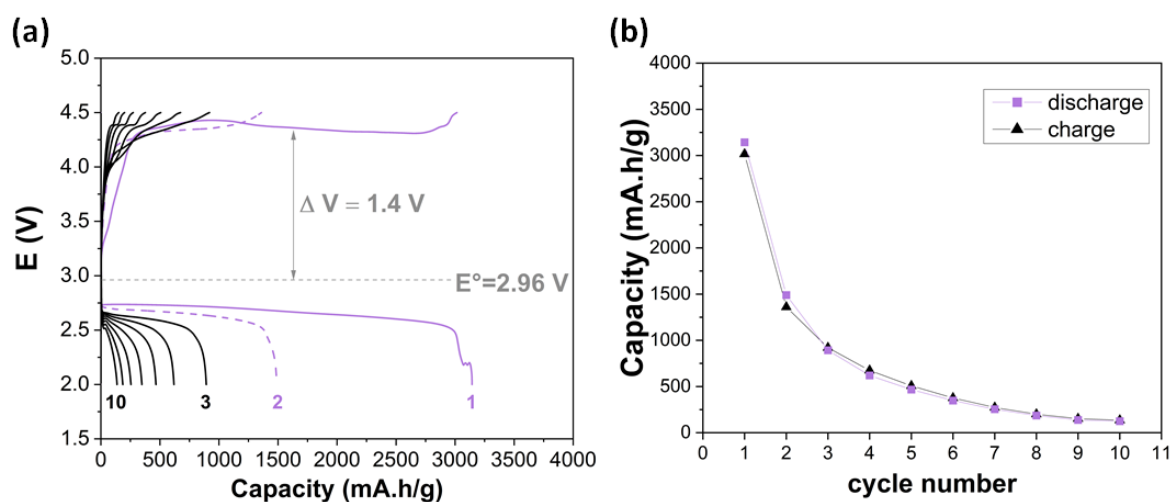


Figure A.-9 : (a) Discharge-charge cycling profile of the Li-O₂ battery with C_{sp} electrode (in 90 / 10 wt. % of C_{sp} /PVDF). The first and the second cycle profiles are represented respectively in purple solid and dash lines, while cycles 3 to 10 are represented in black solid lines. (b) The corresponding discharge / charge capacities with the evolution of cycle number.

1.c. References

- [1] D. Wu *et al.*, "Metal–Organic Frameworks as Cathode Materials for Li–O₂ Batteries," *Adv. Mater.*, vol. 26, n°20, pp. 3258–3262, 2014..
- [2] W.-J. Kwak *et al.*, "Lithium–oxygen batteries and related systems: potential, status, and future," *Chem. Rev.*, vol. 120, n°14, pp. 6626–6683, 2020.
- [3] L. D. Griffith, A. E. S. Sleightholme, J. F. Mansfield, D. J. Siegel, and C. W. Monroe, "Correlating Li/O₂ cell capacity and product morphology with discharge current," *ACS Appl. Mater. Interfaces*, vol. 7, n° 14, pp. 7670–7678, 2015.
- [4] M. Carboni, A. G. Marrani, R. Spezia, and S. Brutti, "Degradation of LiTfO/TEGME and LiTfO/DME electrolytes in Li–O₂ batteries," *J. Electrochem. Soc.*, vol. 165, n°2, p. A118, 2018.
- [5] C. M. Burke, V. Pande, A. Khetan, V. Viswanathan, and B. D. McCloskey, "Enhancing electrochemical intermediate solvation through electrolyte anion selection to increase nonaqueous Li–O₂ battery capacity," *Proc. Natl. Acad. Sci.*, vol. 112, n°30, pp. 9293–9298, 2015.
- [6] S. A. Freunberger, Y. Chen, N. E. Drewett, L. J. Hardwick, F. Bardé, and P. G. Bruce, "The Lithium–oxygen battery with ether-based electrolytes," *Angew. Chem. Int. Ed.*, vol. 50, n° 37, pp. 8609–8613, 2011.
- [7] B. M. Gallant *et al.*, "Chemical and morphological changes of Li–O₂ battery electrodes upon cycling," *J. Phys. Chem. C*, vol. 116, n°39, pp. 20800–20805, 2012.
- [8] A. C. Luntz and B. D. McCloskey, "Nonaqueous Li–air batteries: a status report," *Chem. Rev.*, vol. 114, n°23, pp. 11721–11750, 2014.
- [9] G. Gourdin, N. Xiao, W. McCulloch, and Y. Wu, "Use of polarization curves and impedance analyses to optimize the 'triple-phase boundary' in K–O₂ Batteries," *ACS Appl. Mater. Interfaces*, vol. 11, n°3, pp. 2925–2934, 2019.
- [10] F. Wang and X. Li, "Effects of the electrode wettability on the deep discharge capacity of Li–O₂ batteries," *ACS Omega*, vol. 3, n°6, pp. 6006–6012, 2018.

Appendix 5- *Ex situ* characterization of C_{sp} carbon cathode

1.a. XRD

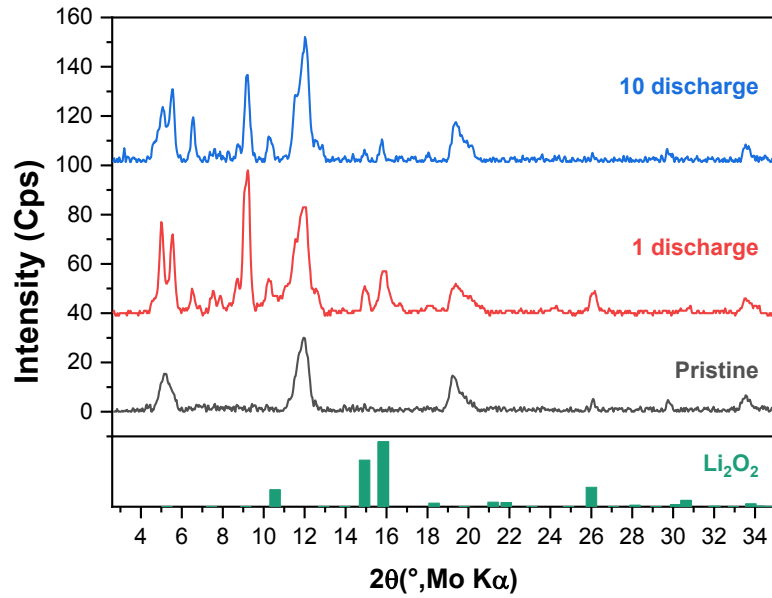
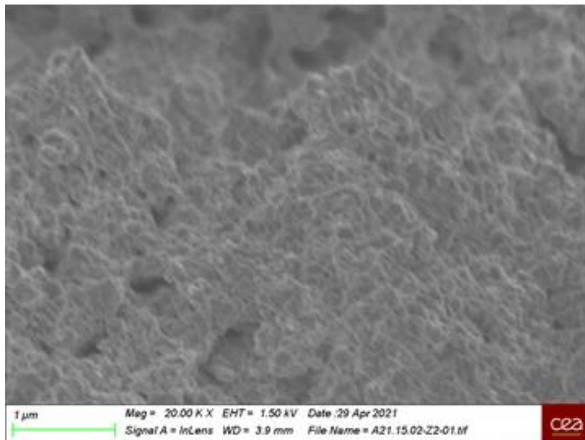


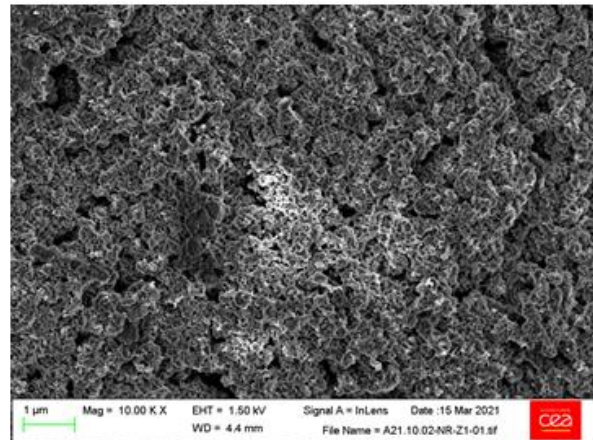
Figure A.- 10 : XRD patterns of pristine, 1 discharged, and 10 discharged C_{sp} electrode (90 / 10 wt.%).

1.b. MEB

1 discharge



2 discharge



pristine

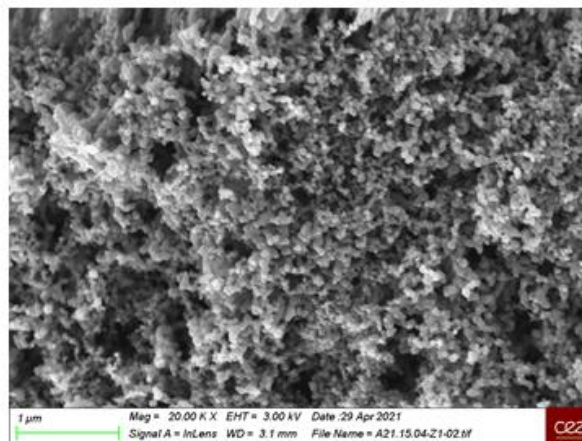


Figure A.- 11 : SEM images of 1 discharged, 2 discharged and pristine C_{sp} electrode (90 / 10 wt.%).